



**UNIVERSITÀ DEGLI STUDI DI TRIESTE**

**XXXI CICLO DEL DOTTORATO DI RICERCA IN**

**NANOTECNOLOGIE**

**SMART MATERIALS FOR ENERGY  
APPLICATIONS**

Settore scientifico-disciplinare: **CHIM/03**

**DOTTORANDA  
ANNA LENARDA**

**COORDINATORE  
PROF. LUCIA PASQUATO**

**SUPERVISORE DI TESI  
PROF. PAOLO FORNASIERO**

**CO-SUPERVISORE DI TESI  
DOTT. MICHELE MELCHIONNA  
PROF. CLAUDIO TAVAGNACCO**

**ANNO ACCADEMICO 2017/2018**



## ABSTRACT

In the last decades, electrochemistry has been regarded as a powerful tool to address some of the key challenges that in the framework of sustainability and green energy. In particular, the application of smart, hierarchical materials as electrocatalysts is generating new opportunities for interesting developments. Nanostructured carbon has been heavily employed as a fundamental component for the proposed catalytic materials due to its outstanding electronic and textural properties. This thesis focuses on the exploitation of strategically designed materials based on carbon as electrocatalysts to be used in devices such as new generation fuel cells, electrolyzers for the production of hydrogen peroxide and sensors for its electrochemical detection. Each of these devices is envisioned as a way of reducing the environmental impact, by either being a sustainable source of energy, or substituting energy consuming and non-environmentally friendly processes. In particular, a hybrid Pd/CeO<sub>2</sub>/C material, prepared through a strategic protocol that allows an intimate contact among the three phases, has been employed as anodic electrocatalyst in both Anion Exchange Membrane Fuel Cells (AEM-FC) and Direct Alcohol Fuel Cells (DAFCs) working in alkaline media and fed with biomass derived polyalcohols. Concerning H<sub>2</sub>O<sub>2</sub> electrosynthesis, N-doped carbon embedding Co nanoparticles have been studied for the Oxygen Reduction Reaction (ORR) in acidic environment, and the material's outstanding selectivity has been correlated to its N-type species distribution, as well as its porosity and the indirect electronic interaction between the doped carbon phase and the internal metal. Finally, a metal-free electrosensor for the detection of hydrogen peroxide has been produced exploiting the electronic properties of a -COOH decorated graphene, obtained through a controlled functionalization protocol. In all cases, the strategic synthetic procedure gives rise to materials with enhanced catalytic performances in terms of activity, selectivity and stability, and the work has been communicated through publication (already published or in the process of being published) in peer-reviewed journals.

## Table of abbreviations

°	Degree
° C	Degree centigrade
1,2-P	1,2-propanediol
AA	Ascorbic acid
ADAFC	Alkaline direct alcohol fuel cell
AEI	Anion exchange ionomer
AEM-FC	Anion exchange membrane fuel cell
AFC	Alkaline fuel cells
AFM	Atomic force microscopy
AOR	Alcohol oxidation reaction
atm	Atmosphere
BET	Brunauer-Emmett-Teller
BJH	Barrett-Joyner-Halenda
CA	Chronoamperometry
cm	Centimetre
CNS	Carbon nanostructure
CNT	Carbon nanotube
CPE	Constant phase element
CR-GO	Chemically reduced graphene oxide
CV	Cyclic voltammetry
DAFC	Direct alcohol fuel cell
DEFC	Direct ethanol fuel cells
DFT	Density functional theory
DMFC	Direct methanol fuel cell
DNA	Deoxyribonucleic acid
EASA	Electrochemically active surface area
EDX	Energy dispersive X-ray spectroscopy
Eg	Ethylene glycol
EIS	Electrochemical impedance spectroscopy
EOR	Ethanol oxidation reaction
EQ	Equivalent circuit

et al.	Et alli (and others)
eV	Electronvolt
FC	Fuel cell
FE	Faradaic efficiency
FFT	Fast Fourier transform
FT-EXAFS	Fourier Transform of the extended X-ray absorption fine structure
FT-IR	Fourier-transform infrared spectroscopy
g	Gram
G	Graphene
GA	Graphene acid
G-CN	Cyanographene
GCE	Glassy carbon electrode
GDE	Gas diffusion electrode
Glu	Glucose
Gly	Glycerol
GO	Graphene oxide
Gt	Gigatonne
HPLC	High performance liquid chromatography
h	Hour
HAADF	High angle annular dark field
HBE	Hydrogen binding energy
HOR	Hydrogen oxidation reaction
HR-TEM	High resolution transmission electron microscopy
Hz	Hertz
ICP-OES	Inductively coupled plasma-optical emission spectrometry
K	Kelvin
K-L	Koutecky-Levich
kW	Kilowatt
L	Litre
LF	Low frequency
LSV	Linear sweep voltammetry
M	Molar
mA	Milliampere

MC-FC	Molten carbonate fuel cell
MEA	Membrane electrode assembly
min	Minute
mmol	Millimoles
MOR	Methanol oxidation reaction
MWCNT	Multi-walled carbon nanotube
NMR	Nuclear magnetic resonance
NP	Nanoparticles
OBE	OH- binding energy
OCP	Open circuit potential
ORR	Oxygen reduction reaction
Par	Paracetamol
PA-FC	Phosphoric acid fuel cell
PANI	Polyaniline
PB	Prussian Blue
PBS	Phosphate buffer solution
PDA	Polydopamine
PEM-FC	Proton exchange membrane fuel cell
R	Resistance
RDE	Rotating disk electrode
RHE	Reversible hydrogen electrode
SCE	Saturated calomel electrode
SO-FC	Solid oxide fuel cells
STEM	Scanning transmission electron microscopy
SWCNH	Single walled carbon nanohorn
T	Temperature
TEM	Transmission electron microscopy
TF-RDE	Thin film rotating disk electrode
TGA	Termogravimetric analysis
TPD	Temperature programmed desorption
V	Volts
wt%	Weight percent
XANES	X-ray absorption near edge structure

XAS	X-ray absorption spectroscopy
XPS	X-ray photoelectron spectroscopy
XRD	X-ray diffraction
$\Omega$	Ohm

# TABLE OF CONTENTS

<b>Chapter 1: Introduction</b>	<b>1</b>
1.1 Global energy challenges: Electrocatalysis as a tool towards the path of sustainable chemistry	1
1.2 Fuel Cells	3
1.2.1 Changing the pH environment: Anion Exchange Membrane Fuel Cells (AEM-FC)	6
1.2.1.1 AEM-FC anodic electrocatalysts state of the art	7
1.2.2 Switching to other renewable fuels: Direct Alcohol Fuel Cells (DAFCs)	10
1.2.2.1 ADAFC anodic electrocatalysts state of the art	11
1.3 The ORR reaction: not only Fuel Cells	14
1.3.1 Combining metal nanoparticles with carbon-based materials for ORR: state of the art	16
1.4 H <sub>2</sub> O <sub>2</sub> sensing	19
1.4.1 Carbon nanostructures application in H <sub>2</sub> O <sub>2</sub> sensing	21
1.5 Motivation and research objectives	24
1.6 The scope of the dissertation	25
1.7 References	26
<b>Chapter 2: Nanostructured smart electrocatalysts for alkaline fuel cells applications</b>	<b>46</b>
2.1 Introduction	46
2.2 Nanostructured carbon supported Pd-ceria as anode catalysts for anion exchange membrane fuel cells	46
2.2.1 Results and discussion	48
2.2.1.1 Catalyst preparation	48
2.2.1.2 Morphologic characterization	49

2.2.1.3 DFT calculations	54
2.2.1.4 Electrochemical characterization	56
2.2.1.5 Fuel cell testing	58
2.2.2 Conclusions	59
2.3 Nanostructured carbon supported Pd-ceria as anode catalysts for anion exchange membrane fuel cells fed with polyalcohols	60
2.3.1 Results and discussion	61
2.3.1.1 Catalyst preparation	61
2.3.1.2 Morphologic characterization	61
2.3.1.3 Electrochemical characterization	65
2.3.1.4 Full Cell Testing	68
2.3.2 Conclusions	70
2.4 References	71
<b>Chapter 3: N-doped carbon encapsulated Co nanoparticles for selective H<sub>2</sub>O<sub>2</sub> electrocatalytic generation</b>	78
3.1 Introduction	78
3.2 Results and discussion	79
3.2.1 Catalyst preparation	79
3.2.2 Morphologic characterization	80
3.2.3 Electrochemical tests	85
3.3 Conclusions	97
3.4 References	98
<b>Chapter 4: Highly sensitive non-enzymatic metal-free H<sub>2</sub>O<sub>2</sub> sensor based on covalently functionalized acid graphene</b>	103
4.1 Introduction	103

<b>4.2 Electrocatalytic graphene-based systems for H<sub>2</sub>O<sub>2</sub> sensing</b>	103
<b>4.3 Results and discussion</b>	105
<b>4.3.1 Material preparation and morphologic characterization</b>	105
<b>4.3.2 Electrochemical characterization</b>	106
<b>4.4 Conclusions</b>	113
<b>4.5 References</b>	114
<b>Chapter 5: Conclusions</b>	119
<b>Appendix A: Review of the experimental methods used and experimental procedures</b>	122
<b>Appendix B: Materials &amp; synthesis</b>	139
<b>Appendix C: Apparatus</b>	142

## CHAPTER 1: Introduction

### 1.1 Global energy challenges: Electrocatalysis as a tool towards the path of sustainable chemistry

Throughout history, the civilization progress of human kind has been constantly driven by its ability to harness energy. All industrial and agricultural revolutions, that allowed an increasing fraction of the world population to access the possibility to heat and light their homes, fertilize and irrigate their crops, connect to one another, and travel around the world, are related to the ability to find, extract and use energy.<sup>1,2</sup> The world energy consumption in 2012 was 549 quadrillion British thermal units (or quad BTUs, where 1 quad BTU = 293 TWh). In the International Energy Outlook 2017 (IEO2017) Reference case, total world energy consumption is expected to rise from 575 quad BTUs in 2015 to 736 quad BTUs in 2040, that is, an increase of 28%. Most of it will occur in countries outside of the Organization for Economic Cooperation and Development (OECD), where strong, long-term economic growth is driving an increasing demand for energy. Non-OECD Asia (including China and India) alone accounts for more than half of the world's total increase in energy consumption over the 2015 to 2040 projection period.<sup>3</sup> Although consumption of non-fossil fuels is expected to grow faster than fossil fuels, fossil fuels still account for a projected 77% of energy use in 2040, with liquid fuels, mostly petroleum-based, remaining the largest world energy source.<sup>3</sup> From the perspective of climate change, expansion of the current fossil fuel-based energy infrastructure to meet the projected energy demand is predicted to add 2986-7402 Gt of CO<sub>2</sub> to the atmosphere by 2100, resulting in a mean rise in global temperature of 2.4–4.5 °C. The carbon dioxide (CO<sub>2</sub>) evolved by the fossil fuels use is the main player of the greenhouse effect, and its rising concentration in the environment has been related to climate change (temperature increase) and environmental issues such as increasing of sea water acidity and gradual erosion of coral reef. Given the graveness of the situation, the 2016 Paris Agreement on climate change has established strict rules for the decreasing of CO<sub>2</sub> emission. The strategies to tackle the CO<sub>2</sub> growing presence in the atmosphere involve the replacement of fossil fuels with renewable energy sources, and the capture and stocking of CO<sub>2</sub>. In this scenario, due also to the current fast depletion fossil fuels reserves, the world of research is looking at the development of new strategies for the efficient exploitation of renewable and alternative energy sources, leading humanity towards the path of higher sustainability.

Chemistry's contribution can affect widely the possibility of walking this path, by proposing chemical processes that are energy-saving, selective and make use of nontoxic and recyclable reagents and, likewise, by introducing efficient processes that allow the harvest of renewable energy sources in the most efficient way. In this context, electrocatalysis gives us the opportunity to exploit two crucially useful tools:

- Novel power source devices such as fuel cells (FCs);
- Environmentally friendly and less energy consuming ways of producing chemicals such as the use of electrolyzers.

Fuel cells are electrochemical devices that continuously convert the chemical energy of a redox reaction into electricity. What is generally referred as fuel is the compound undergoing oxidation at the anode, generating the electrons that, flowing towards the cathode, produce an electric current. At the cathode, the reduction reaction occurs, with oxygen from air being generally the molecule involved. Finally, the anodic and cathodic compartments are in contact through a membrane that allows ion crossing. Their potential as renewable energy sources have been studied thoroughly throughout the last decades. An electrolyzer works on the same principle, but if the driving force of a fuel cell is the spontaneous occurrence of the redox process at the designated potential, in an electrolyzer, an external electric current is used to drive forward a non-spontaneous redox reaction. If the source of the electricity is renewable, this device can be a valid strategy for substituting energy consuming industrial processing in the production of valuable chemicals. In order for both of these systems to work efficiently, they need to be equipped with smart electrocatalysts, that simultaneously are cheap and give adequate performances. Moreover, in the vision of lowering the energy consumption and environmental impact, substituting processes that are heavily energy consuming, complex and expensive is a critical path to follow. In this perspective, employing electrocatalysis as a way of detecting industrially relevant and ubiquitous molecules, such as hydrogen peroxide, represents an important asset for increasing sustainability. The present thesis has been dedicated to the design and development of novel nanostructured electrocatalysts in relation to the multi-disciplinary crusade for sustainability. The scope of the work targeted therefore different objectives, studying the possibility to increase efficiency in different crucial electrochemical reactions. The conceptual development of the nanostructured materials embraces the philosophy of multi-phase hierarchical approach. This strategy allows the assembly of smart materials where each phase plays a specific role, but also

links to the others in a synergistic way. The three key processes that were investigated are in connection with: i) fuel cell development, ii) synthesis of  $H_2O_2$  and iii) detection of  $H_2O_2$ .

## 1.2 Fuel cells

As already mentioned, fuel cells are devices that generate electricity through a redox reaction. Their status as a very promising energy technology is guaranteed by their high efficiency compared to the internal combustion engines (around 50% for the proton exchange membrane fuel cells (PEM-FCs) comparing with 15% for the internal combustion engines) combined with zero emissions. Fuel cells can be compared to batteries as they both convert chemical potential energy into electrical energy. However, where a battery holds a closed store of energy within it and once this is depleted the battery must be discarded or recharged by using an external supply of electricity to drive the electrochemical reaction in the reverse direction, a fuel cell can run indefinitely, as long as it is supplied with a source of fuel and a source of oxygen (usually air).<sup>4</sup> The history of fuel cells technology, dates back in 1839, when Sir William Grove discovered their operation principle. For 100 years, though, they remained little more than a scientific curiosity, until the first working 6kW fuel cell was built in the end of the 1950s by Francis T. Bacon. In the 1960s, NASA's Gemini Space Flights were the first space vehicles equipped with fuel cells: a 1kW PEM-FC was constructed and employed to provide auxiliary power requirements in the space vehicles and drinking water for the astronauts. The research and development of these technology devices kept going through the 1970s and 1980s, prompted by the national governments concerns over energy shortages and higher oil prices. In the beginning of the 1990s government policies to promote clean transport also helped driving the development of PEM-FC for automotive applications.<sup>5</sup> This trend has continued to grow in the last decades until in 2007 they started to become commercial in wide variety of applications ranging from transportation, to large power plants, to powering small portable devices. Until now, different kinds of fuel cells have been developed. The general classification discriminates them according to the nature of the electrolyte involved. Each type has its specific characteristics and offers specific advantages for different applications (Table 1).<sup>5</sup>

**Table 1:** Different kind of fuel cells for different electrolytes

	<b>Proton Exchange Membrane Fuel Cells (PEM-FCs)</b>	<b>Phosphoric Acid Fuel Cells (PA-FCs)</b>	<b>Molten Carbonate Fuel Cells (MC-FCs)</b>	<b>Alkaline Fuel Cells (AFCs)</b>	<b>Solid Oxide Fuel Cells (SO-FCs)</b>
<b>Electrolyte</b>	Polymer Electrolyte	Phosphoric Acid	Molten Carbonate	Alkaline solutions	Solid Oxide
<b>Temperature</b>	25-100°C	160-220°C	600-650°C	100-250°C 25-75°C	800-1000°C
<b>Fuels</b>	H <sub>2</sub> , alcohols, light hydrocarbons	H <sub>2</sub> , light hydrocarbons	H <sub>2</sub> , light hydrocarbons	H <sub>2</sub>	H <sub>2</sub> , hydrocarbons
<b>Applications</b>	Residential Portable Transport	Distribution	Industrial Distribution	Portable	Industrial

Proton exchange membrane fuel cells (PEM-FCs) are the most promising candidate as renewable power sources for transportation, stationary, and portable applications.<sup>6</sup> Their advantages are connected to their low operating temperature, high power density, and easy scale-up. They are generally equipped with Pt-based electrocatalysts and a polymer electrolyte membrane (generally Nafion®) as proton exchange medium. The major application of PEM-FCs is for automotive: the major motor companies are considering PEM-FCs due to their high power density and excellent dynamic characteristics as compared with other kind of fuel cells. The first cars were developed and started hitting the market between 2002-2007, but the world's first mass-market fuel-cell car, was the Mirai, that started being sold by Toyota in Japan between the end of 2014 and the beginning of the 2015. Soon, both Hyundai and Honda released their fuel cell model vehicles on large scale market.<sup>7</sup> In 2017, Germany launched the first fuel cell powered train, which will connect the cities of Cuxhaven, Bremerhaven, Bremervoerde and Buxtehude in the northern part of the country.<sup>8</sup> The functioning of a PEM-FC consists in a series of various and interrelated complex phenomena, including mass/heat transfer, electrochemical reactions, and ionic/electronic transport, as schematically shown in Figure 1.

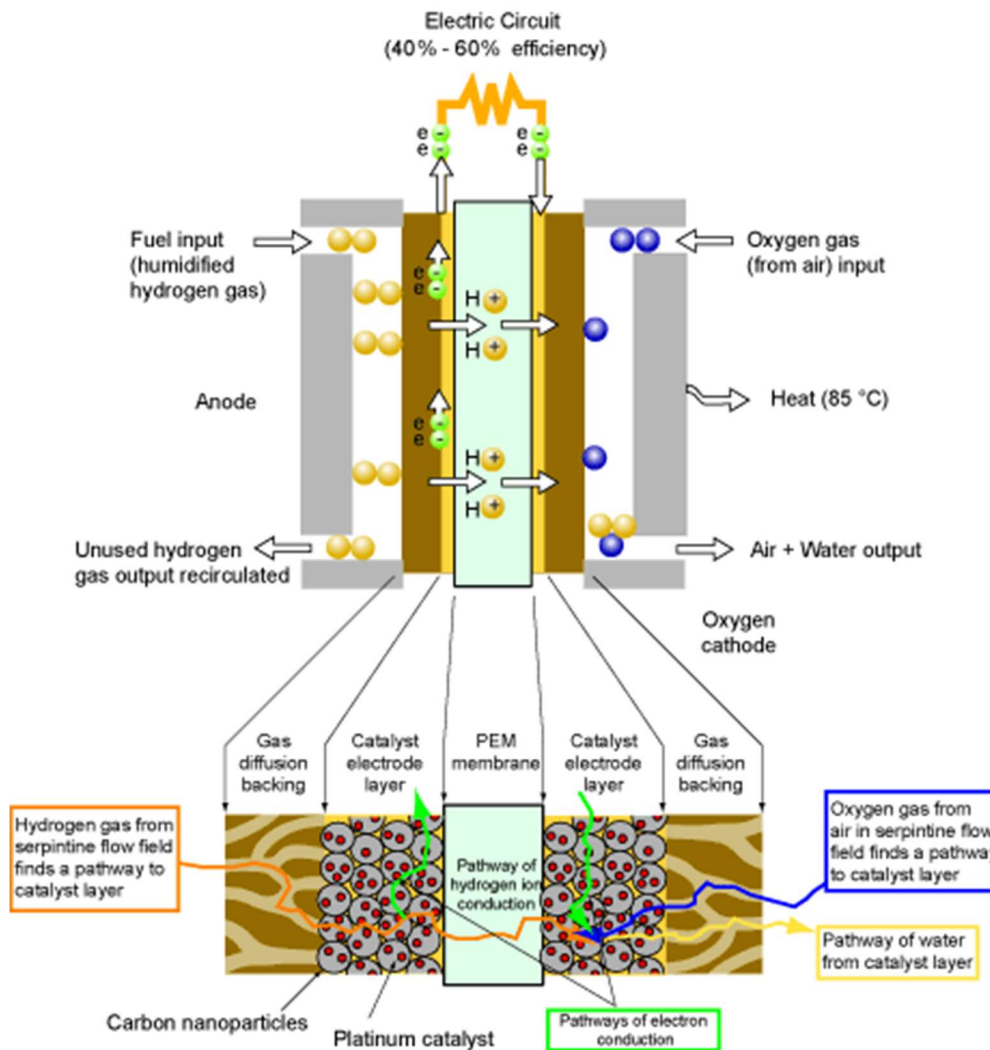
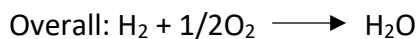


**Figure 1:** Schematic representation of processes occurring in a PEM-FC.<sup>9</sup>

The chemical reactions occurring in a PEM-FC are shown below:

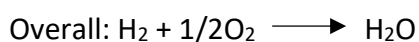
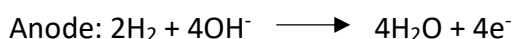


As stated before, the main barrier hindering the widespread employment of PEM-FC technology in this area of market remains their exceptionally high cost. Such cost is to a large extent connected with the precious metal-based electrocatalysts and membrane, components that also are deemed with durability issues, due to degradation during long-term operation.<sup>10</sup> In addition, there are important fuel-related aspects to consider to overcome the barriers to the commercialization of PEM-FCs. Hydrogen is an ideal fuel for PEM-FCs, although its production still leverages on typical reforming processes, thus jeopardizing the overall sustainability of fuel cell technology. The

hydrogen production from water electrolysis represents a valid alternative, generating the required highly pure hydrogen, but the efficiency of the process is still low and the cost of the electrolysis catalyst too high for a realistic translation to industrial set-ups. However, in principle electrolysis could be viable for generating the amounts of hydrogen for small devices such as FCs.

### 1.2.1 Changing the pH environment: Anion Exchange Membrane Fuel Cells (AEM-FC)

As already stated, state-of-the-art PEM-FCs are equipped with perfluorosulfonic acid polymer electrolyte and platinum catalysts. These two components are inherently depending on each other, since it is the harsh condition of working in corrosive acidic environment that makes necessary the employment of Pt catalysts. In fact, because of the working conditions, only noble metals can remain relatively stable, with even Pt sometimes not being stable enough.<sup>11</sup> In the latest decades, a solution was proposed: to break the reliance on precious metal catalysts, solid polymer electrolyte fuel cells with cationic membranes, i.e., anion exchange membrane fuel cells (AEM-FCs), have been suggested.<sup>12-15</sup> The idea of using alkaline electrolytes does not seem such a novelty, since alkaline fuel cells (AFCs) have already been developed and successfully applied in the NASA space programs a long time before. The concept here is different though, as a polymer version of alkali, rather than concentrated KOH solutions, is the target electrolyte, making this kind of cells closer to a PEM-FC than to the old version of AFCs. Operating under alkaline conditions, these cells can be equipped with non-noble metal catalysts, and on top of that, the pH environment can be kinetically favorable for the oxygen reduction reaction occurring at the cathode.<sup>15</sup> The working mechanism of an AEM-FC is similar but not identical to that of a PEM-FC: at the cathodic side of an AEM-FC, O<sub>2</sub> is reduced (ORR) and produces OH<sup>-</sup> ions, which transfer through the hydroxide ion-conductive polymer to the anodic side where they react with H<sub>2</sub> to produce water (HOR).<sup>16</sup> The chemical reactions occurring in a AEM-FC are shown below:



In the overall reaction, both PEM-FC and AEM-FC produce water as a byproduct. However, in contrast to PEM-FC technology, in an AEM-FC water is generated at the anode (twice as much as in

a PEM-FC, per electron), while at same time water is a reactant at the cathode. This distinctive water transport scenario, represent a unique feature of AEM-FCs, which needs to be addressed accordingly by tuning the properties of the membrane, in order to obtain the required hydration of the cathode, while preventing the flooding of the anode. Moreover, the use of a much more diverse selection of potential fuels is possible because their oxidation becomes kinetically favorable in alkaline media. In an attempt to make possible the development of liquid electrolyte-free AFCs, a number of groups have devoted research effort to the fabrication and engineering of anion-exchange membranes and ionomer solutions.<sup>17-22</sup> Over the last decade, developments in anion conducting polymers and membranes technology led to a significant increase in OH<sup>-</sup> conductivities, that now approach the levels of H<sup>+</sup> conductivity observed in low-pH PEM equivalents.<sup>23</sup>

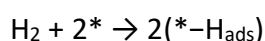
#### **1.2.1.1 AEM-FCs anodic electrocatalysts: state of the art**

The main desired advantage of AEM-FCs over PEM-FCs is the expected ability of the former to operate with platinum-free catalysts for both HOR and ORR. As far as the cathodic process is concerned, the inherently fast kinetics of ORR in alkaline media allowed the study of several different unsupported and supported platinum-free catalysts, from silver metal, which is precious by definition but abundant and relatively inexpensive,<sup>24</sup> through metal oxides, including various forms of MnO<sub>2</sub>,<sup>25,26</sup> Co<sub>3</sub>O<sub>4</sub> grown on N-doped graphene<sup>27</sup> and metal-free catalysts based on carbon nanostructures, including carbon nanotubes (CNTs) and graphene.<sup>28-30</sup> Lately, major attention has been devoted to transition-metal-coordinating nitrogen-doped carbon materials, the so-called M-N/C catalysts. Their use actually began in the 1960s, when it was discovered the ORR activity of a cobalt phtalocyanine.<sup>31</sup> From then on, the pyrolysis of transition-metal macrocycles has been investigated in order to improve their ORR activity and stability in alkaline and acidic conditions.<sup>32-34</sup> More recently, the expensive macrocycle precursors were replaced with a wide variety of more common and cost-effective nitrogen precursors (ammonia, acetonitrile, amines, etc.) and metal coordinating polymers (polyacrylonitrile, polypyrrole, polyaniline, ethylenediamine, and cyanamide) and combined with different transition-metal salts (sulfates, nitrates, acetates, hydroxides, and chlorides), and carbon supports (Vulcan XC-72, Ketjenblack, Black Pearls, etc.).<sup>35-45</sup> While almost every combination of transition-metal, nitrogen, and carbon precursors, if simultaneously pyrolyzed, can yield materials with a certain ORR activity, in order to obtain

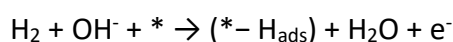
catalysts with truly remarkable performances, a careful choice of precursors and supports, as well as a fine tuning of the synthesis conditions is required.<sup>46</sup> The research progress in this field finally led to the development of pyrolyzed Fe–N/C catalysts, which ORR activity is now in fact comparable to, or even higher than, that of Pt-based catalysts in basic media.<sup>47</sup> The removal of Pt has been proven, however, to be significantly more challenging for HOR. The mechanism of HOR in alkaline media, has been widely agreed to proceed through a combination of the following steps:

- (A) dissociative adsorption of molecular H<sub>2</sub>,
- (B) electron transfer from molecular H<sub>2</sub> to the catalyst,
- (C) discharge of the adsorbed hydrogen atom.

The first step (A), which is known as the Tafel reaction,<sup>48</sup> proceeds as reported in the equation below:

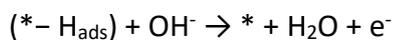


where H<sub>2</sub> is molecular dihydrogen in the vicinity of the catalyst surface, \* is an active site, and H<sub>ads</sub> is a chemisorbed hydrogen atom. In order for this step to occur, an oxide-free metal surface needs to be available for the chemisorption of H<sub>2</sub> up to an anode potential of 0.1 V versus the reversible hydrogen electrode (RHE) and preferably higher, as it is required for the formation of the H<sub>ads</sub> intermediates in the relevant potential range.<sup>49</sup> This requirement is not very easy for metals less noble than platinum. The electron transfer from molecular H<sub>2</sub> to the catalyst, known as the Heyrovsky reaction<sup>50</sup> proceeds as follows



where OH<sup>-</sup> is a hydroxyl ion in the vicinity of the catalyst surface. The species is debated not to be OH<sup>-</sup> but more likely OH<sub>ads</sub>, a chemisorbed hydroxide, with the assumption that the reaction to form water is preceded by hydroxide adsorption.<sup>51–53</sup> If this is true, in alkaline media the catalyst surface is required to provide active sites for the co-adsorption of hydrogen atoms and hydroxide species, whereas all the accessible active sites in acidic environment are dedicated to the chemisorption of H<sub>2</sub>. This could be part of the reason why catalysts in general often exhibit several orders of magnitude lower electrochemical activity towards HOR at high pH compared with low

ones.<sup>54-57</sup> The last step, the discharge of the adsorbed hydrogen atom is called the Volmer reaction<sup>58</sup>:



Lately, substantial effort has been dedicated to understand the pH effect on Pt catalyzed HOR since the exchange current in the two different environments is very different, with the one at high pH being 100 times smaller.<sup>54-56,59</sup> Lately it has been observed that higher catalytic for HOR in an alkaline medium is correlated to the combined presence of surface H binding sites and neighboring oxygen bearing sites in the relevant anode potential range, giving rise to the development of bifunctional catalysts containing an added oxophilic metal component working in tandem with Pt or Pd nanoparticles.<sup>51,53,60</sup> Another interpretation involves hydrogen binding energy (HBE)<sup>55,59,61</sup> on the surface of the catalyst as a relevant descriptor for HOR activity on several metals,<sup>62,63</sup> and ascribe to its variation the two orders of magnitude difference in HOR activity of Pt in acid and in base. Stronger HBE in alkaline electrolytes was proposed recently as the reason for the slower kinetics. Following this line, enhanced HOR kinetics in base could be achieved by tailoring the structural properties of the surface of the catalyst or by combining Pt with other transition metals to obtain a weaker H bond. For example it has been proven that structures with extended surface structure like Pd and Pd nanotubes are more active than nanoparticles.<sup>64,65</sup> In accordance with this principle, it has been observed that generally larger catalyst particles exhibit higher specific HOR activity.<sup>66-68</sup> It has been proposed that even the enhanced activity obtained by adding an oxophilic component could be attributed to lowered Pt-HBE by an electronic effect instead of by the presence of the added metal.<sup>69</sup> Recent reports go further in enforcing this statement observing higher HOR activity at Ru@Pt or Ni@Pt core-shell nanoparticles and excluding a bifunctional mechanism since no Ru or Ni are detected on the surface of the catalyst.<sup>61,70</sup> Anyway, considering HBE as the parameter for the activity of a catalyst for this reaction is to be considered debatable, since the adsorption of oxygenated species can also contribute to the pH-dependent shifts in the voltammetric peaks taken as evidence of this phenomenon.<sup>71,72</sup> The development of catalysts not including Pt or Pd is still in its early days with only a few very recent reported studies, in contrast with the many more reports on noble metal-free ORR catalysts. Active reported HOR catalysts of this kind include NiCoMo ternary alloys and Ni supported, nitrogen- doped carbon nanotubes (Ni/N-CNT).<sup>73,74</sup> The reported activities, anyway, are

still far from the ones obtained with Pt. The main challenge in this case is designing a catalyst that do not passivate due to excessive surface oxidation at the working potential needed to promote HOR (0.1 V vs RHE), since this is the reason why the performance stability and achievable power density are limited with these materials.

### **1.2.2 Switching to other renewable fuels: Direct Alcohol Fuel Cells (DAFCs)**

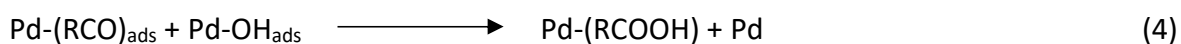
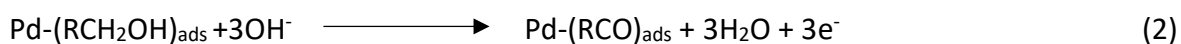
An interesting alternative to hydrogen as a fuel is represented by alcohols derived from renewable sources such as biomasses. The devices which use this kind of fuel are named Direct Alcohol Fuel Cells (DAFCs). DAFCs are acid-based fuel cells, while alkaline direct alcohol fuel cells (ADAFCS) operate in alkaline media and both directly oxidize alcohols, generating electricity in the process. The main advantages they guarantee when compared with their hydrogen fed counterparts (PEM-FCs and AEM-FCs) are related to the liquid state of the alcohols, which makes them easily transportable and handled, as well as highly energy dense. Moreover, many of them can be obtained from biomass. Direct Methanol Fuel Cells (DMFCs) are considered the most promising DAFC systems for portable applications, with the main challenges before worldwide distribution being not different from those faced by hydrogen-fed FCs. Usually, in fact, the DMFC contains a membrane-electrode assembly (MEA) constituted by an anode catalyst based on Pt/C, a Nafion membrane and a Pt/C cathode, the parts known to be the reason for the exorbitantly high cost of PEM-FCs. Moreover, the poor kinetics of the anodic methanol oxidation reaction, poor proton conductivity, and methanol crossover through the polymer electrolyte membrane greatly affect the performance of the cell, which consequently exhibits lower power density compared to the PEM-FCs. As in the case of hydrogen fuel cells, the alkaline environment generates several advantages for DAFCs related to the better kinetics both at the anode and at the cathode,<sup>75,76</sup> including:

- (i) the faster kinetics of the ORR and alcohol oxidation reactions allow the employment of low-cost, non-noble-metal electrocatalysts;
- (ii) alcohol oxidation reactions are allowed at low anodic overpotential;
- (iii) alcohol cross-over is reduced;
- (iv) reduced risks of corrosion, thus ensuring longer life to the electrode materials.

Moreover, while in acidic media CO poisoning is so strong that even Pt easily undergoes its effect, at high pH it is much weaker, making it possible to switch to cheaper electrocatalysts without the risk of them being poisoned.<sup>77,78</sup>

### 1.2.2.1 ADAFCs anodic electrocatalysts: state of the art

The two most investigated primary alcohols are methanol and ethanol, while among the polyhydric alcohols, glycerol and ethylene glycol represent first choices. The popularity of the mentioned polyalcohols stems from their unique advantages of high gravimetric and volumetric energy densities, combined with the fact that they are nontoxic and can be obtained from biomasses. The alcohol oxidation reaction (AOR) is a complex multi-electron process, involving 6 electrons for methanol oxidation up to 10 to 18 electrons for the other alcohol fuels to reach completion. Lately palladium-based catalysts have attracted major attention as anodic electrocatalysts for DAFCs. The interest in Pd stems from its enhanced electrochemical kinetics in alkaline media. In particular, much effort is being devoted to the understanding of the mechanism underlying its catalysis.<sup>79,80</sup> The so-called bifunctional theory<sup>81</sup> claims that the complete electro-oxidation of primary alcohols in alkaline media requires the activation of water at OH adsorbed species ( $\text{OH}_{\text{ads}}$ ) at the catalyst surface, in accordance with the equations below:



It has been proven that the rate determining step is the one described by equation 4, leading to the strict dependence of the rate of the AOR on the coverage of the adsorbed acyl and hydroxyl species,  $\text{RCO}_{\text{ads}}$  and  $\text{OH}_{\text{ads}}$ , on the surface of the catalyst. Several papers report that nanostructured catalysts induce faster hydroxyl adsorption, and that combining Pd with metal oxides (such as NiO, CeO<sub>2</sub>, Co<sub>3</sub>O<sub>4</sub>, and Mn<sub>3</sub>O<sub>4</sub>) can greatly enhance their performance in terms of both activity and stability, as the metal oxide can promote  $\text{OH}_{\text{ads}}$  species formation on the surface of the material as well as the so-called spillover of the primary oxide.<sup>82-85</sup> Therefore, much effort is

being devoted to the design of Pd-based bimetallic and ternary catalysts.<sup>86</sup> As already stated, methanol is the first and most studied as fuel among the primary alcohols: its oxidation reaction (MOR) has attracted attention because of the simplicity of its electrocatalysis. A relatively small number of electrons is involved (6 for the complete oxidation), and the C-H activation is generally easier compared to the C-C activation. Its main disadvantage is its toxicity. Pt is still the metal that gives the best catalytic activity for the reaction, but it has been proven that Pd's activity can be greatly enhanced by coupling it with another metal, often nickel, in the alloyed<sup>87,88</sup> form or in the oxide form.<sup>83,89</sup> The promoting effect of Ni is associated both to the surface transformation it undergoes in alkaline media, that generates a layer of nickel hydroxide, and the supposed anti-poisoning properties in combined materials as PdNiO/C. Recently some non-precious metal oxides have been proposed as valid electrocatalysts for methanol oxidation. A material based on mesoporous zeolite homogeneously decorated with tin oxide nanocrystals was reported by Shi's group<sup>90</sup> as an active and stable electrocatalyst for MOR, with performances comparable to Pt/C. Wu et al. reported a Co<sub>3</sub>O<sub>4</sub>/NiO core-shell nanowire array, prepared through a combination of hydrothermal and electrodeposition techniques, whose synergistic behavior due to the core-shell architecture made MOR possible at low potential and with fast kinetics.<sup>91</sup> As a deeper investigation on the electrocatalytic properties of NiO<sub>x</sub> and MnO<sub>x</sub>, Saleh's group<sup>92</sup> reported a study on the behavior of NiO<sub>x</sub> and MnO<sub>x</sub> nanocomposites electrodeposited on glassy carbon. Apparently, the enhanced catalytic activity is strictly related to the deposition order, with a preference for the configuration with NiO<sub>x</sub> sitting on the MnO<sub>x</sub> surface, because of the superior adsorption ability of MeOH on the MnO<sub>x</sub>. Due to the already mentioned toxicity issues, research efforts are being made towards the substitution of methanol with the nontoxic, renewable ethanol. Ethanol oxidation reaction (EOR) is definitely more complex than methanol's, involving 12 electrons for the process to reach completion and partial 2-electron and 4-electron pathways for CH<sub>3</sub>CHO and CH<sub>3</sub>COOH production, respectively.<sup>93</sup> Since the hardest step is the breaking of the C-C bond, the dominating process will be the partial oxidation, leading to a lower efficiency in the cell, since the number of electrons exchanged is lower.

Pd has been proven to be a much more efficient catalyst than Pt for EOR in alkaline solution, for this reason, most of the recent literature consists in Pd-based bimetallic materials such as Pd-Ag,<sup>94-97</sup> Pd-Ni,<sup>98-102</sup> Pd-Sn,<sup>103-105</sup> Pd-Pb,<sup>106</sup> Pd-Tb,<sup>107</sup> Pd-Bi,<sup>108</sup> Pd-In<sub>2</sub>O<sub>3</sub>,<sup>109</sup> Pd-NiO and Pd-CeO<sub>2</sub>,<sup>85</sup> as well as ternary catalysts, such as Pd-Ir-Ni,<sup>110</sup> Pd-Ru-Sn,<sup>104</sup> FeCo@Fe@Pd,<sup>111</sup> and Pd-Fe<sub>2</sub>CoO<sub>x</sub>.<sup>112</sup>

Various *in situ* spectroscopic techniques have been successfully employed to investigate the mechanisms of Pd-catalyzed EOR, revealing the concurrent contribution of different factors such as the pH of the electrolyte, the potential applied, and the absorption of acyl and hydroxyl species. Recently, Fang et al.<sup>113</sup> used *in situ* FT-IR spectroelectrochemistry to demonstrate that there is a correlation between the breaking of the C-C bond and the exact pH of the electrolyte. At pH 14 in fact only partial oxidation occurs, with acetate as the only oxidation product of the reaction, while at pH 13 the C-C bond breaks leading to the formation of carbonate. This observation leads to the conclusion that at higher pH the oxidation of ethanol on Pd is less efficient. Another study by Yang et al.<sup>114</sup> is focused on the investigation of the role of the applied electrode potential on the C-C bond cleavage employing *in situ* attenuated total reflection surface enhanced infrared adsorption spectroscopy (ATR-SEIRAS). They propose two different mechanisms occurring whether working at open circuit potential (OCP) and lower (<0.1 V), or at high anodic potential (>0.4 V), leading respectively to the formation of either CO<sub>2</sub> or CH<sub>3</sub>COO<sup>-</sup> through an adsorbed acyl species (CH<sub>3</sub>CO<sub>ads</sub>). The relevance of water and OH<sub>ads</sub> species on the EOR mechanism in alkaline media has been recently demonstrated through an *ab initio* molecular dynamics simulations study by Sheng et al.<sup>115</sup> The mechanism they propose for EOR in alkaline medium goes through a concerted-like dehydrogenation pathway in which OH<sub>ads</sub> plays a critical role. A first step where OH<sub>ads</sub> are formed is followed by water dissociation and subsequent formation of fresh OH<sub>ads</sub>, giving rise to further dehydrogenation. Therefore, the complete catalytic cycle consists in ethanol decomposition and water dissociation. Observation from *in-situ* FT-IR spectroscopy validate this mechanism which does not involve the formation of several intermediates, that are indeed not observed experimentally. As far as polyhydric alcohols are concerned, the most studied are ethylene glycol (EG) and glycerol (Gly), together with the lately introduced 1,2-propandiol, 1,3-propandiol and 1,4-butandiol.<sup>116</sup> Reports on EG and Gly oxidation come mainly from the group of Vizza.<sup>117</sup> As occurred with ethanol, complete oxidation of polyalcohols has yet to be achieved, with general production of a mixture of species. Ozoemena et al. recently reported an FeCo@Fe@Pd core-shell-shell nanocatalyst, supported on carboxyl-functionalized multi-walled carbon nanotubes able to oxidize EG and Gly, with high selectivity, to carbonate.<sup>118</sup> The study of the reaction mechanism led to the assumption that, compared to Pd/MWCNT-COOH, FeCo@Fe@Pd/MWCNT-COOH has a stronger ability to break the C-C bond, thereby producing a larger amount of carbonate. This results are quite remarkable, considering that the total oxidation of these alcohols was not achieved with any of the previously proposed Pd-based catalysts (including Pd/C, PdNi/C, and PdAu/C,<sup>119</sup> PdRh/C,<sup>120</sup>

PdAu/C and PdNi,<sup>121</sup> and PdPtBi/C<sup>122</sup>). The design of the Pd-CeO<sub>2</sub>/C hybrid material I will propose as anodic electrocatalyst for fuel cells working in alkaline media was the inspired by the rationalization of the information collected through the examination of the cited past studies.

### 1.3 The ORR reaction: not only Fuel Cells

The main fuel cell cathodic half reaction is the reduction of oxygen. For this reason, it has been extensively studied throughout the years. The oxygen reduction reaction (ORR), as reported in the equations below, can in general lead to two different products: H<sub>2</sub>O<sub>2</sub> through a 2-electron pathway and H<sub>2</sub>O through a 4-electron pathway. For fuel cell performance, the desired mechanism is the direct 4-electron reduction process leading to H<sub>2</sub>O, with the formation of hydrogen peroxide considered as an undesired side reaction that can often affect the stability of the proton exchange membrane.<sup>123</sup> However, in the last decades, the electrochemical selective production of H<sub>2</sub>O<sub>2</sub> is becoming increasingly popular as an alternative to the industrial process currently employed.<sup>124</sup> ORR is considered a challenging process, whose mechanism goes through a proton coupled electron transfer, where the comparative rate of the proton and electron transfer can strongly affect the selectivity. Moreover, the obtained product is affected to large extent by the pH of the solution in which the reaction takes place.<sup>125</sup>

**Table 2:** O<sub>2</sub> reduction half-reactions in acidic and alkaline aqueous medium.

In acidic environment:	$E^0_{\text{redox}}$ (V vs NHE)
$O_2 + 4H^+ + 4e^- \xrightarrow{4e^-} 2H_2O$	1.23
$O_2 + 2H^+ + 2e^- \xrightarrow{2e^-} H_2O_2$	} $2e^-+2e^-$ 0.70
$H_2O_2 + 2H^+ + 2e^- \xrightarrow{2e^-} 2H_2O$	
In alkaline environment:	
$O_2 + 2H_2O + 4e^- \xrightarrow{4e^-} 4OH^-$	0.40
$O_2 + H_2O + 2e^- \xrightarrow{2e^-} HO_2^- + OH^-$	} $2e^-+2e^-$ -0.06
$HO_2^- + H_2O + 2e^- \xrightarrow{2e^-} 3OH^-$	

A recent study by Tse et al.<sup>126</sup> goes deep into the role of proton transfer kinetic in the product formation, controlling the proton transport to the Cu-based catalyst through a lipid-modified electrode. The results suggested that the formation of hydrogen peroxide is linked to a mismatch

between proton and electron transfer rates, where, specifically, faster proton transfer favors H<sub>2</sub>O<sub>2</sub> evolution, while sluggish proton flux favors O<sub>2</sub><sup>-</sup> formation. In order to selectively obtain H<sub>2</sub>O, the proton transfer rate must match the rate of O-O breaking. This insight on the complexity of the task of obtaining selectively one single product through this reaction supports the need to design materials with tunable properties, capable of acting on the proton transfer rate. Lately, density functional theory (DFT) calculations have been employed as a tool for designing catalysts by rationalizing their behavior towards oxygen reduction. Since the electroreduction of O<sub>2</sub> to H<sub>2</sub>O<sub>2</sub> involves two coupled electron and proton transfers<sup>127</sup>



where \* denotes an unoccupied active site, and HOO\* denotes the single adsorbed intermediate for the reaction, in order for the catalyst to provide high activity and selectivity, the kinetic barriers for (1) and (2) need to be minimized, and the reduction or dissociation of HOO\* needs to be inhibited, in order not to favor the formation of O\* and OH\*, which are the intermediates of the four-electron reduction to water. The effects playing their part in this process, are therefore both ensemble and electronic. The binding energy of HOO\*, which is a key parameter for the catalyst activity, is controlled by electronic effects, which can be tuned by varying the catalyst materials. Selectivity, on the other hand, can also be controlled by geometric (or ensemble) effects, which are associated with the geometric arrangement of atoms on the catalyst surface.<sup>128,129</sup> By controlling the geometry of the binding site it is possible to destabilize O\* with respect to HOO\*, improving the selectivity. Computational modelling of the adsorption of HOO\* and O\* on a Pt(111) and Pt<sub>3</sub>Ni surface has provided information on the preferred binding sites for the two.<sup>130</sup> As HOO\* normally binds onto atop sites whereas O\* binds onto hollow sites, eliminating hollow sites will specifically destabilize O\*, without necessarily changing the activity.<sup>131</sup> Putting together experimental and computational studies, a Volcano plot was produced in order to pinpoint the most promising materials.<sup>132</sup> The experimental overpotentials required to reach a current density of 1 mA/cm<sup>2</sup> were compared with the theoretical overpotential for the formation of the intermediate HOO\* ( $\Delta G_{\text{HOO}}$ ), and these considerations were employed to develop a catalyst based on Pt-Hg nanoparticles.<sup>131,133</sup> Selectivities as high as 92%, at positive potentials and under acidic conditions, have been reached with other noble metals such as Pt,<sup>134</sup> or alloys of them such

as Au-Pd,<sup>135</sup> proving that ORR is indeed a successful approach for H<sub>2</sub>O<sub>2</sub> production, giving though overall not satisfying performances for market translation, also considering the cost and geopolitical dependence of the precious metals

### **1.3.1 Combining metal nanoparticles with carbon-based materials for ORR: state of the art**

Throughout the latest decades, the potential application of carbon nanostructures as electrocatalysts for ORR has been investigated extensively, either in combination with metals or as completely metal-free catalysts. Although pure carbon catalysts are known not to be efficient for ORR, the doping of the carbon with heteroatoms, particularly N, is a powerful strategy to boost their catalytic activity of the carbon material, for the mentioned reaction<sup>29,136</sup> as well as for other electrocatalytic conversions.<sup>137–139</sup> There are several synthetic approaches to access N-doped carbon nanostructures, such as arc discharge,<sup>140</sup> laser ablation,<sup>141</sup> chemical vapor deposition,<sup>142</sup> injection,<sup>143</sup> autoclave systems<sup>144</sup> and pyrolysis.<sup>145</sup> Among these methods, pyrolysis of N-containing organic precursors has certainly the advantage of simplicity. Typically, it is performed by using high temperature treatments under inert atmosphere of a suitable organic molecule in presence of a carbon nanostructure acting as a scaffold or more frequently of a metal acting as catalytic seed. Various parameters affect the quality of the doping, including final temperature, the ramp rate, the time of residence and the inert gas flow; consequently, different types of N-species with variable % distribution can be generated: a) graphitic N, b) pyridinic N, c) pyrrolic N, d) pyridonic N, e) N oxides. The ratio between the different types of N atoms can affect ORR catalysis both in terms of activity and selectivity. Many studies have been devoted to the unraveling of the intimate role of the N atoms in the activation of oxygen. The enhanced activity has been associated to the electron deficiency of the carbon atoms surrounding the N moieties, which is able to facilitate the ORR by attracting electrons from the anode.<sup>145</sup> More so, the modified band structure resulting from the N-doping lowers the work function at the C/O<sub>2</sub> interface as compared to undoped nanocarbons.<sup>146</sup> As far as selectivity is concerned, N content and type of N species are still involved: there seems to be a correlation between the N content, the selectivity towards H<sub>2</sub>O<sub>2</sub>; moreover, reports indicate that the pyrrolic N atoms are the ones responsible for favoring the two-electron pathway. In fact, materials treated at higher temperature, with a lower content in pyrrolic N atoms showed lower H<sub>2</sub>O<sub>2</sub> production. The surface area and porosity of the carbon also play a critical role in selectivity, with mesoporosity reportedly

favoring H<sub>2</sub>O<sub>2</sub> formation. Regarding the importance of N atoms distribution, Qu et al.<sup>147</sup> reported their study on how the pyrolysis temperature and the thickness of the N-doped graphitic layer affected the catalyst selectivity. They prepared a N-doped mesoporous carbon network deriving from polydopamine-graphene oxide, and when the precursor was pyrolysed at 900°C, the authors observed an enhanced selectivity towards water production, as a consequence of converting most of pyridinic and pyrrolic N, that are less thermally stable, to graphitic N. Carbon nanostructures can be combined with metal components to create hybrids or composites with improved performance toward ORR. Wang et al.<sup>148</sup> have studied extensively the ORR catalytic activity of carbon supported Pt nanoparticles. Their work investigates systematically the influence of the type of carbon nanoscaffold (amorphous carbon, carbon nanotubes and graphene) on the catalytic performance. They observed in full cell testing that when the catalyst is compressed in the membrane electrode assembly, the fast stacking of graphene sheets inhibits the catalytic activity of the composite material by locking away the Pt active sites, while carbon nanotubes due to their tridimensional structure proved to be the best support for the metal center, yielding very high ORR performances. This is likely correlated to the ability of MWCNTs to construct an ordered catalyst layer, that increases the accessibility of the catalytic metal centers to the O<sub>2</sub> molecules. More cost-effective materials were proposed consisting in non-precious transition-metal oxides, such as manganese oxide<sup>149,150</sup> and iron oxide<sup>151,152</sup> supported on CNTs or graphene. Co<sub>3</sub>O<sub>4</sub>, another non-precious metal oxide, is known as a poor electrocatalyst for ORR. However, upon combination with N-doped carbon supports, the performances can be considerably improved, presumably, following synergistic coupling effects between the metal oxide nanoparticles and the carbon phase, with the latter providing excellent electrical conductivity. A representative example was published by Liang et al.<sup>153</sup> who reported N-doped graphene supported Co<sub>3</sub>O<sub>4</sub> nanoparticles as a highly efficient ORR catalyst. Such catalytic system was later outperformed by substituting the CNTs support with graphene.<sup>154</sup> As already mentioned, an entire class of materials based on transition-metal-coordinating nitrogen-doped carbon obtained by pyrolysis, called M-N/C catalysts, has been studied extensively as electrocatalysts for the ORR reaction. Despite having high activity and stability, the exact nature of the active sites in acidic media is still under debate for this kind of materials, especially as far as the role of the metal is concerned. It is unclear whether the transition metal has an active role in the catalysis or it only facilitates the formation of the active nitrogen-carbon functional sites.<sup>37,41,46,155</sup> Moreover specific surface area and porous structure, which determine the accessible part of active sites and the transport properties of ORR-

relevant species are implied to play an important role in the catalytic behavior of this kind of materials. The traditional method for preparing M-N/C catalysts though, involves direct pyrolysis of the mixture of nitrogen, carbon, and transition-metal precursors which frequently fails in controlling the features of the porous structure. An additional feature of some of the materials belonging to this class, is having metal particles encapsulated in graphitic carbon shells.<sup>32</sup> It was at first assumed that the encapsulated phases contributed very little to the ORR activity,<sup>156</sup> however, Bao and coworkers reported a series of studies<sup>157,158</sup> demonstrating that when a metal nanoparticle is confined inside carbon nanotubes (CNTs), a unique host-guest electronic interaction changes the local work function of the CNT walls. For example Deng et al.<sup>159</sup> reported that encapsulating Fe nanoparticles within N-doped CNTs, can increase their ORR performance. Another interesting example was reported by Li et al.<sup>160</sup>: by pyrolysis under high pressure they obtained a material consisting in hollow spheres comprising Fe<sub>3</sub>C nanoparticles encased by graphitic layers with a negligible amount of nitrogen or metal on the surface, which exhibited excellent ORR activity and stability in both acidic and alkaline media. Although the Fe<sub>3</sub>C nanoparticles were not in direct contact with the electrolyte, it was proven that they still had a key role in the catalysis, most likely correlated to the synergetic interaction between the carbide and the protective graphitic layers. Even with negligible surface nitrogen or iron functionalities, in fact the catalyst was very active towards ORR, suggesting that the presence of the encased carbide nanoparticles was the reason for the activation the graphitic layer. This study provides a unique model material for probing the ORR active sites of this type of encapsulated materials. Meanwhile, Mukerjee et al.<sup>161</sup> and Gewirth et al.<sup>162</sup> synthesized novel core-shell structured catalysts that were devoid of any Fe-N species and proved that FeN<sub>4</sub> sites are not required to generate an active ORR catalyst. In the first case, in particular, the majority of the ORR activity is attributed to the N-doped carbon structure, while iron is supposed to act as a catalyst for the graphitization of the N-doped carbon during the heat treatment and then enhancing its electrocatalytic properties by enabling the 4e<sup>-</sup> reduction of oxygen. A similar conclusion was reached by Xu et al.<sup>163</sup> regarding cobalt: they report a material consisting in N-doped carbon nanosheets embedded Co NPs exhibiting enhanced ORR activity, which is attributed exclusively to the N-doped carbon, by experimentally confirming the absence of Co-N species. DFT calculations suggest that this feature is guaranteed by the electron transfer from Co nanoparticles to the outer N-doped carbon sites, leading to a decreased local work function on the carbon surface. Even though the studies regarding this kind of systems activity is rapidly increasing, most of them are focused on the development of catalysts with

selectivity towards  $\text{H}_2\text{O}$ , to be employed as cathodic electrocatalysts for fuel cells. Only recently the scientific community is focusing its attention towards the development of catalytic materials specifically designed for  $\text{H}_2\text{O}_2$  production, hence the need to rationalize and understand the factors involved in this specific mechanism. These considerations brought me to design a material based on embedded Co nanoparticles to be studied for the selective electrochemical production of  $\text{H}_2\text{O}_2$ .

#### 1.4 $\text{H}_2\text{O}_2$ sensing

As already mentioned, hydrogen peroxide ( $\text{H}_2\text{O}_2$ ) is a molecule that bears great importance, in many manufacturing applications.<sup>164</sup> Due to its cytotoxic effects,  $\text{H}_2\text{O}_2$  must be absent in food products, while for cosmetic and personal care products where it acts as bleaching agent, its concentration must not be higher than 0.1% for oral hygiene products, and 12% in hair care products.<sup>165</sup> In living organisms, besides the cytotoxic effects,  $\text{H}_2\text{O}_2$  is also known to act as a signalling molecule in the regulation of various biological processes and is a side product generated from some biochemical reactions catalyzed by enzymes.<sup>166,167</sup> Therefore, the development of a fast, sensitive and inexpensive method for  $\text{H}_2\text{O}_2$  detection is of great significance for both academic and industrial purposes. While highly sensitive, most of the conventional techniques for  $\text{H}_2\text{O}_2$  determination such as spectrophotometry<sup>168</sup> fluorimetry,<sup>169</sup> fluorescence<sup>170</sup> and chemiluminescence,<sup>171</sup> require complex and expensive instrumentation and long detection times. Since  $\text{H}_2\text{O}_2$  is an electroactive molecule, electrochemistry can be exploited to develop a simple, rapid, sensitive, and cost effective method, able indeed to overcome the major drawbacks of the previously mentioned techniques.<sup>172</sup> Both the reduction to water and the oxidation to molecular oxygen can be exploited for the electrochemical detection of  $\text{H}_2\text{O}_2$  using a conventional solid electrode like a glassy carbon electrode (GCE), but the process suffers from slow electrode kinetics and high overpotentials. More so, a lack of selectivity of the sensing electrode can lead to underestimation or overestimation of the analyte in real samples, due to the natural presence of other electroactive species, like ascorbate, urate, glucose, paracetamol and bilirubin. Hence the interest in the design of novel electroactive materials, able to sense  $\text{H}_2\text{O}_2$  selectively and with improved kinetics. The most studied and widely used catalyst in the field of electrochemical sensors for  $\text{H}_2\text{O}_2$  is ferric hexacyanoferrate, also known as Prussian Blue (PB). Being capable to catalyze the reduction of oxygen peroxide at low potentials (50 mV vs Ag/AgCl), it has earned the

title of “artificial peroxidase” from the peroxidase enzymes.<sup>173,174</sup> Its value stems also from its selectivity for the target molecule due to its polycrystal structure, which does not allow penetration of larger molecules such as ascorbate and other interferents.<sup>175</sup> It has been used in coupling with several enzymes, to modify carbon nanostructures, and both, but still, its major drawback remains its lack of operational stability in neutral and alkaline solutions, due to the fact that its reduced form, Prussian white, can be dissolved by hydroxide ions.<sup>176,177</sup> To overcome this issue, other metal hexacyanoferrates, including copper, cobalt, chromium and vanadium have been investigated: their electrocatalytic activity as sensors resulted similar or lower than that of PB, but with a higher electrochemical stability over a wide pH range.<sup>178</sup> As most physiologic activities occur at neutral pH, this is an important feature for biosensors development through enzyme modification. A lot of research efforts have been devoted to the development of biosensors based on heme-proteins, a class of metalloproteins containing iron-centered porphyrins as their prosthetic groups. Their great potential for biosensing is related to the capability of iron to undergo easily oxidation and reduction over a wide range of potentials, and, being able to operate in a potential range closer to the redox potential of the protein itself, they give less exposure to interfering reactions.<sup>179,180</sup> The main challenge in the development of this kind of biosensors is the optimization of the electron transfer between the heme-protein and the electrode, since the prosthetic group of heme-proteins is shielded by the polypeptides, and, due to the length of the electron transfer distance, it is highly unlikely for the tunnelling mechanism to happen.<sup>181</sup> Because of their cost and low stability over long time use due to protein denaturation, the scientific interest has lately moved towards a non-enzymatic approach, involving the use of nanostructured metals and metal oxides.<sup>182</sup> Their multiple oxidation states and ability to activate small molecules absorbing them on their surface, make transition metals well known for their good catalytic performances. Moreover, nanosized transition metals, due to their size-controlled chemical and physical properties and high surface area can be made even more performing by finely tuning their specific features.<sup>183,184</sup> Many transition metals have been studied for the development of H<sub>2</sub>O<sub>2</sub> electrosensors, including platinum<sup>185</sup>, palladium<sup>185</sup>, copper,<sup>186–188</sup> rhodium,<sup>180</sup> iridium<sup>189,190</sup> and iron.<sup>191</sup> Great scientific efforts have been devoted to the study of gold’s many differently shaped nanostructures such as nanoparticles,<sup>192</sup> nanowires,<sup>193</sup> nanocages<sup>194</sup> and nano-porous Au,<sup>195</sup> with the last two slightly outperforming the others. Other strategies to fully exploit transition metals potential include combining them in nano-alloys: in particular, Xiao et al.<sup>196</sup> reported an advantageous synergy between Pt and Au. Their work

highlights the ability of Au to promote the formation of the electroactive Pt-OH species, lowering the reduction potential of H<sub>2</sub>O<sub>2</sub> while increasing the sensitivity. Later an amorphous ternary FeNiPt nanomaterial with tunable length was reported by Liu et al.<sup>197</sup> Ternary FeNiPt nanorods with large axial ratio were employed to construct an electrochemical sensing platform showing enhanced electrocatalytic activity towards both the oxidation and reduction of H<sub>2</sub>O<sub>2</sub>. As far as transition metal oxides are concerned, some of them have showed electrocatalytic activity towards the oxidation of H<sub>2</sub>O<sub>2</sub> such as manganese oxide,<sup>198–202</sup> cobalt oxide,<sup>203</sup> titanium oxide,<sup>204</sup> copper oxide<sup>205,206</sup> and iridium oxide.<sup>207</sup> The main drawback affecting their successful employment in sensing is related to the high potential needed for the oxidation of hydrogen peroxide, which makes these materials difficult to use in real samples due to interference issues.

#### **1.4.1 Carbon nanostructures application in H<sub>2</sub>O<sub>2</sub> sensing**

The employment of carbon materials in electrochemistry dates back to the historical discovery of their application for electrochemical production of alkali metals. From then on, due to their low cost, wide potential window, and electrocatalytic activity for a variety of redox reactions, they have been widely exploited both in analytical and industrial electrochemistry.<sup>208</sup> The combination of the properties of carbon materials with those of nanostructured materials gave rise to the development of carbon-based nanoscaled materials, which have been extensively used for the preparation of modified electrodes.<sup>209–211</sup> In addition to their extraordinary electrochemical features, differently from metal electrodes, they can also provide a platform for easy modification, supplying additional benefits for electrocatalysis and sensing. Indeed carbon nanostructures have been extensively studied in the field of electrochemical sensors<sup>208</sup> due to their high surface area, high electric conductivity and ability to accumulate analyte. A recently investigated strategy involves the development of hybrid nanomaterials in which CNSs are coupled with metal NPs or metal oxides, which feature high sensitivity, simple immobilization protocols and improved stability. Modern trends are moving toward the utilization of cheaper and more available metals or metal oxides and exploiting the synergistic effect arising when they are combined with nanostructured carbon materials such as carbon nanotubes (CNTs) or graphene (G).<sup>182,212</sup> Studies have shown, though, that carbon nanostructures can electrocatalyze themselves both the oxidation and reduction of H<sub>2</sub>O<sub>2</sub>. Table 3 summarizes the electroanalytic performances of some of

the most recently reported hydrogen peroxide sensors based on carbon nanomaterials both combined with metal and metal oxides and metal-free.

**Table 3:** Summary table of electrochemical performance of recently published hydrogen peroxide sensors based on carbon nanomaterials both combined with metal and metal oxides and metal free.

Nanostructured carbon-based materials	Linear range [ $\mu\text{M}$ ]	Detection limit [ $\mu\text{M}$ ]	Sensitivity [ $\mu\text{A mM}^{-1} \text{cm}^{-2}$ ]	Ref.
Au-PEI/GO	0.5–1680	0.2	460.0	213
PDDA-RGO/MnO <sub>2</sub> /AuNPs	5.0–500	0.6	1132.8	214
NG-hAuPd	0.1–20	0.02	5095.5	215
TiO <sub>2</sub> NTs/r-GO/AgNPs	15,500– 50,000	2.2	1152	216
PtAu/G-CNTs	2.0–8561	0.6	313.4	217
graphene-MWCNT	20–2100	9.4	32.91	218
rGO/Tyrosine	100–2100	80	69.07	219
Nafion/EGO/Co <sub>3</sub> O <sub>4</sub>	1–100	0.3	560	220
CoO <sub>x</sub> NPs/ERGO	5–1000	0.2	148.6	221
Fe <sub>3</sub> O <sub>4</sub> /rGO	1– 20,000	0.17	387.6	222
PFECS/rGO	10–190	1.253	117.142	223
MnO <sub>2</sub> -ERGO	100– 45,400	10	59.0	224

Focusing on some metal-free examples, CNT/Nafion<sup>225</sup> modified electrodes and CNT/Teflon<sup>226</sup> modified electrodes have been reported by Wang's group. These materials based on the dispersion of MWCNTs within Nafion and Teflon as binders, respectively, showed significant oxidation and reduction currents at very low overpotential. To further investigate the electrocatalytic behavior of CNTs towards H<sub>2</sub>O<sub>2</sub>, Xu et al.<sup>227</sup> compared them with N-doped CNTs. The doping has been proven to largely improve the activity of the material, and this effect has been related to the presence of a large number of defective sites acting as active centers for the electron transfer, introduced by this type of modification. In recent years, graphene has been studied for a variety of different applications due to its unique physicochemical properties. Its advantages in comparison with CNTs, are related to its low cost, safety, and easier industrial processing.<sup>228</sup> The cost advantage derives from the process: nanotube synthesis usually requires a

higher energy input, a high-purity gaseous feedstock and catalysts.<sup>229</sup> Graphene is also better suited as a metal-free platform for electrochemical research as it is free from the contamination of transition metals which is apt to exist in CNTs. Moreover, the possibility of obtaining chemically reduced graphene oxide as a single sheet<sup>230–232</sup> has led to its wide application, as it is a cheap and scalable process. Its versatile applications<sup>233</sup> are correlated to the remarkable structure defects (vacancies, holes) and surface functional groups (hydroxyl, epoxy, carbonyl, phenol, etc.), that can be exploited as sites for immobilizing various active species through covalent or noncovalent bonds. Zhou et al.<sup>234</sup> reported a chemically reduced graphene oxide (CR-GO) modified electrode as hydrogen peroxide electrosensor showing wide linear range (0.05–1500  $\mu\text{M}$ ), and improved activity compared to the CNTs previously reported systems. This behavior was attributed to the high density of edge-plane-like defective sites on CR-GO leading to enhanced electron transfer to  $\text{H}_2\text{O}_2$ . The same consideration was made by Takahashi et al.,<sup>235</sup> who tested a reduced graphene oxide electrode prepared through electrodeposition on a glassy carbon electrode. The electrochemical testing revealed enhanced activity towards  $\text{H}_2\text{O}_2$  sensing with respect to the unmodified electrode. One of the issues linked to the utilization of CR-GO, though, is that the sheets produced this way, when treated to become hydrophobic CR-GO from hydrophilic GO, tend to aggregate and this makes them very difficult to disperse in water, restricting their practical applications.<sup>236,237</sup> In order to facilitate the dispersion in aqueous environment, it was recently reported a strategy that involves the employment of substances that aid the dispersion, such as surfactants (dodecyl sulfate, cetyltrimethyl ammonium bromide) or even DNA. Lv et al.<sup>238</sup> reported stable graphene-DNA hybrids based on the non-covalent  $\pi$ - $\pi$  stacking between aromatic rings of graphene and N-containing groups of DNA. This simple self-assembled material has revealed itself to be not only more dispersible in water but also an efficient sensor in terms of detection range and sensitivity due to the enhanced electron transfer properties. Another study by Woo et al.<sup>218</sup> proposes a composite of graphene and multiwalled carbon nanotubes as hydrogen peroxide electrochemical sensor where the nanotubes create a network between the graphene sheets both enhancing the conductivity of graphene and preventing its aggregation. Combining graphene with a polymer is also gaining attention as a strategy to obtain electrochemical sensors with increased electron transfer rate, conductivity and stability. More so, such materials can be prepared through simple chemical procedures like *in situ* chemical or electrochemical polymerization and non-covalent functionalization. For example, a reduced graphene oxide/nanopolypyrrole (CR-GO/nPPy) composite synthesized by oxidative polymerization of pyrrole on graphene sheets using glucose

oxidase in aqueous solution was reported as H<sub>2</sub>O<sub>2</sub> sensor by Zor et al.<sup>239</sup> The sensor showed rapid and sensitive amperometric response due to the fast heterogeneous electron transfer of CR-GO combined with the enhanced electron transfer rate from nPPy and has been successfully employed for the determination of hydrogen peroxide in urine. Another work by Luo et al.<sup>240</sup> reported a composite made through an electrostatic layer-by-layer assembly of positively charged ionic liquid functionalized graphene sheets and negatively charged sulfonated polyaniline. This work shows that the presence of PANI is able to significantly enhance the electron transfer between graphene sheets, giving rise to an electrochemical sensor with fast response time (under 2 s), wide linear range and low detection limit. Since then, other polymers have been employed for the fabrication of graphene-based hydrogen peroxide sensors, due to their ability to improve sensitivity, selectivity and stability, such as tyrosine<sup>219</sup> and poly-o-phenylenediamine.<sup>241</sup> The interesting properties of a newly developed functionalized graphene inspired the collaboration that led to its investigation as metal-free non-enzymatic hydrogen peroxide electrosensor.

### **1.5 Motivation and research objectives**

Energy related processes have been intensively studied in the last decades, and in the field of electrochemistry there is a growing interest in finding new strategies to address the challenges hindering the development of technologies that could lead to a more sustainable society. The possibility to exploit smart, hierarchical materials to be applied in electrochemical devices such as fuel cells, allowed us to explore interesting developments in this research field. The main object of this project revolves on the development of smart electrocatalytic carbon-based materials to be employed in the processes that are at the core of the functioning of new generation fuel cells. In order to tackle the main issue hindering the worldwide scale production of these devices, which is their high cost, platinum is substituted with less noble metals. The instability in harsh acidic conditions of non-precious metals is addressed by either working in alkaline environment or shielding the metal center by encapsulating it in a nanostructured carbon matrix. The project spans from the preparation of the materials, their complete characterization both morphologic and electrochemical, to their test in full fuel cells. The secondary goal of this research project is related to the development of a sensor for the amperometric determination of hydrogen peroxide. Since the best performing electrochemical sensors in literature are either using precious metals or enzymes, both very expensive, there is a need of finding cheaper and more stable

systems. The goal of this section is the development of a metal-free nanocarbon-based material with performance that can be competitive with the state of the art.

### **1.6 The scope of the dissertation**

This thesis aims to demonstrate how the smart design of nanostructured materials can be crucial in determining their electrocatalytic properties. On the side, it's making a point on how electrochemistry is an invaluable tool for leading towards paths that will lower the consumption of energy.

## 1.7 References

- (1) Chu, S.; Cui, Y.; Liu, N. The Path towards Sustainable Energy. *Nat. Mater.* **2016**, *16* (1), 16–22.
- (2) Armaroli, N.; Balzani, V. Towards an Electricity Powered World. *Energy Environ. Sci. Sci.* **2011**, *4*, 3193–3222.
- (3) EIA. International Energy Outlook 2017 Overview. *U.S. Energy Inf. Adm.* **2017**, *IEO2017* (2017), 143.
- (4) Hamnett, A. *Handbook of Fuel Cells - Fundamentals Technology and Applications: The Components of an Electrochemical Cell*; 2010.
- (5) EG&G Technical Services, I. *Fuel Cell Handbook*; 2004; Vol. 7 Edition.
- (6) Debe, M. K. Electrocatalyst Approaches and Challenges for Automotive Fuel Cells. *Nature* **2012**, *486* (7401), 43–51.
- (7) Kurtz, J.; Contact, P.; Wipke, K.; Sprik, S.; Saur, G.; Ainscough, C. DOE 2017 Annual Progress Report. In *Department of energy, Lakewood, Colorado*; 2017; pp 0–3.
- (8) <https://www.theguardian.com/environment/2018/sep/17/germany-launches-worlds-first-hydrogen-powered-train>.
- (9) <https://www.physics.nist.gov/MajResFac/NIF/PemFuelCells.html>.
- (10) Wang, Y.; Chen, K. S.; Mishler, J.; Cho, S. C.; Adroher, X. C. A Review of Polymer Electrolyte Membrane Fuel Cells: Technology, Applications, and Needs on Fundamental Research. *Appl. Energy* **2011**, *88* (4), 981–1007.
- (11) Zhang, J.; Sasaki, K.; Sutter, E.; Adzic, R. R. Stabilization of Platinum Oxygen-Reduction Electrocatalysts Using Gold Clusters. *Science* (80-. ). **2007**, *220* (2007), 10–13.
- (12) Agel, E.; Bouet, J.; Fauvarque, J. F. Characterization and Use of Anionic Membranes for Alkaline Fuel Cells. *J. Power Sources* **2001**, *101* (2), 267–274.
- (13) Varcoe, J. R.; Slade, R. C. T. Prospects for Alkaline Anion-Exchange Membranes in Low Temperature Fuel Cells. *Fuel Cells* **2005**, *5* (2), 187–200.
- (14) Varcoe, J. R.; Atanassov, P.; Dekel, D. R.; Herring, A. M.; Hickner, M. A.; Kohl, P. A.; Kucernak, A. R.; Mustain, W. E.; Nijmeijer, K.; Scott, K.; et al. Anion-Exchange Membranes in Electrochemical Energy Systems. *Energy Environ. Sci.* **2014**, *7* (10), 3135–3191.
- (15) Pan, J.; Chen, C.; Zhuang, L.; Lu, J. Designing Advanced Alkaline Polymer Electrolytes for Fuel Cell Applications. *Acc. Chem. Res.* **2012**, *45* (3), 473–481.

- (16) Wang, Y.-J.; Qiao, J.; Baker, R.; Zhang, J. Alkaline Polymer Electrolyte Membranes for Fuel Cell Applications. *Chem. Soc. Rev.* **2013**, *42* (13), 5768.
- (17) Kreuer, K. D. Ion Conducting Membranes for Fuel Cells and Other Electrochemical Devices. *Chem. Mater.* **2014**, *26* (1), 361–380.
- (18) Marino, M. G.; Kreuer, K. D. Alkaline Stability of Quaternary Ammonium Cations for Alkaline Fuel Cell Membranes and Ionic Liquids. *ChemSusChem* **2015**, *8* (3), 513–523.
- (19) Hugar, K. M.; Kostalik, H. A.; Coates, G. W. Imidazolium Cations with Exceptional Alkaline Stability: A Systematic Study of Structure-Stability Relationships. *J. Am. Chem. Soc.* **2015**, *137* (27), 8730–8737.
- (20) Noonan, K. J. T.; Hugar, K. M.; Kostalik, H. A.; Lobkovsky, E. B.; Abruña, H. D.; Coates, G. W. Phosphonium-Functionalized Polyethylene: A New Class of Base-Stable Alkaline Anion Exchange Membranes. *J. Am. Chem. Soc.* **2012**, *134* (44), 18161–18164.
- (21) Zhang, B.; Kaspar, R. B.; Gu, S.; Wang, J.; Zhuang, Z.; Yan, Y. A New Alkali-Stable Phosphonium Cation Based on Fundamental Understanding of Degradation Mechanisms. *ChemSusChem* **2016**, *9* (17), 2374–2379.
- (22) Nuñez, S. A.; Capparelli, C.; Hickner, M. A. N-Alkyl Interstitial Spacers and Terminal Pendants Influence the Alkaline Stability of Tetraalkylammonium Cations for Anion Exchange Membrane Fuel Cells. *Chem. Mater.* **2016**, *28* (8), 2589–2598.
- (23) Dekel, D. R. Review of Cell Performance in Anion Exchange Membrane Fuel Cells. *J. Power Sources* **2018**, *375*, 158–169.
- (24) Guo, J.; Hsu, A.; Chu, D.; Chen, R. Improving Oxygen Reduction Reaction Activities on Carbon-Supported Ag Nanoparticles in Alkaline Solutions. *J. Phys. Chem. C* **2010**, *114* (10), 4324–4330.
- (25) Meng, Y.; Song, W.; Huang, H.; Ren, Z.; Chen, S. Y.; Suib, S. L. Structure-Property Relationship of Bifunctional MnO<sub>2</sub> nanostructures: Highly Efficient, Ultra-Stable Electrochemical Water Oxidation and Oxygen Reduction Reaction Catalysts Identified in Alkaline Media. *J. Am. Chem. Soc.* **2014**, *136* (32), 11452–11464.
- (26) Cheng, F.; Su, Y.; Liang, J.; Tao, Z.; Chen, J. MnO<sub>2</sub>-Based Nanostructures as Catalysts for Electrochemical Oxygen Reduction in Alkaline Media. *Chem. Mater.* **2010**, *22* (3), 898–905.
- (27) Liang, Y.; Li, Y.; Wang, H.; Zhou, J.; Wang, J.; Regier, T.; Dai, H. Co<sub>3</sub>O<sub>4</sub> Nanocrystals on Graphene as a Synergistic Catalyst for Oxygen Reduction Reaction. *Nat. Mater.* **2011**, *10* (10), 780–786.

- (28) Qu, L.; Liu, Y.; Baek, J.-B.; Dai, L. Nitrogen-Doped Graphene as Efficient Metal-Free Electrocatalyst for Oxygen Reduction in Fuel Cells. *ACS Nano* **2010**, *4* (3), 1321–1326.
- (29) Gong, K.; Du, F.; Xia, Z.; Durstock, M.; Dai, L. Nitrogen-Doped Carbon Nanotube Arrays with High Electrocatalytic Activity for Oxygen Reduction. *Science (80-. )*. **2009**, *323*, 760–764.
- (30) Wang, D. W.; Su, D. Heterogeneous Nanocarbon Materials for Oxygen Reduction Reaction. *Energy Environ. Sci.* **2014**, *7* (2), 576–591.
- (31) Jasinski, R. A New Fuel Cell Cathode Catalyst. *Nature* **1964**, *201*, 1212–1213.
- (32) Wiesener, K. N<sub>4</sub>-Chelates as Electrocatalyst for Cathodic Oxygen Reduction. *Electrochim. Acta* **1986**, *31* (8), 1073–1078.
- (33) Van Veen, J. A. R.; Colijn, H. A.; Van Baar, J. F. On the Effect of a Heat Treatment on the Structure of Carbon Supported Metalloporphyrins and Phthalocyanines. *Electrochim. Acta* **1987**, *33* (6), 801-804.
- (34) Bezerra, C. W. B.; Zhang, L.; Lee, K.; Liu, H.; Marques, A. L. B.; Marques, E. P.; Wang, H.; Zhang, J. A Review of Fe-N/C and Co-N/C Catalysts for the Oxygen Reduction Reaction. *Electrochim. Acta* **2008**, *53* (15), 4937–4951.
- (35) Wu, G.; More, K. L.; Johnston, C. M.; Zelenay, P. High-Performance Electrocatalysts for Oxygen Reduction Derived from Polyaniline, Iron, and Cobalt. *Science (80-. )*. **2011**, *332* (6028), 443–447.
- (36) Bashyam, R.; Zelenay, P. A Class of Non-Precious Metal Composite Catalysts for Fuel Cells. *Nature* **2006**, *443* (7107), 63–66.
- (37) Lefèvre, M.; Proietti, E.; Jaouen, F.; Dodelet, J. P. Iron-Based Catalysts with Improved Oxygen Reduction Activity in Polymer Electrolyte Fuel Cells. *Science (80-. )*. **2009**, *324* (5923), 71–74.
- (38) Lin, L.; Zhu, Q.; Xu, A. W. Noble-Metal-Free Fe-N/C Catalyst for Highly Efficient Oxygen Reduction Reaction under Both Alkaline and Acidic Conditions. *J. Am. Chem. Soc.* **2014**, *136* (31), 11027–11033.
- (39) Chung, H. T.; Johnston, C. M.; Zelenay, P. Synthesis and Evaluation of Heat-Treated, Cyanamide-Derived Non-Precious Catalysts for Oxygen Reduction. *ECS Trans.* **2009**, *25* (1), 485–492.
- (40) Gupta, S.; Tryk, D.; Bae, I.; Aldred, W.; Yeager, E. Heat-Treated Polyacrylonitrile-Based Catalysts for Oxygen Electroreduction. *J. Appl. Electrochem.* **1989**, *19* (1), 19–27.
- (41) Wu, G.; Chen, Z.; Artyushkova, K.; Garzon, F. H.; Zelenay, P. Polyaniline-Derived Non-

- Precious Catalyst for the Polymer Electrolyte Fuel Cell Cathode. *ECS Trans.* **2008**, *16* (2), 159–170.
- (42) Maldonado, S.; Stevenson, K. J. Direct Preparation of Carbon Nanofiber Electrodes via Pyrolysis of Iron(II) Phthalocyanine: Electrocatalytic Aspects for Oxygen Reduction. *J. Phys. Chem. B* **2004**, *108* (31), 11375–11383.
- (43) Jaouen, F.; Herranz, J.; Lefèvre, M.; Dodelet, J. P.; Kramm, U. I.; Herrmann, I.; Bogdanoff, P.; Maruyama, J.; Nagaoka, T.; Garsuch, A.; et al. Cross-Laboratory Experimental Study of Non-Noble-Metal Electrocatalysts for the Oxygen Reduction Reaction. *ACS Appl. Mater. Interfaces* **2009**, *1* (8), 1623–1639.
- (44) Matter, P. H.; Wang, E.; Ozkan, U. S. Preparation of Nanostructured Nitrogen-Containing Carbon Catalysts for the Oxygen Reduction Reaction from SiO<sub>2</sub>- and MgO-Supported Metal Particles. *J. Catal.* **2006**, *243* (2), 395–403.
- (45) Nallathambi, V.; Lee, J. W.; Kumaraguru, S. P.; Wu, G.; Popov, B. N. Development of High Performance Carbon Composite Catalyst for Oxygen Reduction Reaction in PEM Proton Exchange Membrane Fuel Cells. *J. Power Sources* **2008**, *183* (1), 34–42.
- (46) Wu, G.; Johnston, C. M.; Mack, N. H.; Artyushkova, K.; Ferrandon, M.; Nelson, M.; Lezama-Pacheco, J. S.; Conradson, S. D.; More, K. L.; Myers, D. J.; et al. Synthesis-Structure-Performance Correlation for Polyaniline-Me-C Non-Precious Metal Cathode Catalysts for Oxygen Reduction in Fuel Cells. *J. Mater. Chem.* **2011**, *21* (30), 11392–11405.
- (47) Davydova, E. S.; Mukerjee, S.; Jaouen, F.; Dekel, D. R. Electrocatalysts for Hydrogen Oxidation Reaction in Alkaline Electrolytes. *ACS Catal.* **2018**, *8* (7), 6665–6690.
- (48) J. Tafel. Über Die Polarisation Bei Kathodischer Wasserstoffentwicklung. *Zeitschrift für Phys. Chemie, Stöchiometrie und Verwandtschaftslehre* **1905**, *50*, 641–712.
- (49) Gottesfeld, S.; Dekel, D. R.; Page, M.; Bae, C.; Yan, Y.; Zelenay, P.; Kim, Y. S. Anion Exchange Membrane Fuel Cells: Current Status and Remaining Challenges. *J. Power Sources* **2018**, *375*, 170–184.
- (50) Heyrovsky, J. A Theory of Overpotential. *Recl. des Trav. Chim. des Pays-Bas* **1927**, *46* (8), 582–585.
- (51) Miller, H. A.; Lavacchi, A.; Vizza, F.; Marelli, M.; Di Benedetto, F.; D’Acapito, F.; Paska, Y.; Page, M.; Dekel, D. R. A Pd/C-CeO<sub>2</sub> Anode Catalyst for High-Performance Platinum-Free Anion Exchange Membrane Fuel Cells. *Angew. Chem. Int. Ed. Engl.* **2016**, *55* (20), 6004–6007.
- (52) Strmcnik, D.; Uchimura, M.; Wang, C.; Subbaraman, R.; Danilovic, N.; Van Der Vliet, D.; Paulikas, A. P.; Stamenkovic, V. R.; Markovic, N. M. Improving the Hydrogen Oxidation Reaction

Rate by Promotion of Hydroxyl Adsorption. *Nat. Chem.* **2013**, *5* (4), 300–306.

(53) Alesker, M.; Page, M.; Shviro, M.; Paska, Y.; Gershinsky, G.; Dekel, D. R.; Zitoun, D. Palladium/Nickel Bifunctional Electrocatalyst for Hydrogen Oxidation Reaction in Alkaline Membrane Fuel Cell. *J. Power Sources* **2016**, *304*, 332–339.

(54) Sheng, W.; Gasteiger, H. A.; Shao-Horn, Y. Hydrogen Oxidation and Evolution Reaction Kinetics on Platinum: Acid vs Alkaline Electrolytes. *J. Electrochem. Soc.* **2010**, *157* (11), B1529.

(55) Zheng, J.; Sheng, W.; Zhuang, Z.; Xu, B.; Yan, Y. Universal Dependence of Hydrogen Oxidation and Evolution Reaction Activity of Platinum-Group Metals on pH and Hydrogen Binding Energy. *Sci. Adv.* **2016**, *2* (3), 1–8.

(56) Durst, J.; Siebel, A.; Simon, C.; Hasché, F.; Herranz, J.; Gasteiger, H. A. New Insights into the Electrochemical Hydrogen Oxidation and Evolution Reaction Mechanism. *Energy Environ. Sci.* **2014**, *7* (7), 2255–2260.

(57) Woodroof, M. D.; Wittkopf, J. A.; Gu, S.; Yan, Y. S. Exchange Current Density of the Hydrogen Oxidation Reaction on Pt/C in Polymer Solid Base Electrolyte. *Electrochem. commun.* **2015**, *61*, 57–60.

(58) Erdey-Gruz, T.; Volmer, M. Zur Theorie Der Wasserstoff Überspannung. *Zeitschrift für Phys. Chemie* **1929**, 203–213.

(59) Sheng, W.; Zhuang, Z.; Gao, M.; Zheng, J.; Chen, J. G.; Yan, Y. Correlating Hydrogen Oxidation and Evolution Activity on Platinum at Different pH with Measured Hydrogen Binding Energy. *Nat. Commun.* **2015**, *6*, 1–6.

(60) Miller, H. A.; Vizza, F.; Marelli, M.; Zadick, A.; Dubau, L.; Chatenet, M.; Geiger, S.; Cherevko, S.; Doan, H.; Pavlicek, R. K. Highly Active Nanostructured Palladium-Ceria Electrocatalysts for the Hydrogen Oxidation Reaction in Alkaline Medium. *Nano Energy* **2017**, *33*, 293–305.

(61) Schwammlein, J. N.; El-Sayed, H. A.; Stuhmeier, B. M.; Wagenbauer, K. F.; Dietz, H.; Gasteiger, H. A. Origin of Superior Activity of Ru@Pt Core-Shell Nanoparticles towards Hydrogen Oxidation in Alkaline Media. *ECS Trans.* **2016**, *75* (14), 971–982.

(62) Sheng, W.; Myint, M.; Chen, J. G.; Yan, Y. Correlating the Hydrogen Evolution Reaction Activity in Alkaline Electrolytes with the Hydrogen Binding Energy on Monometallic Surfaces. *Energy Environ. Sci.* **2013**, *6* (5), 1509.

(63) Nørskov, J. K.; Bligaard, T.; Logadottir, A.; Kitchin, J. R.; Chen, J. G.; Pandelov, S.; Stimming, U. Trends in the Exchange Current for Hydrogen Evolution. *J. Electrochem. Soc.* **2005**, *152* (3), J23.

(64) Alia, S. M.; Pivovar, B. S.; Yan, Y. Platinum-Coated Copper Nanowires with High Activity for

- Hydrogen Oxidation Reaction in Base. *J. Am. Chem. Soc.* **2013**, *135* (36), 13473–13478.
- (65) Alia, S. M.; Yan, Y. Palladium Coated Copper Nanowires as a Hydrogen Oxidation Electrocatalyst in Base. *J. Electrochem. Soc.* **2015**, *162* (8), F849–F853.
- (66) Ohyama, J.; Sato, T.; Yamamoto, Y.; Arai, S.; Satsuma, A. Size Specifically High Activity of Ru Nanoparticles for Hydrogen Oxidation Reaction in Alkaline Electrolyte. *J. Am. Chem. Soc.* **2013**, *135* (21), 8016–8021.
- (67) Zheng, J.; Zhuang, Z.; Xu, B.; Yan, Y. Correlating Hydrogen Oxidation/Evolution Reaction Activity with the Minority Weak Hydrogen-Binding Sites on Ir/C Catalysts. *ACS Catal.* **2015**, *5* (7), 4449–4455.
- (68) Zheng, J.; Zhou, S.; Gu, S.; Xu, B.; Yan, Y. Size-Dependent Hydrogen Oxidation and Evolution Activities on Supported Palladium Nanoparticles in Acid and Base. *J. Electrochem. Soc.* **2016**, *163* (6), F499–F506.
- (69) Wang, Y.; Wang, G.; Li, G.; Huang, B.; Pan, J.; Liu, Q.; Han, J.; Xiao, L.; Lu, J.; Zhuang, L. Pt-Ru Catalyzed Hydrogen Oxidation in Alkaline Media: Oxophilic Effect or Electronic Effect? *Energy Environ. Sci.* **2015**, *8* (1), 177–181.
- (70) Lu, S.; Zhuang, Z. Investigating the Influences of the Adsorbed Species on Catalytic Activity for Hydrogen Oxidation Reaction in Alkaline Electrolyte. *J. Am. Chem. Soc.* **2017**, *139* (14), 5156–5163.
- (71) Ledezma-Yanez, I.; Wallace, W. D. Z.; Sebastián-Pascual, P.; Climent, V.; Feliu, J. M.; Koper, M. T. M. Interfacial Water Reorganization as a pH-Dependent Descriptor of the Hydrogen Evolution Rate on Platinum Electrodes. *Nat. Energy* **2017**, *2* (4), 1–7.
- (72) Van Der Niet, M. J. T. C.; Garcia-Araez, N.; Hernández, J.; Feliu, J. M.; Koper, M. T. M. Water Dissociation on Well-Defined Platinum Surfaces: The Electrochemical Perspective. *Catal. Today* **2013**, *202* (1), 105–113.
- (73) Sheng, W.; Bivens, A. P.; Myint, M.; Zhuang, Z.; Forest, R. V.; Fang, Q.; Chen, J. G.; Yan, Y. Non-Precious Metal Electrocatalysts with High Activity for Hydrogen Oxidation Reaction in Alkaline Electrolytes. *Energy Environ. Sci.* **2014**, *7* (5), 1719–1724.
- (74) Zhuang, Z.; Giles, S. A.; Zheng, J.; Jenness, G. R.; Caratzoulas, S.; Vlachos, D. G.; Yan, Y. Nickel Supported on Nitrogen-Doped Carbon Nanotubes as Hydrogen Oxidation Reaction Catalyst in Alkaline Electrolyte. *Nat. Commun.* **2016**, *7*, 1–8.
- (75) Tripkovic, A. V.; Popovic, K. D.; Grgur, B. N.; Blizanac, B.; Ross, P. N.; Markovic, N. M. Methanol Electrooxidation on Supported Pt and PtRu Catalysts in Acid and Alkaline Solutions.

*Electrochim. Acta* **2002**, *47* (22–23), 3707–3714.

- (76) Prabhuram, J.; Manoharan, R. Investigation of Methanol Oxidation on Unsupported Platinum Electrodes in Strong Alkali and Strong Acid. *J. Power Sources* **1998**, *74* (1), 54–61.
- (77) Ozoemena, K. I. Nanostructured Platinum-Free Electrocatalysts in Alkaline Direct Alcohol Fuel Cells: Catalyst Design, Principles and Applications. *RSC Adv.* **2016**, *6* (92), 89523–89550.
- (78) Bianchini, C.; Shen, P. K. Palladium-Based Electrocatalysts for Alcohol Oxidation in Half Cells and in Direct Alcohol Fuel Cells. *Chem. Rev.* **2009**, *109* (9), 4183–4206.
- (79) Hu, F.; Chen, C.; Wang, Z.; Wei, G.; Shen, P. K. Mechanistic Study of Ethanol Oxidation on Pd-NiO/C Electrocatalyst. *Electrochim. Acta* **2006**, *52* (3), 1087–1091.
- (80) Yang, J.; Zhou, Y.; Su, H.; Jiang, S. Theoretical Study on the Effective Methanol Decomposition on Pd(111) Surface Facilitated in Alkaline Medium. *J. Electroanal. Chem.* **2011**, *662* (1), 251–256.
- (81) Yajima, T.; Wakabayashi, N.; Watanabe, M. Adsorbed Water for the Electro-Oxidation of Methanol at Pt–Ru Alloy. **2003**, No. C, 828–829.
- (82) Liang, Z. X.; Zhao, T. S.; Xu, J. B.; Zhu, L. D. Mechanism Study of the Ethanol Oxidation Reaction on Palladium in Alkaline Media. *Electrochim. Acta* **2009**, *54* (8), 2203–2208.
- (83) Shen, P. K.; Xu, C. Alcohol Oxidation on Nanocrystalline Oxide Pd/C Promoted Electrocatalysts. *Electrochem. commun.* **2006**, *8* (1), 184–188.
- (84) Xu, C.; Tian, Z.; Shen, P.; Jiang, S. P. Oxide (CeO<sub>2</sub>, NiO, Co<sub>3</sub>O<sub>4</sub> and Mn<sub>3</sub>O<sub>4</sub>)-Promoted Pd/C Electrocatalysts for Alcohol Electrooxidation in Alkaline Media. *Electrochim. Acta* **2008**, *53* (5), 2610–2618.
- (85) Xu, C.; Liu, Y. Ethanol Electrooxidation on Pt/C and Pd/C Catalysts Promoted with Oxide. *J. Power Sources* **2007**, *164*, 527–531.
- (86) Demirci, U. B. Theoretical Means for Searching Bimetallic Alloys as Anode Electrocatalysts for Direct Liquid-Feed Fuel Cells. *J. Power Sources* **2007**, *173* (1), 11–18.
- (87) Liu, Z.; Zhang, X.; Hong, L. Physical and Electrochemical Characterizations of Nanostructured Pd/C and PdNi/C Catalysts for Methanol Oxidation. *Electrochem. commun.* **2009**, *11* (4), 925–928.
- (88) Kumar, K. S.; Haridoss, P.; Seshadri, S. K. Synthesis and Characterization of Electrodeposited Ni-Pd Alloy Electrodes for Methanol Oxidation. **2008**, *202*, 1764–1770.
- (89) Wang, M.; Liu, W.; Huang, C. Investigation of PdNiO/C Catalyst for Methanol Electrooxidation. *Int. J. Hydrogen Energy* **2009**, *34* (6), 2758–2764.

- (90) Cui, X.; Zhu, Y.; Hua, Z.; Feng, J.; Liu, Z.; Chen, L.; Shi, J. SnO<sub>2</sub> Nanocrystals-Decorated Mesoporous ZSM-5 as Precious Metal-Free Electrode Catalyst for Methanol Oxidations. *Energy Environ. Sci.* **2015**, *8* (4), 1261–1266.
- (91) Wu, J. B.; Li, Z. G.; Huang, X. H.; Lin, Y. Porous Co<sub>3</sub>O<sub>4</sub>/NiO Core/Shell Nanowire Array with Enhanced Catalytic Activity for Methanol Electro-Oxidation. **2013**, *224*, 1–5.
- (92) Tammam, R. H.; Fekry, A. M.; Saleh, M. M. Electrocatalytic Oxidation of Methanol on Ordered Binary Catalyst of Manganese and Nickel Oxide Nanoparticles. *Int. J. Hydrogen Energy* **2014**, *40* (1), 275–283.
- (93) Camara, G. A.; Iwasita, T. Parallel Pathways of Ethanol Oxidation: The Effect of Ethanol Concentration. *J. Electroanal. Chem.* **2005**, *578*, 315–321.
- (94) Ji, H.; Frenzel, J.; Qi, Z.; Wang, X.; Zhao, C.; Zhang, Z.; Eggeler, G. An Ultrafine Nanoporous Bimetallic Ag-Pd Alloy with Superior Catalytic Activity. *CrystEngComm* **2010**, *12* (12), 4059–4062.
- (95) Nguyen, S. T.; Yang, Y.; Wang, X. Ethanol Electro-Oxidation Activity of Nb-Doped-TiO<sub>2</sub> Supported PdAg Catalysts in Alkaline Media. *Appl. Catal. B Environ.* **2012**, *113–114*, 261–270.
- (96) Liu, J.; Zhou, H.; Wang, Q.; Zeng, F.; Kuang, Y. Reduced Graphene Oxide Supported Palladium-Silver Bimetallic Nanoparticles for Ethanol Electro-Oxidation in Alkaline Media. *J. Mater. Sci.* **2012**, *47* (5), 2188–2194.
- (97) Nguyen, S. T.; Law, H. M.; Nguyen, H. T.; Kristian, N.; Wang, S.; Chan, S. H.; Wang, X. Enhancement Effect of Ag for Pd/C towards the Ethanol Electro-Oxidation in Alkaline Media. *Appl. Catal. B Environ.* **2009**, *91* (1–2), 507–515.
- (98) Ramulifho, T.; Ozoemena, K. I.; Modibedi, R. M.; Jafta, C. J.; Mathe, M. K. Fast Microwave-Assisted Solvothermal Synthesis of Metal Nanoparticles (Pd, Ni, Sn) Supported on Sulfonated MWCNTs: Pd-Based Bimetallic Catalysts for Ethanol Oxidation in Alkaline Medium. *Electrochim. Acta* **2012**, *59*, 310–320.
- (99) Qi, Z.; Geng, H.; Wang, X.; Zhao, C.; Ji, H.; Zhang, C.; Xu, J.; Zhang, Z. Novel Nanocrystalline PdNi Alloy Catalyst for Methanol and Ethanol Electro-Oxidation in Alkaline Media. *J. Power Sources* **2011**, *196* (14), 5823–5828.
- (100) Wei, Y. C.; Liu, C. W.; Kang, W. Da; Lai, C. M.; Tsai, L. D.; Wang, K. W. Electrocatalytic Activity Enhancement of Pd-Ni Electrocatalysts for the Ethanol Electro-Oxidation in Alkaline Medium: The Promotional Effect of CeO<sub>2</sub> addition. *J. Electroanal. Chem.* **2011**, *660* (1), 64–70.
- (101) Zhang, Z.; Xin, L.; Sun, K.; Li, W. Pd-Ni Electrocatalysts for Efficient Ethanol Oxidation Reaction in Alkaline Electrolyte. *Int. J. Hydrogen Energy* **2011**, *36* (20), 12686–12697.

- (102) Maiyalagan, T.; Scott, K. Performance of Carbon Nanofiber Supported Pd-Ni Catalysts for Electro-Oxidation of Ethanol in Alkaline Medium. *J. Power Sources* **2010**, *195* (16), 5246–5251.
- (103) Du, W.; MacKenzie, K. E.; Milano, D. F.; Deskins, N. A.; Su, D.; Teng, X. Palladium-Tin Alloyed Catalysts for the Ethanol Oxidation Reaction in an Alkaline Medium. *ACS Catal.* **2012**, *2* (2), 287–297.
- (104) Modibedi, R. M.; Masombuka, T.; Mathe, M. K. Carbon Supported Pd-Sn and Pd-Ru-Sn Nanocatalysts for Ethanol Electro-Oxidation in Alkaline Medium. *Int. J. Hydrogen Energy* **2011**, *36* (8), 4664–4672.
- (105) Jou, L.-H.; Chang, J.-K.; Whang, T.-J.; Sun, I.-W. Electrodeposition of Palladium-Tin Alloys from 1-Ethyl-3-Methylimidazolium Chloride–Tetrafluoroborate Ionic Liquid for Ethanol Electro-Oxidation. *J. Electrochem. Soc.* **2010**, *157* (8), D443.
- (106) Wang, Y.; Nguyen, T. S.; Liu, X.; Wang, X. Novel Palladium-Lead (Pd-Pb/C) Bimetallic Catalysts for Electrooxidation of Ethanol in Alkaline Media. *J. Power Sources* **2010**, *195* (9), 2619–2622.
- (107) Nguyen, S. T.; Ling Tan, D. S.; Lee, J. M.; Chan, S. H.; Wang, J. Y.; Wang, X. Tb Promoted Pd/C Catalysts for the Electrooxidation of Ethanol in Alkaline Media. *Int. J. Hydrogen Energy* **2011**, *36* (16), 9645–9652.
- (108) Neto, A. O.; Tusi, M. M.; De Oliveira Polanco, N. S.; Da Silva, S. G.; Coelho Dos Santos, M.; Spinacé, E. V. PdBi/C Electrocatalysts for Ethanol Electro-Oxidation in Alkaline Medium. *Int. J. Hydrogen Energy* **2011**, *36* (17), 10522–10526.
- (109) Chu, D.; Wang, J.; Wang, S.; Zha, L.; He, J.; Hou, Y.; Yan, Y.; Lin, H.; Tian, Z. High Activity of Pd-In<sub>2</sub>O<sub>3</sub>/CNTs Electrocatalyst for Electro-Oxidation of Ethanol. *Catal. Commun.* **2009**, *10* (6), 955–958.
- (110) Shen, S.; Zhao, T. S.; Xu, J.; Li, Y. High Performance of a Carbon Supported Ternary PdIrNi Catalyst for Ethanol Electro-Oxidation in Anion-Exchange Membrane Direct Ethanol Fuel Cells. *Energy Environ. Sci.* **2011**, *4* (4), 1428.
- (111) Fashedemi, O. O.; Ozoemena, K. I. Comparative Electrocatalytic Oxidation of Ethanol, Ethylene Glycol and Glycerol in Alkaline Medium at Pd-Decorated FeCo@Fe/C Core-Shell Nanocatalysts. *Electrochim. Acta* **2014**, *128*, 279–286.
- (112) Wang, W.; Chai, D.; Yang, Y.; Liu, Y.; Kang, Y.; Lei, Z. Fe-Co Hybrid Oxides Promoted Pd Electrocatalysts with Enhanced Catalytic Performance for Ethylene Glycol Oxidation. *Int. J. Hydrogen Energy* **2015**, *40* (32), 10041–10048.

- (113) Fang, X.; Wang, L.; Shen, P. K.; Cui, G.; Bianchini, C. An in Situ Fourier Transform Infrared Spectroelectrochemical Study on Ethanol Electrooxidation on Pd in Alkaline Solution. *J. Power Sources* **2010**, *195* (5), 1375–1378.
- (114) Yang, Y. Y.; Ren, J.; Li, Q. X.; Zhou, Z. Y.; Sun, S. G.; Cai, W. Bin. Electrocatalysis of Ethanol on a Pd Electrode in Alkaline Media: An in Situ Attenuated Total Reflection Surface-Enhanced Infrared Absorption Spectroscopy Study. *ACS Catal.* **2014**, *4* (3), 798–803.
- (115) Sheng, T.; Lin, W. F.; Hardacre, C.; Hu, P. Role of Water and Adsorbed Hydroxyls on Ethanol Electrochemistry on Pd: New Mechanism, Active Centers, and Energetics for Direct Ethanol Fuel Cell Running in Alkaline Medium. *J. Phys. Chem. C* **2014**, *118* (11), 5762–5772.
- (116) Bellini, M.; Bevilacqua, M.; Filippi, J.; Lavacchi, A.; Marchionni, A.; Miller, H. A.; Oberhauser, W.; Vizza, F.; Annen, S. P.; Grützmacher, H. Energy and Chemicals from the Selective Electrooxidation of Renewable Diols by Organometallic Fuel Cells. *ChemSusChem* **2014**, *7* (9), 2432–2435.
- (117) Marchionni, A.; Bevilacqua, M.; Bianchini, C.; Chen, Y. X.; Filippi, J.; Fornasiero, P.; Lavacchi, A.; Miller, H.; Wang, L.; Vizza, F. Electrooxidation of Ethylene Glycol and Glycerol on Pd-(Ni-Zn)/C Anodes in Direct Alcohol Fuel Cells. *ChemSusChem* **2013**, *6* (3), 518–528.
- (118) Fashedemi, O. O.; Miller, H. A.; Marchionni, A.; Vizza, F.; Ozoemena, K. I. Electro-Oxidation of Ethylene Glycol and Glycerol at Palladium-Decorated FeCo@Fe Core-shell Nanocatalysts for Alkaline Direct Alcohol Fuel Cells: Functionalized MWCNT Supports and Impact on Product Selectivity. *J. Mater. Chem. A* **2015**, *3* (13), 7145–7156.
- (119) Villa, A.; Plebani, M.; Schiavoni, M.; Milone, C.; Piperopoulos, E.; Galvagno, S.; Prati, L. Tuning Hydrophilic Properties of Carbon Nanotubes: A Challenge for Enhancing Selectivity in Pd Catalyzed Alcohol Oxidation. *Catal. Today* **2012**, *186* (1), 76–82.
- (120) Ferreira Jr, R. S.; Giz, M. J.; Camara, G. A. Influence of the Local pH on the Electrooxidation of Glycerol on Palladium-Rhodium Electrodeposits. *J. Electroanal. Chem.* **2013**, *697*, 15–20.
- (121) Simoes, M.; Baranton, S.; Coutanceau, C. Electro-Oxidation of Glycerol at Pd Based Nano-Catalysts for an Application in Alkaline Fuel Cells for Chemicals and Energy Cogeneration. *Appl. Catal. B Environ. J.* **2010**, *93*, 354–362.
- (122) Simões, M.; Baranton, S.; Coutanceau, C. Enhancement of Catalytic Properties for Glycerol Electrooxidation on Pt and Pd Nanoparticles Induced by Bi Surface Modification. *Appl. Catal. B Environ.* **2011**, *110*, 40–49.
- (123) Borup, R.; Meyers, J.; Pivovar, B.; Kim, Y. S.; Mukundan, R.; Garland, N.; Myers, D.; Wilson,

- M.; Garzon, F.; Wood, D.; et al. Scientific Aspects of Polymer Electrolyte Fuel Cell Durability and Degradation. *Chem. Rev.* **2007**, *107* (10), 3904–3951.
- (124) G. Pfliegerer, H. J. Riedl, Vol. 2158525, C01B15/023 Ed. (Ed.: U. P. US2158525A), USA, 1939.
- (125) Yuan, X.-Z.; Wang, H. *PEM Fuel Cell Electrocatalysts and Catalyst Layers*; 2008.
- (126) Tse, E. C. M.; Barile, C. J.; Kirchschrager, N. A.; Li, Y.; Gewargis, J. P.; Zimmerman, S. C.; Hosseini, A.; Gewirth, A. A. Proton Transfer Dynamics Control the Mechanism of O<sub>2</sub> Reduction by a Non-Precious Metal Electrocatalyst. *Nat. Mater.* **2016**, *15* (7), 754–759.
- (127) Viswanathan, V.; Hansen, H. A.; Rossmeisl, J.; Nørskov, J. K. Unifying the 2e<sup>-</sup> and 4e<sup>-</sup> Reduction of Oxygen on Metal Surfaces. *J. Phys. Chem. Lett.* **2012**, *3* (20), 2948–2951.
- (128) Maroun, F.; Ozanam, F.; Magnussen, O. M.; Behm, R. J. The Role of Atomic Ensembles in the Reactivity of Bimetallic Electrocatalysts. *Science (80-. )*. **2001**, *293* (5536), 1811–1814.
- (129) Strmcnik, D.; Escudero-Escribano, M.; Kodama, K.; Stamenkovic, V. R.; Cuesta, A.; Markovic, N. M. Enhanced Electrocatalysis of the Oxygen Reduction Reaction Based on Patterning of Platinum Surfaces with Cyanide. *Nat. Chem.* **2010**, *2* (10), 880–885.
- (130) Viswanathan, V.; Hansen, H. A.; Rossmeisl, J.; Jaramillo, T. F.; Pitsch, H.; Nørskov, J. K. Simulating Linear Sweep Voltammetry from First-Principles: Application to Electrochemical Oxidation of Water on Pt(111) and Pt<sub>3</sub>Ni(111). *J. Phys. Chem. C* **2012**, *116* (7), 4698–4704.
- (131) Siahrostami, S.; Verdager-Casadevall, A.; Karamad, M.; Deiana, D.; Malacrida, P.; Wickman, B.; Escudero-Escribano, M.; Paoli, E. A.; Frydendal, R.; Hansen, T. W.; et al. Enabling Direct H<sub>2</sub>O<sub>2</sub> Production through Rational Electrocatalyst Design. *Nat. Mater.* **2013**, *12* (12), 1137–1143.
- (132) She, Z. W.; Kibsgaard, J.; Dickens, C. F.; Chorkendorff, I.; Nørskov, J. K.; Jaramillo, T. F. Combining Theory and Experiment in Electrocatalysis: Insights into Materials Design. *Science (80-. )*. **2017**, *355* (6321), eaad4998.
- (133) Verdager-Casadevall, A.; Deiana, D.; Karamad, M.; Siahrostami, S.; Malacrida, P.; Hansen, T. W.; Rossmeisl, J.; Chorkendorff, I.; Stephens, I. E. L. Trends in the Electrochemical Synthesis of H<sub>2</sub>O<sub>2</sub>: Enhancing Activity and Selectivity by Electrocatalytic Site Engineering. *Nano Lett.* **2014**, *14* (3), 1603–1608.
- (134) Verdager-Casadevall, A.; Hernandez-Fernandez, P.; Stephens, I. E. L.; Chorkendorff, I.; Dahl, S. The Effect of Ammonia upon the Electrocatalysis of Hydrogen Oxidation and Oxygen Reduction on Polycrystalline Platinum. *J. Power Sources* **2012**, *220*, 205–210.
- (135) Jirkovský, J. S.; Panas, I.; Ahlberg, E.; Halasa, M.; Romani, S.; Schiffrin, D. J. Single Atom Hot-

Spots at Au-Pd Nanoalloys for Electrocatalytic H<sub>2</sub>O<sub>2</sub> production. *J. Am. Chem. Soc.* **2011**, *133* (48), 19432–19441.

(136) Zhang, J.; Zhao, Z.; Xia, Z.; Dai, L. A Metal-Free Bifunctional Electrocatalyst for Oxygen Reduction and Oxygen Evolution Reactions. *Nat. Nanotechnol.* **2015**, *10*, 444–452.

(137) Wang, H.; Chen, Y.; Hou, X.; Ma, C.; Tan, T. Nitrogen-Doped Graphenes as Efficient Electrocatalysts for the Selective Reduction of Carbon Dioxide to Formate in Aqueous Solution. *Green Chem.* **2016**, *18* (11), 3250–3256.

(138) Zhang, S.; Kang, P.; Ubnoske, S.; Brennaman, M. K.; Song, N.; House, R. L.; Glass, J. T.; Meyer, T. J. Polyethylenimine-Enhanced Electrocatalytic Reduction of CO<sub>2</sub> to Formate at Nitrogen-Doped Carbon Nanomaterials. *J. Am. Chem. Soc.* **2014**, *136* (22), 7845–7848.

(139) Wu, J.; Yadav, R. M.; Liu, M.; Sharma, P. P.; Tiwary, C. S.; Ma, L.; Zou, X.; Zhou, X. D.; Yakobson, B. I.; Lou, J.; et al. Achieving Highly Efficient, Selective, and Stable CO<sub>2</sub> Reduction on Nitrogen-Doped Carbon Nanotubes. *ACS Nano* **2015**, *9* (5), 5364–5371.

(140) Li, N.; Wang, Z.; Zhao, K.; Shi, Z.; Gu, Z.; Xu, S. Large Scale Synthesis of N-Doped Multi-Layered Graphene Sheets by Simple Arc-Discharge Method. *Carbon N. Y.* **2010**, *48* (1), 255–259.

(141) Guo, L.; Zhang, Y. L.; Han, D. D.; Jiang, H. B.; Wang, D.; Li, X. Bin; Xia, H.; Feng, J.; Chen, Q. D.; Sun, H. B. Laser-Mediated Programmable n Doping and Simultaneous Reduction of Graphene Oxides. *Adv. Opt. Mater.* **2014**, *2* (2), 120–125.

(142) Wei, D.; Liu, Y.; Wang, Y.; Zhang, H.; Huang, L.; Yu, G. Synthesis of N-Doped Graphene by Chemical Vapor Deposition and Its Electrical Properties. *Nano Lett.* **2009**, *9*, 1752–1758.

(143) Qu, D.; Zheng, M.; Zhang, L.; Zhao, H.; Xie, Z.; Jing, X.; Haddad, R. E.; Fan, H.; Sun, Z. Formation Mechanism and Optimization of Highly Luminescent N-Doped Graphene Quantum Dots. *Sci. Rep.* **2014**, *4*, 1–11.

(144) Czerw, R.; Terrones, M.; Charlier, J. C.; Blase, X.; Foley, B.; Kamalakaran, R.; Grobert, N.; Terrones, H.; Tekleab, D.; Ajayan, P. M.; et al. Identification of Electron Donor States in N-Doped Carbon Nanotubes. *Nano Lett.* **2001**, *1* (9), 457–460.

(145) Yu, D.; Zhang, Q.; Dai, L. Highly-Efficient Metal-Free Growth of Nitrogen-Doped Single-Walled Carbon Nanotubes on Plasma-Etched Substrates for Oxygen Reduction Highly-Efficient Metal-Free Growth of Nitrogen-Doped Single-Walled Carbon Nanotubes on Plasma-Etched Substrates for Oxygen. *J. Am. Chem. Soc.* **2010**, No. January, 1–19.

(146) Dorjgotov, A.; Ok, J.; Jeon, Y.; Yoon, S. H.; Shul, Y. G. Activity and Active Sites of Nitrogen-Doped Carbon Nanotubes for Oxygen Reduction Reaction. *J. Appl. Electrochem.* **2013**, *43* (4), 387–

397.

- (147) Qu, K.; Zheng, Y.; Dai, S.; Qiao, S. Z. Graphene Oxide-Polydopamine Derived N, S-Codoped Carbon Nanosheets as Superior Bifunctional Electrocatalysts for Oxygen Reduction and Evolution. *Nano Energy* **2016**, *19*, 373–381.
- (148) Liu, J.; Liu, C. T.; Zhao, L.; Zhang, J. J.; Zhang, L. M.; Wang, Z. B. Effect of Different Structures of Carbon Supports for Cathode Catalyst on Performance of Direct Methanol Fuel Cell. *Int. J. Hydrogen Energy* **2016**, *41* (3), 1859–1870.
- (149) Duan, J.; Chen, S.; Dai, S.; Qiao, S. Z. Shape Control of Mn<sub>3</sub>O<sub>4</sub> Nanoparticles on Nitrogen-Doped Graphene for Enhanced Oxygen Reduction Activity. *Adv. Funct. Mater.* **2014**, *24* (14), 2072–2078.
- (150) Yang, Z.; Zhou, X.; Jin, Z.; Liu, Z.; Nie, H.; Chen, X.; Huang, S. A Facile and General Approach for the Direct Fabrication of 3D, Vertically Aligned Carbon Nanotube Array/Transition Metal Oxide Composites as Non-Pt Catalysts for Oxygen Reduction Reactions. *Adv. Mater.* **2014**, *26* (19), 3156–3161.
- (151) Sun, M.; Dong, Y.; Zhang, G.; Qu, J.; Li, J.  $\alpha$ -Fe<sub>2</sub>O<sub>3</sub> Spherical Nanocrystals Supported on CNTs as Efficient Non-Noble Electrocatalysts for the Oxygen Reduction Reaction. *J. Mater. Chem. A* **2014**, *2* (33), 13635–13640.
- (152) Wu, Z.-S.; Yang, S.; Sun, Y.; Parvez, K.; Feng, X.; Müllen, K. 3D Nitrogen-Doped Graphene Aerogel-Supported Fe<sub>3</sub>O<sub>4</sub> Nanoparticles as Efficient Electrocatalysts for the Oxygen Reduction Reaction. *J. Am. Chem. Soc.* **2012**, *134* (22), 9082–9085.
- (153) Liang, Y.; Li, Y.; Wang, H.; Zhou, J.; Wang, J.; Regier, T.; Dai, H. Co<sub>3</sub>O<sub>4</sub> Nanocrystals on Graphene as a Synergistic Catalyst for Oxygen Reduction Reaction. *Nat. Mater.* **2011**, *10* (10), 780–786.
- (154) Liang, Y.; Wang, H.; Diao, P.; Chang, W.; Hong, G.; Li, Y.; Gong, M.; Xie, L.; Zhou, J.; Wang, J.; et al. Oxygen Reduction Electrocatalyst Based on Strongly Coupled Cobalt Oxide Nanocrystals and Carbon Nanotubes. *J. Am. Chem. Soc.* **2012**, *134* (38), 15849–15857.
- (155) Ferrandon, M.; Kropf, A. J.; Myers, D. J.; Artyushkova, K.; Kramm, U.; Bogdanoff, P.; Wu, G.; Johnston, C. M.; Zelenay, P. Multitechnique Characterization of a Polyaniline-Iron-Carbon Oxygen Reduction Catalyst. *J. Phys. Chem. C* **2012**, *116* (30), 16001–16013.
- (156) Faubert, G.; Dodelet, J. P.; Lefievre, M.; Bertrand, P. Oxygen Reduction Catalysts for Polymer Electrolyte Cells from the Pyrolysis of Fe<sup>II</sup> Acetate Adsorbed 3,4,9,10-Perylenetetracarboxylic Dianhydride. *Electrochim. Acta* **1999**, *44*, 2589–2630.

- (157) Chen, W.; Fan, Z.; Pan, X.; Bao, X. Effect of Confinement in Carbon Nanotubes on the Activity of Fischer-Tropsch Iron Catalyst. *J. Am. Chem. Soc.* **2008**, *130* (29), 9414–9419.
- (158) Zhang, F.; Pan, X.; Hu, Y.; Yu, L.; Chen, X.; Jiang, P.; Zhang, H.; Deng, S.; Zhang, J.; Bolin, T. B.; et al. Tuning the Redox Activity of Encapsulated Metal Clusters via the Metallic and Semiconducting Character of Carbon Nanotubes. *Proc. Natl. Acad. Sci.* **2013**, *110* (37), 14861–14866.
- (159) Deng, D.; Yu, L.; Chen, X.; Wang, G.; Jin, L.; Pan, X.; Deng, J.; Sun, G.; Bao, X. Iron Encapsulated within Pod-like Carbon Nanotubes for Oxygen Reduction Reaction. *Angew. Chemie - Int. Ed.* **2013**, *52* (1), 371–375.
- (160) Hu, Y.; Jensen, J. O.; Zhang, W.; Cleemann, L. N.; Xing, W.; Bjerrum, N. J.; Li, Q. Hollow Spheres of Iron Carbide Nanoparticles Encased in Graphitic Layers as Oxygen Reduction Catalysts. *Angew. Chemie - Int. Ed.* **2014**, *53* (14), 3675–3679.
- (161) Strickland, K.; Miner, E.; Jia, Q.; Tylus, U.; Ramaswamy, N.; Liang, W.; Sougrati, M. T.; Jaouen, F.; Mukerjee, S. Highly Active Oxygen Reduction Non-Platinum Group Metal Electrocatalyst without Direct Metal-Nitrogen Coordination. *Nat. Commun.* **2015**, *6*, 1–8.
- (162) Varnell, J. A.; Tse, E. C. M.; Schulz, C. E.; Fister, T. T.; Haasch, R. T.; Timoshenko, J.; Frenkel, A. I.; Gewirth, A. A. Identification of Carbon-Encapsulated Iron Nanoparticles as Active Species in Non-Precious Metal Oxygen Reduction Catalysts. *Nat. Commun.* **2016**, *7*, 1–9.
- (163) Zhang, X.; Lin, J.; Chen, S.; Yang, J.; Song, L.; Wu, X.; Xu, H. Co Nanoparticles Encapsulated in N-Doped Carbon Nanosheets: Enhancing Oxygen Reduction Catalysis without Metal-Nitrogen Bonding. *ACS Appl. Mater. Interfaces* **2017**, *9* (44), 38499–38506.
- (164) Chen, W.; Cai, S.; Ren, Q.-Q.; Wen, W.; Zhao, Y.-D. Recent Advances in Electrochemical Sensing for Hydrogen Peroxide: A Review. *Analyst* **2012**, *137* (1), 49–58.
- (165) [Http://www.Cosmeticsinfo.Org/Ingredient/Hydrogen-Peroxide-0](http://www.cosmeticsinfo.org/ingredient/hydrogen-peroxide-0).
- (166) Giorgio, M.; Trinei, M.; Migliaccio, E.; Pelicci, P. G. Hydrogen Peroxide: A Metabolic by-Product or a Common Mediator of Ageing Signals? *Nat. Rev. Mol. Cell Biol.* **2007**, *8* (9), 722–728.
- (167) Geiszt, M.; Leto, T. L. The Nox Family of NAD(P)H Oxidases: Host Defense and Beyond. *J. Biol. Chem.* **2004**, *279* (50), 51715–51718.
- (168) Nogueira, R. F. P.; Oliveira, M. C.; Paterlini, W. C. Simple and Fast Spectrophotometric Determination of H<sub>2</sub>O<sub>2</sub> in Photo-Fenton Reactions Using Metavanadate. *Talanta* **2005**, *66* (1), 86–91.
- (169) Lee, J. H.; Tang, I. N.; Weinstein-Lloyd, J. B. Nonenzymatic Method for the Determination of

- Hydrogen Peroxide in Atmospheric Samples. *Anal. Chem.* **1990**, *62* (21), 2381–2384.
- (170) Gomes, A.; Fernandes, E.; Lima, J. L. F. C. Fluorescence Probes Used for Detection of Reactive Oxygen Species. *J. Biochem. Biophys. Methods* **2005**, *65* (2–3), 45–80.
- (171) Hanaoka, S.; Lin, J. M.; Yamada, M. Chemiluminescent Flow Sensor for H<sub>2</sub>O<sub>2</sub> Based on the Decomposition of H<sub>2</sub>O<sub>2</sub> Catalyzed by Cobalt(II)-Ethanolamine Complex Immobilized on Resin. *Anal. Chim. Acta* **2001**, *426* (1), 57–64.
- (172) Wang, J. Electrochemical Biosensors: Towards Point-of-Care Cancer Diagnostics. *Biosens. Bioelectron.* **2006**, *21* (10), 1887–1892.
- (173) Karyakin, A. A.; Karyakina, E. E.; Gorton, L. Amperometric Biosensor for Glutamate Using Prussian Blue-Based “artificial Peroxidase” as a Transducer for Hydrogen Peroxide. *Anal. Chem.* **2000**, *72* (7), 1720–1723.
- (174) Karyakin, A. A. Prussian Blue and Its Analogues: Electrochemistry and Analytical Applications. *Electroanalysis* **2001**, *13* (10), 813–819.
- (175) Karyakin, A. A.; Karyakina, E. E.; Gorton, L. Prussian-Blue-Based Amperometric Biosensors in Flow-Injection Analysis. *Talanta* **1996**, *43* (9), 1597–1606.
- (176) Ricci, F.; Palleschi, G. Sensor and Biosensor Preparation, Optimisation and Applications of Prussian Blue Modified Electrodes. *Biosens. Bioelectron.* **2005**, *21* (3), 389–407.
- (177) Koncki, R. Chemical Sensors and Biosensors Based on Prussian Blues. *Crit. Rev. Anal. Chem.* **2002**, *32* (1), 79–96.
- (178) Garjonyte, R.; Malinauskas, A. Operational Stability of Amperometric Hydrogen Peroxide Sensors, Based on Ferrous and Copper Hexacyanoferrates. *Sensors Actuators, B Chem.* **1999**, *56* (1), 93–97.
- (179) Rodríguez, M. C.; Rivas, G. A. An Enzymatic Glucose Biosensor Based on the Codeposition of Rhodium, Iridium, and Glucose Oxidase onto a Glassy Carbon Transducer. *Anal. Lett.* **2001**, *34* (11), 1829–1840.
- (180) Miscoria, S. A.; Barrera, G. D.; Rivas, G. A. Glucose Biosensors Based on the Immobilization of Glucose Oxidase and Polytyramine on Rodhinized Glassy Carbon and Screen Printed Electrodes. *Sensors Actuators, B Chem.* **2006**, *115* (1), 205–211.
- (181) Gorton, L.; Lindgren, A.; Larsson, T.; Munteanu, F. D.; Ruzgas, T.; Gazaryan, I. Direct Electron Transfer between Heme-Containing Enzymes and Electrodes as Basis for Third Generation Biosensors. *Anal. Chim. Acta* **1999**, *400* (1–3), 91–108.
- (182) Bracamonte, M. V.; Melchionna, M.; Giuliani, A.; Nasi, L.; Tavagnacco, C.; Prato, M.;

- Fornasiero, P. H<sub>2</sub>O<sub>2</sub> sensing Enhancement by Mutual Integration of Single Walled Carbon Nanohorns with Metal Oxide Catalysts: The CeO<sub>2</sub> case. *Sensors Actuators, B Chem.* **2017**, *239*, 923–932.
- (183) Lee, E. P.; Peng, Z.; Chen, W.; Chen, S.; Yang, H.; Xia, Y. Electrocatalytic Properties of Pt Nanowires Supported on Pt and W Gauzes. *ACS Nano* **2008**, *2* (10), 2167–2173.
- (184) Hrapovic, S.; Liu, Y.; Male, K. B.; Luong, J. H. T. Electrochemical Biosensing Platforms Using Platinum Nanoparticles and Carbon Nanotubes. *Anal. Chem.* **2004**, *76* (4), 1083–1088.
- (185) Miscoria, S. A.; Barrera, G. D.; Rivas, G. A. Analytical Performance of a Glucose Biosensor Prepared by Immobilization of Glucose Oxidase and Different Metals into a Carbon Paste Electrode. *Electroanalysis* **2002**, *14* (14), 981–987.
- (186) Rodriguez, M. C.; Rivas, G. A. Amperometric Glucose Biosensor Based on the Deposition of Copper and Glucose Oxidase onto Glassy Carbon Transducer. *Anal. Lett.* **2000**, *33* (12), 2373–2389.
- (187) Rodriguez, M. C.; Rivas, G. A. Highly Selective First Generation Glucose Biosensor Based on Carbon Paste Containing Copper and Glucose Oxidase. *Electroanalysis* **2001**, *14* (13), 1179–1184.
- (188) Luque, G. L.; Ferreyra, N. F.; Rivas, G. A. Glucose Biosensor Based on the Use of a Carbon Nanotube Paste Electrode Modified with Metallic Particles. *Microchim. Acta* **2006**, *152* (3–4 SPEC. ISS.), 277–283.
- (189) Rivas, G. A.; Maestroni, B. Iridium-Dispersed Carbon Paste Amino Acid Oxidase Electrodes. *Anal. Lett.* **1997**, *30* (3), 489–501.
- (190) Rodriguez, M. C.; Rivas, G. A. Glucose Biosensor Prepared by the Deposition of Iridium and Glucose Oxidase on Glassy Carbon Transducer. *Electroanalysis* **1999**, *11* (8), 558–564.
- (191) Comba, F. N.; Rubianes, M. D.; Herrasti, P.; Rivas, G. A. Glucose Biosensing at Carbon Paste Electrodes Containing Iron Nanoparticles. *Sensors Actuators, B Chem.* **2010**, *149* (1), 306–309.
- (192) Maduraiveeran, G.; Ramaraj, R. Gold Nanoparticles Embedded in Silica Sol-Gel Matrix as an Amperometric Sensor for Hydrogen Peroxide. *J. Electroanal. Chem.* **2007**, *608* (1), 52–58.
- (193) Guo, S.; Wen, D.; Dong, S.; Wang, E. Gold Nanowire Assembling Architecture for H<sub>2</sub>O<sub>2</sub> Electrochemical Sensor. *Talanta* **2009**, *77* (4), 1510–1517.
- (194) Zhang, Y.; Sun, Y.; Liu, Z.; Xu, F.; Cui, K.; Shi, Y.; Wen, Z.; Li, Z. Au Nanocages for Highly Sensitive and Selective Detection of H<sub>2</sub>O<sub>2</sub>. *J. Electroanal. Chem.* **2011**, *656* (1–2), 23–28.
- (195) Meng, F.; Yan, X.; Liu, J.; Gu, J.; Zou, Z. Nanoporous Gold as Non-Enzymatic Sensor for Hydrogen Peroxide. *Electrochim. Acta* **2011**, *56* (12), 4657–4662.
- (196) Xiao, F.; Zhao, F.; Zhang, Y.; Guo, G.; Zeng, B. Ultrasonic Electrodeposition of Gold-Platinum

- Alloy Nanoparticles on Ionic Liquid-Chitosan Composite Film and Their Application in Fabricating Nonenzyme Hydrogen Peroxide Sensors. *J. Phys. Chem. C* **2009**, *113* (3), 849–855.
- (197) Liu, H.; Wen, M.; Zhang, F.; Liu, D.; Tian, Y. Electrochemical Sensing Platform for Hydrogen Peroxide Using Amorphous FeNiPt Nanostructures. *Anal. Methods* **2010**, *2* (2), 143–148.
- (198) Lin, Y.; Cui, X.; Li, L. Low-Potential Amperometric Determination of Hydrogen Peroxide with a Carbon Paste Electrode Modified with Nanostructured Cryptomelane-Type Manganese Oxides. *Electrochem. commun.* **2005**, *7* (2), 166–172.
- (199) Cui, X.; Liu, G.; Lin, Y. Amperometric Biosensors Based on Carbon Paste Electrodes Modified with Nanostructured Mixed-Valence Manganese Oxides and Glucose Oxidase. *Nanomedicine Nanotechnology, Biol. Med.* **2005**, *1* (2), 130–135.
- (200) Xu, B.; Ye, M. L.; Yu, Y. X.; Zhang, W. De. A Highly Sensitive Hydrogen Peroxide Amperometric Sensor Based on MnO<sub>2</sub>-Modified Vertically Aligned Multiwalled Carbon Nanotubes. *Anal. Chim. Acta* **2010**, *674* (1), 20–26.
- (201) Chen, X.; Zhang, X.; Yang, W.; Evans, D. G. Biopolymer-Manganese Oxide Nanoflake Nanocomposite Films Fabricated by Electrostatic Layer-by-Layer Assembly. *Mater. Sci. Eng. C* **2009**, *29* (1), 284–287.
- (202) Šljukić, B.; Compton, R. G. Manganese Dioxide Graphite Composite Electrodes Formed via a Low Temperature Method: Detection of Hydrogen Peroxide, Ascorbic Acid and Nitrite. *Electroanalysis* **2007**, *19* (12), 1275–1280.
- (203) Salimi, A.; Hallaj, R.; Soltanian, S.; Mamkhezri, H. Nanomolar Detection of Hydrogen Peroxide on Glassy Carbon Electrode Modified with Electrodeposited Cobalt Oxide Nanoparticles. *Anal. Chim. Acta* **2007**, *594* (1), 24–31.
- (204) Jiang, L. C.; Zhang, W. D. Electrodeposition of TiO<sub>2</sub> Nanoparticles on Multiwalled Carbon Nanotube Arrays for Hydrogen Peroxide Sensing. *Electroanalysis* **2009**, *21* (8), 988–993.
- (205) Luque, G. L.; Rodríguez, M. C.; Rivas, G. A. Glucose Biosensors Based on the Immobilization of Copper Oxide and Glucose Oxidase within a Carbon Paste Matrix. *Talanta* **2005**, *66* (2 SPEC. ISS.), 467–471.
- (206) Miao, X. M.; Yuan, R.; Chai, Y. Q.; Shi, Y. T.; Yuan, Y. Y. Direct Electrocatalytic Reduction of Hydrogen Peroxide Based on Nafion and Copper Oxide Nanoparticles Modified Pt Electrode. *J. Electroanal. Chem.* **2008**, *612* (2), 157–163.
- (207) Elzanowska, H.; Abu-Irhayem, E.; Skrzynecka, B.; Birss, V. I. Hydrogen Peroxide Detection at Electrochemically and Sol-Gel Derived Ir Oxide Films. *Electroanalysis* **2004**, *16* (6), 478–490.

- (208) McCreery, R. L. Advanced Carbon Electrode Materials for Molecular Electrochemistry. *Chem. Rev.* **2008**, *108* (7), 2646–2687.
- (209) Banks, C. E.; Davies, T. J.; Wildgoose, G. G.; Compton, R. G. Electrocatalysis at Graphite and Carbon Nanotube Modified Electrodes: Edge-Plane Sites and Tube Ends Are the Reactive Sites. *Chem. Commun.* **2005**, No. 7, 829–841.
- (210) Zhou, M.; Guo, J.; Guo, L.-P.; Bai, J. Electrochemical Sensing Platform Based on the Highly Ordered Mesoporous Carbon-Fullerene System. *Anal. Chem.* **2008**, *80*, 4642–4650.
- (211) Wu, L.; Zhang, X.; Ju, H. Detection of NADH and Ethanol Based on Catalytic Activity of Soluble Carbon Nanofiber with Low Overpotential. *Anal. Chem.* **2007**, *79* (2), 453–458.
- (212) Jia, N.; Huang, B.; Chen, L.; Tan, L.; Yao, S. A Simple Non-Enzymatic Hydrogen Peroxide Sensor Using Gold Nanoparticles-Graphene-Chitosan Modified Electrode. *Sensors Actuators, B Chem.* **2014**, *195*, 165–170.
- (213) Yuan, B.; Xu, C.; Liu, L.; Shi, Y.; Li, S.; Zhang, R.; Zhang, D. Polyethylenimine-Bridged Graphene Oxide-Gold Film on Glassy Carbon Electrode and Its Electrocatalytic Activity toward Nitrite and Hydrogen Peroxide. *Sensors Actuators, B Chem.* **2014**, *198*, 55–61.
- (214) Zhang, C.; Zhang, Y.; Miao, Z.; Ma, M.; Du, X.; Lin, J.; Han, B.; Takahashi, S.; Anzai, J. I.; Chen, Q. Dual-Function Amperometric Sensors Based on Poly(Diallyldimethylammonium Chloride)-Functionalized Reduced Graphene Oxide/Manganese Dioxide/Gold Nanoparticles Nanocomposite. *Sensors Actuators, B Chem.* **2016**, *222*, 663–673.
- (215) Shang, L.; Zeng, B.; Zhao, F. Fabrication of Novel Nitrogen-Doped Graphene-Hollow AuPd Nanoparticle Hybrid Films for the Highly Efficient Electrocatalytic Reduction of H<sub>2</sub>O<sub>2</sub>. *ACS Appl. Mater. Interfaces* **2015**, *7* (1), 122–128.
- (216) Wang, W.; Xie, Y.; Xia, C.; Du, H.; Tian, F. Titanium Dioxide Nanotube Arrays Modified with a Nanocomposite of Silver Nanoparticles and Reduced Graphene Oxide for Electrochemical Sensing. *Microchim. Acta* **2014**, *181* (11–12), 1325–1331.
- (217) Lu, D.; Zhang, Y.; Lin, S.; Wang, L.; Wang, C. Synthesis of PtAu Bimetallic Nanoparticles on Graphene-carbon Nanotube Hybrid Nanomaterials for Nonenzymatic Hydrogen Peroxide Sensor. *Talanta* **2013**, *112*, 111–116.
- (218) Woo, S.; Kim, Y. R.; Chung, T. D.; Piao, Y.; Kim, H. Synthesis of a Graphene-Carbon Nanotube Composite and Its Electrochemical Sensing of Hydrogen Peroxide. *Electrochim. Acta* **2012**, *59*, 509–514.
- (219) Wang, Q.; Li, M.; Szunerits, S.; Boukherroub, R. Environmentally Friendly Reduction of

- Graphene Oxide Using Tyrosine for Nonenzymatic Amperometric H<sub>2</sub>O<sub>2</sub> Detection. *Electroanalysis* **2014**, *26* (1), 156–163.
- (220) Ensafi, A. A.; Jafari-Asl, M.; Rezaei, B. A Novel Enzyme-Free Amperometric Sensor for Hydrogen Peroxide Based on Nafion/Exfoliated Graphene Oxide-Co<sub>3</sub>O<sub>4</sub> nanocomposite. *Talanta* **2013**, *103*, 322–329.
- (221) Li, S. J.; Du, J. M.; Zhang, J. P.; Zhang, M. J.; Chen, J. A Glassy Carbon Electrode Modified with a Film Composed of Cobalt Oxide Nanoparticles and Graphene for Electrochemical Sensing of H<sub>2</sub>O<sub>2</sub>. *Microchim. Acta* **2014**, *181* (5–6), 631–638.
- (222) Fang, H.; Pan, Y.; Shan, W.; Guo, M.; Nie, Z.; Huang, Y.; Yao, S. Enhanced Nonenzymatic Sensing of Hydrogen Peroxide Released from Living Cells Based on Fe<sub>3</sub>O<sub>4</sub>/Self-Reduced Graphene Nanocomposites. *Anal. Methods* **2014**, *6* (15), 6073–6081.
- (223) Yang, X.; Wang, L.; Zhou, G.; Sui, N.; Gu, Y.; Wan, J. Electrochemical Detection of H<sub>2</sub>O<sub>2</sub> Based on Fe<sub>3</sub>O<sub>4</sub> Nanoparticles with Graphene Oxide and Polyamidoamine Dendrimer. *J. Clust. Sci.* **2015**, *26* (3), 789–798.
- (224) Dong, S.; Xi, J.; Wu, Y.; Liu, H.; Fu, C.; Liu, H.; Xiao, F. High Loading MnO<sub>2</sub> nanowires on Graphene Paper: Facile Electrochemical Synthesis and Use as Flexible Electrode for Tracking Hydrogen Peroxide Secretion in Live Cells. *Anal. Chim. Acta* **2015**, *853* (1), 200–206.
- (225) Wang, J.; Musameh, M.; Lin, Y. Solubilization of Carbon Nanotubes by Nafion toward the Preparation of Amperometric Biosensors. *J. Am. Chem. Soc.* **2003**, *125* (9), 2408–2409.
- (226) Wang, J.; Musameh, M. Carbon Nanotube/Teflon Composite Electrochemical Sensors and Biosensors. *Anal. Chem.* **2003**, *75* (9), 2075–2079.
- (227) Xu, X.; Jiang, S.; Hu, Z.; Liu, S. Nitrogen-Doped Carbon Nanotubes: High Electrocatalytic Activity toward the Oxidation of Hydrogen Peroxide and Its Application for Biosensing. *ACS Nano* **2010**, *4* (7), 399–400.
- (228) Zhang, R.; Chen, W. Recent Advances in Graphene-Based Nanomaterials for Fabricating Electrochemical Hydrogen Peroxide Sensors. *Biosens. Bioelectron.* **2017**, *89*, 249–268.
- (229) Segal, M. Selling Graphene by the Ton. *Nat. Nanotechnol.* **2009**, *4* (10), 612–614.
- (230) Gilje, S.; Han, S.; Wang, M.; Wang, K. L.; Kaner, R. B. A Chemical Route to Graphene for Device Applications. *Nano Lett.* **2007**, *7* (11), 3394–3398.
- (231) Li, D.; Müller, M. B.; Gilje, S.; Kaner, R. B.; Wallace, G. G. Processable Aqueous Dispersions of Graphene Nanosheets. *Nat. Nanotechnol.* **2008**, *3* (2), 101–105.
- (232) Eda, G.; Fanchini, G.; Chhowalla, M. Large-Area Ultrathin Films of Reduced Graphene Oxide

as a Transparent and Flexible Electronic Material. *Nat. Nanotechnol.* **2008**, *3* (5), 270–274.

(233) Li, D.; Kaner, R. B. Graphene-Based Materials. *Science (80-. )*. **2008**, *320* (May), 1170–1171.

(234) Zhou, M.; Zhai, Y.; Dong, S. Electrochemical Sensing and Biosensing Platform Based on Chemically Reduced Graphene Oxide. *Anal. Chem.* **2009**, *81* (4), 5603–5613.

(235) Takahashi, S.; Abiko, N.; Anzai, J. I. Redox Response of Reduced Graphene Oxide-Modified Glassy Carbon Electrodes to Hydrogen Peroxide and Hydrazine. *Materials (Basel)*. **2013**, *6* (5), 1840–1850.

(236) Hamilton, C. E.; Lomeda, J. R.; Sun, Z.; Tour, J. M.; Barron, A. R. High-Yield Organic Dispersions of Unfunctionalized Graphene. *Nano Lett.* **2009**, *9* (10), 3460–3462.

(237) Liang, Y.; Wu, D.; Feng, X.; Müllen, K. Dispersion of Graphene Sheets in Organic Solvent Supported by Ionic Interactions. *Adv. Mater.* **2009**, *21* (17), 1679–1683.

(238) Lv, W.; Guo, M.; Liang, M. H.; Jin, F. M.; Cui, L.; Zhi, L.; Yang, Q. H. Graphene-DNA Hybrids: Self-Assembly and Electrochemical Detection Performance. *J. Mater. Chem.* **2010**, *20* (32), 6668–6673.

(239) Zor, E.; Saglam, M. E.; Akin, I.; Saf, A. O.; Bingol, H.; Ersoz, M. Green Synthesis of Reduced Graphene Oxide/Nanopolypyrrole Composite: Characterization and H<sub>2</sub>O<sub>2</sub> Determination in Urine. *RSC Adv.* **2014**, *4* (24), 12457–12466.

(240) Luo, J.; Chen, Y.; Ma, Q.; Liu, R.; Liu, X. Layer-by-Layer Assembled Ionic-Liquid Functionalized Graphene-Polyaniline Nanocomposite with Enhanced Electrochemical Sensing Properties. *J. Mater. Chem. C* **2014**, *2* (24), 4818–4827.

(241) Nguyen, V. H.; Tran, T. H.; Shim, J. J. Glassy Carbon Electrode Modified with a Graphene Oxide/Poly(o-Phenylenediamine) Composite for the Chemical Detection of Hydrogen Peroxide. *Mater. Sci. Eng. C* **2014**, *44*, 144–150.

## **CHAPTER 2: Nanostructured smart electrocatalysts for alkaline fuel cells applications**

### **2.1 Introduction**

The main issue hindering the large-scale application of fuel cells is their high cost. Recent analyses have shown that among PEM-FCs components around 45% of the cost comes from the platinum electrocatalyst.<sup>1</sup> Therefore, in order to allow this technology to become an affordable solution for automotive as well as other applications, it is crucial to try and find ways of substituting Pt with metals that are less expensive and more abundant in nature.<sup>2,3</sup> As an alternative to PEM-FCs that operate under corrosive acidic conditions, anion exchange membrane fuel cells (AEM-FCs) are receiving increasing attention, as this technology has the potential to ease the replacement of expensive platinum and platinum alloys. Significant progress is being obtained in improving material components for AEM-FCs, in particular, cell hardware, membranes, ionomers and cathode catalysts for the oxygen reduction reaction (ORR).<sup>4,5,6,7</sup> As far as the anodic electrocatalyst is concerned, the interest is shifting towards Pd, and stems from its better electrochemical kinetics in alkaline media. A number of different strategies have been investigated to prepare Pd-based electrocatalysts with higher activity, including controlling the morphology of Pd<sup>8,9</sup> and combining palladium with other metals to prepare Pd-M catalysts.<sup>10-13</sup> CeO<sub>2</sub> has been the subject of many studies because of its oxygen storage capacity, rapid saturation with OH<sup>-</sup> ions in alkaline media and spillover of OH<sup>-</sup> to supported metal nanoparticles.<sup>14</sup> Its ability to enhance Pd catalysis has been associated to the Pd-CeO<sub>2</sub> interfacial structure, and is remarkably improved by maximizing the contact between the two phases. It is therefore highly important to develop smart synthetic techniques to afford composites with optimum Pd-CeO<sub>2</sub> interface.

### **2.2: Nanostructured carbon supported Pd-ceria as anode catalysts for anion exchange membrane fuel cells**

It has been recently proven that the two main obstacles to the development of high performance AEM-FCs are the low efficiency and poor stability of anion exchange membranes combined with the high overpotential for the hydrogen oxidation reaction (HOR) in alkaline media.<sup>15,16</sup> Due to the well-known kinetic slowness of HOR at higher pH,<sup>17,18</sup> the catalytic activity of carbon supported noble metals decreases by around two orders of magnitude when changing from low to high pH.<sup>19</sup>

Researchers are addressing this issue in a systematic manner, by investigating the mechanism in detail, and, most importantly the role of the hydroxyl anion, which is still unclear. There are two possible mechanisms in which the adsorbed hydrogen species ( $H_{ads}$ ) on the surface of the metal catalyst can interact with  $OH^-$ . The one that typically occurs in an acidic environment, involves first the desorption of  $H_{ads}$  as a proton, and then its combination with  $OH^-$  to generate water. The sole determining factor for the HOR in this case is the hydrogen binding energy (HBE).



A second mechanism considers the simultaneous adsorption of a  $OH^-$  ion, and the combination of  $OH_{ads}$  with  $H_{ads}$  to form water occurring on the surface of the metal. In this case, HOR activity would be affected by both HBE and the OBE ( $OH^-$  Binding Energy).



The general opinion derived from a series of careful studies on Pt and Pt alloys catalysts is that HBE is the main descriptor for HOR activity on noble metals.<sup>20,21</sup> Markovic and co-workers<sup>22</sup> were the first to propose the bifunctional mechanism involving adsorbed OH groups. They were able to demonstrate that improving the HOR is possible through a careful balance of the active sites required for respectively the dissociation and adsorption of  $H_2$  and the adsorption of  $OH^-$ .<sup>22</sup> This was achieved through the preparation and testing of multiple bimetallic catalysts with increasing  $OH^-$  adsorption characteristics, and allowed to conclude that the presence of both types of adsorption sites is highly beneficial in terms of HOR activity. Further proof of this mechanism was recently provided for a Ru doped Pt/C catalyst.<sup>23</sup> The promoting effect on the oxidation of  $H_{ads}$  provided by the presence of  $OH_{ads}$  species on the surface of Ru in the HOR potential region was demonstrated thereby, and is an experimental proof of the bifunctional mechanism occurrence under alkaline conditions. While these considerations can explain why certain nanostructured metal alloys display enhanced HOR activity, they do not give any information on why metal oxide supported nanoparticles such as Pd NPs on  $CeO_2$  or nickel oxides show the same enhancement in activity.<sup>2,3,12</sup> This chapter is a collaboration with Vizza's group of the ICCOM-CNR of Sesto

Fiorentino (FI), who recently reported a catalyst based on Pd NPs deposited on a mixed support of Vulcan carbon and CeO<sub>2</sub> and observed enhanced HOR activity in base, as well as high power densities when deployed in a Pt-free AEM-FC.<sup>2,3</sup> The study presented herein is dedicated to the investigation on how the HOR activity is directly related to the interfacial structure between Pd and CeO<sub>2</sub>, and how it can be remarkably improved by maximizing the contact between the two phases. The material presented as anodic electrocatalyst is obtained through a smart and scalable synthesis involving the integration of CeO<sub>2</sub> starting from an alkoxide precursor followed by the Pd NPs deposition. This strategy allows to improve the interfacial structure between Pd and CeO<sub>2</sub>, as demonstrated by scanning transmission electron microscopy with energy dispersive X-ray spectroscopy (STEM/EDX). Furthermore, density functional theory calculations (DFT) were performed in order to support the bifunctional mechanism. We were able to demonstrate that the adsorption of H on Pd-CeO<sub>2</sub> is weaker than that on Pd(111), and that this is the reason why the catalytic activity for the HOR reaction is enhanced. Finally, more than 1.4 W cm<sup>-2</sup> peak power density was obtained in fuel cell testing.

## **2.2.1 Results and Discussion**

### **2.2.1.1 Catalyst preparation**

The Pd-CeO<sub>2</sub>/C catalytic system was prepared in three steps: first, the carbon support (C) Vulcan XC-72 was modified by mild oxidation with HNO<sub>3</sub>. This step is necessary for the functionalization of the carbon surface with oxygen bearing groups, which can act as anchor points for the deposition of ceria nanoparticles and also to improve dispersibility of the carbon phase in liquid media. CeO<sub>2</sub> was attached through a sol-gel technique already known to our group<sup>24</sup>, employing Ce(ODe)<sub>4</sub> as precursor. The functionalized carbon black interacts with the cerium alkoxide, guaranteeing uniformity of coverage and intimate contact between the two phases. The most crucial step, however, is the subsequent controlled hydrolysis to form CeO<sub>2</sub>, as it needs to be conducted very slowly in order not to disrupt the organized system just assembled. The Pd nanoparticles were then reduced and deposited on this mixed support by a polyol method with ethanol as reducing agent (Pd content 10 wt%). The sample was prepared with nominal weight ratio of (C:CeO<sub>2</sub>:Pd) 50:40:10. Finally the combined material was treated by calcination at 200 °C under air in order to crystallize the CeO<sub>2</sub> and remove any organic residues.

### 2.2.1.2 Morphologic characterization

In order to investigate the morphologic distribution of the three components, the catalyst sample was first characterized by TEM, HAADF-STEM and EDX. The images reported in Figure 1 show a homogeneous thin layer of nanostructured  $\text{CeO}_2$  covering the carbon support. STEM-EDX mapping confirms that the three components are distributed homogeneously throughout the material. Since the objective of this new synthetic strategy was to improve the phase contact between the Pd NP and the  $\text{CeO}_2$  layer, in Figure 2 more details are reported, including EDX maps, as well as the images for a previously reported catalyst integrating the same three components but prepared via a different synthetic method as a comparison.<sup>2,3</sup> It is noted that the images and maps (top row) show a fine dispersion of the Pd NPs on the carbon support particles, and a homogeneous coverage with  $\text{CeO}_2$  nanocrystals, leaving uncoated a relatively low portion of the carbon support. The pictures on the row below show the old Pd- $\text{CeO}_2$ /C catalyst imaged under the same conditions. The morphology is quite different: Pd NP are not homogeneously distributed, and  $\text{CeO}_2$  forms large crystalline aggregates that stand isolated from the carbon phase, leaving it largely uncovered. It is plausible that these differences in morphology and distribution of the three phases are responsible for the observed difference in performance, with the improved contact between Pd and  $\text{CeO}_2$  being a key factor for the enhanced HOR activity.

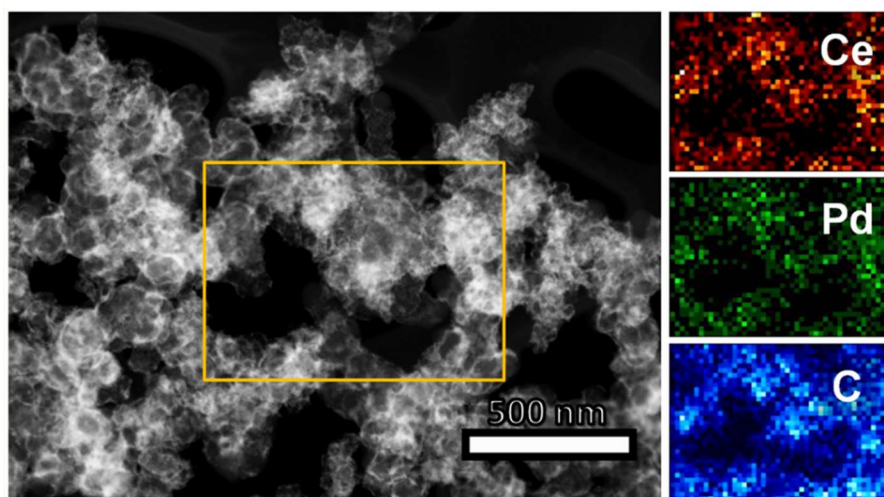


**Figure 1:** STEM images of Pd- $\text{CeO}_2$ /C: HAADF micrograph (left side) and STEM-EDX mapping (right side) of the selected area showing the Ce (red), Pd (green) and C (blue) elemental maps.

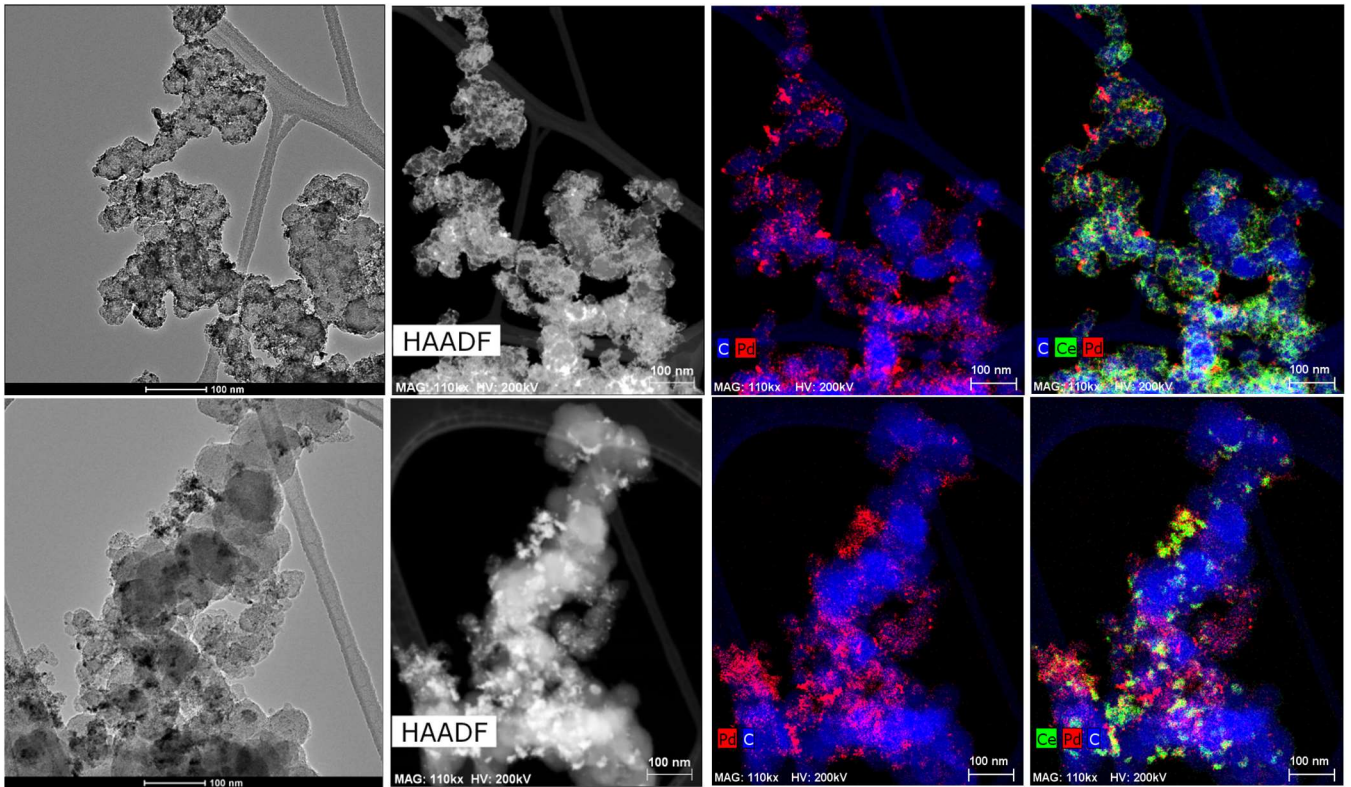


**Figure 2:** Comparative TEM, HAADF images, and EDX elemental maps of the new (top row) and old (bottom row) Pd-CeO<sub>2</sub>/C catalyst showing the Ce (green), Pd (red) and C (blue) regions.

XRD patterns were collected for CeO<sub>2</sub>/C and Pd-CeO<sub>2</sub>/C and are reported in Figure 3. For both materials, the reflections associated to the cubic structure of CeO<sub>2</sub> are the most prominent, and the breadth of the lines suggest that the nanoparticles are small and crystalline. In the pattern of Pd-CeO<sub>2</sub>/C the signal representative of metallic Pd(0) at 2θ = 40° is only barely visible; this suggests that the NPs are small, non-crystalline and highly oxidized.

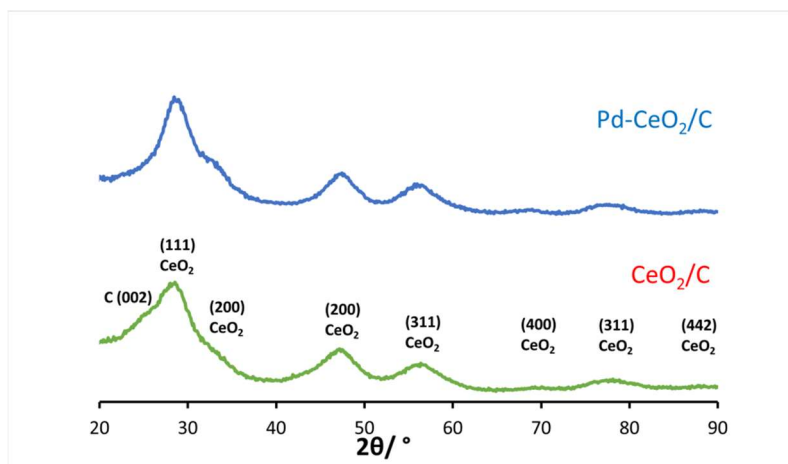


**Figure 3:** XRD patterns of CeO<sub>2</sub>/C and Pd-CeO<sub>2</sub>/C.

In order to investigate with increased depth the features of Pd-CeO<sub>2</sub>/C, in particular regarding the electronic state and local coordination environment of Pd, X-ray absorption near edge structure (XANES) was collected and combined with the Fourier Transform of the extended X-ray absorption fine structure (FT-EXAFS) of the spectra recorded at the Pd L<sub>3</sub>-edge. Figure 4 reports the spectra of Pd-CeO<sub>2</sub>/C compared with those performed at the same conditions using a Pd metallic foil as a reference. In the XANES spectrum (Figure 4a), the prominent white line confirms that the Pd in Pd-CeO<sub>2</sub>/C is highly oxidized, together with the presence of a prominent peak around 1.5 Å (without phase correction) in the FT-EXAFS spectrum, associated to Pd-O. The existence of some metallic Pd is suggested by the small peak at around 2.5 Å, which should be either a small amount, or very small in particle size, which is further supported by a reasonable EXAFS fitting without including the Pd-Pd scattering path (Figure 4b). EXAFS fitting parameters show that Pd is surrounded on average by 3.9 oxygen atoms in the first shell, with a typical bond distance of 2.0 Å (Table 1). The X-ray absorption spectroscopy results together, convey the image of a single Pd atom embedded in CeO<sub>2</sub> as the most frequent structure in the Pd-CeO<sub>2</sub>/C catalyst, with the palladium mostly in contact with the oxygen from CeO<sub>2</sub>. This feature considerably diversifies this material from the previously reported one, in which a significant portion of the Pd nanoparticles were accumulated on bare carbon because of the incomplete ceria coverage.<sup>2,3</sup> The exclusive interaction between Pd nanoparticles and the ceria layer in this new version of the catalyst is guaranteed by the homogeneity of the layer obtained through the sol-gel synthetic protocol. This optimized Pd-O interfacial structure leading to the maximization of favorable electronic interactions results in enhanced HOR activity. In particular, Pd-H interaction appears to be weakened by this kind of configuration, as demonstrated below through H<sub>2</sub>-TPD analyses and DFT calculations.

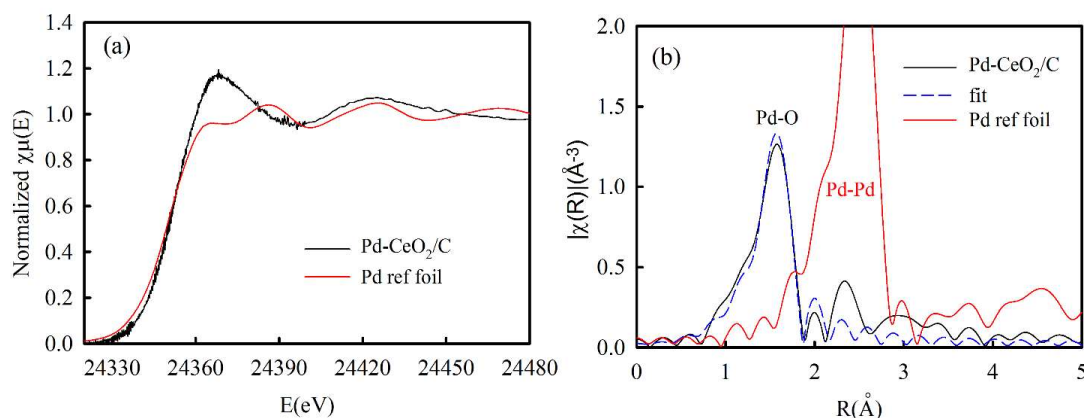


**Figure 4:** (a) XANES and (b) FT-EXAFS of the Pd L<sub>3</sub>-edge spectra of the Pd reference foil and the Pd-CeO<sub>2</sub>/C with curve fitting.

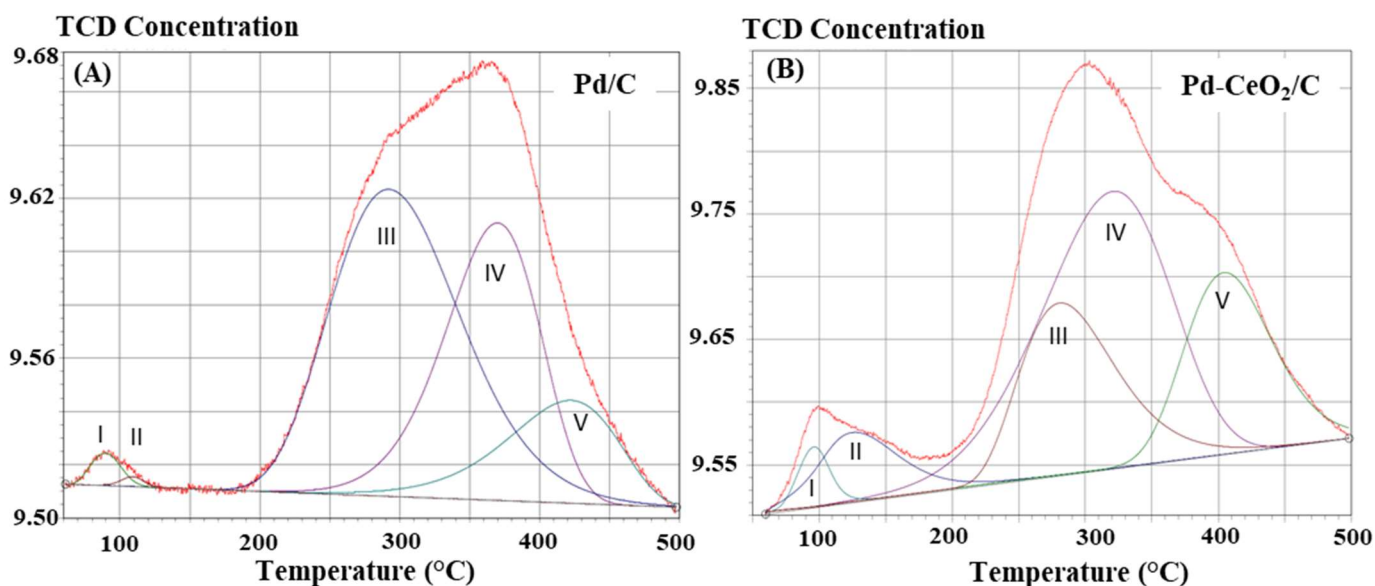
**Table 1:** Summary of EXAFS results\*

Scattering path	Edge (eV)	Bond length (Å)	Coordination number	D-W factor (Å <sup>2</sup> )
Pd-O	3.9±1.8	2.00± 0.01	3.9±0.4	0.002±0.001

\*S<sub>0</sub><sup>2</sup> fixed at 0.62 as obtained by fitting the reference foil. Fits were done in *R*-space, *k*<sup>1,2,3</sup> weighting at the Pt L<sub>3</sub>-edge with the windows of 1.0 < *R* < 2.4 Å and Δ*k* = 2.93 - 12.86 Å<sup>-1</sup>. Statistical errors of the least-squares fits were determined by ARTEMIS.

Overall, the X-ray absorption analysis indicates that Pd-CeO<sub>2</sub>/C presents a unique structure resulting in an unusually highly oxidized Pd closely coordinated to the oxygen atoms of CeO<sub>2</sub>.

In order to determine the way this feature is involved in the reported enhancement of HOR activity, the catalyst was studied through Temperature Programmed Desorption (TPD) analysis, and the results compared with those obtained with a Pd/C catalyst with the same metal loading. Figure 5 shows the spectra for the two different materials: in both distinguishable low temperature (< 200 °C) and high temperature (> 200 °C) hydrogen desorption peaks are visible and were appropriately deconvoluted.

**Figure 5:** Deconvolution of H<sub>2</sub>-TPD spectra for Pd-CeO<sub>2</sub>/C and Pd/C catalysts. Temperature ramp 10 °C min<sup>-1</sup>

**Table 2:** Comparison of H<sub>2</sub>-TPD for Pd-CeO<sub>2</sub>/C and Pd/C used as a reference.

Peak	10% Pd/C				10% Pd-CeO <sub>2</sub> /C			
	<i>t</i> °C	<i>mmol</i> (H <sub>2</sub> )/ <i>g<sub>cat</sub></i>	Ratio	H/Pd <sup>a</sup>	<i>t</i> °C	<i>mmol</i> (H <sub>2</sub> )/ <i>g<sub>cat</sub></i>	Ratio	H/Pd
I	91.5	0.00706	0.016	0.015	95.8	0.00954	0.016	0.020
II					121.7	0.04747	0.083	0.101
Σ <sub>I+II</sub>	-	0.00706	0.016	0.015	-	0.05701	0.099	0.121
III	292.0	0.20307	0.470	0.432	275.9	0.06447	0.113	0.138
IV	370.3	0.12546	0.290	0.267	313.8	0.30893	0.537	0.658
V	411.5	0.09641	0.284	0.205	405.8	0.08673	0.151	0.185
Σ <sub>III+IV+V</sub>	-	0.42494	0.984	0.904	-	0.46039	0.801	0.980
Σ	-	0.42494	1.00	0.919	-	0.57441	1.00	1.223

<sup>a</sup> Amount of H atoms per one Pd atom.

Table 2 reports the data collected for the two Pd-based materials. It is noticeable that the mass specific amount of H<sub>2</sub> desorbed from Pd-CeO<sub>2</sub>/C (~0.57 mmol g<sub>cat</sub><sup>-1</sup>) is higher than that measured for Pd/C (~0.42 mmol g<sub>cat</sub><sup>-1</sup>). Moreover, at temperatures lower than 200 °C the ratio of hydrogen desorption is higher for Pd-CeO<sub>2</sub>/C (9.9%) than for Pd/C (1.6%). Two different thermal shifts are observed for the two different materials: the desorption peaks I and II appear at higher temperature values for Pd-CeO<sub>2</sub>/C than for Pd/C, on the other hand, peaks III, IV and V present the opposite trend, the maximum desorption rate temperatures are higher for Pd/C. For Pd/C, the peak showing the highest intensity is peak III (292 °C) while for Pd-CeO<sub>2</sub>/C is peak IV (311.8°C). In Pd-H binary systems, two phases can coexist below a critical temperature of 298 °C: the α-phase, a solid solution of H in Pd, and the β-phase, also known as Pd hydride.<sup>25</sup> At room temperature, if the partial pressure exceeds 0.013 atm, Pd can absorb H<sub>2</sub> to form Pd hydride, when the H<sub>2</sub> partial pressure is lower it will dissolve to form α-phase but only sparingly. Decomposition of Pd hydride from supported Pd at temperatures between 50-100 °C has been reported in literature.<sup>26</sup> Therefore, based on the literature data<sup>27</sup>, peaks I and II at temperatures lower than 150 °C (Figure

5), can be associated to the  $\beta$ -phase decomposition. Since in this region, the amount of atoms of H per one Pd atom is 0.015 for Pd/C and almost one order of magnitude more for Pd-CeO<sub>2</sub>/C (H/Pd ratio, Table 2), comparison between these data and DFT calculations (reported below) led us to explain that the higher affinity of Pd-CeO<sub>2</sub>/C to hydrogen dissolution might result in its lower affinity to hydrogen chemisorption. Earlier reported results are in good agreement with this theory, showing that H binds less strongly to Pd hydride than to Pd.<sup>25</sup> Peaks arising at higher temperature (III, IV and V) are associated to strong adsorption of hydrogen. This can be correlated to the well-known phenomenon of spillover, transport and storage of chemisorbed H atoms on the ceria phase.<sup>27,28</sup> Also, the higher overall adsorption ratio of H<sub>2</sub> in Pd-CeO<sub>2</sub>/C (1.223) compared to Pd/C (0.919) reported in Table 2 can be the result of the spillover capacity of CeO<sub>2</sub>.<sup>29–32</sup> Nonetheless, literature reports a wide range of values associated to the H/Pd ratio for Pd/C catalysts, ranging from 0.005 to 0.77.<sup>33</sup>

### 2.2.1.3 DFT calculations

Pd atoms deposited on the top of the CeO<sub>2</sub> (110) surface was used as model for the supported Pd system. Different adsorption sites were investigated for the Pd binding on the CeO<sub>2</sub> (110) surface: the results led to the conclusion that Pd prefers to be absorbed at the bridge position between the O atoms of CeO<sub>2</sub> (Figure 6a), which is consistent with previously reported data.<sup>34,35</sup> Similarly, we discovered that H adsorbs preferentially in the site bridging between two Pd atoms (Figure 6b). We calculated the HBE of the Pd-CeO<sub>2</sub> as compared to Pd, as one possible descriptor for the HOR.<sup>36,37</sup> Its value relative to the gas phase resulted more positive for Pd(111) (-0.80 eV) than for the Pd/CeO<sub>2</sub> surface (-0.46 eV), as shown in Table 3, and this might be related to the enhancement of the HOR activity. In fact, the HBE of Pd is located on the left side of the volcano curve of HOR activity; therefore, the weaker adsorption of H on Pd-CeO<sub>2</sub> is consistent with the experimental activity we observed for the catalyst. We also investigated how HBE varies with the number of Pd layers on the CeO<sub>2</sub> (110) surface. The monolayer of Pd on CeO<sub>2</sub> appears from our calculations to be catalytically more active for HOR than multiple layers (Table 3). In fact, it is the first layer of metal that most undergoes the effect of H-bond deactivation due to the interaction with the O atoms in CeO<sub>2</sub>, whereas the second and third layers of Pd tend to behave almost like bulk Pd since they lack the direct metal-substrate contact. Nevertheless a difference in behavior with respect to Pd(111) is noticeable even for layers two and three, suggesting that the effect of HBE deactivation is still relevant, and so, that very small particles on CeO<sub>2</sub> will produce the highest HOR activity in

this kind of system. We confirmed through XAS data that the Pd in the Pd-CeO<sub>2</sub>/C is perfectly represented by this description. Moreover, this results in an actual enhancement in activity for HOR in alkaline conditions, as reported in the following electrochemical studies.

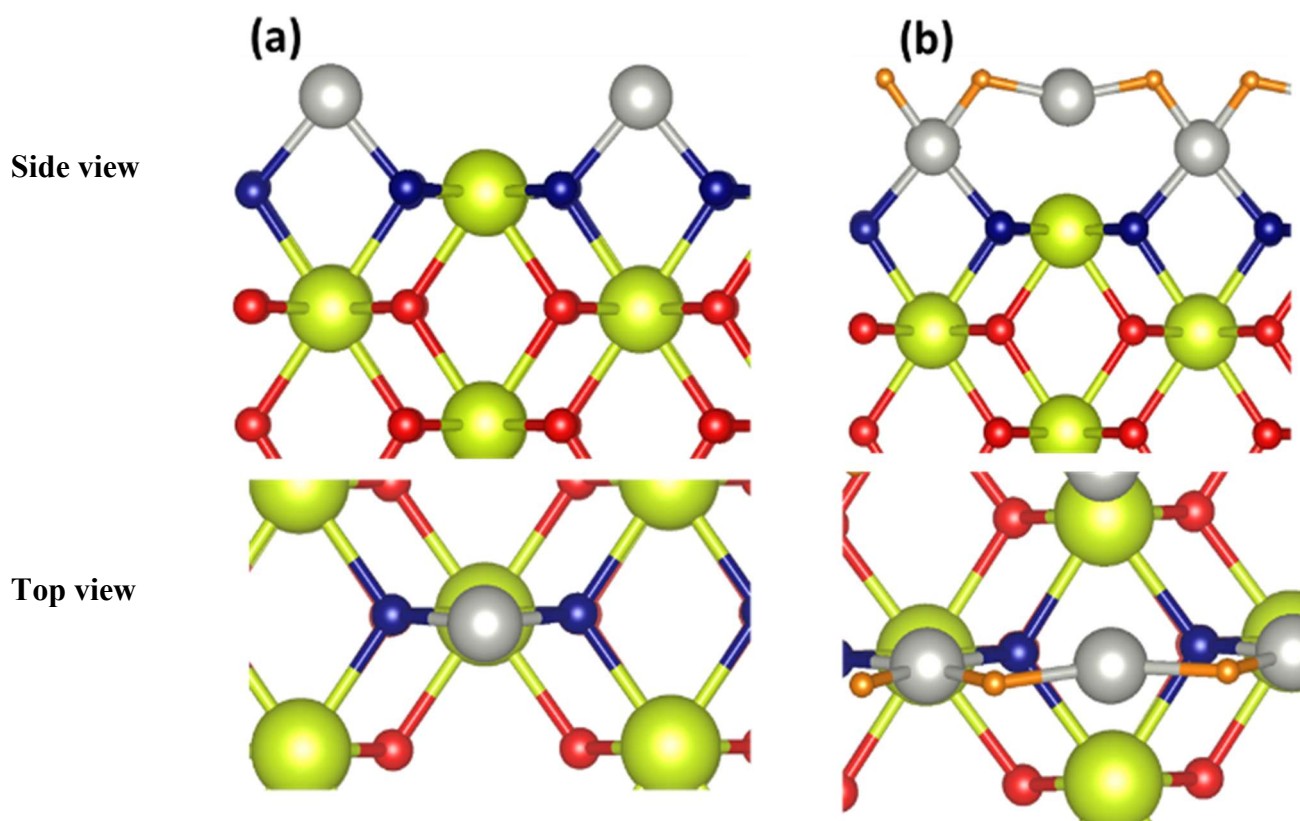


**Figure 6:** (a) Adsorption of Pd on bridge site between the O atoms of the CeO<sub>2</sub> (110) (b) Adsorption of H in between the Pd atoms. Green, grey and orange color ball represents Ce, Pd and H atoms, respectively. O atoms are in red and blue color, in order to distinguish the surface O atoms (blue) from other O atoms (red) in the slab.

**Table 3:** H binding energy on Pd-CeO<sub>2</sub> substrate. The HBE is in eV per H atom.

Structure	$E_{\text{ads}}$	HBE (1/2 H <sub>2</sub> as ref)	$U=0$ (1/2 H <sub>2</sub> )
Pd(111)	-4.14	-0.80	-1.03
Pd-CeO <sub>2</sub>	-3.80	-0.46	-0.67
2 layer of Pd on CeO <sub>2</sub>	-4.05	-0.71	-0.94
3 layer of Pd on CeO <sub>2</sub>	-4.03	-0.70	-0.93

#### 2.2.1.4 Electrochemical characterization

In order to investigate how the CeO<sub>2</sub>-Pd interaction affects the electrochemical performance of the material, a cyclic voltammetry (CV) study was performed on Pd-CeO<sub>2</sub>/C both in N<sub>2</sub> saturated 0.1 M KOH and N<sub>2</sub> saturated 0.2 M HClO<sub>4</sub>. As seen in Figure 7a, the usually well-defined Pd redox transitions are very broad and include a much higher capacitive current density. In the H uptake zone, the contribution from CeO<sub>2</sub> is large under alkaline conditions, but absent in acidic media. For the determination of the Electrochemically Active Surface Area (EASA), CO stripping voltammetry was undertaken in both alkaline (Figure 5C) and acidic (Figure 5D) conditions. The EASA determined by integration of the CO stripping peak had an average value of 63 m<sup>2</sup> g<sub>Pd</sub><sup>-1</sup>.

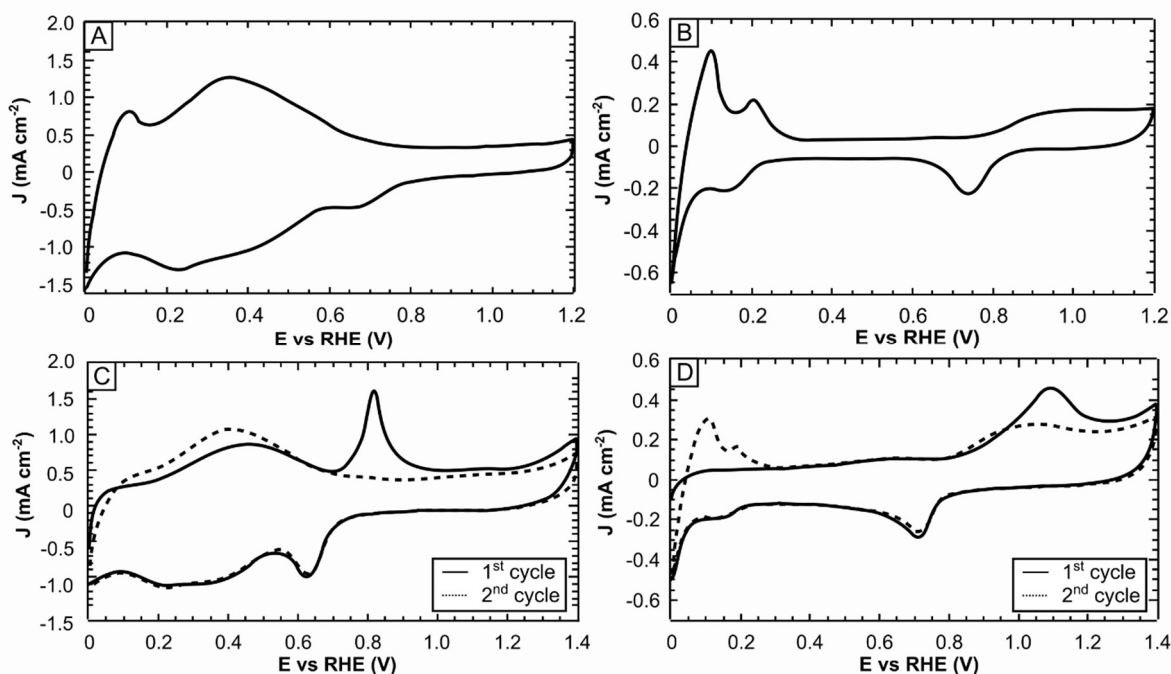


**Figure 7:** A) Cyclic voltammetry of Pd-CeO<sub>2</sub>/C in (A) N<sub>2</sub>-saturated 0.1 M KOH and (B) N<sub>2</sub>-saturated 0.2 M HClO<sub>4</sub> (50 mA s<sup>-1</sup>), (C) CO stripping voltammetry in 2 M KOH and (D) in 0.2 M HClO<sub>4</sub> (20 mA s<sup>-1</sup>).

The HOR activity of Pd-CeO<sub>2</sub>/C and in a fuel cell environment was evaluated through H<sub>2</sub> pump electrochemical tests. Two known catalysts were used as comparison: commercial 40% Pt/C (Alfa Aesar) and the Pd-CeO<sub>2</sub>/C catalyst previously reported.<sup>3</sup> The membrane electrode assemblies (MEAs) were formed by pressing together within the cell hardware the anode containing the selected HOR electrocatalysts, a cathode made with 40% Pt/C, and an anion exchange membrane. They were tested at 60 °C with humidified gases at fixed flow of 0.1 L min<sup>-1</sup> at both electrodes, N<sub>2</sub> at the cathode and H<sub>2</sub> at the anode. Table 4 reports the details for each catalyst and relevant

experimental data, while Figure 4 shows polarization curves and constant current density test results. The polarization curves in Figure 8a make clear how the activity of the new Pd-CeO<sub>2</sub>/C catalyst outperforms both the previously reported version and the Pt/C electrode with half the metal loading (0.20 vs 0.44 mg cm<sup>-2</sup>) at current densities above 150 mA cm<sup>-2</sup>. Moreover, both the catalysts containing CeO<sub>2</sub> operate at a lower cell potential (lower overpotential) than Pt/C, under a current density load of 300 mA cm<sup>-2</sup> and in the same conditions (Figure 8b).

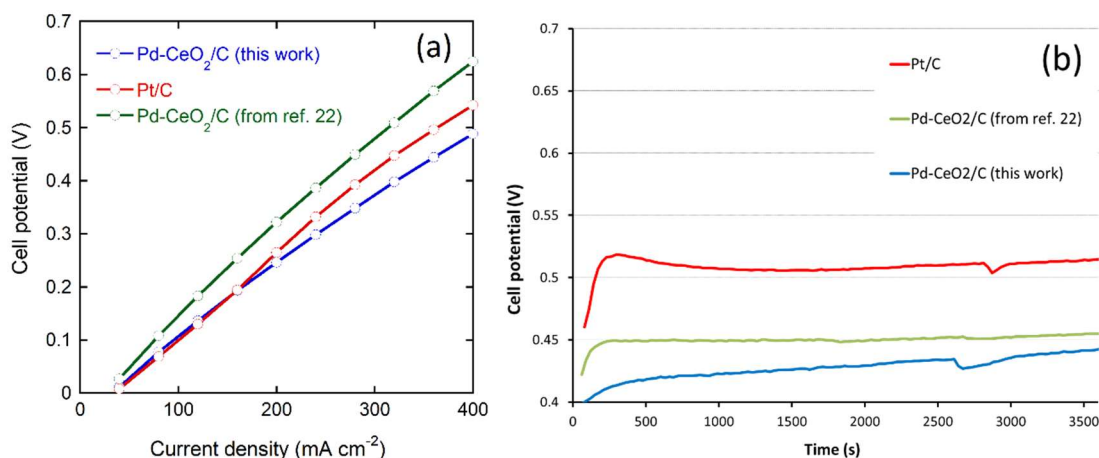


**Figure 8:** (a) Polarization curves of the hydrogen pumping tests comparing cell performance with the Pd-CeO<sub>2</sub>/C catalyst of this work as compared to both the previously reported Pd-CeO<sub>2</sub>/C<sup>3</sup> and Pt/C; (b) cell performance at a constant current density of 300 mA cm<sup>-2</sup> for 1 h ( $T_{\text{cell}}$  60 °C, anode H<sub>2</sub> 0.1 L min<sup>-1</sup> and cathode N<sub>2</sub> 0.1 L min<sup>-1</sup>).

**Table 4:** H<sub>2</sub> pump test data

Catalyst	mg <sub>metal</sub> cm <sup>-2</sup>	mV @ 200 mA cm <sup>-2</sup>	mV @ 400 mA cm <sup>-2</sup>	mV @ 300 mA cm <sup>-2</sup> (after 1 h)
Pt/C (40%)	0.44	265	542	510
Pd-CeO <sub>2</sub> /C (this thesis)	0.20	246	488	440
Pd-CeO <sub>2</sub> /C (previous work) <sup>3</sup>	0.20	321	624	455

### 2.2.1.5 Fuel cell testing

Fuel cell testing was carried out combining the Pd-CeO<sub>2</sub>/C anode catalyst reported here with a state-of-the-art anion exchange membrane (AEM) of the benzyltrimethylammonium-type, prepared by the radiation grafting of vinylbenzyl chloride onto a thin (15 μm) low density polyethylene. This class of AEMs has been reported to be extremely effective in fuel cells equipped with commercial Pt as the cathode and PtRu as the anode, producing exceptional maximum power density values, as high as 1.4-2.0 W cm<sup>-2</sup>).<sup>38-42</sup> Catalyst inks were obtained by mixing the catalyst with an anion-exchange ionomer (AEI) powder, sprayed onto the gas diffusion electrode (GDE) and pressed together with the membrane within the cell hardware to form the MEA. The cell was tested with the two different versions of Pd-CeO<sub>2</sub>/C with the same Pd loading as anodic catalyst, while all the other cell conditions and materials were kept constant including the cathode electrode and membrane. The compared performances at 80 °C are reported in Figure 9 (left), and show the higher densities obtained with the newly designed catalyst (1.4 vs 1.0 W cm<sup>-2</sup>). The better performance is especially evident in the ohmic and mass transport limited regions and can be associated to the higher Pd-CeO<sub>2</sub> contact obtained through this new synthetic protocol: we can hypothesize that in this case all of the Pd present is in contact with CeO<sub>2</sub> and active, thus can operate at higher current densities with less mass transport losses. An Ag/C (40%) cathode catalyst was used to evaluate the performance of Pd-CeO<sub>2</sub>/C in a Pt-free fuel cell MEA. The preliminary test results are presented in Figure 9 (right) showing a peak power density of over 0.6 W cm<sup>-2</sup>.

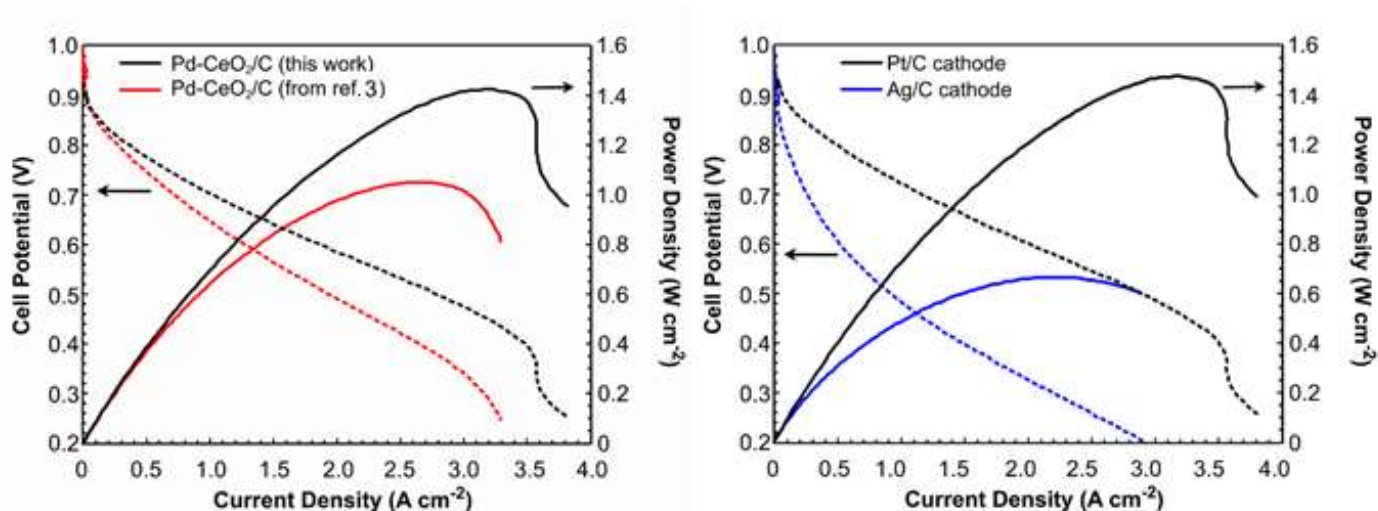


**Figure 9:** H<sub>2</sub>/O<sub>2</sub> AEM-FC performance data: (Left) with Pd-CeO<sub>2</sub>/C (the one described in this work and the one reported previously<sup>3</sup>) as anodic catalysts (0.3 mg cm<sup>-2</sup> Pd loading), and a 40 % Pt/C cathode (0.4 mg cm<sup>-2</sup> Pt loading). Both electrodes contain 20 wt % powder ionomer. H<sub>2</sub> was provided to the anode at 1.0 L min<sup>-1</sup>. O<sub>2</sub> was fed to the cathode at 2.0 L min<sup>-1</sup>. The cell temperature is 80 °C and anode/cathode dew-points are 76 °C/ 76 °C. (Right) Comparison of AEMFC performance with a Pt/C cathode and an Ag/C cathode (0.75 mg<sub>Ag</sub> cm<sup>-2</sup>) both with the herein reported Pd-CeO<sub>2</sub>/C as anode.

## 2.2.2 Conclusions

In conclusion, the study presented in this first part of the chapter highlights the importance of a smart, hierarchical design and synthesis of nanostructured electrocatalysts in order to optimize their efficiency in the selected application. We demonstrated that non-platinum HOR electrocatalysts can be developed for high power density AEM-FCs and endeavored to understand the origin of this activity enhancement and well as designing the catalyst structure and synthesis method to maximize the activity of this new class of fuel cell catalysts. Having discovered that certain Pd-CeO<sub>2</sub> interactions can enhance the HOR activity of Pd, we used a synthetic procedure involving a cerium alkoxide precursor that allowed us to obtain an optimized Pd-CeO<sub>2</sub> contact on the nanoscale. The combination of XAS techniques and DFT calculations indicates that this type of structure is related with a weakened interaction with adsorbed H. Moreover, the H<sub>2</sub> spillover capacity of CeO<sub>2</sub> facilitates the adsorption of more H<sub>2</sub> per Pd for this catalyst compared to Pd/C. The HOR activity is therefore greatly enhanced with respect to the previously studied version of the catalyst and allowed us to obtain a peak power current of 1.4 W cm<sup>-2</sup> in AEM-FC testing.

### **2.3: Nanostructured carbon supported Pd-CeO<sub>2</sub> as anode catalysts for anion exchange membrane fuel cells fed with polyalcohols**

Direct alcohol fuel cells are gaining attention in the recent years as a viable option for combining sustainable energy and chemical production from biomass.<sup>43,44,45</sup> The possibility for co-production of electrical energy from renewable sources with simultaneous selective formation of value added chemicals represents an interesting pathway for sustainability and human life quality.<sup>46</sup> The use of alcohols as fuels shows a variety of advantages with respect to hydrogen due to their easier handling, storage, and transport.<sup>47</sup> This is mainly due to the fact that they are liquid at room temperature, and they have high energy density. Moreover, alcohols with molecular weights higher than ethanol, such as ethylene glycol and 1,2-propanediol, are lately attracting a lot of attention as fuels in direct alcohol fuel cells (DAFCs) for various reasons, such as their relatively low toxicity, high boiling point, high specific energy, the capacity of some of them to be renewable as well as their interesting partial oxidation products.<sup>48,49,50,51</sup> To obtain these valuable chemicals though, the anode electrocatalyst needs to be finely tuned to favor the partial oxidation of the polyalcohol with high selectivity.<sup>52</sup> Moreover, when the DAFC is operated under alkaline conditions, polyalcohols can be effectively converted into various oxygenates, such as monocarboxylates, providing at the same time high power densities. The direct methanol fuel cell (DMFC) has been described in the literature as the most promising DAFC system for portable applications.<sup>53</sup> However, their high cost due to precious catalyst and membrane-electrode assembly (MEA) parts, still challenges their widespread commercialization. Moreover, the toxicity of methanol is pushing the research towards its substitution with the less toxic and less volatile ethanol, due also to the fact that the latter can be obtained from biomass.<sup>13,54</sup> The large majority of direct ethanol fuel cells (DEFCs) described in the literature employs Pt-based electrocatalysts at both electrodes and operates in acidic environment with cation-exchange membranes, typically Nafion.<sup>55</sup> Their efficiency, however, is strongly hindered by the slow kinetics of the oxidation reaction, and the propensity of Pt-based anode catalysts to be poisoned by intermediates like CO. This, together with the high price and low availability of platinum, gives rise to the necessity of replacing it with less expensive and more efficient substitutes. As already mentioned, the possibility of employing palladium in alkaline conditions, has pushed the scientific efforts towards its employment for manufacturing anodes for fuel cells equipped with anion exchange membranes. Vulcan XC-72 supported nanostructured Pd electrocatalysts have already proven to be effective in DEFCs. Moreover, it has been demonstrated that the addition of CeO<sub>2</sub> is effective in

enhancing the energy efficiency of the DEFC.<sup>56,57</sup> Such an increase in efficiency appears to be related to the cerium oxide driven formation of Pd-OH<sub>ads</sub> species at lower potentials, which leads to the lowering of the E<sub>onset</sub> of ethanol oxidation.<sup>56,58</sup> The material investigated in this chapter has been designed following a hierarchical approach, in order to combine the properties and possible interactions of nanostructured Pd and nanostructured CeO<sub>2</sub> and using an inexpensive yet effective nanostructured C material, Carbon Vulcan X-72, as a support. A Pd-CeO<sub>2</sub>/C hybrid nanostructured material has been synthesized, and then fully characterized by means of HR-TEM, EDX, XRD, TGA, Raman, N<sub>2</sub> physisorption and CO chemisorption. The novel Pd-CeO<sub>2</sub>/C material has been tested in full active direct alcohol fuel cells equipped with an anion-exchange membrane and fed with two different polyalcohols (ethylene glycol and 1,2-propandiol). It has been compared with a state-of-the-art Pd/C electrocatalyst, and the energy produced by the alkaline DAFCs and its selectivity for various valuable partial oxidation products has been evaluated.

### **2.3.1 Results and discussion**

#### **2.3.1.1 Catalyst preparation**

The Pd-CeO<sub>2</sub>/C catalytic system was prepared in the same way as the one reported in the previous chapter, but decreasing the Pd loading: after a mild oxidation of the carbon support, the CeO<sub>2</sub> layer was deposited by sol-gel.<sup>24</sup> The Pd nanoparticles are then added by a polyol method with ethanol as reducing agent (Pd content 5 wt%). The sample was prepared with nominal weight ratio of (C:CeO<sub>2</sub>:Pd) 50:45:5. The combined material was finally treated by calcination at 200 °C under air. The carbon supported catalyst Pd/C (5 wt% Pd) used as a reference was prepared as described elsewhere.<sup>56</sup>

#### **2.3.1.2 Morphologic characterization**

The obtained material Pd-CeO<sub>2</sub>/C was fully characterized using several techniques. Thermogravimetric analysis (TGA) was used to evaluate the carbon/metal composition in terms of weight. The reported plot (Figure 10) shows a weight loss of 56% at around 400 °C that can be related to the complete combustion of the carbon phase. It is also consistent with the nominal 50 wt% of carbon in the sample. It is interesting to note that the presence of cerium oxide, a very powerful oxidant, significantly lowers the burning temperature of the Carbon Vulcan, whose combustion normally occurs around 650 °C, as also shown in Figure 10. The decreased combustion

temperature is an indication of the intimate interfacing between the carbon phase and the CeO<sub>2</sub> layer.

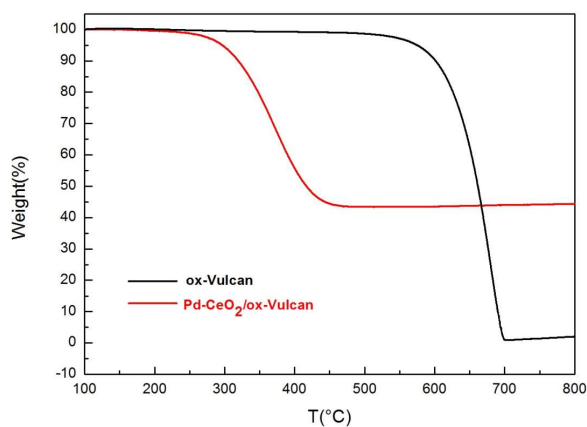


**Figure 10:** TGA analysis in air of ox-Vulcan and Pd-CeO<sub>2</sub>/C calcined sample

Raman analysis of Pd-CeO<sub>2</sub>/C in Figure 11 shows that, together with the nanostructured carbon signature (D, G and 2D bands), a band assigned to CeO<sub>2</sub> is visible at 455 cm<sup>-1</sup>. The other Raman band at 637 cm<sup>-1</sup> can be attributed to PdO that is known to be characterized by two allowed Raman modes at respectively 651 and 445 cm<sup>-1</sup>.<sup>59</sup> The latter, being of weaker intensity, is likely obscured by the much stronger ceria band. It is also noticeable that the band related to CeO<sub>2</sub> is broad and asymmetric, both of which are signs of the small size and high crystallinity of the nanostructured particles. In addition, the fact that the peak is shifted to lower energy with respect to the characteristic band for cerium oxide (464 cm<sup>-1</sup>) is another indication of small size for the nanoparticles.<sup>60</sup>

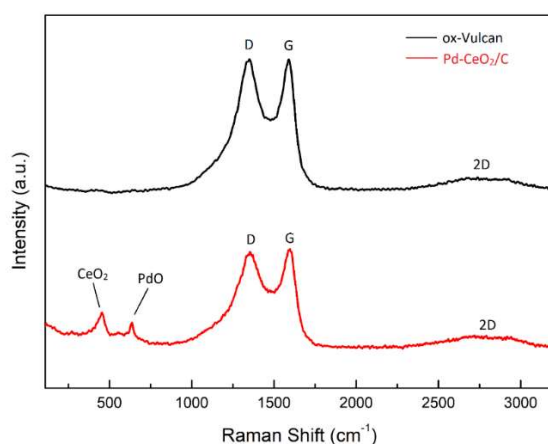


**Figure 11:** Raman spectra of Pd-CeO<sub>2</sub>/C calcined sample (red) and the bare oxidized carbon support as a reference (black)

The results obtained with the X-ray diffraction (XRD) experiments carried out on the Pd-CeO<sub>2</sub>/C material (Figure 12) are consistent with those obtained with Raman spectroscopy. The XRD pattern predominantly shows the reflections associated with the cubic structure of CeO<sub>2</sub>; the breadth of the reflections is consistent with the small dimension of the prepared nanostructured particles. The presence of Pd in its metallic state is revealed by the reflection at 40°, although it was not visible in the Raman spectrum. It appears that the metal nanoparticles are partially oxidized with some metallic Pd present. Moreover, the shoulder with maximum near 25.5° is in agreement with the main reflection of graphite (26.6°) and can be safely assigned to the carbon component of the sample.

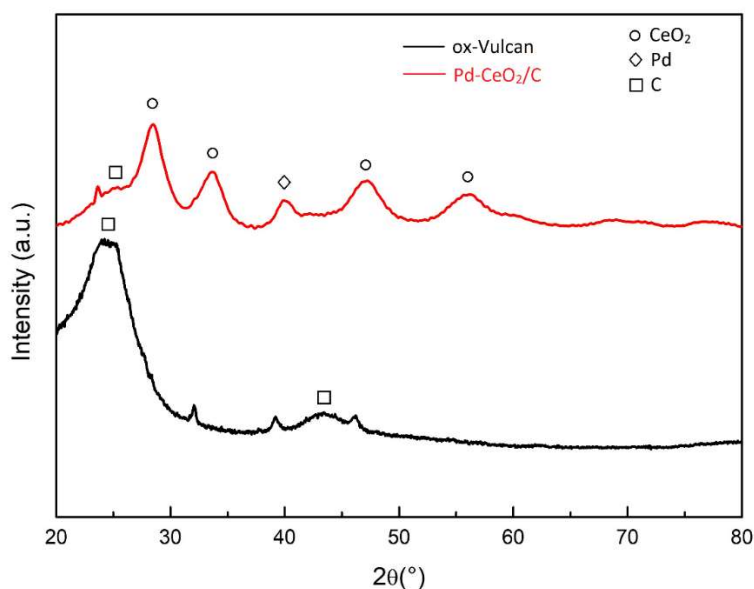


**Figure 12:** Powder XRD patterns of the sample calcined at 200 °C in air (red) and of the bare oxidized carbon support (black).

High angle annular dark field (HAADF), high-resolution transmission electron microscopy (HR-TEM) and energy dispersive X-ray analysis (EDX) were employed to investigate with more detail the morphology and composition of the sample. The average diameter of both CeO<sub>2</sub> and Pd nanoparticles has been estimated from the HR-TEM micrographs, (Figure 13) as well as the distribution of the two species on the surface of the carbon nanostructures. Both CeO<sub>2</sub> and Pd nanoparticles present crystalline structure, with average diameter around 3-6 nm for the cerium oxide ones and between 5-7 nm for the Pd ones. The cerium oxide nanoparticles partly cover the carbon structures quite uniformly, while part of them form free-standing aggregates. From the

EDX maps it is clear that the Pd nanoparticles deposit preferentially on the ceria portions of the sample. This observation concurs with our previous studies on similar Pd/C-CeO<sub>2</sub> catalysts.<sup>2,3</sup>

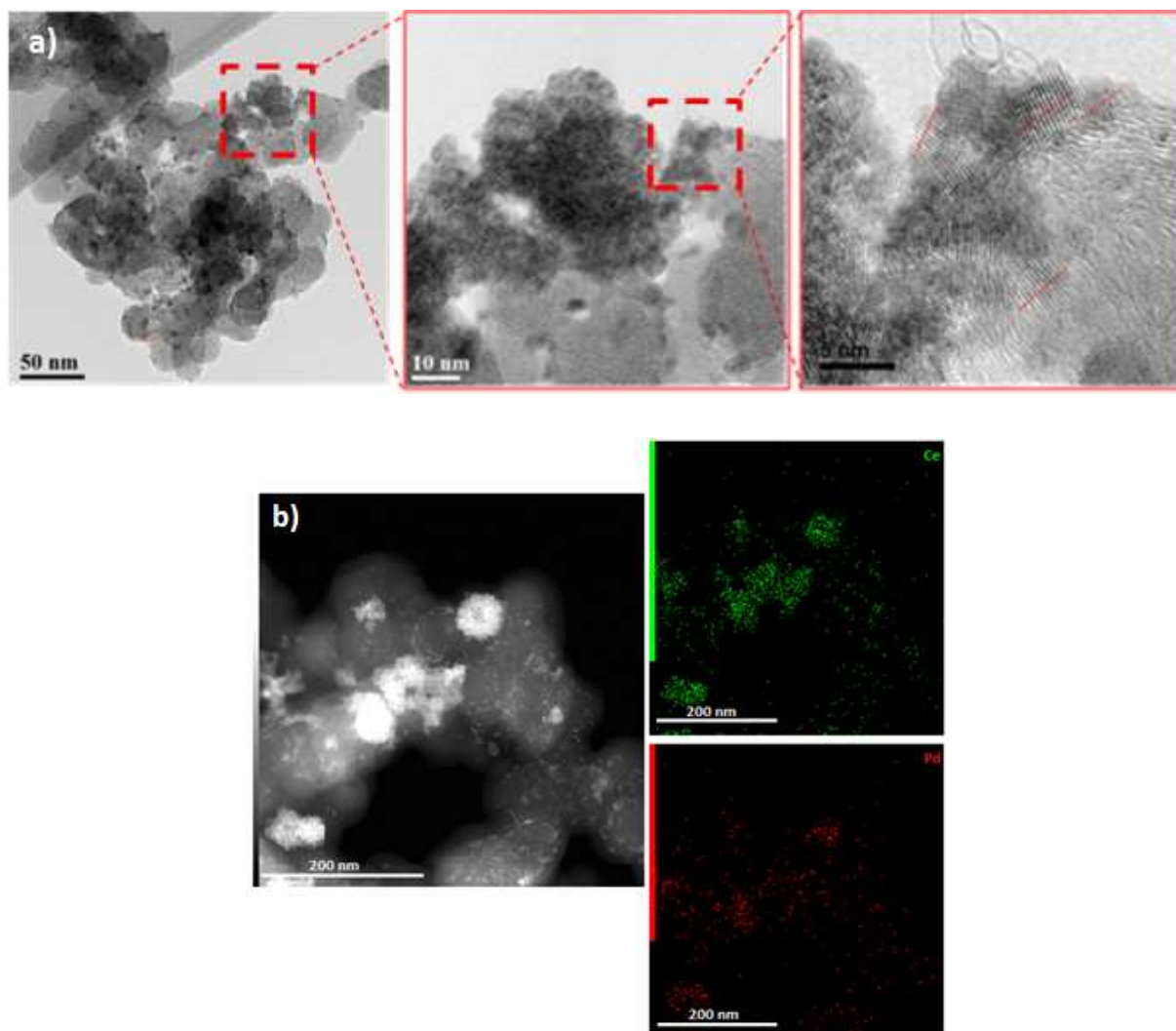


**Figure 13:** a) HR-TEM of the catalyst showing the tight contact between the carbon phase and the metal oxide phase; inset: higher magnification showing the crystalline character of the oxide phase b) HAADF and EDX maps of the sample showing the collocation of Ce and Pd atoms

The surface area and pore distribution were investigated by means of N<sub>2</sub> physisorption at 78 K. Figure 14 shows the N<sub>2</sub> adsorption-desorption isotherm of the sample. The isotherm appears to be type IV, indicating presence of some very large mesopores, with the distribution maximum around 62 nm, (Figure 14b). The small relative maximum around 3.6 nm indicates a very small contribution of microporous component. The interstitial space between the structures is likely constituting the bigger pores portion, while the micropores can be ascribed to the crystalline phase. The accessibility of the Pd metal surface was assessed by CO chemisorption experiments. The results are summarized in Table 5.

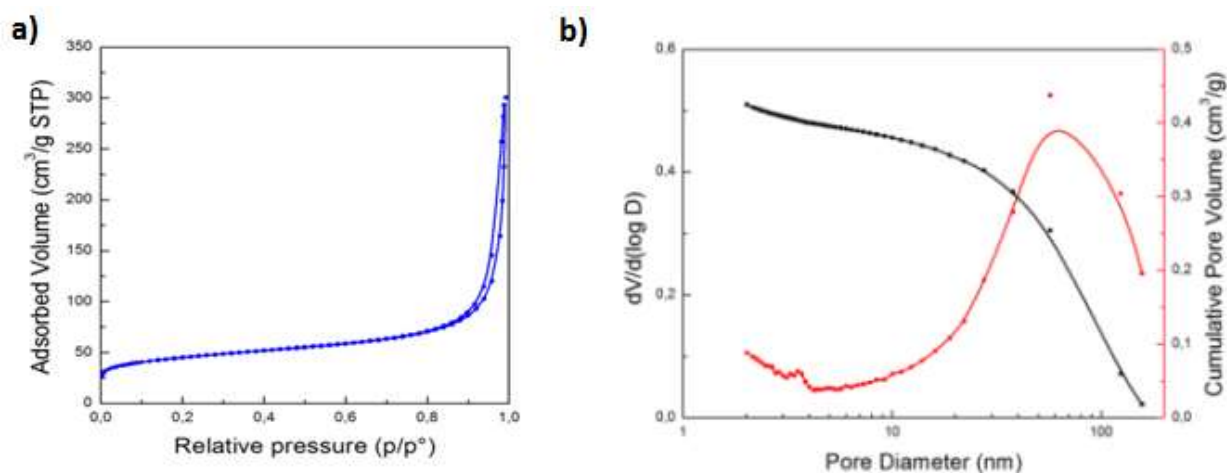


**Figure 14:** a) N<sub>2</sub> physisorption isotherm and b) BJH pore size distribution

**Table 5:** Summary of the textural properties of the investigated material

<b>Specific surface area (m<sup>2</sup>/g)</b>	249
<b>Cumulative pore volume (mL/g)</b>	87,8
<b>Micropore volume (mL/g)</b>	0,04
<b>External surface area (m<sup>2</sup>/g)</b>	62
<b>Metal surface area (m<sup>2</sup>/g)</b>	47

### 2.3.1.3 Electrochemical characterization

Cyclic voltammetry (CV) was performed on Pd-CeO<sub>2</sub>/C in both N<sub>2</sub> saturated 2 M KOH and 2 M KOH + 2 M ethylene glycol and 1,2-propanediol solutions to evaluate the effect of the CeO<sub>2</sub>-Pd interaction on the electrochemical performance of the material. As a comparison, the performance of an analogous Pd/C catalyst prepared with the same Pd loading was also investigated. All the potential values in this chapter are referred to the RHE. The CVs of both catalysts in 2 M KOH are shown in Figure 15. The interpretation of the Pd/C voltammogram is straightforward as this material has been widely investigated in the past.<sup>56</sup> Briefly, in the low potential region it is possible to observe a broad anodic peak attributable to oxidation of adsorbed hydrogen. At higher potentials, the slight increase of current density accompanies the oxidation of the palladium surface. The formed surface Pd-O species start to be reduced during the reverse

cathodic scan giving rise to a well-defined peak at 0.62 V. The cathodic peak at 0.1 V is assigned to the adsorption of hydrogen. As far as the CeO<sub>2</sub>-containing material is concerned, the CV in 2 M KOH shows a very pronounced broad peak at around 0.3 V due to oxidative hydrogen desorption. Moving toward more positive potentials on the anodic scan, peaks ascribable to the formation of surface-adsorbed Pd-hydroxide species (Pd-OH<sub>ads</sub>) can be noticed and then current-density slowly increases as Pd is further oxidized. In the cathodic scan, the peak at 0.62 V can again be assigned to the reduction of Pd-O, whereas the signals appearing in the cathodic region at potentials lower than 0.5 V can be attributed to the hydrogen uptake by both Pd and ceria.

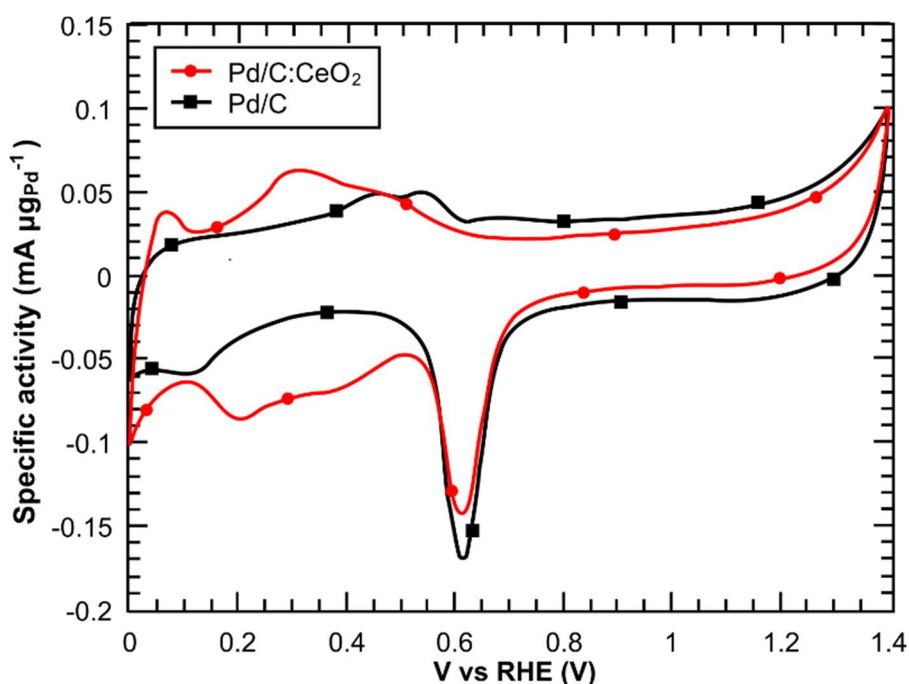


**Figure 15:** Cyclic voltammetry in 2 M KOH, scan rate 50 mV s<sup>-1</sup>

The Electrochemically Active Surface Area (EASA) of Pd for both samples was calculated using the charge associated with the reduction peak of the first monolayer of PdO at 0.62 V.<sup>61</sup> The results are reported in Table 6.

Sample	EASA Pd (m <sup>2</sup> g <sup>-1</sup> )
Pd-CeO <sub>2</sub> /C	81
Pd /C	103

**Table 6:** Electrochemically Active Surface Area of both Pd/C and Pd-CeO<sub>2</sub>/C samples

The cyclic voltammetries performed on the Pd/C and Pd-CeO<sub>2</sub>/C coated electrodes in 2 M KOH + 2 M alcohol solutions (ethylene glycol and 1,2-propanediol) are shown in Figure 16. Table 7 reports

the electrochemical data relevant for assessing the activity of the catalysts towards the targeted reactions such as peak current density per gram of Pd for each catalyst and for each alcohol fuel. The oxidation peak in the forward scan is related to the progressive coverage of the electrode surface by inactive Pd-O.<sup>62</sup> The alcohol oxidation peak appears in the signal observed on the return scan as the fresh Pd surface is liberated of oxide species. The Pd-ceria catalyst shows significantly higher mass specific current density compared to the Pd/C material for both polyalcohols. The enhanced performance of the ceria containing catalyst for alcohol oxidation in basic media is due to the ability of ceria to promote the formation of active Pd-OH<sub>ads</sub> species at low potentials. This is the first time that this phenomenon has been observed for polyol oxidation.

**Table 7:** CV data for the electrooxidation of 2 M ethylene glycol and 1,2-propanediol in KOH 2 M on Pd-CeO<sub>2</sub>/C and Pd/C.

Catalyst	E <sub>onset</sub> (V)	E <sub>forward peak</sub> (V)	S <sub>aforward peak</sub> (mA μg <sub>Pd</sub> <sup>-1</sup> )	J <sup>ECSA</sup> <sub>forward peak</sub> (μA m <sup>-2</sup> g <sup>-2</sup> )
<b>Ethylene glycol</b>				
Pd/C	0.50	0.92	3.5	190.0
Pd-CeO <sub>2</sub> /C	0.50	0.86	10.6	181.3
<b>1,2-propanediol</b>				
Pd/C	0.55	0.95	3.94	227.8
Pd-CeO <sub>2</sub> /C	0.45	0.80	6.07	75.2

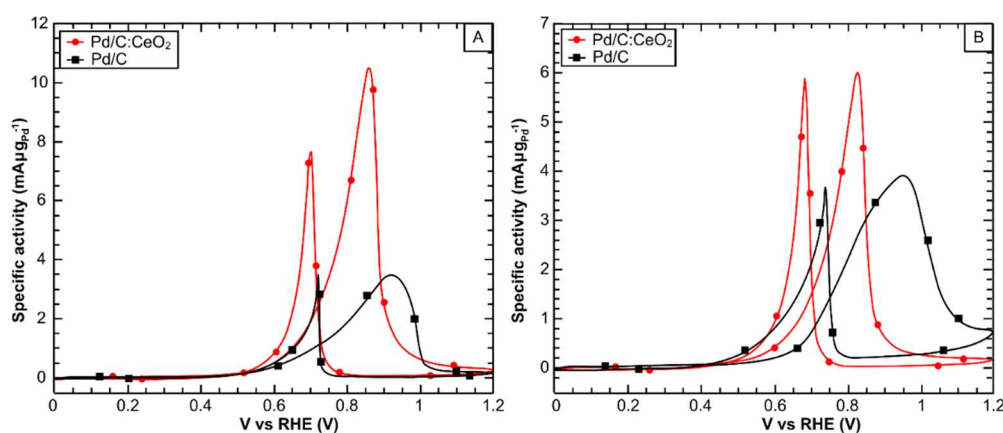


**Figure 16:** CV in 2 M KOH 2 M ethylene glycol (a) or 2 M 1,2-propanediol (b) on Pd-CeO<sub>2</sub>/C (●) and Pd/C (■) electrodes. Scan rate 50 mV s<sup>-1</sup>

### 2.3.1.4 Full Cell Testing

The performance of Pd-CeO<sub>2</sub> and the reference material Pd/C in an active fuel cell was evaluated by recording potentiodynamic and power density curves at 60°C with MEAs containing either anodic electrocatalyst, a Tokuyama A-201 anion-exchange membrane, and Fe-Co/C as cathode electrocatalyst (Figure 17).<sup>63</sup> An aqueous 2 M KOH solution containing either 2 M ethylene glycol (EG) or 1,2-propanediol (1,2-P) was used as fuel. It is clearly visible from the reported curves that both the cells with the Pd-CeO<sub>2</sub>/C electrocatalyst exhibit a considerably higher peak power density compared to the cell with the Pd/C electrocatalyst at the same Pd loading (Table 8). This is evidence that the use of the CeO<sub>2</sub>-C as support for the Pd nanoparticles increases significantly the fuel-cell power density output when compared to a simple carbon support, confirming the high activity for polyalcohol electrooxidation.

**Table 8:** Product distribution of exhausts after galvanostatic experiments, max power density, fuel conversion, energy delivered and energy efficiency.

Fuel	Max Power Density (mW cm <sup>-2</sup> )	Fuel conversion % [mmol of products]	Selectivity	Energy delivered (J)	Energy Efficiency %
EG	53.9	28% [16.9]	79% glycolate 10.5% carbonate 2.6% oxalate 7.9% formate	1231	1.5%
1,2-P	45.2	44.2% [26.5]	57.6% lactate 23.3% carbonate 13.3% acetate 6.7% formate	2411	2.0%

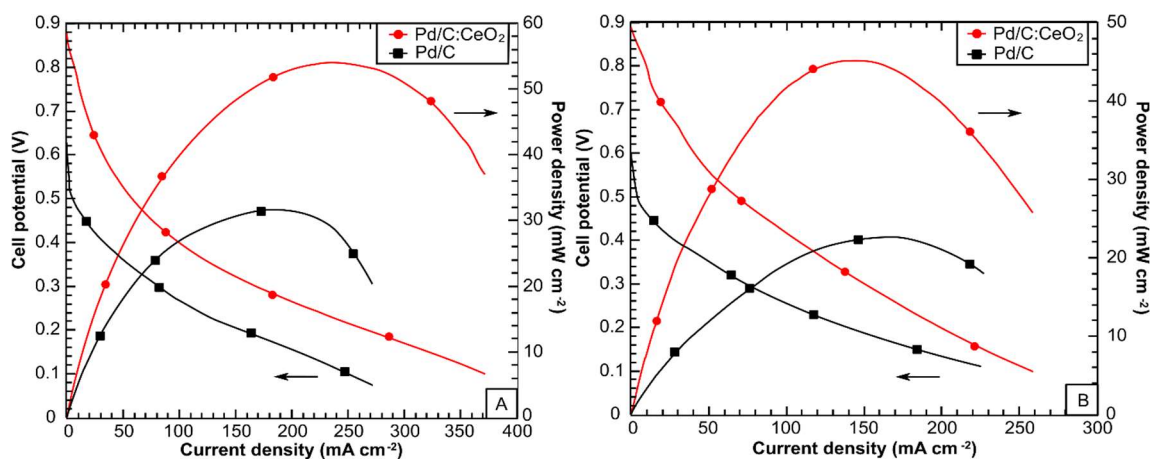


**Figure 17:** Potentiodynamic and power density curves of the cell fed with 30 mL of 2 M KOH 2 M Ethylene glycol (A) or 2 M 1,2-propanediol (B). Operating temperature: 60 °C; oxygen flow: 0.05 mL min<sup>-1</sup>; fuel flow: 1 mL min<sup>-1</sup>; cathode: 5 cm<sup>2</sup> of FeCo/C (2 mg cm<sup>-2</sup>) brushed on carbon cloth, anode: 1 mg cm<sup>-2</sup> of (●) Pd/C:CeO<sub>2</sub> or (■) Pd/C, spread on 2.25 cm<sup>2</sup> of nickel foam.

In addition to the power output, the selectivity for the different intermediates derived from the partial oxidation of the two polyalcohols was investigated. Galvanostatic experiments were performed on single fuel loads, that were recycled through the anode compartment until the cell potential reached 0 V. Two typical runs for each fuel are reported in Figure 18. The key parameters obtained from this study, such as fuel conversion (%), energy delivered on a single fuel load (J) and overall energy efficiency (%) are reported in Table 8. Despite the cell running on EG being the one producing higher peak power density, the cell fueled with 1,2-propanediol showed higher fuel conversion, energy delivered and energy efficiency.

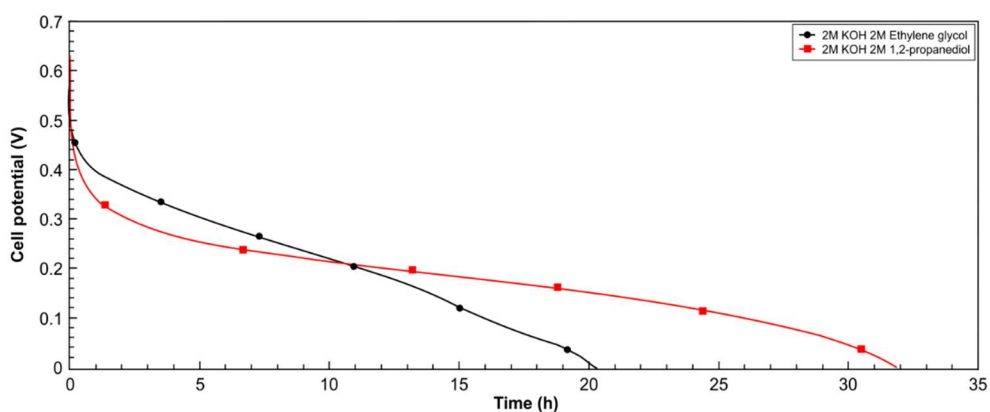


**Figure 18:** Chronopotentiometries (45 mA cm<sup>-2</sup> current load) of the DAFCs fed with 30 mL of 2 M KOH 2 M Ethylene glycol (●) or 2M 1,2-propanediol (■). Operating temperature: 60°C; oxygen flow: 0.05 mL min<sup>-1</sup>; fuel flow: 1 mL min<sup>-1</sup>; cathode: 5 cm<sup>2</sup> of FeCo/C (2 mg cm<sup>-2</sup>) brushed on carbon cloth, anode: 1 mg cm<sup>-2</sup> of Pd-CeO<sub>2</sub>/C spread on 2.25 cm<sup>2</sup> of nickel foam.

After each chronopotentiometry, the fuel exhausts were collected and examined by HPLC and  $^{13}\text{C}$  NMR spectroscopy. These techniques allowed us to determine the oxidation products obtained both qualitatively and quantitatively. The results are reported in Table 8. Glycolate was the major product as far as EG is concerned, with 79%. It is the result of the oxidation of a single OH group. Three other products were identified: formate, carbonate and a small amount of oxalate, that is the product obtained when both alcohol groups of ethylene glycol undergo oxidation. When 1,2-propanediol was the fuel, lactate was the major product (57%), together with significant formation of further oxidation products (formate, acetate and carbonate). Therefore, in both cases the main product is the one where only one OH group is oxidized.

### 2.3.2 Conclusions

In this second part of the chapter, a Pd-CeO<sub>2</sub>/C material is discussed as electrocatalysts for the electrooxidation of ethylene glycol and 1,2-propanediol in electrochemical cells and complete fuel cells. The material was first fully characterized by means of TEM, HR-TEM, EDX, XRD, N<sub>2</sub> adsorption-desorption, CO chemisorption, Raman and TGA techniques. The data reported suggest that the presence of the CeO<sub>2</sub> phase in close contact with Pd enhances significantly the performance of the catalyst, if compared with a carbon-supported palladium catalyst with the same metal loading. The promoting effect of the ceria in the support was associated to the formation of Pd-OH<sub>ads</sub> species, that are active in the oxidation of polyalcohols, at lower overpotentials. Moreover, this catalyst appears to be selective for the oxidative formation of glycolate and lactate, which are molecules of industrial relevance as intermediates. For the first time, these particular alcohols have been tested for energy efficiency and fuel selectivity, allowing us to demonstrate that this kind of fuel cells can be used effectively to combine energy production with selective formation of valuable chemicals.

## 2.4 References

- (1) Spendelow, J.; Marcinkoski, J.; Satyapal, S. Fuel Cell System Cost - 2013. *DOE Fuel Cell Technol. Off. Rec.* **2013**, No. 13012, 1–8.
- (2) Miller, H. A.; Lavacchi, A.; Vizza, F.; Marelli, M.; Di Benedetto, F.; D'Acapito, F.; Paska, Y.; Page, M.; Dekel, D. R. A Pd/C-CeO<sub>2</sub> Anode Catalyst for High-Performance Platinum-Free Anion Exchange Membrane Fuel Cells. *Angew. Chem. Int. Ed. Engl.* **2016**, *55* (20), 6004–6007.
- (3) Miller, H. A.; Vizza, F.; Marelli, M.; Zadick, A.; Dubau, L.; Chatenet, M.; Geiger, S.; Cherevko, S.; Doan, H.; Pavlicek, R. K. Highly Active Nanostructured Palladium-Ceria Electrocatalysts for the Hydrogen Oxidation Reaction in Alkaline Medium. *Nano Energy* **2017**, *33*, 293–305.
- (4) Nie, Y.; Li, L.; Wei, Z. Recent Advancements in Pt and Pt-Free Catalysts for Oxygen Reduction Reaction. *Chem. Soc. Rev.* **2015**, *44* (8), 2168–2201.
- (5) Varcoe, J. R.; Atanassov, P.; Dekel, D. R.; Herring, A. M.; Hickner, M. A.; Kohl, P. A.; Kucernak, A. R.; Mustain, W. E.; Nijmeijer, K.; Scott, K.; et al. Anion-Exchange Membranes in Electrochemical Energy Systems. *Energy Environ. Sci.* **2014**, *7* (10), 3135–3191.
- (6) Sa, Y. J.; Park, C.; Jeong, H. Y.; Park, S. H.; Lee, Z.; Kim, K. T.; Park, G. G.; Joo, S. H. Carbon Nanotubes/Heteroatom-Doped Carbon Core-Sheath Nanostructures as Highly Active, Metal-Free Oxygen Reduction Electrocatalysts for Alkaline Fuel Cells. *Angew. Chemie - Int. Ed.* **2014**, *53* (16), 4102–4106.
- (7) Wu, G.; Zelenay, P. Nanostructured Nonprecious Metal Catalysts for Oxygen Reduction Reaction. *Acc. Chem. Res.* **2013**, *46* (8), 1878–1889.
- (8) Wang, A.; Xu, H.; Feng, J.; Ding, L.; Tong, Y.; Li, G. Design of Pd/PANI/Pd Sandwich-Structured Nanotube Array Catalysts with Special Shape Effects and Synergistic Effects for Ethanol Electrooxidation. *J. Am. Chem. Soc.* **2013**, *135*, 10703–10709.
- (9) Zhang, Y.; Huang, Q.; Chang, G.; Zhang, Z.; Xia, T.; Shu, H.; He, Y. Controllable Synthesis of Palladium Nanocubes/Reduced Graphene Oxide Composites and Their Enhanced Electrocatalytic Performance. *J. Power Sources* **2015**, *280*, 422–429.
- (10) Lim, E. J.; Kim, Y.; Choi, S. M.; Lee, S.; Noh, Y.; Kim, W. B. Binary PdM Catalysts (M = Ru, Sn,

- or Ir) over a Reduced Graphene Oxide Support for Electro-Oxidation of Primary Alcohols (Methanol, Ethanol, 1-Propanol) under Alkaline Conditions. *J. Mater. Chem. A* **2015**, *3* (10), 5491–5500.
- (11) Huang, H.; Wang, X. Recent Progress on Carbon-Based Support Materials for Electrocatalysts of Direct Methanol Fuel Cells. *J. Mater. Chem. A* **2014**, *2* (18), 6266.
- (12) Alesker, M.; Page, M.; Shviro, M.; Paska, Y.; Gershinsky, G.; Dekel, D. R.; Zitoun, D. Palladium/Nickel Bifunctional Electrocatalyst for Hydrogen Oxidation Reaction in Alkaline Membrane Fuel Cell. *J. Power Sources* **2016**, *304*, 332–339.
- (13) Bianchini, C.; Shen, P. K. Palladium-Based Electrocatalysts for Alcohol Oxidation in Half Cells and in Direct Alcohol Fuel Cells. *Chem. Rev.* **2009**, *109* (9), 4183–4206.
- (14) Montini, T.; Melchionna, M.; Monai, M.; Fornasiero, P. Fundamentals and Catalytic Applications of CeO<sub>2</sub>-Based Materials. *Chem. Rev.* **2016**, *116* (10), 5987–6041.
- (15) Dekel, D. R. Review of Cell Performance in Anion Exchange Membrane Fuel Cells. *J. Power Sources* **2018**, *375*, 158–169.
- (16) Gottesfeld, S.; Dekel, D. R.; Page, M.; Bae, C.; Yan, Y.; Zelenay, P.; Kim, Y. S. Anion Exchange Membrane Fuel Cells: Current Status and Remaining Challenges. *J. Power Sources* **2018**, *375*, 170–184.
- (17) Elbert, K.; Hu, J.; Ma, Z.; Zhang, Y.; Chen, G.; An, W.; Liu, P.; Isaacs, H. S.; Adzic, R. R.; Wang, J. X. Elucidating Hydrogen Oxidation/Evolution Kinetics in Base and Acid by Enhanced Activities at the Optimized Pt Shell Thickness on the Ru Core. *ACS Catal.* **2015**, *5* (11), 6764–6772.
- (18) Ramaswamy, N.; Ghoshal, S.; Bates, M. K.; Jia, Q.; Li, J.; Mukerjee, S. Hydrogen Oxidation Reaction in Alkaline Media: Relationship between Electrocatalysis and Electrochemical Double-Layer Structure. *Nano Energy* **2017**, *41* (August), 765–771.
- (19) Durst, J.; Siebel, A.; Simon, C.; Hasché, F.; Herranz, J.; Gasteiger, H. A. New Insights into the Electrochemical Hydrogen Oxidation and Evolution Reaction Mechanism. *Energy Environ. Sci.* **2014**, *7* (7), 2255–2260.
- (20) Sheng, W.; Myint, M.; Chen, J. G.; Yan, Y. Correlating the Hydrogen Evolution Reaction

Activity in Alkaline Electrolytes with the Hydrogen Binding Energy on Monometallic Surfaces. *Energy Environ. Sci.* **2013**, *6* (5), 1509.

- (21) Henning, S.; Herranz, J.; Gasteiger, H. A. Bulk-Palladium and Palladium-on-Gold Electrocatalysts for the Oxidation of Hydrogen in Alkaline Electrolyte. *J. Electrochem. Soc.* **2014**, *162* (1), F178–F189.
- (22) Strmcnik, D.; Uchimura, M.; Wang, C.; Subbaraman, R.; Danilovic, N.; Van Der Vliet, D.; Paulikas, A. P.; Stamenkovic, V. R.; Markovic, N. M. Improving the Hydrogen Oxidation Reaction Rate by Promotion of Hydroxyl Adsorption. *Nat. Chem.* **2013**, *5* (4), 300–306.
- (23) Li, J.; Ghoshal, S.; Bates, M. K.; Miller, T. E.; Davies, V.; Stavitski, E.; Attenkofer, K.; Mukerjee, S.; Ma, Z. F.; Jia, Q. Experimental Proof of the Bifunctional Mechanism for the Hydrogen Oxidation in Alkaline Media. *Angew. Chemie - Int. Ed.* **2017**, *56* (49), 15594–15598.
- (24) Cargnello, M.; Wieder, N. L.; Montini, T.; Gorte, R. J.; Fornasiero, P. Synthesis of Dispersible Pd@CeO<sub>2</sub> Core-Shell Nanostructures by Self-Assembly. *J. Am. Chem. Soc.* **2010**, *132* (4), 1402–1409.
- (25) Johansson, M.; Skúlason, E.; Nielsen, G.; Murphy, S.; Nielsen, R. M.; Chorkendorff, I. Hydrogen Adsorption on Palladium and Palladium Hydride at 1 Bar. *Surf. Sci.* **2010**, *604* (7–8), 718–729.
- (26) Amorim, C.; Keane, M. A. Palladium Supported on Structured and Nonstructured Carbon: A Consideration of Pd Particle Size and the Nature of Reactive Hydrogen. *J. Colloid Interface Sci.* **2008**, *322* (1), 196–208.
- (27) Redjel, A.; Boudjahem, A. G.; Bettahar, M. Effect of Palladium Precursor and Preparation Method on the Catalytic Performance of Pd/SiO<sub>2</sub> catalysts for Benzene Hydrogenation. *Part. Sci. Technol.* **2018**, *36* (6), 710–715.
- (28) Konda, S. K.; Chen, A. Palladium Based Nanomaterials for Enhanced Hydrogen Spillover and Storage. *Mater. Today* **2016**, *19* (2), 100–108.
- (29) Vayssilov, G. N.; Lykhach, Y.; Migani, A.; Staudt, T.; Petrova, G. P.; Tsud, N.; Skála, T.; Bruix, A.; Illas, F.; Prince, K. C.; et al. Support Nanostructure Boosts Oxygen Transfer to Catalytically Active Platinum Nanoparticles. *Nat. Mater.* **2011**, *10* (4), 310–315.

- (30) Dutta, G.; Waghmare, U. V.; Baidya, T.; Hegde, M. S. Hydrogen Spillover on CeO<sub>2</sub> / Pt : Enhanced Storage of Active Hydrogen. *Chem. Mater.* **2007**, *19* (26), 6430–6436.
- (31) Yan, Z.; Tomer, A.; Perrussel, G.; Ousmane, M.; Katryniok, B.; Dumeignil, F.; Ponchel, A.; Liebens, A.; Pera-Titus, M. A Pd/CeO<sub>2</sub> “H<sub>2</sub> Pump” for the Direct Amination of Alcohols. *ChemCatChem* **2016**, *8* (21), 3347–3352.
- (32) Zhang, H.; Wang, J.; Zhang, Y.; Jiao, Y.; Ren, C.; Gong, M.; Chen, Y. A Study on H<sub>2</sub>-TPR of Pt/Ce<sub>0.27</sub>Zr<sub>0.73</sub>O<sub>2</sub> and Pt/Ce<sub>0.27</sub>Zr<sub>0.70</sub>La<sub>0.03</sub>O<sub>x</sub> for Soot Oxidation. *Appl. Surf. Sci.* **2016**, *377*, 48–55.
- (33) Krishnankutty, Nalini; Vannice, M. A. The Effect of Pretreatment on Pd/C Catalysts. *J. Catal.* **1995**, *155*, 312–326.
- (34) Song, W.; Su, Y.; Hensen, E. J. M. A DFT Study of CO Oxidation at the Pd-CeO<sub>2</sub>(110) Interface. *J. Phys. Chem. C* **2015**, *119* (49), 27505–27511.
- (35) Li, W. Q.; Goverapet Srinivasan, S.; Salahub, D. R.; Heine, T. Ni on the CeO<sub>2</sub>(110) and (100) Surfaces: Adsorption: Vs. Substitution Effects on the Electronic and Geometric Structures and Oxygen Vacancies. *Phys. Chem. Chem. Phys.* **2016**, *18* (16), 11139–11149.
- (36) Skulason, E.; Tripkovic, V.; Bjo, M. E.; Karlberg, G.; Rossmeisl, J.; Bligaard, T.; Jo, H.; Nørskov, J. K. Modeling the Electrochemical Hydrogen Oxidation and Evolution Reactions on the Basis of Density Functional Theory Calculations. *J. Phys. Chem. C* **2010**, *114* (12), 110913.
- (37) Zheng, J.; Nash, J.; Xu, B.; Yan, Y. Perspective Towards Establishing Apparent Hydrogen Binding Energy as the Descriptor for Hydrogen Oxidation/Evolution Reactions. *J. Electrochem. Soc.* **2018**, *165* (2), H27–H29.
- (38) Wang, L.; Magliocca, E.; Cunningham, E. L.; Mustain, W. E.; Poynton, S. D.; Escudero-Cid, R.; Nasef, M. M.; Ponce-Gonzalez, J.; Bance-Souahli, R.; Slade, R. C. T.; et al. An Optimised Synthesis of High Performance Radiation-Grafted Anion-Exchange Membranes. *Green Chem.* **2017**, *19* (3), 831–843.
- (39) Lu, Y.; Wang, L.; Preuß, K.; Qiao, M.; Titirici, M. M.; Varcoe, J.; Cai, Q. Halloysite-Derived Nitrogen Doped Carbon Electrocatalysts for Anion Exchange Membrane Fuel Cells. *J. Power Sources* **2017**, *372*, 82–90.

- (40) Ponce-González, J.; Ouachan, I.; Varcoe, J. R.; Whelligan, D. K. Radiation-Induced Grafting of a Butyl-Spacer Styrenic Monomer onto ETFE: The Synthesis of the Most Alkali Stable Radiation-Grafted Anion-Exchange Membrane to Date. *J. Mater. Chem. A* **2018**, *6* (3), 823–827.
- (41) Omasta, T. J.; Wang, L.; Peng, X.; Lewis, C. A.; Varcoe, J. R.; Mustain, W. E. Importance of Balancing Membrane and Electrode Water in Anion Exchange Membrane Fuel Cells. *J. Power Sources* **2018**, *375*, 205–213.
- (42) Wang, L.; Brink, J. J.; Liu, Y.; Herring, A. M.; Ponce-González, J.; Whelligan, D. K.; Varcoe, J. R. Non-Fluorinated Pre-Irradiation-Grafted (Peroxidated) LDPE-Based Anion-Exchange Membranes with High Performance and Stability. *Energy Environ. Sci.* **2017**, *10* (10), 2154–2167.
- (43) Armaroli, N.; Balzani, V. The Future of Energy Supply: Challenges and Opportunities. *Angew. Chemie - Int. Ed.* **2007**, *46*, 52–66.
- (44) Armaroli, N.; Balzani, V. Towards an Electricity Powered World. *Energy Environ. Sci. Sci.* **2011**, *4*, 3193–3222.
- (45) Armaroli, N.; Balzani, V. Solar Electricity and Solar Fuels: Status and Perspectives in the Context of the Energy Transition. *Chem. - A Eur. J.* **2016**, *22*, 32–57.
- (46) Bellini, M.; Bevilacqua, M.; Filippi, J.; Lavacchi, A.; Marchionni, A.; Miller, H. A.; Oberhauser, W.; Vizza, F.; Annen, S. P.; Grützmacher, H. Energy and Chemicals from the Selective Electrooxidation of Renewable Diols by Organometallic Fuel Cells. *ChemSusChem* **2014**, *7* (9), 2432–2435.
- (47) Miller, H.; Vizza, F.; Lavacchi, A. *Direct Alcohol Fuel Cells: Nanostructured Materials for the Electrooxidation of Alcohols in Alkaline Media*, Springer.; K.I.a.C. Ozoemena, 2016.
- (48) Qi, J.; Benipal, N.; Liang, C.; Li, W. PdAg/CNT Catalyzed Alcohol Oxidation Reaction for High-Performance Anion Exchange Membrane Direct Alcohol Fuel Cell (Alcohol = Methanol, Ethanol, Ethylene Glycol and Glycerol). *Appl. Catal. B Environ.* **2016**, *199*, 494–503.
- (49) An, L.; Chen, R. Recent Progress in Alkaline Direct Ethylene Glycol Fuel Cells for Sustainable Energy Production. *J. Power Sources* **2016**, *329*, 484–501.
- (50) Miller, H. A.; Bellini, M.; Vizza, F.; Hasenohrl, C.; Tilley, R. D. Carbon Supported Au-Pd Core-

Shell Nanoparticles for Hydrogen Production by Alcohol Electroreforming. *Catal. Sci. Technol.* **2016**, *6*, 6870–6878.

- (51) Chadderdon, D. J.; Xin, L.; Qi, J.; Brady, B.; Miller, J. A.; Sun, K.; Janik, M. J.; Li, W. Selective Oxidation of 1,2-Propanediol in Alkaline Anion-Exchange Membrane Electrocatalytic Flow Reactors: Experimental and DFT Investigations. *ACS Catal.* **2015**, *5*, 6926–6936.
- (52) Vigier, F.; Rousseau, S.; Coutanceau, C.; Leger, J. M.; Lamy, C. Electrocatalysis for the Direct Alcohol Fuel Cell. *Top. Catal.* **2006**, *40* (1–4), 111–121.
- (53) Antolini, E.; Gonzalez, E. R. Alkaline Direct Alcohol Fuel Cells. *J. Power Sources* **2010**, *195* (11), 3431–3450.
- (54) Matsuoka, K.; Iriyama, Y.; Abe, T.; Matsuoka, M.; Ogumi, Z. Alkaline Direct Alcohol Fuel Cells Using an Anion Exchange Membrane. *J. Power Sources*, **2005**, *150*, 27–31.
- (55) Antolini, E. Catalysts for Direct Ethanol Fuel Cells. *J. Power Sources* **2007**, *170* (1), 1–12.
- (56) Bambagioni, V.; Bianchini, C.; Chen, Y.; Filippi, J.; Fornasiero, P.; Innocenti, M.; Lavacchi, A.; Marchionni, A.; Oberhauser, W.; Vizza, F. Energy Efficiency Enhancement of Ethanol Electrooxidation on Pd–CeO<sub>2</sub>/C in Passive and Active Polymer Electrolyte-Membrane Fuel Cells. *ChemSusChem* **2012**, *5* (7), 1266–1273.
- (57) Wang, L.; Lavacchi, A.; Bevilacqua, M.; Bellini, M.; Fornasiero, P.; Filippi, J.; Innocenti, M.; Marchionni, A.; Miller, H. A.; Vizza, F. Energy Efficiency of Alkaline Direct Ethanol Fuel Cells Employing Nanostructured Palladium Electrocatalysts. *ChemCatChem* **2015**, *7* (14), 2214–2221.
- (58) Xu, C.; Liu, Y. Ethanol Electrooxidation on Pt/C and Pd/C Catalysts Promoted with Oxide. *J. Power Sources* **2007**, *164*, 527–531.
- (59) Weber, W. H.; Baird, R. J.; Graham, G. W. Raman Investigation of Palladium Oxide, Rhodium Sesquioxide and Palladium Rhodium Dioxide. *J. Raman Spectrosc.* **1988**, *19* (4), 239–244.
- (60) Zhang, F.; Chan, S. W.; Spanier, J. E.; Apak, E.; Jin, Q.; Robinson, R. D.; Herman, I. P. Cerium Oxide Nanoparticles: Size-Selective Formation and Structure Analysis. *Appl. Phys. Lett.* **2002**, *80* (1), 127–129.
- (61) Grden, M.; Lukaszewski, M.; Jerkiewicz, G.; Czerwinski, A. Electrochemical Behaviour of

Palladium Electrode: Oxidation, Electrodisolution and Ionic Adsorption. *Electrochim. Acta* **2008**, *53*, 7583–7598.

(62) Wang, L.; Lavacchi, A.; Bellini, M.; D'Acapito, F.; Benedetto, F. Di; Innocenti, M.; Miller, H. A.; Montegrossi, G.; Zafferoni, C.; Vizza, F. Deactivation of Palladium Electrocatalysts for Alcohols Oxidation in Basic Electrolytes. *Electrochim. Acta* **2015**, *177*, 100–106.

(63) Chen, Y.; Bellini, M.; Bevilacqua, M.; Fornasiero, P.; Lavacchi, A.; Miller, H. A.; Wang, L.; Vizza, F. Direct Alcohol Fuel Cells: Toward the Power Densities of Hydrogen-Fed Proton Exchange Membrane Fuel Cells. *ChemSusChem* **2015**, *8* (3), 524–533.

## CHAPTER 3: N-doped carbon encapsulated Co nanoparticles for selective H<sub>2</sub>O<sub>2</sub> electrocatalytic generation

### 3.1 Introduction

In the last decades, consistent scientific efforts have been dedicated to the design and development of novel electrocatalysts for the electroreduction of oxygen, because of its high relevance for fuel cells efficiency.<sup>1,2</sup> Most of known fuel cells in fact, as mentioned before, operate with oxygen reduction occurring at the cathode while the selected fuel gets oxidized at the anode. The possible reduction products obtained by O<sub>2</sub> reduction are two, H<sub>2</sub>O and H<sub>2</sub>O<sub>2</sub>, formed respectively from an overall 4-electron reduction process and a 2-electron reduction process. In the context of fuel cells, the selective conversion to water is definitely the desired pathway, as the current efficiency is maximized (4 electrons involved), and the product (water) is benign and does not interfere with the fuel cell operation. From this perspective, the formation of H<sub>2</sub>O<sub>2</sub> is regarded as an undesirable by-process, and the vast majority of reports have focused on the development of new efficient and selective catalysts for the 4-electron ORR. On the other hand, a very recent trend has recognized that the selective production of hydrogen peroxide can represent an interesting development of the ORR process. H<sub>2</sub>O<sub>2</sub> is in fact a highly relevant compound for several industrial sectors such as pulp and paper, food, mining, textile bleaching, waste water treatment, packaging and chemical synthesis, as justified by the over 2 megatons produced annually worldwide.<sup>3-6</sup> Despite this central role, hydrogen peroxide is currently produced industrially through a process called “anthraquinone process” which is both energy intensive and non-environmentally friendly.<sup>7</sup> More sustainable alternatives have been proposed,<sup>8</sup> and using cheap catalysts to perform electrocatalytic ORR to obtain H<sub>2</sub>O<sub>2</sub> selectively is an appealing alternative.<sup>9</sup> Anyhow, in the process of developing a new electrocatalytic system for selective O<sub>2</sub> reduction, many factors need to be considered, since, as mentioned before its kinetics strongly affects the selectivity of the process and, for this reason, most catalysts show low selectivity, leading to mixed mechanisms. Moreover, the strict dependence on the pH affects the reaction mechanism and consequently the products distribution. While the selective reduction of O<sub>2</sub> to H<sub>2</sub>O has been thoroughly investigated in the field of fuel cells electrocatalysts development, with Pt/C catalyst representing the benchmark for the process,<sup>1,10,11</sup> there are still very few examples of materials showing both high activity and selectivity for the reduction of O<sub>2</sub> to H<sub>2</sub>O<sub>2</sub>. Bimetallic nanoparticles

based materials, combining Pd, Pt, Au with several other transition metals have been recently tested and reported as selective electrocatalysts for hydrogen peroxide production.<sup>12,13</sup> Among them, Au-Hg and Pt-Hg have been identified as the most promising candidates leading to highly selective H<sub>2</sub>O<sub>2</sub> formation.<sup>14</sup> However, the industrial viability of these catalysts is hampered by the high cost and low availability of noble metals, combined with a low long-term stability and easy poisoning. In order to find a way around this issue, there is a growing interest in developing metal-free catalysts.<sup>15</sup> Most of the results found in literature involve heteroatom-doped carbon nanomaterials, especially with nitrogen as the dopant. Several different structures including N-doped carbon nanotubes (CNTs),<sup>16,17</sup> N-doped graphene,<sup>18</sup> carbon nitride (g-C<sub>3</sub>N<sub>4</sub>),<sup>19</sup> nanofibers (N-CNFs)<sup>20</sup> or N-doped mesoporous carbons<sup>21</sup> have been tested, but they were reported to provide mostly mixed 4-, (2+2)-, and 2-electron ORR mechanisms, with H<sub>2</sub>O being often the prevalent product. Recently, our group reported a metal-free carbon nanocatalyst showing very high H<sub>2</sub>O<sub>2</sub> selectivity in a wide range of pH, whose catalytic features are correlated with the type and distribution of the N dopant atoms and on the porosity of the carbon.<sup>22</sup> Moreover, integrating non-noble metal nanoparticles, particularly if the latter are embedded in the carbon matrix seems to be an efficient strategy to boost stability and tune selectivity. Both our group<sup>23</sup> and Deng et al.<sup>24</sup> separately reported materials based on endohedrally Fe-modified CNTs as ORR electrocatalysts. More recently the embedding of cobalt nanoparticles within porous carbon has been studied by Wu et al.<sup>25</sup> and Jiang et al.<sup>26</sup> The material reported in this chapter was designed building on these concepts: it consists in cobalt nanoparticles embedded within porous N-doped graphitic carbon shells. Its behavior towards ORR has been correlated to its specific microstructure: through a fine tuning of the N-type species distribution and the porosity of the material, the catalyst displays an almost complete selectivity to H<sub>2</sub>O<sub>2</sub> in acidic electrolytes (~100% Faradaic Efficiency (FE)) at a relatively positive potential (0.5 V vs RHE).

## **3.2 Results and discussion**

### **3.2.1 Catalyst preparation**

The synthetic protocol for the carbon encapsulated cobalt nanoparticles consists in the pyrolysis of the precursors, imidazole and cobalt acetate, in Ar atmosphere. This step is crucial as the morphology and properties of the composite depend on several parameters that are set during this phase. The temperature ramp, the final upper temperature, the time of residence of the precursor in the furnace, the gas carrier and its flow are all in fact contributing in the final

morphology of the graphitized carbon phase that is produced in this step. After a 2h pyrolysis at 900°C the as obtained powder is washed with diluted perchloric acid in order to remove any trace of metal on the surface. The final material Co-NC-im, has been characterized both structurally and morphologically with several techniques. Four materials have been prepared for comparison following this protocol using a different nitrogen bearing carbon precursor, phenantroline, and different metals, iron, manganese and nickel, and called respectively Co-NC-phen, Fe-NC-im, Mn-NC-im and Ni-NC-im.

### 3.2.2 Morphologic characterization

The morphology of Co-NC-im was first inspected by TEM (Figure 1). The micrographs clearly reveal the presence of metal nanoparticles encapsulated within onion-like graphitic shells, though the N-doped carbon phase does not look geometrically well-defined. This can be correlated to the high argon flow used in the synthesis, as lower argon carrier flows are reported to generate carbon nanotube-type architectures.<sup>27</sup>

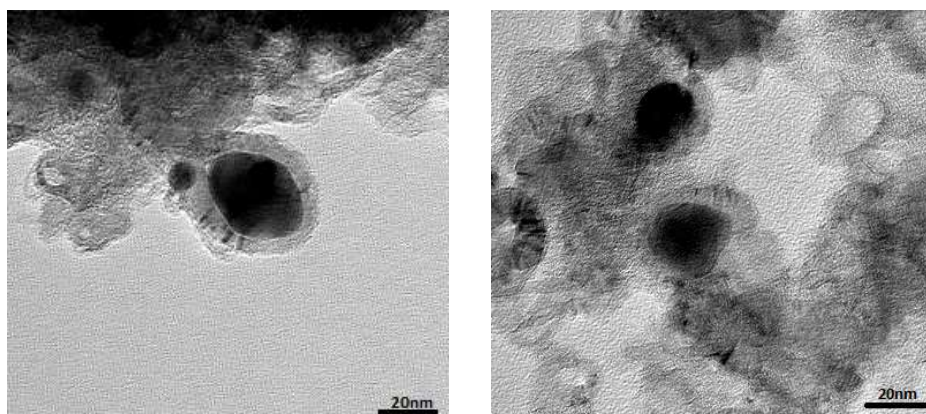


**Figure 1:** TEM images showing Co-NC-im morphology

High angle annular dark field (HAADF), high-resolution transmission electron microscopy (HR-TEM) and energy dispersive X-ray analysis (EDX) were used to investigate with more detail the morphology and composition of Co-NC-im (Figure 2, 3, 4 and 5). The overall size distribution of the Co NP appears quite broad, ranging from 3 to 30 nm with a maximum around 10 nm (Figure 3). FFT analysis of the embedded cobalt nanoparticles indicates that the cobalt is not oxidized and that all the nanoparticles exhibit a *fcc* crystal system (Figure 2D). HAADF and EDX confirm the composition and distribution of the phases in the material showing spatially well dispersed metal NP embedded in the carbon phase while also ruling out any residual unshelled cobalt nanoparticles, confirming the effectiveness of the acid washing (Figure 4 and 5).

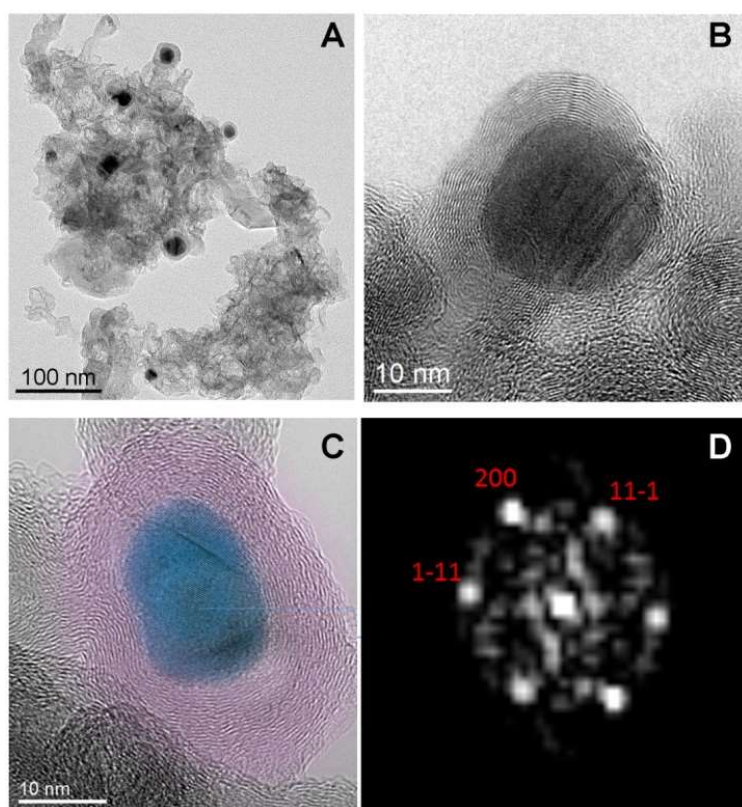


**Figure 2:** A) Typical TEM image of the Co-NC-im material; B) and C) representative High resolution TEM showing cobalt nanoparticles (blue) encapsulated within a N-doped graphitic shell (purple); D) FFT of the inner cobalt nanoparticle of C), showing the diffraction pattern of the cubic fcc crystal system.

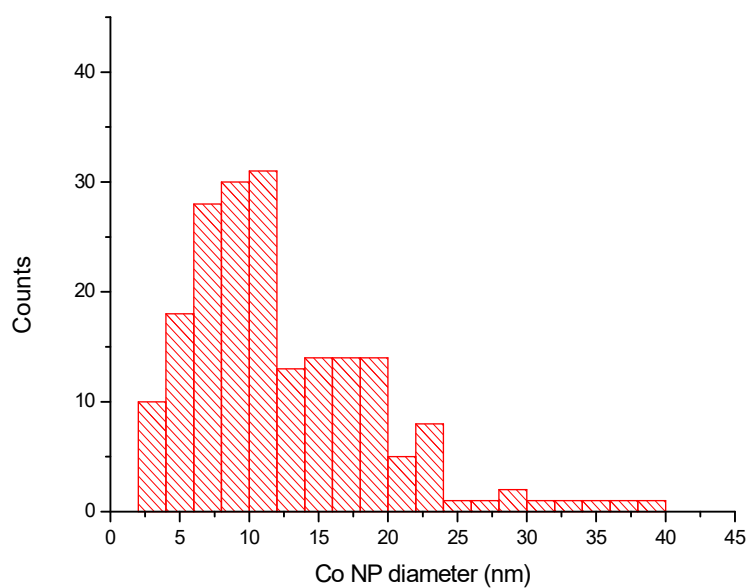


**Figure 3:** Co NP particle size distribution in Co-NC-im

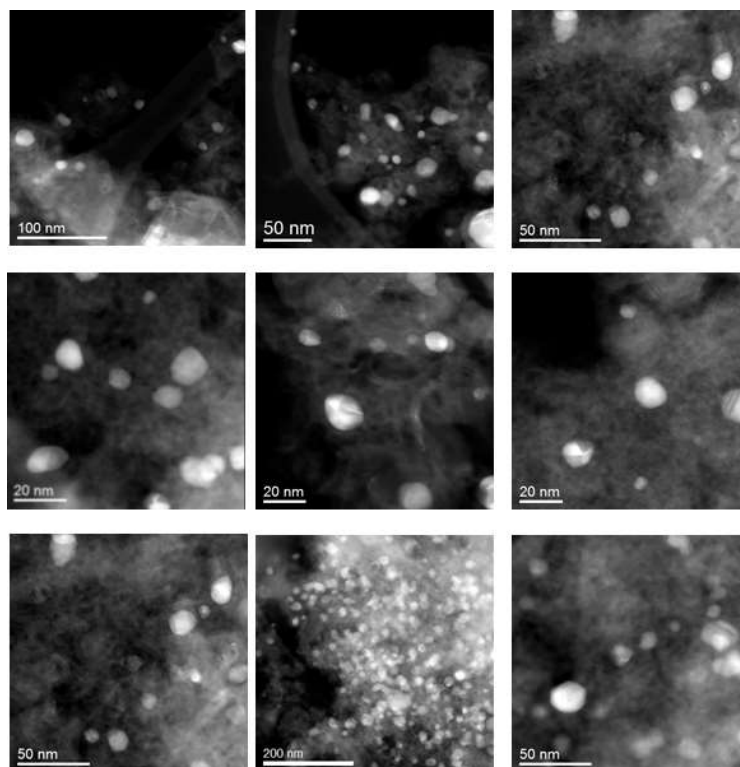


**Figure 4:** HAADF-STEM images of Co-NC-im; the bright regions correspond to Co NPs.

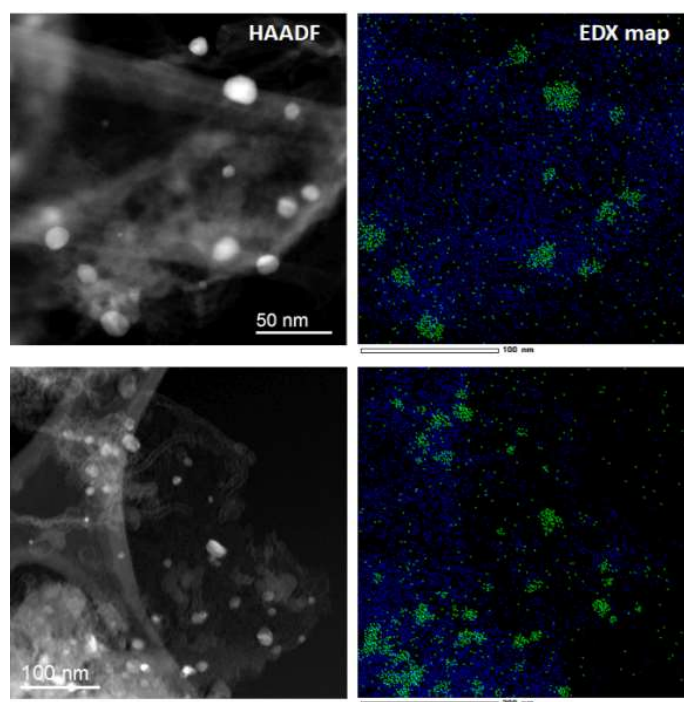


**Figure 5:** HAADF-STEM and EDX maps of Co-NC-im showing the collocation of C (blue) and Co (green) atoms. Raman analysis confirmed this assumption with no detected signal attributed to Co oxides, underlining the zero oxidation state; the only bands observed are related to the graphitic carbon (Figure 6). The 1:1 ratio of the intensities of the D and G bands, attributed respectively to the

structural disorder of the graphitic framework and to the graphitic domain suggests a high defect distribution across the graphitic layers.

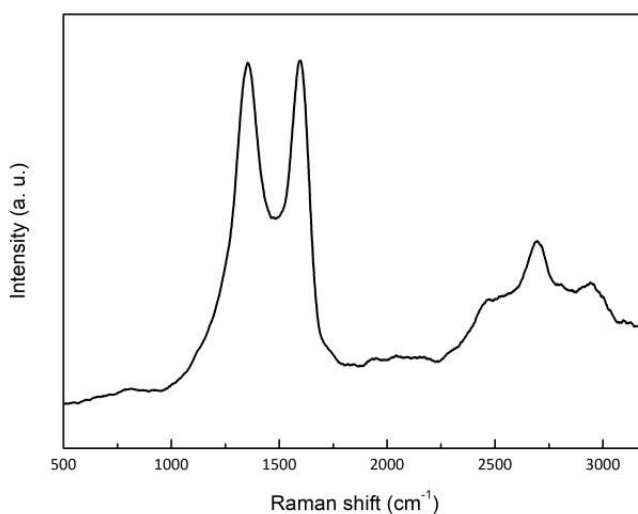


**Figure 6:** Raman spectrum of Co-NC-im

In order to evaluate the metal load, Co-NC-im was characterized both through thermogravimetric analysis (TGA) (Figure 7) under air flow and inductively coupled plasma-optical emission spectrometry (ICP-OES). There is a slight discrepancy between the two results, since TGA reports 85% weight loss relative to the carbon phase with the remaining 15% accountable to the inorganic phase, while ICP-OES provides a weight load of the cobalt equal to 6%. This difference is likely due to the formation of Co oxide during the TGA analysis which leads to weight gain.

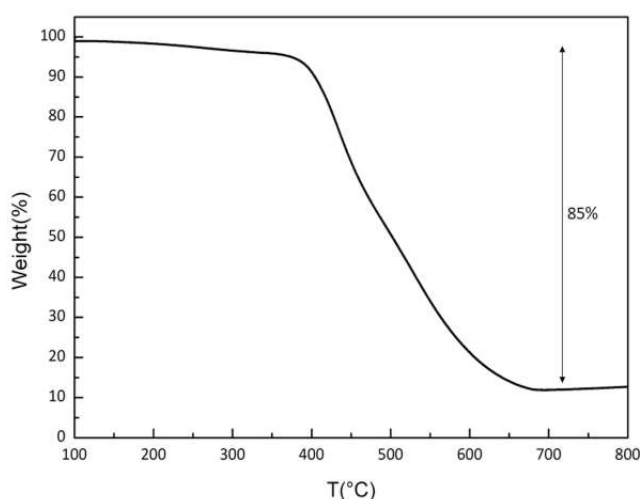


**Figure 7:** TGA analysis in air of Co-NC-im

X-Ray Photoelectron Spectroscopy (XPS) was employed to investigate quantitatively the surface of the Co-NC-im sample, since the amount and type distribution of N-doping atoms is a key parameter to consider in ORR catalysis. As far as metals are concerned, the sample did not display any peak for cobalt or any other metal on its surface, confirming the efficacy of the acid washing, and, being XPS a technique that reaches only about 12nm depth, the deep encapsulation of the cobalt nanoparticles in the multi-layered carbon matrix (Figure 8A). The dominant signal in the C<sub>1s</sub> binding energy (BE) region is the one at 284.4 eV, which is characteristic for C=C aromatic patterns and confirms the graphitic nature of the carbon phase (Figure 8C). The peaks associated to C-O and C=O display quite low intensity, indicating moderate levels of oxidation (Figure 8D). Two peaks can be observed in the N<sub>1s</sub> range, confirming the successful N-doping with an atomic percentage of 2.92% (Figure 8B). The two peaks, respectively at 400.6 eV and 398.6 eV indicate the sole formation of respectively pyrrolic (C-N bonds) and pyridinic (C=N bonds) N atoms.<sup>18</sup> This is an interesting feature, since most of materials prepared by pyrolysis reported in literature are characterized by a percentage of quaternary, oxidized or other types of N<sup>28</sup> and pyrrolic and pyridinic N have been shown to be unstable after high temperature treatments.<sup>29</sup> In a recently reported study by our group, the same unusual composition was observed for a graphite-covered carbon nanohorns material. In that case, too, the presence of a certain ratio of pyrrolic N and pyridinic N ( $N_{\text{pyridinic}}/N_{\text{pyrrolic}} = 0.89$ ) and absence of other N type atoms has revealed itself to be crucial to obtain a totally selective 2-electron mechanism under acidic conditions.<sup>22</sup> Co-NC-im has a  $N_{\text{pyridinic}}/N_{\text{pyrrolic}}$  atomic ratio of 0.93, which is very close to the value of the previously reported material.

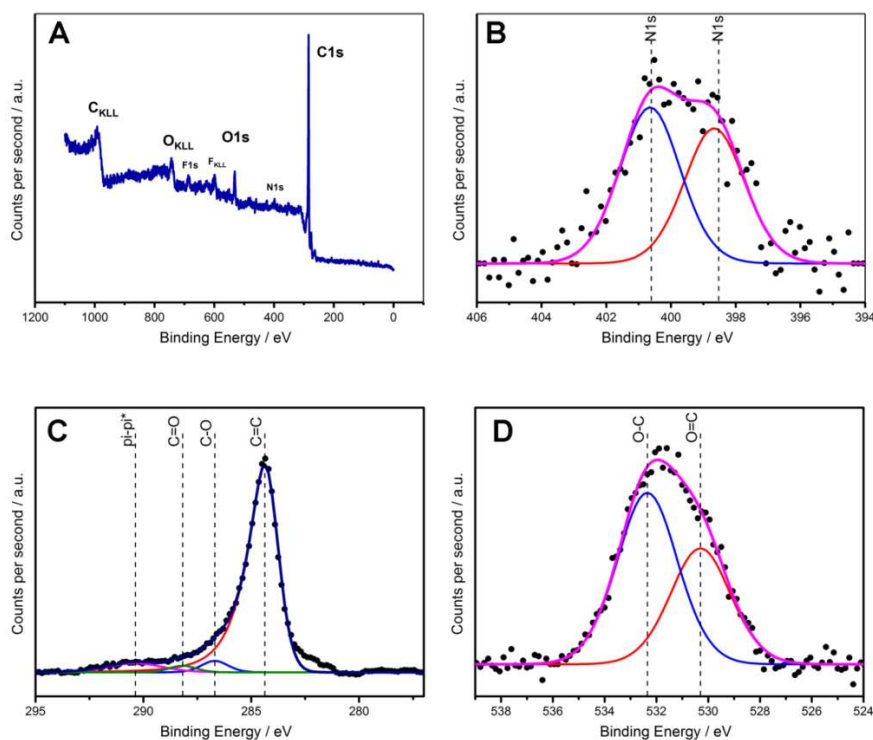


**Figure 8:** A) XPS survey of Co-NC-im; B), XPS in the  $N_{1s}$  BE range; C) XPS in the  $C_{1s}$  BE range; D) XPS in the  $O_{1s}$  BE range

### 3.2.3 Electrochemical tests

Co-NC-Im electrochemical activity in acidic environment was first evaluated through cyclic voltammetry (CV). All the potential values reported in this chapter are referred to RHE. The electrochemical response was studied in the potential range between +0.8 V and -0.1 V in Ar-saturated 0.10 M  $H_2SO_4$  (pH 1) at a scan rate of  $0.05 \text{ V s}^{-1}$ . The CV recorded in nitrogen (Figure 9, black curve) showed only capacitive current ( $i_{cap}$ ) in the investigated potential range. The capacitive current is the current necessary to charge and discharge the electrical double layer at the interface between electrode and electrolyte. This observation suggests that the cobalt nanoparticles are either electrochemically inaccessible, or do not undergo redox reactions in the selected potential range. The CV collected with the same setup and conditions in presence of  $O_2$  (Figure 9, red curve) show a distinct increase in cathodic current, that begins at 0.75 V and is associated to the reduction of oxygen. Notably, this onset value is very close to the one observed for Pt/C (0.8 V), the benchmark catalyst for this reaction, suggesting the great prospect of the proposed material.

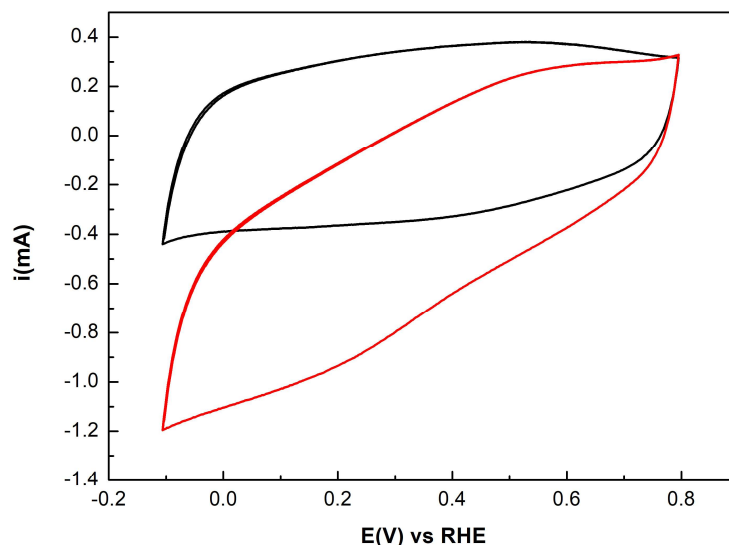


**Figure 9:** CVs under Ar (black line) and O<sub>2</sub> (red line) collected on a glassy carbon slide modified with Co-NC-im (scan rate 50 mV s<sup>-1</sup>);

The material's selectivity was evaluated performing chronoamperometric experiments at several different potentials and calculating the Faradaic yield in H<sub>2</sub>O<sub>2</sub> after permanganometric titration. The trend observed correlates a decrease in selectivity towards H<sub>2</sub>O<sub>2</sub>, together with an increase of the current density, when the potential shifts towards more negative values. This result is in line with what previously observed with a graphitized PDA layers based material recently studied by our group.<sup>22</sup>

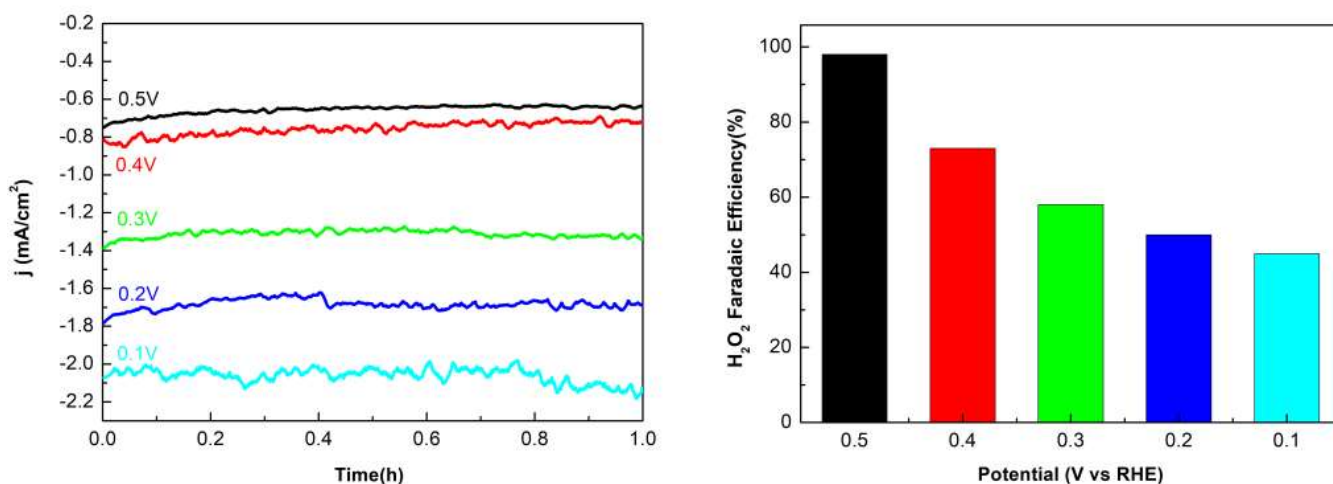


**Figure 10:** Current density/time profiles at different fixed potentials in H<sub>2</sub>SO<sub>4</sub> 0.1 M and corresponding H<sub>2</sub>O<sub>2</sub> Faradaic Efficiency.

As reported in Figure 10, the material displays complete H<sub>2</sub>O<sub>2</sub> selectivity (almost 100%) at 0.5 V, while decreasing the potential value leads to a drop in FE.

It has been reported that to achieve such high selectivity with N-doped carbon materials, it is crucial to obtain a specific relative distribution of pyrrolic and pyridinic nitrogen atoms. Pyridinic atoms have been proven to be the most efficient ORR sites, because of their ability to weaken the O-O bond, by either enhancing the N-C $\alpha$  bond polarization,<sup>30</sup> or through exploitation of the electron pair to facilitate charge transfer into the O-O antibonding orbital.<sup>31</sup> Since the formation of H<sub>2</sub>O<sub>2</sub> is promoted by the preservation of the O-O bond, controlling the N<sub>pyridinic</sub> sites by tuning their characteristics appears to be instrumental to alter their ability to rupture such bond. Therefore, the fact that basic nitrogen sites are protonated in acidic environment strongly influences their properties. This assumption was confirmed by performing the same selectivity screening in alkaline environment (pH 13), where the material displayed a much lower selectivity towards H<sub>2</sub>O<sub>2</sub> (Figure 11).

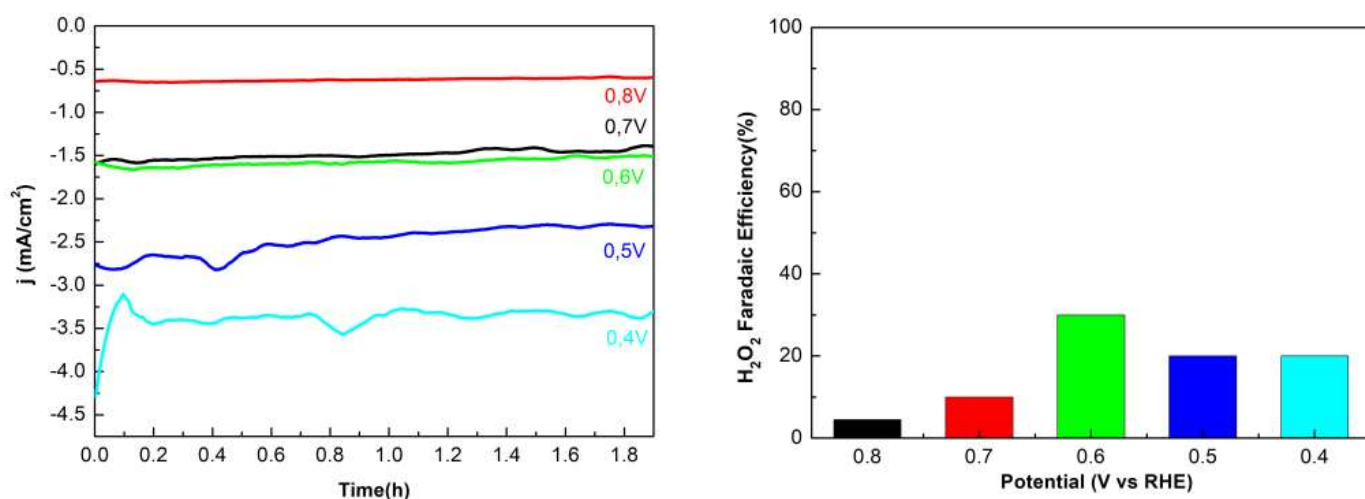


**Figure 11:** Current density/time profiles at different fixed potentials in KOH 0.1 M and corresponding H<sub>2</sub>O<sub>2</sub> Faradaic Efficiency.

As already mentioned, though, N<sub>pyridinic</sub> sites are indeed the most active for oxygen reduction, therefore it is not desirable for them to be completely quenched. To confirm that the selectivity is strictly correlated to the correct tuning of the N atom type distribution, a parent material Co-NC-phen was prepared, using phenantroline as a precursor. Co-NC-phen displays a morphology comparable to Co-NC-Im, as TEM images show (Figure 12) but results richer in pyridinic N atoms, with a N<sub>pyridinic</sub>/N<sub>pyrrolic</sub> ratio of 1.65.

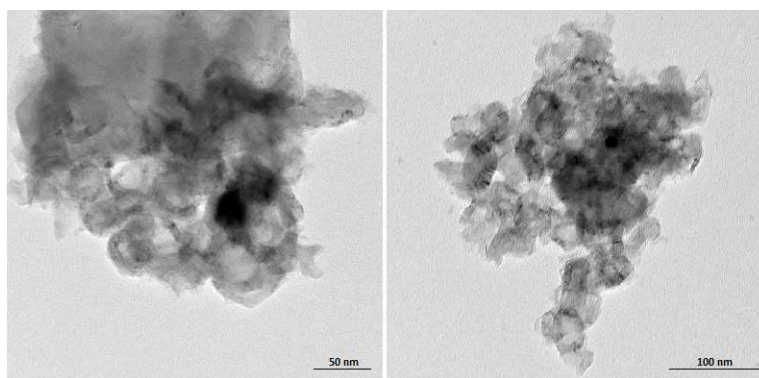


**Figure 12:** TEM images showing Co-NC-phen morphology

Its electrocatalytic activity and selectivity at pH 1 was tested at 0.5 V as a comparison. The FE calculated was 59%, significantly lower than the one obtained with Co-NC-Im working in the same condition and at the same potential, suggesting, as hypothesized, that the higher content in pyridinic N atoms is detrimental for H<sub>2</sub>O<sub>2</sub> production at low pH. In order to further investigate the mechanism of the oxygen electroreduction catalysed by Co-NC-Im, rotating disk electrode (RDE) experiments were performed (Figure 13) and the number of electrons involved calculated according to the Koutecky-Levich theory.<sup>32</sup> The average number of electrons calculated for the potential range between 0.2 and 0.5 V was 1.9, confirming the high selectivity of the process through a 2-electron step leading to H<sub>2</sub>O<sub>2</sub> formation. The drop in FE occurring at more negative potentials can be rationalized with the promotion of a second, fast 2-electron step that furtherly reduces H<sub>2</sub>O<sub>2</sub> to water, lowering the FE. On the other hand, the same experiment performed in alkaline environment gave an average  $ne^-$  value of 2.5 in the potential range between 0.8 and 0.3 V, suggesting a competition between the 2-electron pathway and the 4-electron one, leading, again, to a lower selectivity towards H<sub>2</sub>O<sub>2</sub>.

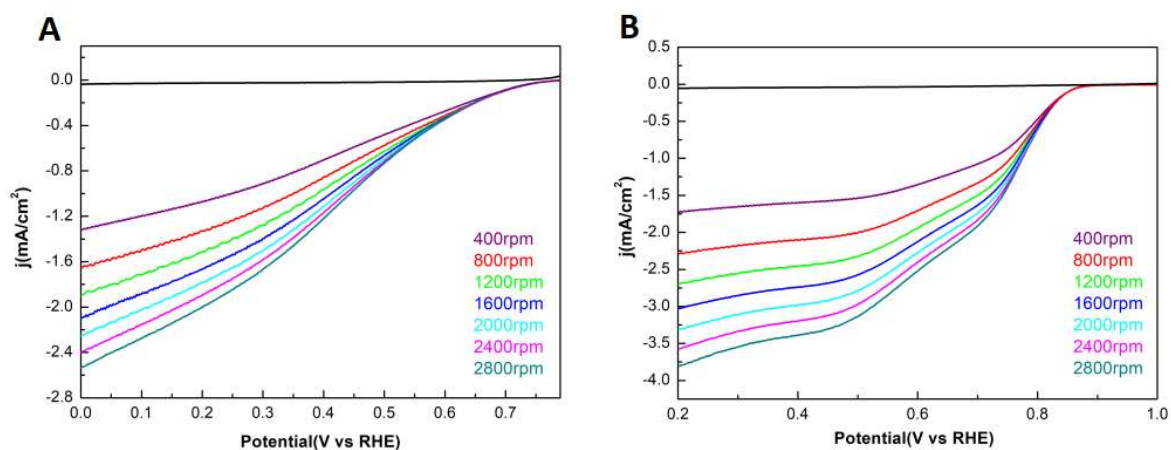
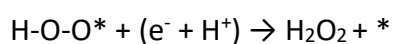
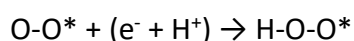
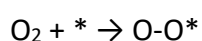


**Figure 13:** A) Rotating disk electrode (RDE) linear sweep voltammeteries at different rotation speed (scan rate 5 mV s<sup>-1</sup>) in H<sub>2</sub>SO<sub>4</sub> 0.1 M and B) in KOH 0.1 M.

In a recent work<sup>33</sup> first principle calculations were employed to investigate the mechanism involved in the ORR catalysis by N-doped carbon materials. The study suggested the possibility for this kind of materials to give rise to an indirect mechanism, with H<sub>2</sub>O<sub>2</sub> as intermediate, when working in acidic environment. Following this assumption, we explored the possible mechanisms that the process can follow. A very relevant theoretical study by Nørskov et al.<sup>34</sup> describe a pathway, called the associative mechanism, that doesn't involve the dissociation of hydrogen before its hydrogenation. Given the high amount of hydrogen peroxide found at low overpotential, we assumed that our catalyst may proceed through this kind of pathway:



Where \* represents a catalytic site on the surface of the material where O<sub>2</sub> adsorbs in a chain configuration, which makes favorable the preservation of the O-O bond.<sup>35</sup> The catalytic behavior of this catalyst is likely complex and connected to different factors, one of which derives from the strength of O<sub>2</sub> absorption on its surface.<sup>36</sup> For this reason the porosity of the material was studied, as its influence on mass transfer can have a role in the selectivity of the process, likely promoting strong O<sub>2</sub> and poor H<sub>2</sub>O<sub>2</sub> adsorption. N<sub>2</sub> physisorption experiments were performed on Co-NC-im and Co-NC-phen as a comparison. Co-NC-im's presents a type IV isotherm with a hysteresis loop characteristic of the presence of mesopores (Figure 14). The surface area was calculated employing the Brunauer-Emmet-Teller (BET) theory and resulted as high as 337 m<sup>2</sup> g<sup>-1</sup>, with a bimodal pore size distribution with two relative maxima at around 2.4 and 77 nm, implying that there is also a small contribution from micropores. On the other hand, Co-NC-phen, which also exhibits a type IV isotherm, displays a lower BET surface area of 246 m<sup>2</sup> g<sup>-1</sup> and a significant microporous volume of (0.04 cm<sup>3</sup> g<sup>-1</sup>). The microporous surface area associated of 62 m<sup>2</sup> g<sup>-1</sup> was calculated as the difference between the BET surface area and the external surface area. Pore size distribution, with the bimodal pattern consisting of two relative maxima at 2.4 and 7 nm, is also quite different. We concluded that the presence of larger pores and higher mesoporosity of Co-NC-im is another factor contributing to the increased selectivity towards H<sub>2</sub>O<sub>2</sub> in the working conditions. These considerations fit perfectly in the landscape of older<sup>37,38</sup> and newer<sup>39</sup> studies

involving mesoporous carbon, and correlate the extensive mesoporosity with high H<sub>2</sub>O<sub>2</sub> selectivity. High surface area has also been linked to high activity before.<sup>40</sup>

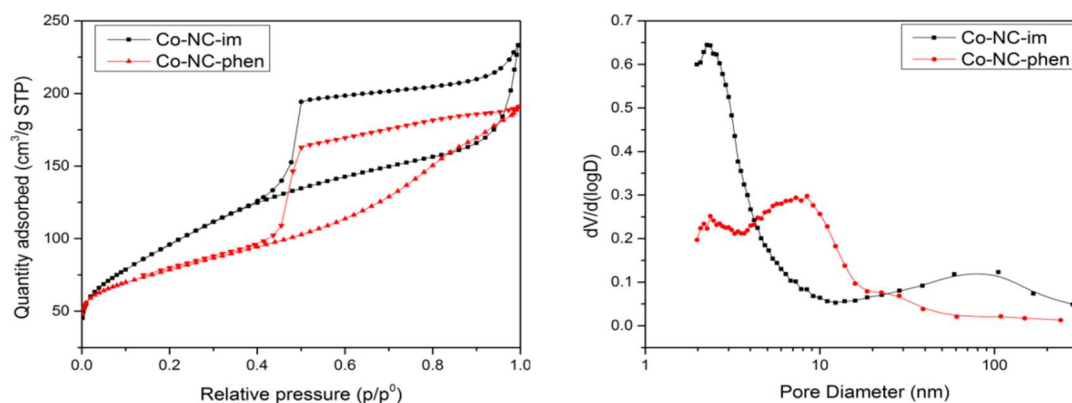


**Figure 14:** N<sub>2</sub> physisorption isotherm (left) and Barrett-Joyner-Halenda (BJH) pore size distributions (right) of Co-NC-im and Co-NC-phen.

Electrochemical impedance spectroscopy (EIS)<sup>32</sup> was performed on Co-CN-im and Co-CN-phen catalysts, in order to gain a deeper insight on the different electrochemical properties of the two materials. EIS studies of ORR in a three-electrode RDE setup were seldom reported in the literature, except for a few examples restricted to Pt-based electrocatalysts.<sup>41,42</sup> ORR kinetic studies for a wide range of electrocatalysts, including Pd- and non-precious metal-based materials, have been deepened by the use of RDE hydrodynamic technique, without EIS being employed.<sup>43–47</sup> Since complete fuel cells and half-membrane electrode assembly (MEA) configurations involve several interfaces, the method based on the single electrode study with TF-RDE is convenient and cost-effective: in fact, a reduced quantity (micrograms) of the catalyst is enough for the characterization of the electrode; moreover, the complications arising from the other components of the fuel cell system (i.e. anode and membrane electrolyte) are eliminated. Notably, the EI spectra of ORR in RDE configuration are completely different from those of the theoretical and experimental impedance spectra reported in literature on fuel cell cathodes with a porous gas-diffusion electrode and it is strongly affected by both the ionomer content in the ink formulation and the film thickness.<sup>48</sup> For this study, the EIS characterization of the ORR process was performed in a three electrode system with an optimized Nafion (5 mL) containing thin-film catalyst. The spectra were recorded for Co-CN-im and Co-CN-phen in different regions of the ORR polarization curve, spanning from the kinetic to the diffusion/mass transport-controlled region: (i) open circuit potential (OCP); (ii) + 0.7 V; (iii) + 0.5 V; (iv) + 0.2 V. Figure 15 reports two typical polarization curves for the two materials, evidencing the different potential regions.

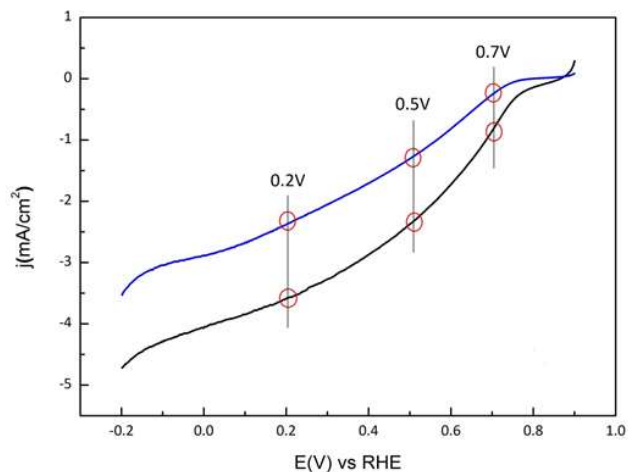


**Figure 15:** LSVs on RDE for Co-NC-im (blue trace) and Co-NC-phen (black trace) in  $O_2$ -saturated acid electrolyte at 0.7 V at 1600 rpm and a  $5 \text{ mV s}^{-1}$  scan rate.

For both materials, the measurement at OCP in Ar-saturated acid solution produced a curve that is almost parallel to the y-axis, coincident to a Bode plot in which the low frequency region to the x-axis with a constant phase angle of around  $80^\circ$  (Figure 16). Two main reason for this very high phase angle were hypothesized: it could be due to the high capacitive nature of the carbon phase, as noticeable from the shape of the CVs (Figure 9), or because of the  $H^+$  ion transport limitations through the distributed resistance/capacitance in the porous carbon electrode; it is worth reminding carbon's hydrophobicity and Nafion's poor conductivity at room temperature.

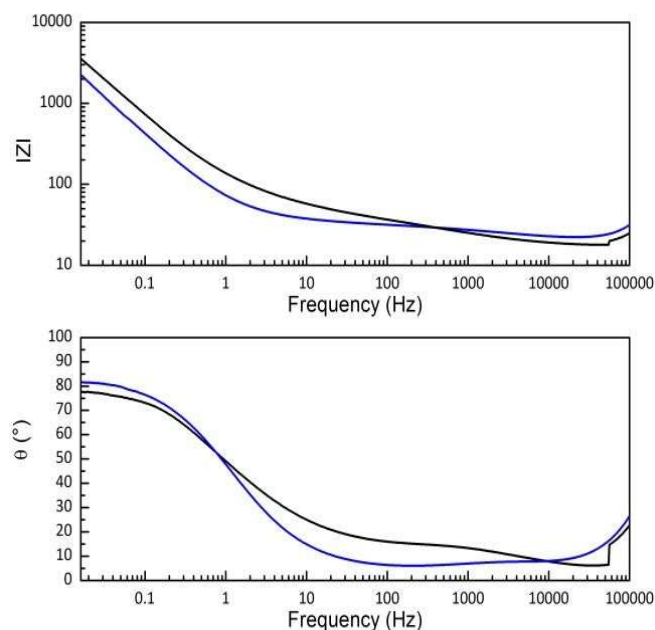


**Figure 16:** Bode diagrams for Co-NC-im (blue trace) and Co-NC-phen (black trace) in Ar-saturated acid electrolyte at OCP.

The spectra recorded at OCP in presence of oxygen, exhibit the same behavior, which is not dependent on O<sub>2</sub> diffusion limitations, despite the Nyquist plot being slightly tilted towards the x-axis because of the arise of diffusion limitations related to oxygen in the low frequency (LF) regime. When shifting to the mixed-controlled kinetic and diffusion region (0.7 V), the polarization resistance (R<sub>p</sub>) of the electrochemical process calculated from the diameter of the Nyquist plot semi-circle is 166 Ω cm<sup>2</sup> for Co-NC-im (Figure 17A). The value of R<sub>p</sub> calculated for Co-NC-im, (Figure 17B) on the other hand, is slightly lower (143 Ω cm<sup>2</sup>) and constituted by a series of different resistance contributes. An increase in R<sub>p</sub> for both materials is otherwise noticed when lowering the working potential. Since the pure charge-transfer resistance should decrease with the potential, this phenomenon can be explained considering mass-transfer resistance to be higher in this case.

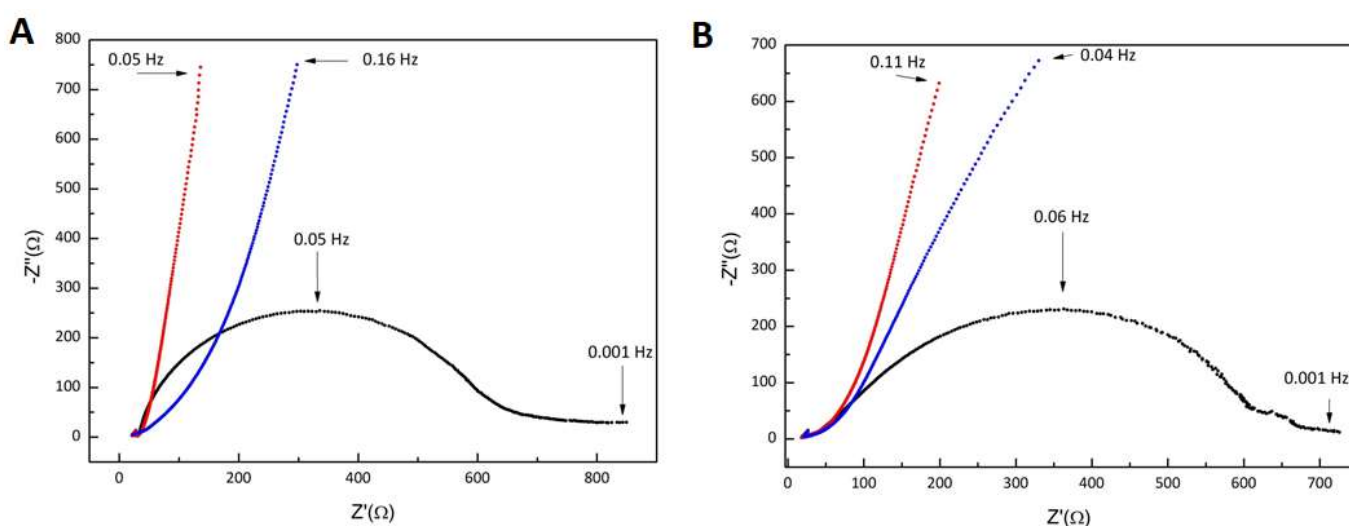
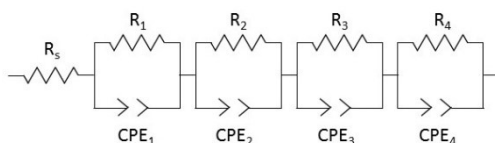


**Figure 17:** Nyquist plots of: A) Co-NC-im and B) Co-NC-phen. **Red trace:** Ar- saturated acid electrolyte at OCP. **Blue trace:** O<sub>2</sub>- saturated acid electrolyte at OCP. **Black trace:** O<sub>2</sub>-saturated acid electrolyte at 0.7 V.

For the fitting of both materials spectra in this region, a simple equivalent circuit (EQ) of four (R, CPE) elements along with the series resistance R<sub>s</sub> (Table 1) was employed. Although the charge transfer contributes result comparable, the mass-transport limitations in the LF region are different, especially at frequency values lower than 0.05 Hz.

**Table 1:** Summary of equivalent resistance data ( $\Omega \text{ cm}^2$ ) obtained from the EQ reported in the Scheme below. EIS experimental conditions:  $\text{O}_2$ - saturated acid electrolyte at 0.7 V.

Sample	$R_s$	$R_1$	$R_2$	$R_3$	$R_4$
Co-NC-im	2.9	3.9	29.2	112.8	20.0
Co-NC-phen	2.9	4.1	24.3	77.7	37.1



The Nyquist plots acquired at 0.5 V (Figure 18) and 0.2 V (Figure 19), where diffusional limits predominate, confirm the identified trend. The lower mass-transport limitation when approaching the frequency value of 0.01 in the case of Co-NC-im appears related to its higher selectivity for  $\text{H}_2\text{O}_2$  with respect to Co-NC-phen, in good agreement with the results of porosimetry analysis and bulk electrolysis tests.

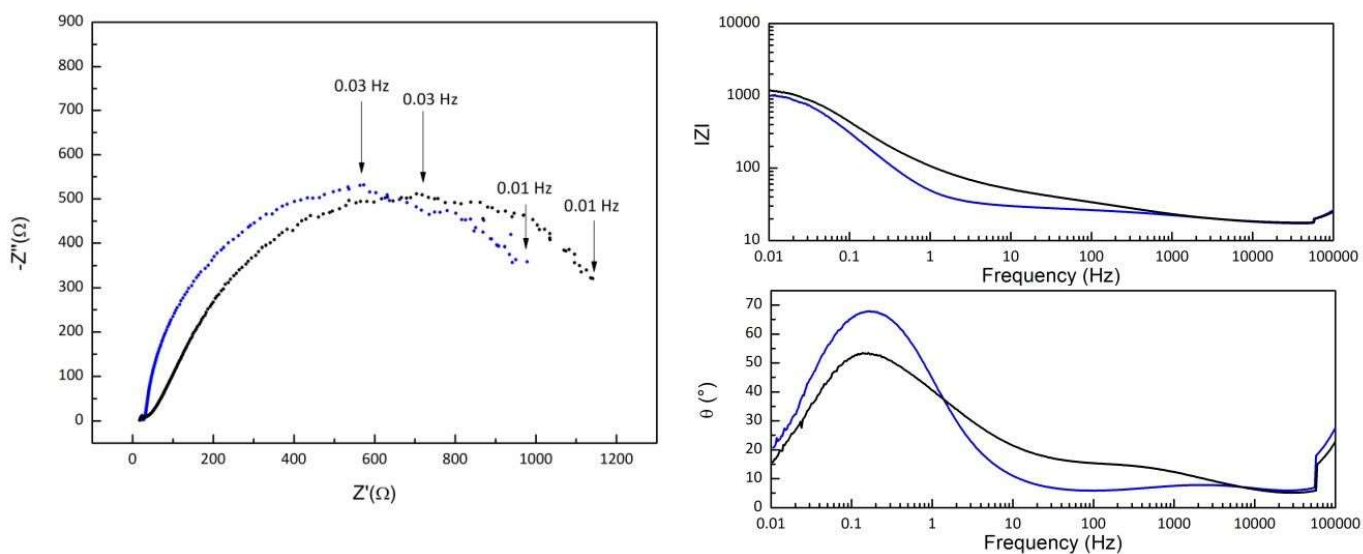


**Figure 18:** Nyquist and Bode diagrams of Co-NC-im (blue trace) and Co-NC-phen (black trace) in  $\text{O}_2$ - saturated acid electrolyte at 0.5 V.

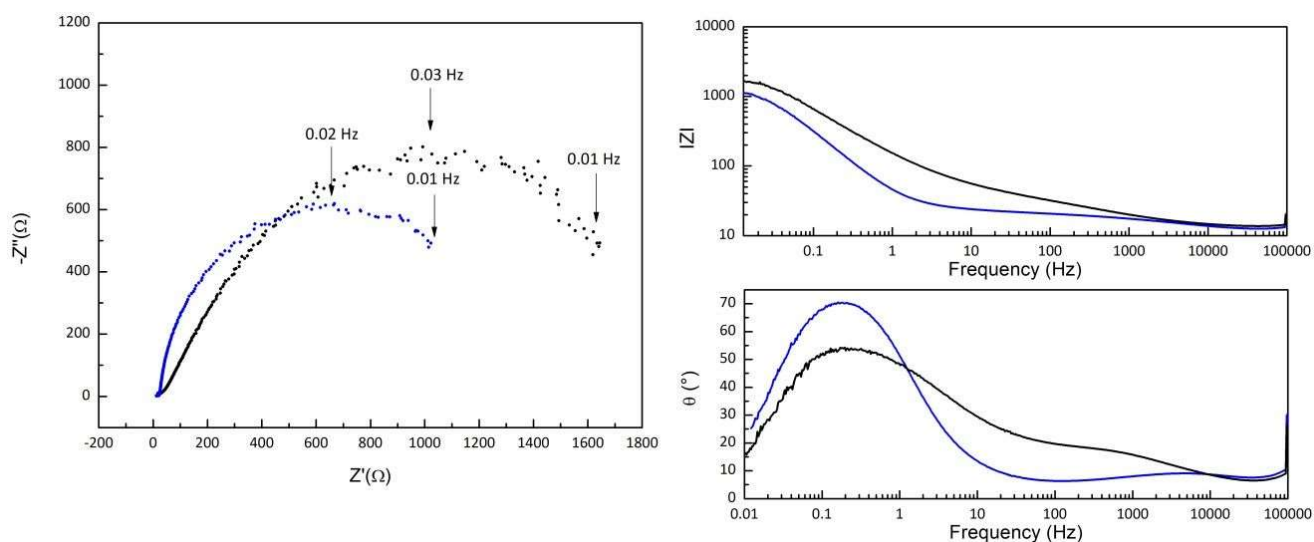


**Figure 19:** Nyquist and Bode diagrams of Co-NC-im (blue trace) and Co-NC-phen (black trace) in  $O_2$ -saturated acid electrolyte at 0.2 V.

Finally, the role of the metal was investigated since its possible contribution to the electron transfer rates and the  $O_2$  binding strength seems plausible. For this reason, parent composites, featuring respectively Fe, Ni and Mn as the encapsulated metal (Fe-NC-im, Ni-NC-im and Mn-NC-im) were prepared, using a synthetic strategy that allowed the formation of materials with a morphology similar to the one of the Co analogue, as shown by the TEM micrographs (Figure 20).

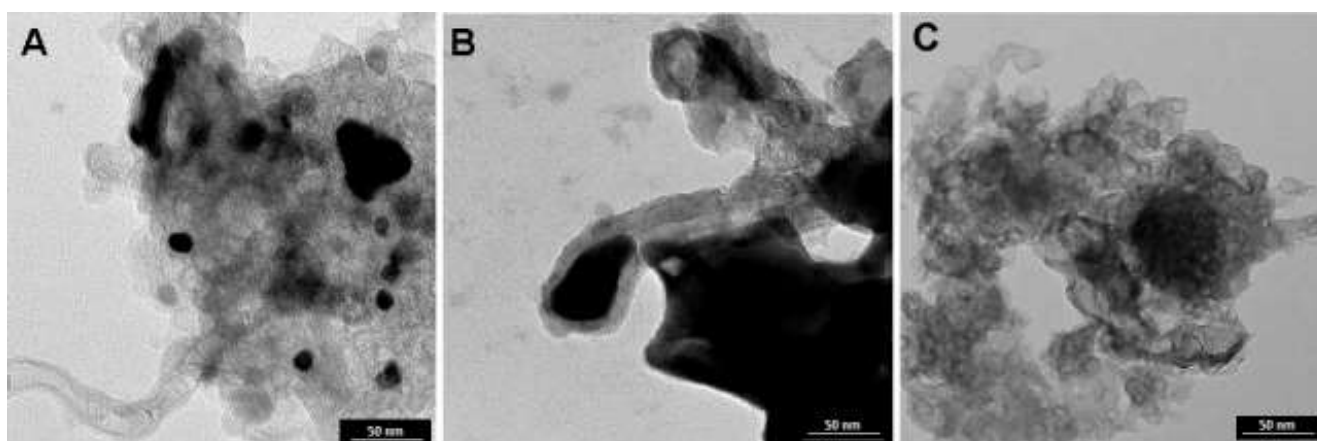


**Figure 20:** TEM images showing A) Ni-NC-im, B) Fe-NC-im and C) Mn-NC-im morphologies

The same electrocatalytic tests were run for the three samples, and it was found that Fe-NC-im and Mn-NC-im show a much more negative onset potential than Ni-NC-im (0.55 V for the formers and 0.50 V for the latter) (Figure 21).

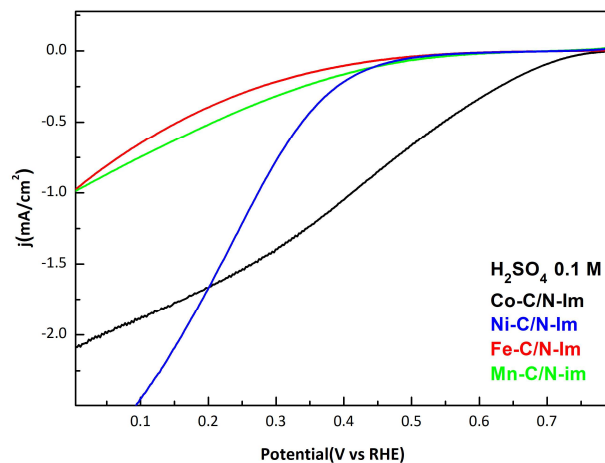


**Figure 21:** LSV profiles at pH 1 under O<sub>2</sub> saturation conditions of Co-NC-im, Fe-NC-im, Mn-NC-im and Ni-NC-im showing the different onset potentials

Moreover, the Faradaic Efficiency for all three comparative materials, calculated after chrono amperometries at different potentials, was significantly lower compared to the cobalt-based material. Note that since their onset potential is lower, the chosen fixed potentials were necessarily different than those selected for the Co-NC-im catalyst (Figure 22)

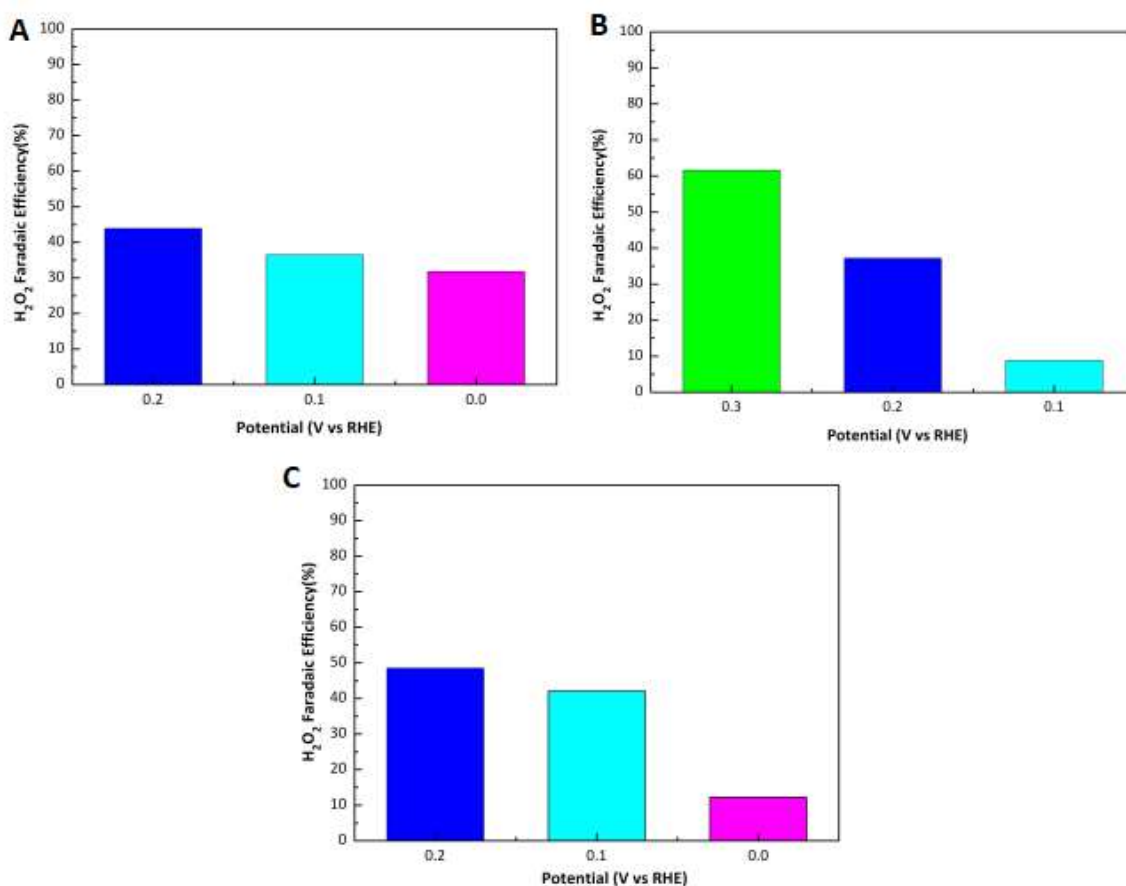


**Figure 22:** FE(H<sub>2</sub>O<sub>2</sub>) of A) Fe-NC-im, B) Ni-NC-im and C) Mn-NC-im at the respective explored potentials

XPS analysis was performed on the three new samples. A difference in terms of N-type distribution has been observed, suggesting that the templating ability of each metal has an influence on this parameter. The results have been summarized in Table 2.

**Table 2:** XPS calculated atomic ratio of the catalysts prepared with the different metals, Co, Fe, Mn, Ni.

Sample	Pyrrolic N-C (%)	Pyridinic N=C (%)	N <sub>1s</sub> atomic ratio (%)	Metal atomic ratio (%)
Co-NC-im	54.6	45.34	2.9	-
Fe-NC-im	49.9	50.1	2.1	-
Mn-NC-im	47.5	52.5	2.2	-
Ni-NC-im	37.8	62.2	4.4	Ni <sub>2p3/2</sub> = 2.6

The  $N_{\text{pyridinic}}/N_{\text{pyrrolic}}$  relative ratio for Fe-NC-im, Mn-NC-im and Ni-NC-im where calculated as respectively 1.0, 1.1 and 1.6. Notably, Fe-NC-im and Mn-NC-im show very similar  $N_{\text{pyridinic}}/N_{\text{pyrrolic}}$  relative ratios, and this reflects on their similar catalytic activity, in terms of both onset potential and H<sub>2</sub>O<sub>2</sub> selectivity. Different is the case of Ni-NC-im, but since a small fraction of Ni has remained in the outer layers of the carbon phase, the metal could be participating directly in the catalysis, and this could explain also the higher current densities observed in the LSV. Otherwise, the direct participation of the metal in the catalytic process is likely to be ruled out, given that the encapsulation in the thick carbon layers isolates them from the reaction environment. It has been reported though that embedded metals in carbon nanotubes can facilitate electron transfer processes to the carbon surface through an interlayer electron hopping mechanism, therefore some kind of active participation of the metal cannot be completely excluded.<sup>23</sup> In an additional hypothesis, the internal metal can modify the orbital energies of the outer doping N atoms, thus indirectly contributing to the selectivity of the process, as a result of different alteration depending on the nature of the metal. In order to evaluate the stability of Co-NC-im, recycling tests were performed by doing successive 1.5 h chronoamperometric experiments. The electrolyte solution was titrated and refreshed each time. Between the first and the second cycle, a small decrease of current is noticeable, likely assignable to a physical detachment of some catalyst from the electrode, but the material reveals an overall good stability. Interestingly, as far as selectivity towards H<sub>2</sub>O<sub>2</sub> is concerned, the FE remain very similar and close to 100% throughout the cycles (Figure 23).

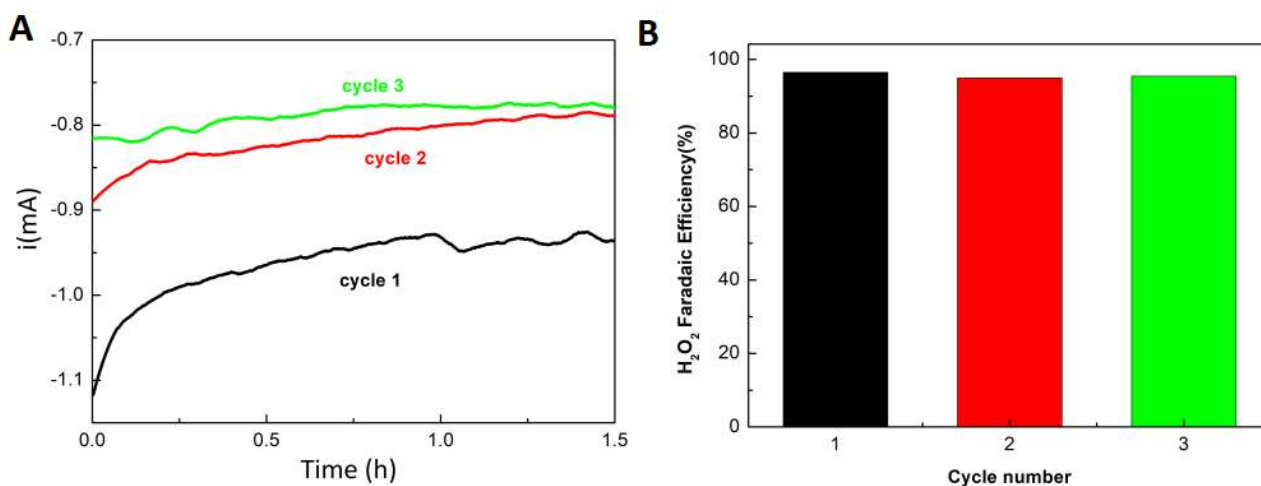


**Figure 23:** Chronoamperometry over 1.5 hours repeated for three cycles (left) and corresponding Faradaic Efficiency toward  $H_2O_2$  (right).

### 3.3 Conclusions

In conclusion, the performance towards ORR achieved with the proposed catalyst based on Co nanoparticles encapsulated within N-doped graphitic carbon have been investigated under acidic and alkaline conditions. At low pH and higher positive potentials, an almost total selectivity towards  $H_2O_2$  production have been observed, likely correlated to a series of concomitant factors such as the pH itself, the N-type species relative distribution and the textural properties of the material. The chemical identity of the encapsulated metal has also revealed itself as crucial in determining the final distribution of the N doping atoms, or possibly to indirectly participate to the reduction process. The absence of precious metals and scalable synthetic protocol makes this material a highly promising catalyst for the sustainable production of hydrogen peroxide. Moreover, the results presented contribute to a deeper understanding of the characteristics needed in the design of carbon-based electrocatalyst able to selectively trigger the 2-electron reduction of  $O_2$ , opening an important field that goes beyond the application in fuel cells.

### 3.4 References

- (1) Jaouen, F.; Proietti, E.; Lefèvre, M.; Chenitz, R.; Dodelet, J.-P.; Wu, G.; Chung, H. T.; Johnston, C. M.; Zelenay, P. Recent Advances in Non-Precious Metal Catalysis for Oxygen-Reduction Reaction in Polymer Electrolyte Fuel Cells. *Energy Environ. Sci.* **2011**, *4* (1), 114–130.
- (2) Rabis, A.; Rodriguez, P.; Schmidt, T. J. Electrocatalysis for Polymer Electrolyte Fuel Cells: Recent Achievements and Future Challenges. *ACS Catal.* **2012**, *2* (5), 864–890.
- (3) López, F.; Díaz, M. J.; Eugenio, M. E.; Ariza, J.; Rodríguez, A.; Jiménez, L. Optimization of Hydrogen Peroxide in Totally Chlorine Free Bleaching of Cellulose Pulp from Olive Tree Residues. *Bioresour. Technol.* **2003**, *87* (3), 255–261.
- (4) Mussatto, S. I.; Rocha, G. J. M.; Roberto, I. C. Hydrogen Peroxide Bleaching of Cellulose Pulps Obtained from Brewer's Spent Grain. *Cellulose* **2008**, *15* (4), 641–649.
- (5) Tundo, P.; Anastas, P.; Black, D. S.; Breen, J.; Collins, T. J.; Memoli, S.; Miyamoto, J.; Polyakoff, M.; Tumas, W. Synthetic Pathways and Processes in Green Chemistry. Introductory Overview. *Pure Appl. Chem.* **2000**, *72* (7), 1207–1228.
- (6) Sanderson, W. R. Cleaner Industrial Processes Using Hydrogen Peroxide. *Pure Appl. Chem.* **1998**, *72* (7), 1289–1304.
- (7) G. Pfeleiderer, H. J. Rledl, Vol. 2158525, C01B15/023 Ed. (Ed.: U. P. US2158525A), USA, 1939.
- (8) Campos-Martin, J. M.; Blanco-Brieva, G.; Fierro, J. L. G. Hydrogen Peroxide Synthesis: An Outlook beyond the Anthraquinone Process. *Angew. Chemie - Int. Ed.* **2006**, *45* (42), 6962–6984.
- (9) Lu, Z.; Chen, G.; Siahrostami, S.; Chen, Z.; Liu, K.; Xie, J.; Liao, L.; Wu, T.; Lin, D.; Liu, Y.; et al. High-Efficiency Oxygen Reduction to Hydrogen Peroxide Catalysed by Oxidized Carbon Materials. *Nat. Catal.* **2018**, *1*, 156–162.
- (10) Winter, M.; Brodd, R. J. What Are Batteries, Fuel Cells, and Supercapacitors? *Chem. Rev.* **2004**, *104* (10), 4245–4269.
- (11) Thomas, S. C.; Ren, X.; Gottesfeld, S.; Zelenay, P. Direct Methanol Fuel Cells: Progress in Cell Performance and Cathode Research. **2002**, *47*, 3741–3748.
- (12) Greeley, J.; Stephens, I. E. L.; Bondarenko, A. S.; Johansson, T. P.; Hansen, H. A.; Jaramillo, T. F.; Rossmeisl, J.; Chorkendorff, I.; Nørskov, J. K. Alloys of Platinum and Early Transition Metals as Oxygen Reduction Electrocatalysts. *Nat. Chem.* **2009**, *1* (7), 552–556.
- (13) Stamenkovic, V. R.; Fowler, B.; Mun, B. S.; Wang, G.; Ross, P. N.; Lucas, C. A.; Marković, N.

M. Improved Oxygen Reduction Activity on Pt<sub>3</sub>Ni(111) via Increased Surface Site Availability *Science (80-. )*. **2007**, *315* (5811), 493 LP-497.

- (14) Verdager-Casadevall, A.; Deiana, D.; Karamad, M.; Siahrostami, S.; Malacrida, P.; Hansen, T. W.; Rossmeisl, J.; Chorkendorff, I.; Stephens, I. E. L. Trends in the Electrochemical Synthesis of H<sub>2</sub>O<sub>2</sub>: Enhancing Activity and Selectivity by Electrocatalytic Site Engineering. *Nano Lett.* **2014**, *14* (3), 1603–1608.
- (15) Dai, L.; Xue, Y.; Qu, L.; Choi, H.-J.; Baek, J.-B. Metal-Free Catalysts for Oxygen Reduction Reaction. *Chem. Rev.* **2015**, *115* (11), 4823–4892.
- (16) Gong, K.; Du, F.; Xia, Z.; Durstock, M.; Dai, L. Nitrogen-Doped Carbon Nanotube Arrays with High Electrocatalytic Activity for Oxygen Reduction. *Science (80-. )*. **2009**, *323*, 760–764.
- (17) Rocha, I. M.; Soares, O. S. G. P.; Fernandes, D. M.; Freire, C.; Figueiredo, J. L.; Pereira, M. F. R. N-Doped Carbon Nanotubes for the Oxygen Reduction Reaction in Alkaline Medium: Synergistic Relationship between Pyridinic and Quaternary Nitrogen. *ChemistrySelect* **2016**, *1* (10), 2522–2530.
- (18) Ding, W.; Wei, Z.; Chen, S.; Qi, X.; Yang, T.; Hu, J.; Wang, D.; Wan, L. J.; Alvi, S. F.; Li, L. Space-Confinement-Induced Synthesis of Pyridinic- and Pyrrolic-Nitrogen- Doped Graphene for the Catalysis of Oxygen Reduction. *Angew. Chemie - Int. Ed.* **2013**, *52* (45), 11755–11759.
- (19) Yu, H.; Shang, L.; Bian, T.; Shi, R.; Waterhouse, G. I. N.; Zhao, Y.; Zhou, C.; Wu, L. Z.; Tung, C. H.; Zhang, T. Nitrogen-Doped Porous Carbon Nanosheets Templated from g-C<sub>3</sub>N<sub>4</sub> as Metal-Free Electrocatalysts for Efficient Oxygen Reduction Reaction. *Adv. Mater.* **2016**, 5080–5086.
- (20) Liang, H. W.; Wu, Z. Y.; Chen, L. F.; Li, C.; Yu, S. H. Bacterial Cellulose Derived Nitrogen-Doped Carbon Nanofiber Aerogel: An Efficient Metal-Free Oxygen Reduction Electrocatalyst for Zinc-Air Battery. *Nano Energy* **2015**, *11*, 366–376.
- (21) Li, X.; Fang, Y.; Zhao, S.; Wu, J.; Li, F.; Tian, M.; Long, X.; Jin, J.; Ma, J. Nitrogen-Doped Mesoporous Carbon Nanosheet/Carbon Nanotube Hybrids as Metal-Free Bi-Functional Electrocatalysts for Water Oxidation and Oxygen Reduction. *J. Mater. Chem. A* **2016**, *4* (34), 13133–13141.
- (22) Iglesias, D.; Giuliani, A.; Melchionna, M.; Marchesan, S.; Criado, A.; Nasi, L.; Bevilacqua, M.; Tavagnacco, C.; Vizza, F.; Prato, M.; et al. N-Doped Graphitized Carbon Nanohorns as a Forefront Electrocatalyst in Highly Selective O<sub>2</sub> Reduction to H<sub>2</sub>O<sub>2</sub>. *Chem* **2018**, *4* (1), 106–123.

- (23) Bracamonte, M. V.; Melchionna, M.; Stopin, A.; Giuliani, A.; Tavagnacco, C.; Garcia, Y.; Fornasiero, P.; Bonifazi, D.; Prato, M. Carboxylated, Fe-Filled Multiwalled Carbon Nanotubes as Versatile Catalysts for O<sub>2</sub> Reduction and H<sub>2</sub> Evolution Reactions at Physiological pH. *Chem. - A Eur. J.* **2015**, *21* (36), 12769–12777.
- (24) Deng, D.; Yu, L.; Chen, X.; Wang, G.; Jin, L.; Pan, X.; Deng, J.; Sun, G.; Bao, X. Iron Encapsulated within Pod-like Carbon Nanotubes for Oxygen Reduction Reaction. *Angew. Chemie - Int. Ed.* **2013**, *52* (1), 371–375.
- (25) Wu, G.; More, K. L.; Johnston, C. M.; Zelenay, P. High-Performance Electrocatalysts for Oxygen Reduction Derived from Polyaniline, Iron, and Cobalt. *Science (80-. )*. **2011**, *332* (6028), 443–447.
- (26) Jiang, H.; Liu, Y.; Hao, J.; Wang, Y.; Li, W.; Li, J. Self-Assembly Synthesis of Cobalt- and Nitrogen-Coembedded Trumpet Flower-Like Porous Carbons for Catalytic Oxygen Reduction in Alkaline and Acidic Media. *ACS Sustain. Chem. Eng.* **2017**, *5* (6), 5341–5350.
- (27) Zhou, T.; Ma, R.; Zhou, Y.; Xing, R.; Liu, Q.; Zhu, Y.; Wang, J. Efficient N-Doping of Hollow Core-Mesoporous Shelled Carbon Spheres via Hydrothermal Treatment in Ammonia Solution for the Electrocatalytic Oxygen Reduction Reaction. *Microporous Mesoporous Mater.* **2018**, *261* (October 2017), 88–97.
- (28) Yu, D.; Zhang, Q.; Dai, L. Highly-Efficient Metal-Free Growth of Nitrogen-Doped Single-Walled Carbon Nanotubes on Plasma-Etched Substrates for Oxygen Reduction Highly-Efficient Metal-Free Growth of Nitrogen-Doped Single-Walled Carbon Nanotubes on Plasma-Etched Substrates for Oxygen. *J. Am. Chem. Soc.* **2010**, No. January, 1–19.
- (29) Yang, S.; Feng, X.; Wang, X.; Müllen, K. Graphene-Based Carbon Nitride Nanosheets as Efficient Metal-Free Electrocatalysts for Oxygen Reduction Reactions. *Angew. Chemie - Int. Ed.* **2011**, *50* (23), 5339–5343.
- (30) Tuci, G.; Zafferoni, C.; D'Ambrosio, P.; Caporali, S.; Ceppatelli, M.; Rossin, A.; Tsoufis, T.; Innocenti, M.; Giambastiani, G. Tailoring Carbon Nanotube N-Dopants While Designing Metal-Free Electrocatalysts for the Oxygen Reduction Reaction in Alkaline Medium. *ACS Catal.* **2013**, *3* (9), 2108–2111.
- (31) Wan, K.; Long, G. F.; Liu, M. Y.; Du, L.; Liang, Z. X.; Tsiakaras, P. Nitrogen-Doped Ordered Mesoporous Carbon: Synthesis and Active Sites for Electrocatalysis of Oxygen Reduction Reaction. *Appl. Catal. B Environ.* **2015**, *165*, 566–571.
- (32) Bard, A. J.; Faulkner, L. R. *Electrochemical Methods Fundamentals and Applications*; John

Wiley & Sons, I., Ed.; 2001.

- (33) Chai, G.-L.; Boero, M.; Hou, Z.; Terakura, K.; Cheng, W. Indirect Four-Electron Oxygen Reduction Reaction on Carbon Materials Catalysts in Acidic Solutions. *ACS Catal.* **2017**, *7*, 7908–7916.
- (34) Nørskov, J. K.; Rossmeisl, J.; Logadottir, A.; Lindqvist, L.; Kitchin, J. R.; Bligaard, T.; Jónsson, H. Origin of the Overpotential for Oxygen Reduction at a Fuel-Cell Cathode. *J. Phys. Chem. B* **2004**, *108* (46), 17886–17892.
- (35) Li, Y.; Zhong, G.; Yu, H.; Wang, H.; Peng, F. O<sub>2</sub> and H<sub>2</sub>O<sub>2</sub> Transformation Steps for the Oxygen Reduction Reaction Catalyzed by Graphitic Nitrogen-Doped Carbon Nanotubes in Acidic Electrolyte from First Principles Calculations. *Phys. Chem. Chem. Phys.* **2015**, *17* (34), 21950–21959.
- (36) She, Z. W.; Kibsgaard, J.; Dickens, C. F.; Chorkendorff, I.; Nørskov, J. K.; Jaramillo, T. F. Combining Theory and Experiment in Electrocatalysis: Insights into Materials Design. *Science (80-. )*. **2017**, *355* (6321), eaad4998.
- (37) Fellingner, T. P.; Hasché, F.; Strasser, P.; Antonietti, M. Mesoporous Nitrogen-Doped Carbon for the Electrocatalytic Synthesis of Hydrogen Peroxide. *J. Am. Chem. Soc.* **2012**, *134* (9), 4072–4075.
- (38) Sakaushi, K.; Fellingner, T. P.; Antonietti, M. Bifunctional Metal-Free Catalysis of Mesoporous Noble Carbons for Oxygen Reduction and Evolution Reactions. *ChemSusChem* **2015**, *8* (7), 1156–1160.
- (39) Sun, Y.; Sinev, I.; Ju, W.; Bergmann, A.; Dresch, S.; Köhl, S.; Spöri, C.; Schmies, H.; Wang, H.; Bernsmeier, D.; et al. Efficient Electrochemical Hydrogen Peroxide Production from Molecular Oxygen on Nitrogen-Doped Mesoporous Carbon Catalysts. *ACS Catal.* **2018**, *8* (4), 2844–2856.
- (40) Yang, W.; Fellingner, T.-P.; Antonietti, M. Efficient Metal-Free Catalysis of ORR in Alkaline Medium on High-Surface-Area Mesoporous N-Doped Carbons Made from Ionic Liquids and Nucleobases. *J. Am. Chem. Soc.* **2011**, *133*, 206–209.
- (41) Shinozaki, K.; Zack, J. W.; Pylypenko, S.; Pivovar, B. S.; Kocha, S. S. Oxygen Reduction Reaction Measurements on Platinum Electrocatalysts Utilizing Rotating Disk Electrode Technique: II. Influence of Ink Formulation, Catalyst Layer Uniformity and Thickness. *J. Electrochem. Soc.* **2015**, *162* (12), F1384–F1396.
- (42) Singh, R. K.; Devivaraprasad, R.; Kar, T.; Chakraborty, A.; Neergat, M. Electrochemical

Impedance Spectroscopy of Oxygen Reduction Reaction (ORR) in a Rotating Disk Electrode Configuration: Effect of Ionomer Content and Carbon-Support. *J. Electrochem. Soc.* **2015**, *162* (6), F489–F498.

- (43) Neergat, M.; Gunasekar, V.; Singh, R. K. Oxygen Reduction Reaction and Peroxide Generation on Ir, Rh, and Their Selenides – A Comparison with Pt and RuSe. *J. Electrochem. Soc.* **2011**, *158* (9), B1060–B1066.
- (44) Choi, C. H.; Park, S. H.; Woo, S. I. Oxygen Reduction Activity of Pd–Mn<sub>3</sub>O<sub>4</sub> Nanoparticles and Performance Enhancement by Voltammetrically Accelerated Degradation. *Phys. Chem. Chem. Phys.* **2012**, *14* (19), 6842–6848.
- (45) Maheswari, S.; Sridhar, P.; Pitchumani, S. Pd-TiO<sub>2</sub>/C as a Methanol Tolerant Catalyst for Oxygen Reduction Reaction in Alkaline Medium. *Electrochem. commun.* **2013**, *26* (1), 97–100.
- (46) Alexeyeva, N.; Sarapuu, A.; Tammeveski, K.; Vidal-Iglesias, F. J.; Solla-Gullón, J.; Feliu, J. M. Electroreduction of Oxygen on Vulcan Carbon Supported Pd Nanoparticles and Pd-M Nanoalloys in Acid and Alkaline Solutions. *Electrochim. Acta* **2011**, *56* (19), 6702–6708.
- (47) Erikson, H.; Liik, M.; Sarapuu, A.; Marandi, M.; Sammelseg, V.; Tammeveski, K. Electrocatalysis of Oxygen Reduction on Electrodeposited Pd Coatings on Gold. *J. Electroanal. Chem.* **2013**, *691*, 35–41.
- (48) Antoine, O.; Bultel, Y.; Durand, R. Oxygen Reduction Reaction Kinetics and Mechanism on Platinum Nanoparticles inside Nafion®. *J. Electroanal. Chem.* **2001**, *499* (1), 85–94.

## **CHAPTER 4: Highly sensitive non-enzymatic metal-free H<sub>2</sub>O<sub>2</sub> sensor based on covalently functionalized acid graphene**

### **4.1 Introduction**

Several different methods have been employed to determine the industrially and biologically highly relevant H<sub>2</sub>O<sub>2</sub> molecule, mostly based on titration or spectrophotometry.<sup>1-3</sup> However, these methods are all affected by either lack of selectivity, or other inherent problems that often compromise their direct utilization in real sample matrices. This has inspired the development of electrochemical sensing methods, that are indeed becoming a trending topic on account of their simplicity, robustness and sensitivity.<sup>4</sup> The topic of this chapter is the application of an acidic graphene-based material prepared with an innovative functionalization technique as a highly sensitive and selective electrosensor for hydrogen peroxide. The material, thanks to the exclusive controlled functionalization with carboxylic acid groups, shows improved sensitivity and stability, outperforming many previously reported carbon-based electrochemical sensors. The control on the functionalization step turns out to be a key aspect for the resulting performance, as proven by a comparative study with samples subjected to diversely strong acidic treatments. Moreover, the selectivity and reliability has been assessed through an investigation in the presence of interferences or in real commodity matrices, such as milk.

### **4.2 Electrocatalytic graphene-based systems for H<sub>2</sub>O<sub>2</sub> sensing**

Different classes of electrochemical sensors based on graphene for the detection of H<sub>2</sub>O<sub>2</sub> have been reported. One big categorization discriminates them between enzymatic and non-enzymatic. Several graphene-supported enzymatic sensors have confirmed that graphene can provide a suitable microenvironment to retain the redox bioactivity of proteins while facilitating the electron-transfer between the active centers of the redox proteins and the underlying electrode.<sup>5,6</sup> Enzymatic sensors are generally characterized by excellent selectivity because the commonly used enzymes, such as horseradish peroxidase, catalase, cytochrome c, hemoglobin, microperoxidase and myoglobin show specific active sites for the involved reaction.<sup>7,8</sup> However, some disadvantages include the relatively high cost, susceptibility to temperature and pH value, complicated immobilization procedures and inherent instability of heme proteins.<sup>9</sup> The poor stability of natural enzymes, in fact, together with their high price even in mass manufacturing, has limited the fabrication process of biosensors and their long-time usage in real applications.<sup>10</sup> On one hand, the

scientific community is trying to address this issue by developing artificial enzymes, which can be more robust and more easily tailored to the desired properties.<sup>11,12</sup> On the other hand, numerous efforts have been devoted to the development of non-enzymatic H<sub>2</sub>O<sub>2</sub> sensors. As already mentioned in the introduction, many of them involve the utilization of metal and metal oxide nanoparticles, although the recent emergence of non-enzymatic, metal free graphene-based sensors sets an intriguing stage for cost-effective strategies. Some examples of their performances are summarized in Table 1.

**Table 1:** Summary table of analytical performance of metal free graphene-based H<sub>2</sub>O<sub>2</sub> electro sensors

<b>Catalyst</b>	<b>Linear range (<math>\mu\text{M}</math>)</b>	<b>Sensitivity</b>	<b>LOD (<math>\mu\text{M}</math>)</b>	<b>Ref</b>
<b>CR-GO</b>	0.05-1500	-	0.05	13
<b>Graphene-MWCNTS</b>	20-2100	32.91 $\mu\text{A mM}^{-1} \text{cm}^{-2}$	9.4	14
<b>rGO/nPPy</b>	0.1-4	47.69 $\mu\text{A } \mu\text{M}^{-1}$	0.034	15
<b>IL-GR-s-PANI</b>	0.5-2000	280.0 $\mu\text{A mM}^{-1}$	0.06	16
<b>rGO/Tyrosine</b>	100-2100	69.07 $\mu\text{A mM}^{-1} \text{cm}^{-2}$	80	17
<b>Poly(o-phenylenediamine)/GO</b>	2.5-25	16.2 $\mu\text{A M}^{-1} \text{cm}^{-2}$	0.84	18
<b>BGNs</b>	1000-20000	266.7 $\mu\text{A mM}^{-1} \text{cm}^{-2}$	3.8	19
<b>NB-G</b>	0.5-5000	-	0.05	20

As previously mentioned, the high quality of graphene is crucial for the electro sensing purpose. Its direct functionalization, that might be strategic for improving its properties in terms of dispersibility in liquid media and electrocatalytic activity towards specific reactions, is often a challenging process due to graphene's intrinsic low reactivity.<sup>21,22</sup> Often, the harsh reaction conditions required to achieve its covalent functionalization, forbid to control finely the product's structure and composition. The widely employed graphene oxide itself, for instance, is prepared through oxidation in harsh conditions, that deeply affects its stoichiometry, chemical structure and properties without a good control.<sup>23</sup> In fact, the resulting material is normally characterized by a non-homogeneous distribution of different oxygen containing groups. In this chapter, a new type of graphene developed by our collaborator Prof Zboril at the Regional Centre for Advanced Technologies and Materials of Olomouc, Czech Republic, following a synthetic scheme that allows

the introduction on the graphene surface of only carboxylic acid groups without disrupting the structure of the graphene sheets was applied in the framework of H<sub>2</sub>O<sub>2</sub> electro-sensing.

### 4.3 Results and discussion

#### 4.3.1 Material preparation and morphologic characterization

The proposed material has been designed, prepared and characterized by prof. Zboril's group.<sup>24</sup> The synthetic process is a multi-step sequence that starts from fluorographene, a stable, stoichiometric and well-defined graphene derivative.<sup>25</sup> For a long time, being a perfluorinated hydrocarbon, fluorographene has been considered unsuitable for further derivatization because of its low reactivity, but lately it's been proven that it can indeed react as an electrophile under mild conditions.<sup>26-30</sup> This discovery allows its exploitation as a synthetic platform for the preparation of other graphene derivatives. In our case, fluorographene was subjected to nucleophilic substitution with NaCN, leading to a fluorine-free G-CN. The second step of the synthesis consisted in its acid hydrolysis with HNO<sub>3</sub> in order to convert the -CN groups in -COOH groups. This step was optimized by testing different acid concentrations and times of treatment; the optimal conditions for sensing were determined to be 20% in HNO<sub>3</sub> at 100°C for 24 h. The success of this synthetic step was checked through FT-IR, by comparing the spectra of the intermediates of the reaction and the final product. The gradual disappearance of the -CN band at 2200 cm<sup>-1</sup> and the emergence of a new band at 1725 cm<sup>-1</sup> corresponds to the total conversion of CN groups into carboxylic units. Characterization with HR-XPS allowed to estimate from the relative atomic ratio of carboxylic oxygen atoms and carboxylic carbon atoms, the functionalization degree, which sets at 13%, which is quite high if compared with other covalently functionalized graphene derivatives.<sup>31-39</sup>

The high functionalization degree was confirmed by the Raman spectrum, which showed broad G and D bands with a ratio I<sub>D</sub>/I<sub>G</sub> of around 1.1, indicative of a disruption of the graphene sp<sup>2</sup> framework.<sup>36,40,41</sup> HR-TEM showed highly transparent sheets and EDX mapping indicates a homogeneous distribution of -COOH groups on the graphene surface. AFM and TGA also support the successful achievement of a two-dimensional acid. The material is able to form stable aqueous dispersions at high concentrations, due to the hydrophilicity guaranteed by the high degree of COOH-functionalization. Furthermore, the acid behavior was precisely investigated via titration of the acid groups. It is worth noticing that this last possibility is largely precluded to traditional

graphene oxide, where titration curve is poorly defined because of the more complex and irregular surface chemical functionalization.<sup>23,42</sup> A combination of DFT calculations and electrochemical measurements including impedance spectroscopy indicated the high conductivity of the sample despite its high degree of functionalization. This is relevant because generally electronic properties of oxidized graphene are severely deteriorated. As far as functionalized graphene is concerned, the electronic properties are intimately connected to the nature of the functional group, arrangement of functionalities and sublattice symmetry, with formation of impurities, defects, atom vacancies and structural distortion. Their presence can indeed influence the electronic properties of the material, including its conductivity.<sup>43–48</sup> DFT was employed to calculate the average band gap for acid graphene, revealing a smaller band gap with respect to the precursor fluorographene, and a pronounced density of states near the Fermi level, suggesting appreciable conductivity. This hypothesis was corroborated by electrochemical impedance spectroscopy, which allowed to measure the resistivity of the sample. The result obtained corresponds to a value of resistivity to charge transfer of 81  $\Omega$ , which is 40 times lower to the one calculated for regular graphene oxide (3542  $\Omega$ ).

#### **4.3.2 Electrochemical characterization**

Three samples prepared employing a different  $\text{HNO}_3$  concentration in the hydrolysis step, 20%, 40% and 65%, named GA-20, GA-40 and GA-65, were compared in order to determine the influence of the different functionalization degree on the electroensing performance.

First, the electrochemical behavior of the three materials was investigated by cyclic voltammetry using a three-electrode system. All potentials in this chapter are reported vs the saturated calomel electrode (SCE). The working electrode, a glassy carbon electrode modified by drop casting with 10  $\mu\text{l}$  of a 2.5  $\text{mg mL}^{-1}$  ink (50% water 50% ethanol 1% Nafion) of GA-20, GA-40 and GA-65 was tested within a potential window of -0.5 V to 0.9 V in a  $\text{N}_2$ -saturated buffer solution of 0.1 M PBS pH 7, with a scan rate of 0.05  $\text{V s}^{-1}$ . The comparison between the different electrochemical responses of the three materials is reported in Figure 1. The three samples all show two broad peaks, one anodic and one cathodic, likely ascribed to the redox processes of the carboxyl groups. It is noticeable, however, a drop in current when moving from GA-20 to GA-65, confirming the importance of the mild acid treatment in preserving the conductivity properties of the graphene. It should also be noted that GA-65 was the sample whose ink was significantly less stable; an initial

detaching of part of the material from the electrode was noticed and was indication of a lessened coherence of the carbon phase.

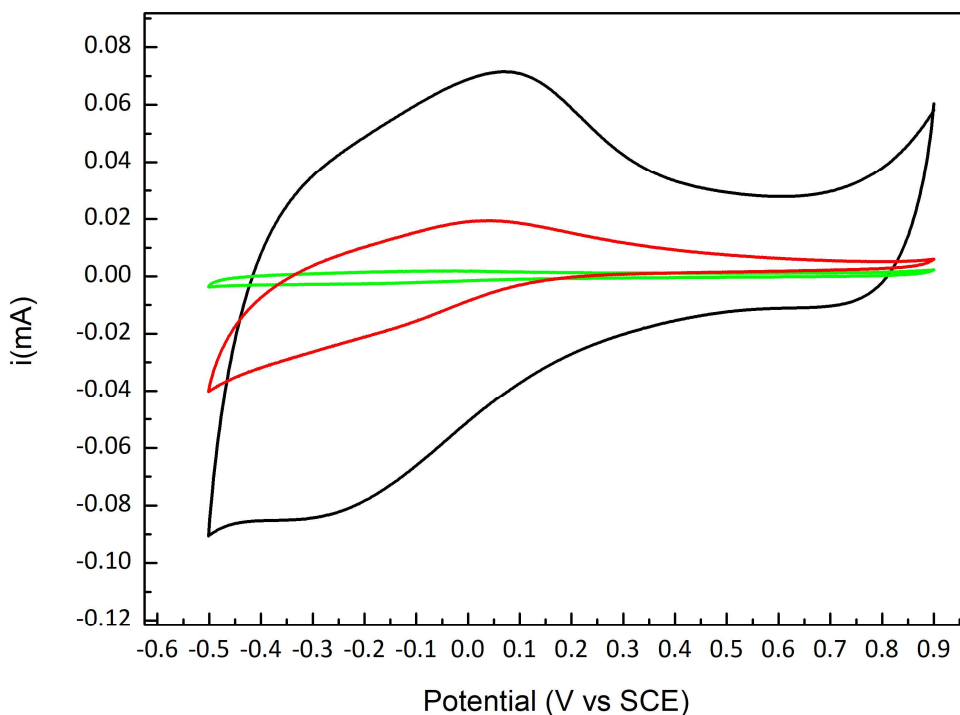


**Figure 1:** CVs obtained on GCE modified with GA-20 (black line), GA-40 (redline) and GA-65 (green line) in 0.10 M PBS buffer solution pH 7 under  $N_2$  between -0.50 V and 0.90 V. Scan rate:  $0.05 \text{ V s}^{-1}$ .

In order to determine the electrocatalytic response of the materials towards  $H_2O_2$ , CVs in the absence and presence of a 5 mM concentration of  $H_2O_2$  were compared in  $N_2$ -saturated buffer solutions 0.1 M of PBS at pH 7. All three samples show an increase in cathodic current in presence of  $H_2O_2$  with an onset potential of -0.15 V indicating the activity of the materials towards its reduction (Figure 2). As expected though, the current response decreases dramatically going from GA-20, to GA-40, to GA-65, with values at -0.4 V of respectively -0.12, -0.04 and -0.01 mA.

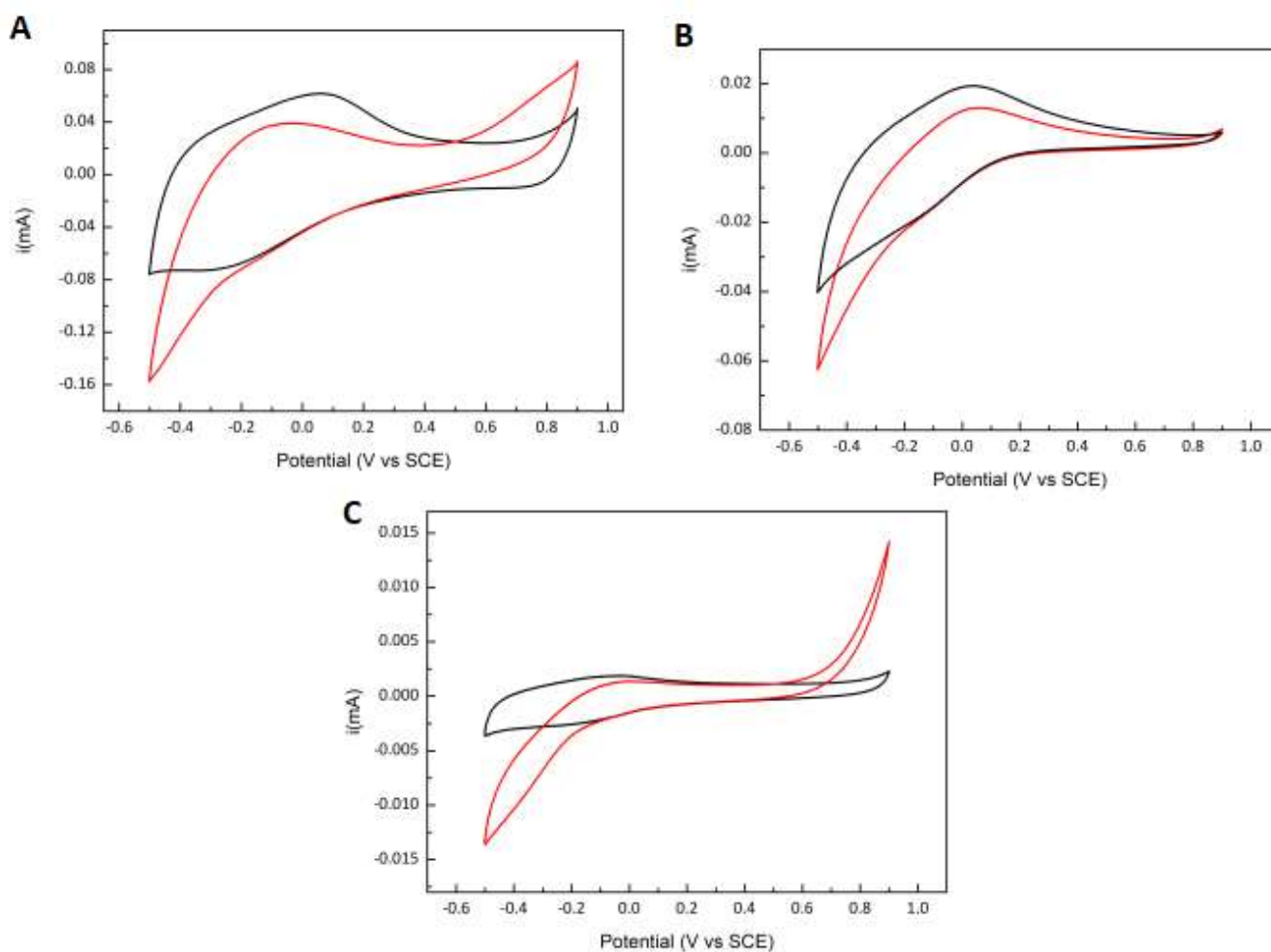


**Figure 2:** CVs at GCE modified with GA-20 (A), GA-40 (B) and GA-65 (C) in 0.10 M PBS buffer solution without (black line) and with (red line) 5mM  $\text{H}_2\text{O}_2$ . Scan rate:  $0.05 \text{ V s}^{-1}$ .

Again, this result is hypothesized to be related to the enhanced conductivity of GA-20. As already mentioned, graphene oxide is a widely employed functionalized graphene material, but the harsh conditions required to obtain it often disrupt the graphene sheets generating a high number of defects, that while might constitute an interesting feature for other type of catalysis, can result detrimental in the framework of electroensing applications by lowering the conductivity properties of the material. As a comparison, we prepared graphene oxide and tested its electrocatalytic response to hydrogen peroxide in the same way as we proceeded for the other materials. The cyclic voltammeteries in absence and presence of  $\text{H}_2\text{O}_2$  are reported in Figure 3.

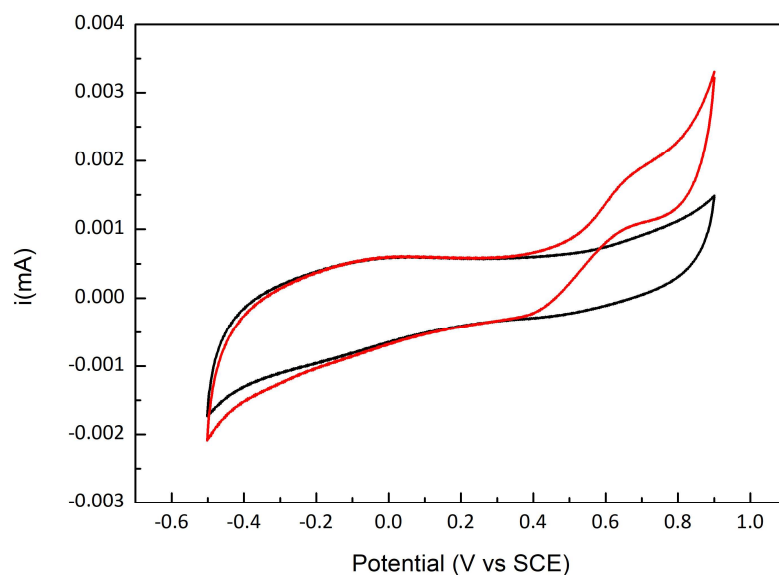


**Figure 3:** CVs at GCE modified with Graphene oxide in 0.10 M PBS buffer solution without (black line) and with (red line) 5 mM  $\text{H}_2\text{O}_2$ . Scan rate:  $0.05 \text{ V s}^{-1}$ .

As expected, the capacitive current is noticeably lower, and although an increase in cathodic current in presence of hydrogen peroxide is visible, it is very low even with respect to the worst performing GA sample. To investigate with increased depth the electrochemical properties of the GA modified electrodes, EIS was employed. In this context, EIS characterization has been conducted in a three-electrode configuration with an optimized Nafion containing thin-film catalyst. The experiments were carried out in a solution 25 mmol of  $\text{H}_2\text{O}_2$  in 0.1 M PBS pH 7 at -0.40 V using a RDE modified with GA-20 and GA-40. The resulting Nyquist plots are reported in Figure 4. Note that it was not possible to perform the tests on the GA-65 sample due to its instability when drop-cast. In this case, adding more Nafion to increase its adherence to the supporting electrode would have compromised the result, since it has been proven that the amount of Nafion in the ink has major effects on the impedance of the system.

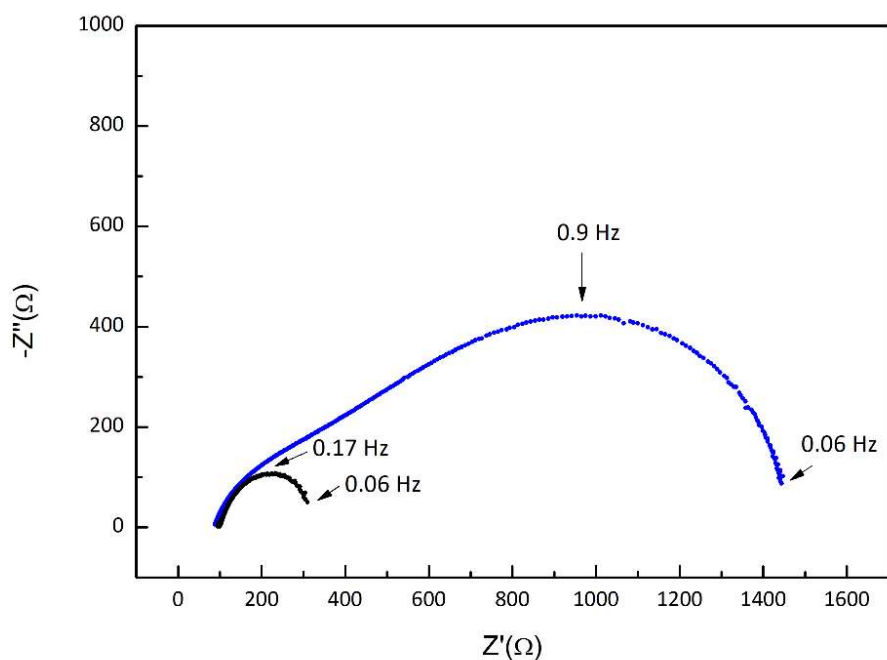
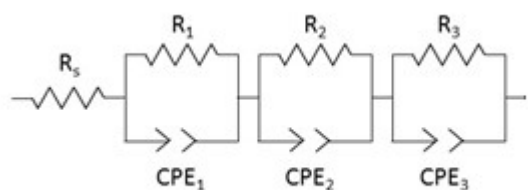


**Figure 4:** Nyquist plots obtained for GA-20 (black line) and GA-40 (blue line)

The equivalent circuit (EQ) used to fit both the electrodes impedance response is reported in Table 2, and it consists in three (R, CPE) elements along with the series resistance  $R_s$ , associated to the solution resistance. The next element ( $R_1$ , CPE) describes the charge transfer resistance in parallel with the double layer capacitance, while the following two elements ( $R_2$ , CPE and  $R_3$ , CPE) are correlated with the diffusion processes. The values obtained through the fitting are reported in Table 2. As far as the charge transfer resistance is concerned, the value associated to the GA-20 modified electrode ( $8,34 \Omega \text{ cm}^2$ ) resulted much lower with respect to the value obtained for the GA-40 modified one ( $25,82 \Omega \text{ cm}^2$ ). This result is in good agreement with the higher current density generated by the former.

**Table 2:** Summary of equivalent resistance data ( $\Omega \text{ cm}^2$ ) obtained from the EQ reported in the scheme below. EIS experimental conditions: Ar- saturated PBS 0.1M (pH = 7) electrolyte with  $\text{H}_2\text{O}_2$  25 mmol at -0.4 V vs SCE.

Sample	$R_s$	$R_1$	$R_2$	$R_3$
GO-20	18.74	8.34	19.14	13.33
GO-40	16.904	25.82	195.15	54.01



The analytical performance of the GA-based materials was evaluated by chronoamperometry, collecting the current-time profile obtained at  $-0.40$  V for successive additions of  $20 \mu\text{L}$  of a  $50 \text{ mM}$   $\text{H}_2\text{O}_2$  solution. In Figure 4A a typical amperometric plot for GA-20 is reported as an example. The response for the three materials were compared and the calibration plots obtained are reported in Figure 4B.

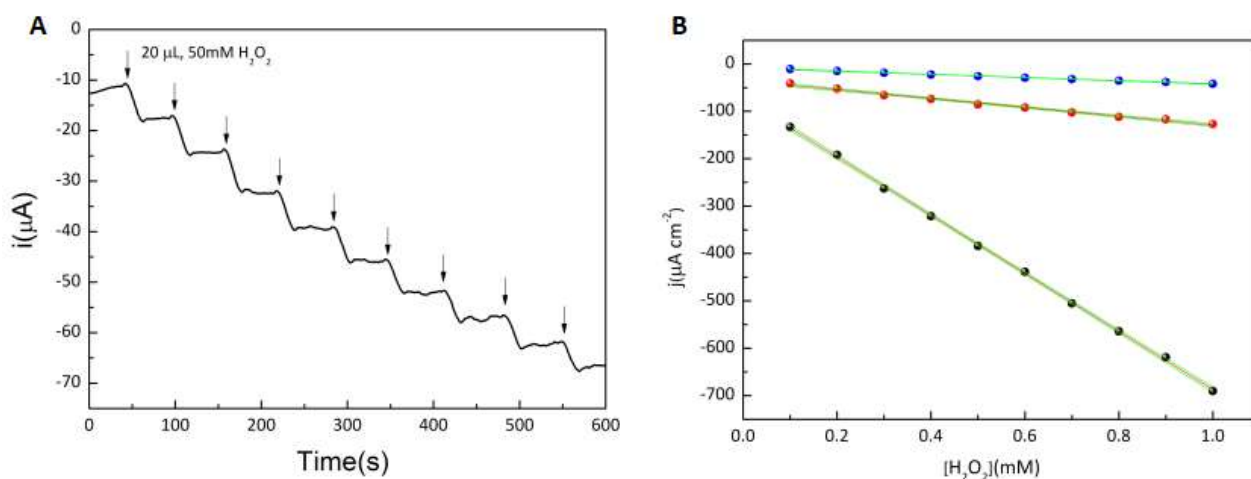


**Figure 4:** A) Typical amperometric plot for additions of  $50 \text{ mM}$   $\text{H}_2\text{O}_2$  solution using GA-20/GCE. Arrows indicate the addition. B) Calibration plots obtained from the amperometric response presented in A with GA-20 (●) GA-40 (●) and GA-65 (●). (—) is the linear fit to the data and (—) indicate the 95% confidence bands.

The calibration plots obtained present a linear relationship between the current density and the  $\text{H}_2\text{O}_2$  concentration in the range investigated for all the samples. The experiment has been repeated using the same working electrode multiple times and an average sensitivity for each material has been calculated and reported in Table 3.

**Table 3:** Sensitivity calculated for GA-20, GA-40 and GA-65

Sample	Sensitivity ( $\mu\text{A cm}^{-2} \text{ mM}^{-1}$ )
GA-20	$525 \pm 105$
GA-40	$94 \pm 25$
GA-65	$40 \pm 9$

As expected GA-20 presents the highest sensitivity, more than one order of magnitude with respect to GA-65. This result has been rationalized in terms of better quality of the graphene sheets obtained by treating the sample more mildly, which gives rise to a material with excellent conductivity properties as suggested by impedance spectroscopy measurements. The linear range of the electrosensor obtained was also evaluated by performing the same experiments in various concentration windows. The sensor is able to detect  $\text{H}_2\text{O}_2$  with the reported sensitivity between 20 to 2000  $\mu\text{mol}$ , making it a good candidate for different kind of applications. Since  $\text{H}_2\text{O}_2$  can degrade and its degradation products, such as oxygen radicals, can interfere with the performance of the catalyst, the stability of the material has been evaluated by checking the analytical performance of the same working electrode with amperometric experiments at  $-0.40\text{ V}$  for 7 consecutive days. The sample shows excellent stability since no drop in average sensitivity has been noticed. This data makes acid graphene very promising for  $\text{H}_2\text{O}_2$  real sensor development. The selectivity of the GA-20 containing sensor was evaluated by testing the response to the interfering presence of easily oxidizable compounds usually present in commercial samples such as ascorbic acid, glucose and paracetamol as it is a crucial parameter to assess the reliability of a sensor.<sup>49</sup> Figure 5 reports the amperometric recordings at  $-0.40\text{ V}$  obtained after addition of  $\text{H}_2\text{O}_2$  in order to reach a final concentration of  $2.00 \times 10^{-4}\text{ M}$ , followed by the same additions of ascorbic acid, glucose and paracetamol. While there is a definite sudden drop of current upon addition of  $\text{H}_2\text{O}_2$ , there is no obvious current response observed with the addition of these interfering substances, indicating high selectivity towards the target molecule.

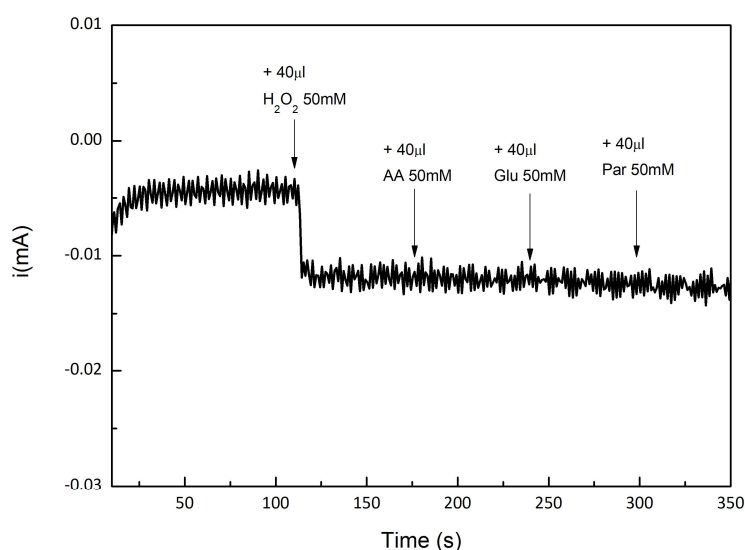


**Figure 5:** Current-time profile at GA-20/GCE for one addition of  $\text{H}_2\text{O}_2$  in order to reach a final concentration of  $0.2\text{ mM}$ , followed by the same additions of ascorbic acid (AA), glucose (Glu) and paracetamol (Par).

Finally, the reliability of the sensor was validated in a real sample, in this case by adding commercial milk to the electrolyte solution. Hydrogen peroxide is widely employed in dairy manufacturing industry because it inhibits microbial proliferation and milk spoilage, and concentration levels of  $H_2O_2$  in milk must be carefully controlled for safety reasons. However, milk is a complex mixture of different compounds that may interfere with the electrosensor's functioning. To investigate its behavior in this complex matrix, 10  $\mu$ L of Italian UHT milk (3.5% fat content) was diluted in 10 ml of 0.1 M PBS buffer. The same amperometric tests employed to verify the analytical performance of the sensor were performed in presence and absence of milk and the recovery percentage was calculated. The recovery percentage of a sensor corresponds to the percent ratio between the response obtained from an amount of analyte in a matrix and the response obtained for the same concentration of analyte in the pure electrolyte. For GA-20 we calculated a recovery percentage of 102% in the milk containing solution. This result demonstrates that the selectivity and reliability of the material as a sensor allows its application also in commercial products bearing complex matrices.

#### **4.4 Conclusions**

The reported results demonstrated the superior performance achieved by functionalizing graphene in a controlled way. The high quality of the sample allowed to obtain a metal-free non-enzymatic sensor which is sensitive to and selective for  $H_2O_2$  and can compete with similar systems reported in literature. The sensitivity towards  $H_2O_2$  detection obtained for GA-20 was ten times higher than the one corresponding to GA-65 suggesting that the fine tuning and milder treatment during the synthetic protocol deeply affects the conductivity properties of the material. Moreover, the obtained material exhibits high stability and reproducibility. The test carried out in presence of interfering compounds and in real samples such as milk confirmed its high selectivity, and the good tolerance towards matrix effects. In the light of the obtained results, and the already reported biocompatibility of the material<sup>24</sup> it is possible to consider its employment for the development of a novel class of commercial sensors for  $H_2O_2$  detection.

## 4.5 References

- (1) Hu, A. L.; Liu, Y. H.; Deng, H. H.; Hong, G. L.; Liu, A. L.; Lin, X. H.; Xia, X. H.; Chen, W. Fluorescent Hydrogen Peroxide Sensor Based on Cupric Oxide Nanoparticles and Its Application for Glucose and L-Lactate Detection. *Biosens. Bioelectron.* **2014**, *61*, 374–378.
- (2) Khorami, H. A.; Botero-Cadavid, J. F.; Wild, P.; Djilali, N. Spectroscopic Detection of Hydrogen Peroxide with an Optical Fiber Probe Using Chemically Deposited Prussian Blue. *Electrochim. Acta* **2014**, *115*, 416–424.
- (3) Tsaplev, Y. B. Chemiluminescence Determination of Hydrogen Peroxide. *J. Anal. Chem.* **2012**, *67* (6), 506–514.
- (4) Ujjain, S. K.; Das, A.; Srivastava, G.; Ahuja, P.; Roy, M.; Arya, A.; Bhargava, K.; Sethy, N.; Singh, S. K.; Sharma, R. K.; et al. Nanoceria Based Electrochemical Sensor for Hydrogen Peroxide Detection. *Biointerphases* **2014**, *9* (3), 031011.
- (5) Cheng, Y.; Feng, B.; Yang, X.; Yang, P.; Ding, Y.; Chen, Y.; Fei, J. Electrochemical Biosensing Platform Based on Carboxymethyl Cellulose Functionalized Reduced Graphene Oxide and Hemoglobin Hybrid Nanocomposite Film. *Sensors Actuators, B Chem.* **2013**, *182*, 288–293.
- (6) Dinesh, B.; Mani, V.; Saraswathi, R.; Chen, S. M. Direct Electrochemistry of Cytochrome c Immobilized on a Graphene Oxide-Carbon Nanotube Composite for Picomolar Detection of Hydrogen Peroxide. *RSC Adv.* **2014**, *4* (54), 28229–28237.
- (7) He, Y.; Zheng, J.; Li, K.; Sheng, Q.; Qiao, N. A Hydrogen Peroxide Biosensor Based on Room Temperature Ionic Liquid Functionalized Graphene Modified Carbon. *Chinese J. Chem.* **2010**, *28*, 2507–2512.
- (8) Zuo, X.; He, S.; Li, D.; Peng, C.; Huang, Q.; Song, S.; Fan, C. Graphene Oxide-Facilitated Electron Transfer of Metalloproteins at Electrode Surfaces. *Langmuir* **2010**, *26* (3), 1936–1939.
- (9) Breslow, R. Biomimetic Chemistry and Artificial Enzymes: Catalysis by Design. *Acc. Chem. Res.* **1995**, *28* (3), 146–153.
- (10) Chen, W.; Cai, S.; Ren, Q.-Q.; Wen, W.; Zhao, Y.-D. Recent Advances in Electrochemical Sensing for Hydrogen Peroxide: A Review. *Analyst* **2012**, *137* (1), 49–58.
- (11) Day, B. J. Catalase and Glutathione Peroxidase Mimics. *Biochem. Pharmacol.* **2009**, *77* (3), 285–296.
- (12) Triller, M. U.; Hsieh, W. Y.; Pecoraro, V. L.; Rompel, A.; Krebs, B. Preparation of Highly

Efficient Manganese Catalase Mimics. *Inorg. Chem.* **2002**, *41* (21), 5544–5554.

- (13) Zhou, M.; Zhai, Y.; Dong, S. Electrochemical Sensing and Biosensing Platform Based on Chemically Reduced Graphene Oxide. *Anal. Chem.* **2009**, *81* (4), 5603–5613.
- (14) Woo, S.; Kim, Y. R.; Chung, T. D.; Piao, Y.; Kim, H. Synthesis of a Graphene-Carbon Nanotube Composite and Its Electrochemical Sensing of Hydrogen Peroxide. *Electrochim. Acta* **2012**, *59*, 509–514.
- (15) Zor, E.; Saglam, M. E.; Akin, I.; Saf, A. O.; Bingol, H.; Ersoz, M. Green Synthesis of Reduced Graphene Oxide/Nanopolypyrrole Composite: Characterization and H<sub>2</sub>O<sub>2</sub> Determination in Urine. *RSC Adv.* **2014**, *4* (24), 12457–12466.
- (16) Luo, J.; Chen, Y.; Ma, Q.; Liu, R.; Liu, X. Layer-by-Layer Assembled Ionic-Liquid Functionalized Graphene-Polyaniline Nanocomposite with Enhanced Electrochemical Sensing Properties. *J. Mater. Chem. C* **2014**, *2* (24), 4818–4827.
- (17) Wang, Q.; Li, M.; Szunerits, S.; Boukherroub, R. Environmentally Friendly Reduction of Graphene Oxide Using Tyrosine for Nonenzymatic Amperometric H<sub>2</sub>O<sub>2</sub> Detection. *Electroanalysis* **2014**, *26* (1), 156–163.
- (18) Nguyen, V. H.; Tran, T. H.; Shim, J. J. Glassy Carbon Electrode Modified with a Graphene Oxide/Poly(o-Phenylenediamine) Composite for the Chemical Detection of Hydrogen Peroxide. *Mater. Sci. Eng. C* **2014**, *44*, 144–150.
- (19) Yeh, M. H.; Li, Y. S.; Chen, G. L.; Lin, L. Y.; Li, T. J.; Chuang, H. M.; Hsieh, C. Y.; Lo, S. C.; Chiang, W. H.; Ho, K. C. Facile Synthesis of Boron-Doped Graphene Nanosheets with Hierarchical Microstructure at Atmosphere Pressure for Metal-Free Electrochemical Detection of Hydrogen Peroxide. *Electrochim. Acta* **2015**, *172*, 52–60.
- (20) Yang, G.-H.; Zhou, Y.; Wu, J.; Cao, J.-T.; Li, L.-L.; Liu, H.-Y.; Zhu, J.-J. Microwave-Assisted Synthesis of Nitrogen and Boron Co-Doped Graphene and Its Application for Enhanced Electrochemical Detection of Hydrogen Peroxide. *RSC Adv.* **2013**, *3* (44), 22597–22604.
- (21) Liao, L.; Peng, H.; Liu, Z. Chemistry Makes Graphene beyond Graphene. *J. Am. Chem. Soc.* **2014**, *136* (35), 12194–12200.
- (22) Park, J.; Yan, M. Covalent Functionalization of Graphene with Reactive Intermediates. *Acc. Chem. Res.* **2013**, *46* (1), 181–189.
- (23) Eng, A. Y. S.; Chua, C. K.; Pumera, M. Refinements to the Structure of Graphite Oxide: Absolute Quantification of Functional Groups via Selective Labelling. *Nanoscale* **2015**, *7* (47), 20256–20266.

- (24) Bakandritsos, A.; Pykal, M.; Boński, P.; Jakubec, P.; Chronopoulos, D. D.; Poláková, K.; Georgakilas, V.; Čépe, K.; Tomanec, O.; Ranc, V.; et al. Cyanographene and Graphene Acid: Emerging Derivatives Enabling High-Yield and Selective Functionalization of Graphene. *ACS Nano* **2017**, *11* (3), 2982–2991.
- (25) Karlický, F.; Kumara Ramanatha Datta, K.; Otyepka, M.; Zbořil, R. Halogenated Graphenes: Rapidly Growing Family of Graphene Derivatives. *ACS Nano* **2013**, *7* (8), 6434–6464.
- (26) Urbanová, V.; Holá, K.; Bourlinos, A. B.; Čépe, K.; Ambrosi, A.; Loo, A. H.; Pumera, M.; Karlický, F.; Otyepka, M.; Zbořil, R. Thiofluorographene-Hydrophilic Graphene Derivative with Semiconducting and Genosensing Properties. *Adv. Mater.* **2015**, *27* (14), 2305–2310.
- (27) Lazar, P.; Chua, C. K.; Holá, K.; Zbořil, R.; Otyepka, M.; Pumera, M. Dichlorocarbene-Functionalized Fluorographene: Synthesis and Reaction Mechanism. *Small* **2015**, *11* (31), 3790–3796.
- (28) Dubecký, M.; Otyepková, E.; Lazar, P.; Karlický, F.; Petr, M.; Čépe, K.; Banáš, P.; Zbořil, R.; Otyepka, M. Reactivity of Fluorographene: A Facile Way toward Graphene Derivatives. *J. Phys. Chem. Lett.* **2015**, *6* (8), 1430–1434.
- (29) Chronopoulos, D. D.; Bakandritsos, A.; Lazar, P.; Pykal, M.; Čépe, K.; Zbořil, R.; Otyepka, M. High-Yield Alkylation and Arylation of Graphene via Grignard Reaction with Fluorographene. *Chem. Mater.* **2017**, *29* (3), 926–930.
- (30) Whitener, K. E.; Stine, R.; Robinson, J. T.; Sheehan, P. E. Graphene as Electrophile: Reactions of Graphene Fluoride. *J. Phys. Chem. C* **2015**, *119* (19), 10507–10512.
- (31) Lomeda, J. R.; Doyle, C. D.; Kosynkin, D. V.; Hwang, W. F.; Tour, J. M. Diazonium Functionalization of Surfactant-Wrapped Chemically Converted Graphene Sheets. *J. Am. Chem. Soc.* **2008**, *130* (48), 16201–16206.
- (32) Zhong, X.; Jin, J.; Li, S.; Niu, Z.; Hu, W.; Li, R.; Ma, J. Aryne Cycloaddition: Highly Efficient Chemical Modification of Graphene. *Chem. Commun.* **2010**, *46* (39), 7340–7342.
- (33) Quintana, M.; Spyrou, K.; Grzelczak, M.; Browne, W. R.; Rudolf, P.; Prato, M. Functionalization of Graphene via 1,3-Dipolar Cycloaddition. *ACS Nano* **2010**, *4* (6), 3527–3533.
- (34) Strom, T. A.; Dillon, E. P.; Hamilton, C. E.; Barron, A. R. Nitrene Addition to Exfoliated Graphene: A One-Step Route to Highly Functionalized Graphene. *Chem. Commun.* **2010**, *46* (23), 4097–4099.
- (35) Economopoulos, S. P.; Rotas, G.; Miyata, Y.; Shinohara, H.; Tagmatarchis, N. Exfoliation and

Chemical Modification Using Microwave Irradiation Affording Highly Functionalized Graphene. *ACS Nano* **2010**, *4* (12), 7499–7507.

- (36) Englert, J. M.; Dotzer, C.; Yang, G.; Schmid, M.; Papp, C.; Spiecker, E.; Hauke, F.; Hirsch, A.; Gottfried, J. M.; Steinru, H. Covalent Bulk Functionalization of Graphene. *Nat. Chem.* **2011**, *3* (April), 279–286.
- (37) Bian, S.; Scott, A. M.; Cao, Y.; Liang, Y.; Osuna, S.; Houk, K. N.; Braunschweig, A. B. Covalently Patterned Graphene Surfaces by a Force-Accelerated Diels-Alder Reaction. *J. Am. Chem. Soc.* **2013**, *135*, 9240–9243.
- (38) Zhu, Y.; Higginbotham, A. L.; Tour, J. M. Covalent Functionalization of Surfactant-Wrapped Graphene Nanoribbons. *Chem. Mater.* **2009**, *21* (9), 5284–5291.
- (39) Dubey, G.; Urcuyo, R.; Abb, S.; Rinke, G.; Burghard, M.; Rauschenbach, S.; Kern, K. Chemical Modification of Graphene via Hyperthermal Molecular Reaction. *J. Am. Chem. Soc.* **2014**, *136*, 13482–13485.
- (40) Criado, A.; Melchionna, M.; Marchesan, S.; Prato, M. The Covalent Functionalization of Graphene on Substrates. *Angew. Chemie - Int. Ed.* **2015**, *54* (37), 10734–10750.
- (41) Englert, J. M.; Vecera, P.; Knirsch, K. C.; Scha, R. A.; Hauke, F.; Hirsch, A. Scanning-Raman-Microscopy for the Statistical Analysis of Covalently Functionalized Graphene. *ACS Nano* **2013**, *7* (6), 5472–5482.
- (42) Szabó, T.; Tombácz, E.; Illés, E.; Dékány, I. Enhanced Acidity and pH-Dependent Surface Charge Characterization of Successively Oxidized Graphite Oxides. *Carbon N. Y.* **2006**, *44* (3), 537–545.
- (43) Francis, P.; Majumder, C.; Ghaisas, S. V. The Nonchalant Magnetic Ordering of Vacancies in Graphene. *Carbon N. Y.* **2015**, *91*, 358–369.
- (44) Tuček, J.; Holá, K.; Bourlinos, A. B.; Błoński, P.; Bakandritsos, A.; Ugolotti, J.; Dubecký, M.; Karlický, F.; Ranc, V.; Čépe, K.; et al. Room Temperature Organic Magnets Derived from  $Sp^3$  functionalized Graphene. *Nat. Commun.* **2017**, *8*.
- (45) Pykal, M.; Jurečka, P.; Karlický, F.; Otyepka, M. Modelling of Graphene Functionalization. *Phys. Chem. Chem. Phys.* **2016**, *18* (9), 6351–6372.
- (46) Cocchi, C.; Prezzi, D.; Ruini, A.; Caldas, M. J.; Molinari, E. Electronics and Optics of Graphene Nanoflakes: Edge Functionalization and Structural Distortions. *J. Phys. Chem. C* **2012**, *116* (33), 17328–17335.
- (47) Sheka, E. F.; Popova, N. A. Molecular Theory of Graphene Oxide. *Phys. Chem. Chem. Phys.*

**2013**, 15 (32), 13304–13322.

- (48) Yuan, S.; Rösner, M.; Schulz, A.; Wehling, T. O.; Katsnelson, M. I. Electronic Structures and Optical Properties of Partially and Fully Fluorinated Graphene. *Phys. Rev. Lett.* **2015**, 114 (4), 1–5.
- (49) Bracamonte, M. V.; Melchionna, M.; Giuliani, A.; Nasi, L.; Tavagnacco, C.; Prato, M.; Fornasiero, P. H<sub>2</sub>O<sub>2</sub> sensing Enhancement by Mutual Integration of Single Walled Carbon Nanohorns with Metal Oxide Catalysts: The CeO<sub>2</sub> case. *Sensors Actuators, B Chem.* **2017**, 239, 923–932.

## Chapter 5

### Conclusions

This research project has tackled the synthesis and electrocatalytic application of several nanostructured materials, sharing the common feature of bearing carbon (with various morphologies) as the essential component. In particular, the investigated applicative fields have included fuel cells, H<sub>2</sub>O<sub>2</sub> sustainable synthesis and H<sub>2</sub>O<sub>2</sub> sensing. The designed composites were synthesized using strategic synthetic protocols in order to obtain specific structural and chemical features, enabling the enhancement of their catalytic performances. The project relied on the use of a combination of characterization techniques such as TEM, HR-TEM, EDX, STEM, XRD, TGA, XPS, N<sub>2</sub>-physisorption and Raman spectroscopy in order to define the relevant properties of the proposed catalysts. On the other hand, the electrochemical behavior of all materials was unraveled through systematic electrochemical experiments in relation to the specific catalytic process under investigation. In more details, the work objectives and outcomes were the following for the three catalytic topics:

1) **Development of catalyst for fuel cells.** Fuel cells working in alkaline media have attracted great interest in the last decades due to the possibility to equip them with metals less precious than platinum, lowering considerably the fabrication cost. Although the substitution with non-precious catalysts has already been successful for the cathodic side of this type of cells, there is still a need for the development of anodic electrocatalysts, where the oxidation of the fuel takes place. The catalytic system proposed in the first chapter of this thesis consists in a Pd/CeO<sub>2</sub>/C hybrid obtained through a synthetic procedure that allows a tight contact between the three phases, especially CeO<sub>2</sub> and Pd. This feature has been evidenced by performing a series of characterizations including HR-TEM, EDX and XRD. The catalytic system has been applied first to the hydrogen oxidation reaction (HOR) in alkaline media and provided high power density in full anion exchange membrane fuel cells (AEM-FC). I endeavored to understand the origin of this activity enhancement and associated it to the weakened interaction with adsorbed H guaranteed by certain Pd-CeO<sub>2</sub> interactions. This hypothesis was corroborated by XAS experiments and DFT calculations carried out by collaborators of the project. For this reason, *vis-à-vis* the H<sub>2</sub> spillover ability of cerium oxide, that allows more H<sub>2</sub> to be adsorbed per Pd site, the HOR activity was considerably enhanced, producing a peak power current of 1.4 W cm<sup>-2</sup> in AEM-FC testing, exceeding that obtained with a similar system where the phases were not in the same tight contact. The same material has been

employed as electrocatalyst for the oxidation of biomass derived polyalcohols in the framework of developing polyalcohol-fed direct alcohol fuel cells (DAFCs). Again, the enhanced catalytic performance has been associated to the promoting effect of CeO<sub>2</sub>, in this case in terms of formation of Pd-OH<sub>ads</sub> species, which are active in the oxidation of polyalcohols, at lower overpotentials. The full fuel cells equipped with the proposed material as anodic electrocatalyst displayed higher peak power density compared with the ones equipped with a carbon-supported palladium catalyst with the same metal loading, upon feeding with either ethylene glycol or with 1,2-propanediol. The main oxidation products obtained for each cell were glycolate and lactate, which are molecules of pronounced industrial relevance. This feature allows to combine energy production with selective generation of added-value chemicals, giving new perspectives to the application of these kind of fuel cells.

2) **ORR for the synthesis of H<sub>2</sub>O<sub>2</sub>.** ORR is a multi-electron reduction reaction, that can lead to the formation of two different products: H<sub>2</sub>O<sub>2</sub> or H<sub>2</sub>O. The importance of H<sub>2</sub>O<sub>2</sub> is stated by its ubiquitous presence in daily used products, wide employment in clinical applications as well as in industry. The selectivity of the process has been proven to be related to many different factors, including the pH of the solution. The designed material was prepared by pyrolysis of an appropriate precursors under Ar atmosphere driven by Co centers, and resulted in the formation of Co nanoparticles embedded within N-doped carbon shells. HR-TEM, Raman and XPS confirmed the deep encapsulation and the metallic nature of the nanoparticles. At low pH and highly positive potentials (0.5 V vs RHE), the material achieved an almost 100% selectivity towards H<sub>2</sub>O<sub>2</sub> generation, and this feature has been correlated, by comparing it with several comparative samples, to the pH itself, the relative N type distribution and the textural properties of the material. The role of the metal was also investigated and determined to be crucial for directing the final N species distribution. It has also been hypothesized a possible electronic interaction with the carbon phase leading to different activity and selectivity towards ORR. In the framework of developing new strategies for sustainable chemicals production, the simple synthetic protocol and absence of precious metals make this material interesting for possible application in electrocatalytic generation of hydrogen peroxide.

3) **Sensors for H<sub>2</sub>O<sub>2</sub>.** As for the synthesis, the detection of H<sub>2</sub>O<sub>2</sub> is very important, given the ubiquity of this molecule in industrial products and the regulated maximum levels. For this reason, there is a need to be able to efficiently monitor its concentration in a cheap, fast and easy way. The material proposed as metal-free non-enzymatic electrosensor, consisting in a -COOH

functionalized graphene, has proven to be sensitive to and selective for H<sub>2</sub>O<sub>2</sub> and able to compete with similar benchmark catalysts reported in literature. The high quality of the sample obtained with the correct tuning of the synthetic protocol demonstrated higher sensitivity than the comparative materials, in particular, ten times higher than the catalyst with lowest performance. The consecutive measure over 7 days allowed us to positively assess its robustness, while its selectivity towards hydrogen peroxide was tested against several common interfering molecules such as ascorbic acid, glucose and paracetamol, and was proven solid since their presence did not affect the material's sensing ability. The acid graphene-based sensor was also successfully employed for detecting H<sub>2</sub>O<sub>2</sub> in a milk containing solution, simulating its interaction with a real sample, confirming its high selectivity towards the target molecule even in complex matrices. In conclusion, this project framework can be seen as a way to underline the importance of tailoring the properties of electrocatalytic materials through a careful evaluation of synthetic pathways, and how these properties are crucial in determining their electronic behavior. In particular, it demonstrates how the employment of different kinds of nanostructured carbon, which feature different chemical and textural properties, can greatly affect the catalytic performance of the material in terms of both activity and selectivity towards the target reaction. Hopefully, this research work can be used as a platform for the development of new generation electrocatalysts to be employed in energy related and sensing processes.

## **Appendix A: Review of the experimental methods used**

### **A1. Electrochemical techniques.**

Electrochemical techniques such as Cyclic Voltammetry (CV), Linear sweep Voltammetry (LSV), Chrono-amperometry (CA) and Impedance Electrochemical Spectroscopy (EIS) have been widely employed for the characterization and the electrocatalytic testing of the materials reported in this thesis.<sup>1</sup>

#### **A.1.1 WE preparation**

Here the procedure used to assembly the modified GCE electrodes using the materials presented in this thesis are reported. Before the ink drop casting, the glassy carbon electrode (GC) has been mechanically polished using in the sequence 1  $\mu\text{m}$  and 0.3  $\mu\text{m}$  alumina slurry for 1 minute, followed by milliQ water washing.

#### **A.1.2 Set-up of the electrochemical cell used**

The set-up cell used for the experiments was a three-electrode system consisting of: a commercial GC (CH instruments) modified with the prepared electrocatalysts as working electrode (WE), a platinum wire as the counter electrode (CE) and a saturated calomel electrode (SCE) that was separated from the solution by a bridge equipped with a Vycor frit as reference electrode (RE). Each ink was prepared as a 2.5 mg mL<sup>-1</sup> dispersion of the selected catalyst in an ethanol/water mixture 1:1 and 1% of Nafion<sup>®</sup> 117 solution.

#### **A.1.3 Cyclic Voltammetry**

Cyclic Voltammetry (CV) is a potential sweep technique in which the current evolved at the working electrode is collected while scanning the potential using a triangular impulse (Figure 1

left), and studying it using a selected scan rate  $v$ , depending on the designed experiment. The scan rate influences the shape of the current potential profile.

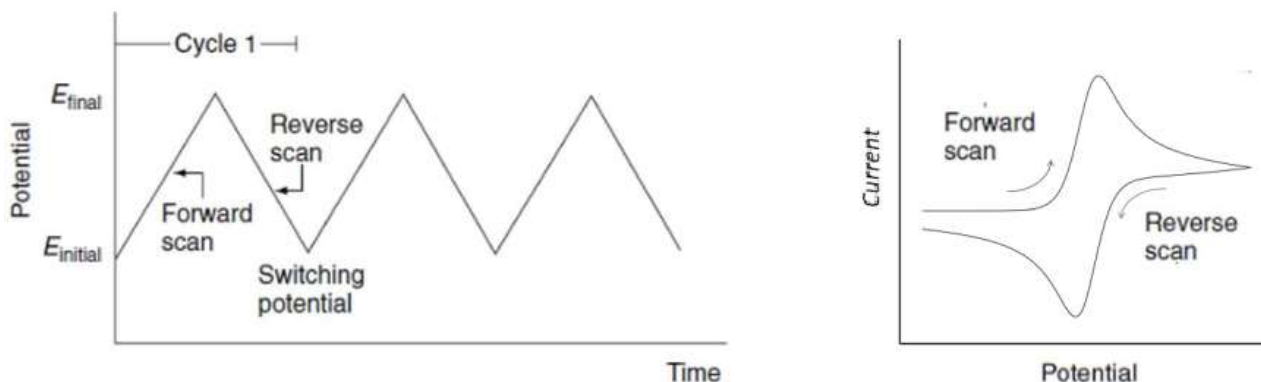


**Figure 1:** CV potential-time profile for 3 cycles (left). CV recorded signal, current-potential profile for one cycle (right).

CV has been employed to characterize the redox behavior of each material presented in this thesis. It is a very powerful technique, as it is non-destructive, fast and sensitive towards low concentration of the ionic species in solution. Through the forward scan (Figure 1), following the oxidation sweep, the current peaks, and then decreases as the potential reaches the value at which the process is limited by the diffusion of the substrate to the electrode surface. The reverse scan can be discussed in the same way. The redox process represented in Figure 1 is that of a reversible system, as the ratio of the anodic and cathodic current peaks is 1.

#### A.1.4 Rotating disk electrode technique (RDE)

Rotating Disk Electrode (RDE) experiments have been employed to investigate the number of electrons involved in the ORR process.

RDE is a hydrodynamic working electrode, which can be rotated at different speeds through an electric motor. When the electrode rotates, a laminar flow of the solution towards the electrode is generated. In this way, a constant flow of fresh solution from the bulk to the electrode surface is assured, and, taking the rotating electrode as reference system, the solution nearby can be considered stagnant, a condition known as hydrodynamic boundary layer. The bulk solution far from the electrode surface remains well-stirred, meanwhile the solution closer to the electrode rotate with it. This way, the flow can reach conditions in which the steady-state current is

dominated by the solution flow rather than diffusion, in contrast with the still and unstirred experiments where the steady-state current is limited by the diffusion of species in solution. LSV is carried out at a very slow scan rate (usually  $5 \text{ mV s}^{-1}$ ) and can be used to observe electrochemical phenomena including the kinetics of a slow electron transfer, adsorption/desorption steps, and electrochemical reaction mechanisms. The Levich equation is the model for the diffusion and solution flow conditions around a RDE. It is named after Veniamin Grigorievich Levich who first developed an RDE as a tool for electrochemical research. Its mathematical formulation is reported below

$$i_L = 0.062nFA(D_o)^{2/3}\nu^{-1/6}C_0\omega^{-1/2}$$

where  $i_L$  is the limiting current observed at the rotating electrode,  $C_0$  is the concentration of the bulk solution,  $n$  is the number of the electrons,  $A$  is the electrode geometric area,  $D_o$  is the diffusion coefficient,  $\nu$  is the viscosity kinematic coefficient,  $F$  is the Faraday constant and  $\omega$  is the rotation speed of the rotating electrode. This equation can describe efficiently a process that is reversible and not complicated by sluggish electron transfer kinetic or chemical reaction coupled to the redox reaction. When the studied reaction is complicated by these factors, the LSVs have no longer the regular sigmoidal shape correctly described by the Levich equation, and the Koutecky-Levich equation needs to be used

$$\frac{1}{i} = \frac{1}{i_k} + \frac{1}{0.062nFA(D_o)^{2/3}\nu^{-1/6}C_0} \omega^{1/2} = \frac{1}{i_k} + \frac{1}{B} \omega^{-1/2}$$

In this equation, together with the other terms already present in the Levich equation, a term related to kinetic current is present,  $i_k$ . This term describes the current observed in absence of mass transport limitation.  $B$  is normally referred as the Levich constant.

#### **A.1.4.1 Experimental procedure for the determination of the number of electrons involved in ORR**

The Koutecky-Levich plots can be obtained by plotting the inverse of the measured current density  $j_m$  at fixed potentials, in function of the square root of the rotation rate  $\omega^{-1/2}$ . The K-L plots can be

used to calculate the number of electrons involved in the redox process. In Figure 2 (left) is reported a graph with LSV collected at different  $\omega$ , and in Figure 2 (right) the relative K-L plot.

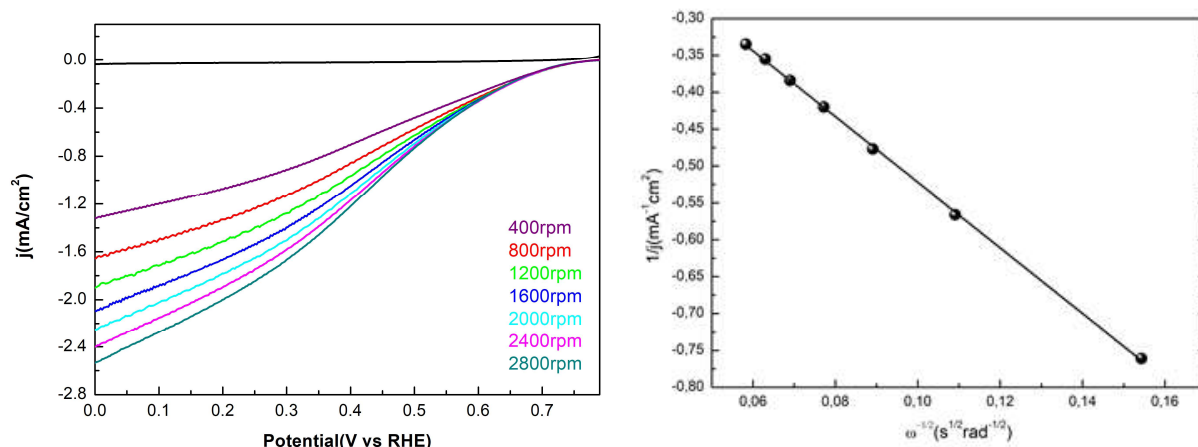


**Figure 2:** (Left) LSVs collected at different  $\omega$ , the black curve is the background LSV collected in absence of the reactive species and (Right) the relative K-L plot.

The slope of the curve obtained by fitting the K-L plot corresponds to  $1/B$ , and from this value, the number of electrons involved in the slow step of the redox process at a determined potential can be determined. For the rotating disk electrode (RDE) tests a catalyst-coated glassy-carbon rotating disk electrode (Autolab RDE, Metrohm) with surface area of 0.196 cm<sup>2</sup> modified with 10  $\mu$ L of catalyst ink was used as working electrode. Linear sweep voltammeteries (LSV) were collected at different rotation speeds (from 400rpm to 2800rpm) and scan rate of 5 mV s<sup>-1</sup>.

### A.1.5 Chronoamperometry

Chronoamperometry (CA) is an electrochemical technique where a potential value is fixed and the current generated is followed through time. CA has been employed to determine the efficiency and stability of ORR electrocatalysts investigated in this thesis. This experiment allows to compare the quantity of current produced in a determined amount of time with the moles of product generated, calculating the yield of the redox reaction involved. The yield, called faradaic efficiency (FE %) is described by the equation below as the ratio between the charge employed to form the selected product ( $Q_p$ ) and the total charge that flowed through the cell ( $Q_{tot}$ )

$$FE\% = \frac{Q_p}{Q_{tot}}$$

Where:

$$Q_p = n \times F \times mol_p$$

$n$  is the number of electrons involved in the product formation,  $F$  is the faraday constant (96485 C mol<sup>-1</sup>) and  $mol_p$  is the moles of product evolved during the experiment.

$$Q_{tot} = \int_0^t i dt$$

For chronoamperometry experiments, the working electrode was prepared by drop casting of 5 drops of 10  $\mu$ L on each face of a glassy carbon slide (0.5 cm x 1.0 cm). Each ink was prepared as a 2.5 mg ml<sup>-1</sup> dispersion of the selected catalyst in an ethanol/water mixture 1:1 and 1% of Nafion<sup>®</sup> 117 solution. Bulk electrolysis tests were conducted in a 20 mL solution of electrolyte for ca. 2 h for every different potential (0.1, 0.2, 0.3, 0.4, 0.5 V). Permanganometric titration was used to determine the H<sub>2</sub>O<sub>2</sub> obtained immediately after each electrolysis test. Each test was repeated three times at each potential, and the values averaged.

#### **A.1.6 Impedance electrochemical spectroscopy**

Electrochemical Impedance Spectroscopy (EIS) was employed in order to gain a deeper knowledge of the redox behavior of some materials. EIS provides information about the resistive and capacitive properties of materials as response to a perturbation of the system caused by a small alternate current (AC) sinusoidal excitation signal. Collecting the impedance value varying the perturbation frequency, the Nyquist plot and the Bode plot can be obtained. By the fitting of the Nyquist plot the equivalent circuit can be determined, from which resistive and capacitive parameters can be calculated.

##### **A.1.6.1 Basic Knowledges**

The concept of electrical resistance is well known: it is the ability of a circuit element to resist the flow of electrical current. Ohm's law defines resistance as the ratio between voltage,  $E$  and current,  $I$ .

$$R = \frac{V}{I}$$

This law anyway is accurate to describe only a one-element circuit: an ideal resistor. To be able to describe circuits with elements that exhibit a more complex behavior, a more general circuit parameter is needed. Like resistance, impedance is a measure of the ability of a circuit to resist the flow of electrical current, but unlike resistance, it does not follow the classic Ohm law, but a modified one:

$$Z = \frac{V(t)}{I(t)} = \frac{V_0 \cos(\omega t)}{I_0 \cos(\omega t - \phi)} = Z_0 \frac{\cos(\omega t)}{\cos(\omega t - \phi)}$$

where Z is the impedance, t is the time,  $\omega$  is the radial frequency and  $\phi$  is phase shift. Z has a real component and an imaginary component, as the following equation reports:

$$Z = \frac{V}{I} = Z_0 \exp(j\phi) = Z_0 (\cos\phi - j\sin\phi)$$

If the real part is plotted on the X-axis and the imaginary part is plotted on the Y-axis of a chart, the so-called Nyquist plot is obtained.

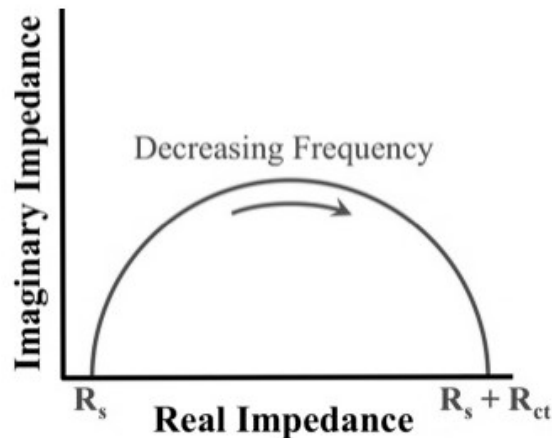


**Figure 3:** Representation of Nyquist plot.

Each point on the Nyquist Plot is the impedance at one frequency: Figure 3 has been annotated to show that low frequency points are on the right side of the plot and higher frequencies are on the left. At each region of frequency, there is one contribution from the electrode's behavior that

prevails. For example, at high frequencies, the diffusion effect is the one most affecting impedance.

#### A.1.6.2 Equivalent circuits

In order to rationalize the different contributions to the impedance profile, the system considered needs to be associated to an electric circuit, called the equivalent circuit. It may be composed of different elements, the most common are: R, the resistive element, C, the capacitive element and L the inductive element. The elements in the model should have a basis in the physical electrochemistry of the system. For example, most models include a resistor that models the cell's solution resistance. This value depends on the ionic concentration of the solution and geometric area of the electrode and can be defined by the following equation:

$$R_s = \rho \frac{l}{A}$$

where  $\rho$  is the solution resistivity,  $l$  is the length carrying a uniform current and  $A$  is the geometric area of the electrode surface. Another element that needs to be represented in the equivalent circuit is the resistance to charge transfer. The resistance to the charge transfer is dependent on the exchange current and the number of the electrons involved, it can be calculated using the equation reported below:

$$R_{CT} = \frac{RT}{nFi_0}$$

where  $R$  is the gas constant,  $T$  is the temperature,  $n$  is the number of the electrons involved,  $F$  is the Faraday constant and  $i_0$  is the current density. The electrical double layer that generates at the interphase between electrode and solution can be described as a capacitor as the charged electrode is separated from the charged ions by an insulating space. Since real capacitors don't behave like ideal ones, an element called CPE (constant phase element) is normally used to refer to this effect. Diffusion can create a different effect called a Warburg impedance. It is calculated as reported below:

$$Z_w = \sigma(\omega)^{-1/2}(1 - j)$$

where  $\sigma$  is the Warburg coefficient and  $\omega$  is the radial frequency.

In Table 1 the most common circuit elements are reported with their current versus potential relationship, and their impedance.

Circuit element	Relationship	Impedance
<b>R</b>	$V = IR$	$Z_R = R$
<b>C</b>	$I = C \frac{dV}{dt}$	$Z_C = \frac{1}{j\omega C} = -\frac{1}{\omega C}$
<b>L</b>	$V = L \frac{dI}{dt}$	$Z_L = j\omega L$

**Table 1:** List of the common circuit elements.

### A1.6.3 Data elaboration

There are three different plots representing EIS data, the Nyquist plot and two Bode plots. As mentioned before, the Nyquist plot shows the relation between the imaginary and the real component of Z. The Bode plots report how either the modulus or the phase of Z varies with frequency.

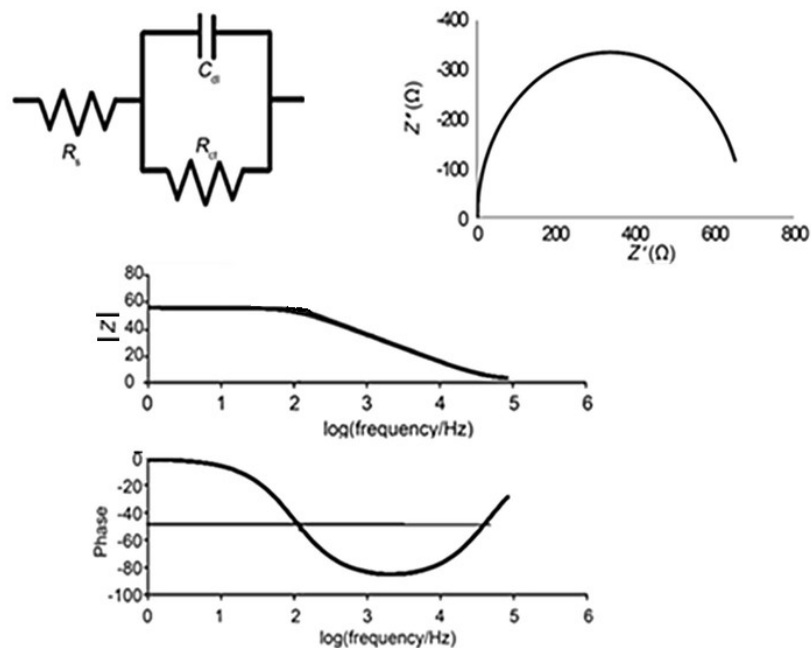


**Figure 4** Representation of the Randles model circuit and the relative Nyquist and Bode plots.

The Randles circuit is the simplest equivalent circuit. Its associated Nyquist and Bode plots are reported in Figure 4. The elements composing the circuit are a resistive one, representing the solution resistance, in series with a constant phase element representing the double layer capacitance, in parallel with another CPE associated to the charge transfer resistance. From the fitting of the plots with the model circuit, the values of capacitance and resistance associated with the specific system can be determined. EIS spectra were recorded in the just described three-electrode thin film rotating disc electrode (TF-RDE) configuration. EIS spectra (single sine measurements) were acquired at various constant potential values, under pure Ar or O<sub>2</sub> atmosphere or in presence of 25mmol H<sub>2</sub>O<sub>2</sub> with a 10 mV amplitude voltage perturbation in the maximum frequency range from 100 kHz to 0.001 Hz, at a rotation speed of 1600 rpm. The resulted plots were fitted by using Z View Software from Scribner Corporation. The ink formulation used to prepare the TF-RDE was optimized in terms of the ionomer loading in order to minimize the equivalent diffusion resistance at high frequency, mainly due to protonic diffusion limitation. 2 mg of catalyst were dispersed in a solution of 300 μL of water, 100 μL of isopropyl alcohol and 5 μL Nafion suspension in alcohol (5%), and sonicated for 30 minutes to get a uniform dispersion of the catalyst (5 mg mL<sup>-1</sup> of catalyst). Two drops of 10 μL of the catalyst ink were drop-cast on the RDE surface and dried in air at 200 rpm in order to obtain a catalyst load on the electrode of ca. 0.1 mg.

#### A.1.7 EASA calculation

The electroactive surface area (EASA) of the Pd-based materials catalyst has been measured using a technique based on the assumption that when the potential reaches 1.4 V vs RHE a monolayer of Pd oxide is generated homogeneously on the surface of palladium. Using the electrode modified with our material as WE, we collected a CV between 0 V and 1.4 V vs RHE in KOH 0.1 M. After that, the peak associated to the reduction of PdO has been integrated and the EASA calculated using the equations below

$$Q = \frac{Area}{\nu}$$

$$EASA = \frac{Q}{420 * 10^{-6}}$$

Where Q is the charge associated to the reduction of a PdO monolayer, and  $\nu$  is the scan rate of the experiment.

## **A.2 Thermogravimetric Analysis**

Thermogravimetric Analysis (TGA) has been used to quantify the amount of metal oxide deposited onto the nanostructured carbon supports or in general the % weight metal load of the reported catalysts. TGA is a thermal analysis technique in which the mass of a sample is measured over time as the temperature changes. It can be used for monitoring different temperature related processes, but in this case, the information acquired is the temperature of decomposition of the carbon phase and the consequent weight loss of the sample. For this purpose, TGA was operated using oxygen flow. The metal in the sample was therefore converted into the correspondent oxide and associated to the residual weight at the end of the experiment. The accuracy of the technique relies on the precision of the power supply in providing the temperature ramp to the furnace, and of the internal balance. The analysis procedure adopted in this thesis is the same for all the samples: an equilibration step followed by the linear temperature ramp. After a 20 minutes equilibration step at 100 °C allows the removal of adsorbed water molecules on the sample, the linear temperature ramp (10 °C min<sup>-1</sup>) starts and data are collected until it reaches 830 °C.

## **A.3 Raman Spectroscopy**

Raman spectroscopy is a powerful tool for carbon nanostructured materials investigation. This technique was employed to characterize most of the materials investigated in this thesis. Raman spectroscopy belongs to the group of non-linear spectroscopic techniques and is based on the inelastic scattering of monochromatic light. This effect, called in fact Raman effect, is correlated to the polarizability of electrons in the molecule. The excitation of a molecule by monochromatic light, usually a laser beam, puts it into a virtual energy state, then the photon is emitted. If the response is elastic, the electron will return to the original energy state through what is called Rayleigh scattering. If it ends up in a different vibrational state, it is behaving inelastically and that is called Raman scattering. There are two types of Raman scattering: it is called Stokes scattering if the ending state is higher in energy than the starting state, if it's the other way, the scattering is called anti-Stokes (Figure 5). The probability to observe a Stokes scattering is higher since most of the molecules at room temperature are in their ground state

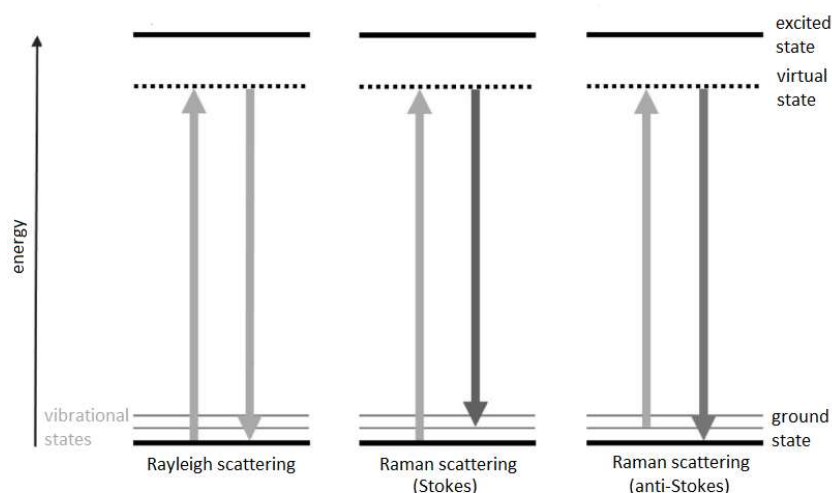


**Figure 5:** Schematic representation of Rayleigh and Raman scattering (Anti-Stokes and Stokes level)

The Raman spectra consists in the plot of the intensity of the Raman shift, defined

$$\Delta\nu = \nu - \nu_m$$

where  $\nu$  is the wavenumber ( $\text{cm}^{-1}$ ) of the incident light, and  $\nu_m$  is the wavenumber ( $\text{cm}^{-1}$ ) of the energy transition between the lowest and first excited vibration energy level. Raman spectroscopy is generally employed to identify molecules and study chemical bonding. Nanostructured carbon has its own characteristic Raman bands, the D and G bands, which allow to gain information on the defects of the carbon nanostructure surface. The D band, occurring at  $1350 \text{ cm}^{-1}$  is associated to the presence of  $\text{sp}^3$  carbon atoms in the carbon nanostructure. It may be originated by a decrease of symmetry due to defects like pentagon rings, typical of CNTs caps and SWCNHs tips or introduced by covalently linked functional groups, presence of carbon nanoparticles or amorphous carbon. The G band, where G indicates graphite, is in general the more intense band, and is related to the conductive properties of the materials. The ratio  $I_D/I_G$  can be used as tool to gain information about the carbon nanostructure functionalization. Raman is also very useful in the characterization of metal oxide nanocrystals, since from the shape and intensity of the Raman band, information on the dimension and crystallinity of the crystals can be obtained.

#### **A.4 Transmission Electron Microscopy, High Resolution-Transmission Electron Microscopy and High-Angle Annular Dark Field imaging**

Transmission Electron Microscopy (TEM) and High Resolution-Transmission Electron Microscopy (HR-TEM) has been used as tool to investigate the morphology and elemental composition of each material presented in this thesis. TEM is a microscopy technique operating under vacuum in which a beam of electrons is transmitted through a sample to form an image. The electrons are diffracted during the passage through the sample and then focused by electromagnetic objective lens in the image plane generating a picture. HR-TEM is able to detect differences in phase of the scattered electrons, allowing to investigate the crystalline structure of nanoparticles. HR-TEM allows also to perform Energy Dispersive X-Ray (EDX) analysis, which is a powerful tool for elemental recognition. In this thesis it has been employed to investigate the interface between the different phases of the hierarchical materials presented. The elemental recognition is allowed by the X-rays generated when the electron beams interact with the sample, which have characteristic energies for each element. In tandem with EDX, High-Angle Annular Dark Field (HAADF) imaging was performed. This technique is based on collecting scattered electrons with an annular dark-field detector and elaborating them into images. Since it is highly sensitive to variations in the atomic number of atoms in the sample, it's very useful when analyzing the composition of metal-carbon based hybrid materials. The samples were prepared depositing the samples on grids made from a metallic framework and covered with a carbon film.

#### **A.5 X-Ray Powder Diffraction Spectroscopy**

X-ray powder diffraction (XRD) is an analytical technique used mainly for phase identification in crystalline materials since diffraction patterns are the fingerprint of all crystalline substances. The analyzed material is finely ground, homogenized, and its average bulk composition is determined. This technique has been employed for the characterization of all the materials in order to obtain information about the crystallinity, dimension and phase of metal and metal oxide nanoparticles. X-ray diffraction techniques are based on the constructive interference between monochromatic X-rays and a crystalline sample. The X-rays are usually generated by a cathode ray tube, filtered to produce monochromatic radiation, collimated to concentrate it, and directed toward the sample. Their constructive interaction is described by Bragg's Law

$$n\lambda = 2d \sin \vartheta$$

where  $n$  is a positive integer and  $\lambda$  is the wavelength of the incident wave. The scansion of the sample through a range of  $2\theta$  angles, allows the diffracted X-rays to be detected, processed and counted. Since the material is powdered, its orientation is random, and all the diffraction directions of the lattice can be attained.

#### **A.6 X-Ray Photoelectron Spectroscopy**

X-ray Photoelectron Spectroscopy (XPS) is the most widely used surface analysis technique and in this thesis framework it has been employed to investigate the surface chemical composition of N-doped carbon encapsulated Co nanoparticles, in particular the ratio between the different types of N atoms present on the surface. XPS is performed by irradiating in high vacuum or ultra-high vacuum a material with a beam of X-rays of the proper energy, while simultaneously measuring the kinetic energy and number of electrons that escape from the most superficial layers of the sample material. Since each element is characterized by a set of XPS peaks at characteristic binding energies, which correspond to a specific electron configuration, this technique allows to determine the amount of element in each oxidation state on the surface of the sample. The ability to produce information on the chemical bond environment for every element present on the topmost few nm of any surface makes XPS a unique and valuable tool to rationalize any superficial property of a material.

#### **A.7 X-Ray absorption spectroscopy**

X-ray absorption spectroscopy (XAS) is a widely used technique for determining the local geometric and/or electronic structure of matter. The experiment is usually performed at synchrotron radiation facilities, which provide intense and tunable X-ray beams. Samples can be in the gas-phase, solution, or as solids. The technique is based on the measurement of the x-ray absorption coefficient of a material as a function of energy, and the data is collected by shining x-rays of a narrow energy resolution on the sample. As the X-rays energy is incremented, the incident and transmitted X-ray intensity is recorded. The number of transmitted photons is related to the type of atoms in the sample, its absorption coefficient  $\mu$  and its thickness  $x$ .

$$I_t = I_0 e^{-\mu x}$$

When the incident x-ray energy matches the binding energy of an electron in a sample's atom, there is a peak in the absorbed x-rays that causes a drop in the intensity of the transmitted ones. This phenomenon is known as an absorption edge and as each element has its own set of unique edges related to the binding energy of its electrons, this technique can be used to gain information on the elemental composition of a sample. Extended X-Ray Absorption Fine Structure (EXAFS) is the graph of the absorption coefficient of a material in function of energy, typically collected in a 500 – 1000 eV range beginning before an absorption edge of an element in the sample. The normalized absorption spectra are often called X-ray Absorption Near Edge Structure (XANES) spectra. The normalization to unit step height of the x-ray absorption coefficient is usually done through a linear regression to the region before and after the absorption edge and subtracting the pre-edge line from the entire data set while dividing by the absorption step height. The absorption step height can be determined by the difference between the pre-edge and post-edge lines at the value of energy associated to the absorption edge. XANES spectra can be employed to determine average oxidation state of the element in the sample.

#### **A.8 H<sub>2</sub>-Temperature programmed desorption**

H<sub>2</sub>-Temperature programmed desorption (H<sub>2</sub>-TPD) technique was employed to determine how H<sub>2</sub> interacts with the Pd-CeO<sub>2</sub>/C catalyst surface, and better understanding how the enhancement of HOR activity is correlated to this interaction. H<sub>2</sub>-TPD is a method that allow to observe how a target molecule desorb from a surface when its temperature is increased, giving information on the binding energy involved. Thermal desorption is described by the Arrhenius equation

$$r(\sigma) = -\frac{d\sigma}{dt} = v(\sigma)\sigma^n e^{-E_{act}(\sigma)/RT}$$

Where  $r(\sigma)$  is the desorption rate as a function of  $\sigma$ , the surface coverage,  $n$  is the order of desorption,  $v(\sigma)$  is a pre-exponential factor function of  $\sigma$  and  $E_{act}(\sigma)$  is the activation energy of desorption. This complex equation can be simplified by assuming the pre-exponential factor and the activation energy to be independent of the coverage and a linear heating rate, this way, the activation energy can be calculated. In a typical H<sub>2</sub>-TPD experiment, the sample is first exposed to a flux H<sub>2</sub> at a given temperature, until the desired initial surface coverage is reached. The sample's temperature is subsequently increased at a constant rate, in such a way to induce the thermal

desorption. The desorbed gas is collected and analyzed through a thermal conductivity detector. During the experiment, the partial gas pressure of hydrogen is measured in such a way to monitor its desorption rate as a function of the temperature. The measured increase in partial pressure as a function of time can be fitted in order to obtain relevant parameters, in particular the desorption energy. The analysis of the desorption curves, in particular the position of the desorption maxima and the shape of the spectra can also provide information on the desorption kinetics and on the adsorption mechanisms on the analyzed substrate.

### A.9 N<sub>2</sub> physisorption analysis

Adsorption techniques are fundamental when characterizing a catalyst since they allow to acquire information on two extremely important parameters: surface area and porosity. The activity of a catalyst is normally expressed as the rate per unit area of active surface, so, gaining information on this parameter is crucial to be able to compare the data obtained. N<sub>2</sub> physisorption technique is based on the physical adsorption of an inert gas, such as N<sub>2</sub>, on the surface of the sample, including the pores. Assuming that the gas adsorbed is a molecular monolayer, measuring the amount of N<sub>2</sub> adsorbed on the surface in relationship with its partial pressure allow us to calculate the specific surface area. The Brunauer, Emmett and Teller theory (BET) rationalize this process in the form of a mathematical model expressed as:

$$\frac{1}{v[(p_0/p) - 1]} = \frac{c - 1}{v_m c} \left( \frac{p}{p_0} \right) + \frac{1}{v_m c}$$

Where  $p$  and  $p_0$  are the equilibrium pressure and the saturated vapor pressure of the adsorbed gas,  $v$  is the amount of gas adsorbed,  $v_m$  is the monolayer adsorbed gas quantity, and  $c$  is called BET constant, defined as:

$$c = \exp\left(\frac{H_1 - H_L}{RT}\right)$$

Where  $H_1$  is the enthalpy of adsorption of the first layer and  $H_L$  is the enthalpy liberated on forming the second and subsequent layers. The plot of  $(p_0/p)$  in function of the volume adsorbed generates a curve that is called an isotherm. There are six types of isotherms and their shape give information on the morphology and dimension of the pores.

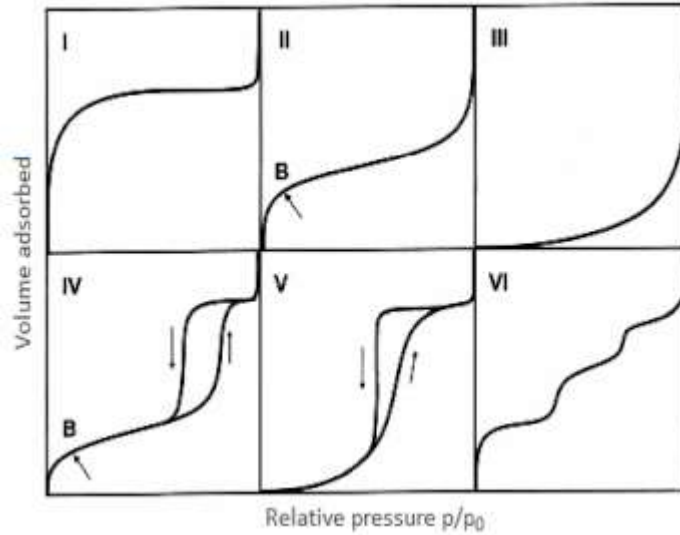


**Figure 6:** Classification of isotherms according to BET theory

Regardless of the shape of the curve, in the range  $0.05 < (p_0/p) < 0.35$  the profile is linear, and by knowing the slope and the intercept values associated, the total surface and the specific surface area can be calculated using the following equation:

$$S_{total} = \frac{(v_m N s)}{V}$$

$$S_{BET} = \frac{S_{total}}{a}$$

Where  $N$  is the Avogadro number,  $s$  is the adsorption cross section,  $V$  is molar volume of the adsorbate gas,  $a$  is the material mass. This technique has been used to characterize most of the materials presented in this thesis.

### A.10 Density functional theory (DFT)

Density functional theory (DFT) is a technique that, using computational quantum mechanical modelling, allows to investigate the electronic structure (principally the ground state), and therefore predict the behaviour of complex systems, like atoms, molecules, and the condensed phases. Using this theory, the properties of a many-electron system can be determined by using the spatially dependent electron density functionals. When dealing with heterogeneous catalysts, or in general material science, *ab initio* DFT calculations can be used to predict, on the basis of quantum mechanical considerations, how the material will behave in determinate conditions simulated with a model. The electronic structure of a system is evaluated through the application of a potential. This potential can be described as the sum of external potentials  $V_{ext}$  which are

determined by the structure and the elemental composition of the system and an effective potential  $V_{\text{eff}}$ , which represents interelectronic interactions. This approach allows to study a system with  $n$  electrons as a set of  $n$  one-electron Schrödinger-like equations. In this thesis framework, DFT has been used to model the way Pd binds on  $\text{CeO}_2$  in the Pd- $\text{CeO}_2/\text{C}$  catalyst and how  $\text{H}_2$  adsorbs on the material. Calculations were performed with all electron full potential method implemented in the Fritz-Haber-Institute ab-initio molecular simulations (FHI-aims) package.<sup>2</sup> The atomic zero-order regular approximation (ZORA) was used to treat relativistic effects for all the atoms in the system.<sup>3</sup> We used the “tight” settings for integration grids and the exchange-correlation energy was evaluated with the Perdew-Burke-Ernzerhof (PBE) functional.<sup>4</sup> The convergence criteria for the energy and force were set to  $10^{-6}$  eV and  $10^{-4}$  eV  $\text{\AA}^{-1}$ , respectively. Gaussian smearing with the width of 0.1 eV was used to speed up the convergence of the states near the Fermi level.  $\text{CeO}_2$  (110) surface model was used in this work, consisting of five atomic layers and has a vacuum gap of 10  $\text{\AA}$  perpendicular to the surface. Monkhorst–Pack Brillouin zone sampling was used with a 13x13x1 grid. During the geometry optimization, all the atoms are allowed to relax. The adsorption energy  $E_{\text{ads}}$  is defined as;

$$E_{\text{ads}} = (E_{\text{surface+adsorbate}}) - (E_{\text{surface}} + E_{\text{adsorbate}})$$

where  $E_{\text{surface}}$  and  $E_{\text{adsorbate}}$  are the energies of the bare surface and the free adsorbate in the gas phase, respectively and is the total energy of the interacting surface and the adsorbate. According to this equation, a more negative  $E_{\text{ads}}$  value corresponds to stronger adsorption. The HBE is calculated relative to  $\text{H}_2$  in the gas phase and is given by;

$$\text{HBE} = E_{\text{surface+adsorbate}} - E_{\text{surface}} - 0.5 E_{\text{H}_2}$$

where  $E_{\text{H}_2}$  is the energy of the gas-phase hydrogen molecule. The differential adsorption free energy is given by using the equation reported by Nørskov and coworkers.<sup>5</sup>

## Appendix B: Materials & Synthesis

### B1. Materials

Carbon Vulcan X-72 was purchased from Cabot Corporation. Cobalt acetate ( $\text{Co}(\text{ac})_2 \cdot 4\text{H}_2\text{O}$ ) perchloric acid ( $\text{HClO}_4$ , 65%) and isopropyl alcohol (99.5%) were purchased from Carlo Erba; imidazole, 1-10 phenanthroline, Nafion<sup>®</sup> 117 solution, nitric acid ( $\text{HNO}_3$ , 65%), potassium tetrachloropalladate ( $\text{K}_2\text{PdCl}_4$ ) and ethanol (96.0% and 99.0%) were purchased from Sigma-Aldrich. All the reagents were used as they were. All the experiments were conducted using milliQ water obtained using a Direct-Q<sup>®</sup> (Millipore) water purification system.

### B2. Mild oxidation of Carbon Vulcan X-72: Synthesis of ox-Vulcan

Carbon Vulcan X-72 was dispersed in a 4 M nitric acid solution in order to get a  $1 \text{ mg mL}^{-1}$  suspension. The suspension was sonicated for 15 minutes and then stirred for three hours. This optimized time is the more suitable to obtain the optimal degree of oxygenic groups and the lowest damage on the structure surface. The solid was then filtered on  $0.45 \mu\text{m}$  PTFE filter and washed with distilled water until the washing water reached neutrality and then recovered and left overnight in an oven at  $80 \text{ }^\circ\text{C}$ .

### B3. Synthesis of $\text{CeO}_2$ /ox-Vulcan hybrid

Ox-Vulcan was dispersed in ethanol by sonication for 30 minutes in order to get a  $0.5 \text{ mg mL}^{-1}$  suspension and a THF solution of  $\text{Ce}(\text{ODE})_4$ , freshly prepared with a procedure already reported by our group,<sup>6</sup> was added dropwise in order to obtain a metal oxide load of 45%. After 30 min of sonication, 20 mL of a 10% solution of  $\text{H}_2\text{O}$  in EtOH was added dropwise in order to hydrolyse the alkoxide and form amorphous  $\text{CeO}_2$ , and then sonicated again for 30 min. The solid was filtered through a  $0.45 \mu\text{m}$  PTFE filter and washed thoroughly with ethanol.

### B4. Synthesis of Pd- $\text{CeO}_2$ /ox-Vulcan hybrid

CeO<sub>2</sub>/ox-Vulcan was dispersed in ethanol in order to obtain a 0.5 mg mL<sup>-1</sup> suspension and alkalinized with NaOH 2 M (15 mL) until it reached pH ~ 10. A 5 mL water solution of K<sub>2</sub>PdCl<sub>4</sub> (Pd loading as to have a nominal 5 or 10 wt% in the final material) was added to the dispersion and the reaction mixture refluxed with stirring at 100 °C for 2 h. The solid was filtered through a 0.45 μm PTFE filter and washed with water and ethanol. The material was dried at 80 °C overnight and subjected to calcination in air at 200 °C for 5 h in order to crystallize the CeO<sub>2</sub> and remove the organic ligands.

## **B5. Synthesis of Co-CN-im and parent materials**

The synthesis of all the catalysts was performed by thermal decomposition. A 1:1 solution of the metal precursor (Co(ac)<sub>2</sub>·4H<sub>2</sub>O for Co-NC-im, Fe(NO<sub>3</sub>)<sub>3</sub>·9H<sub>2</sub>O for Fe-NC-im, Ni(NO<sub>3</sub>)<sub>2</sub>·H<sub>2</sub>O for Ni-NC-im and Mn(ac)<sub>2</sub>·4H<sub>2</sub>O for Mn-NC-im) and an organic precursor (imidazole for Co-NC-im, Fe-NC-im, Ni-NC-im and Mn-NC-im, 1,10-phenanthroline for Co-NC-phen) in milliQ water (typically 1.0 g in 6.5 mL) was prepared and agitated overnight. The solvent was then removed and the as obtained solid was transferred in an open alumina ceramic vessel and treated in a tubular furnace under Ar flow. After 1.5 h at 40 °C under Ar atmosphere, the temperature was raised to 900 °C with a rate of 5 °C per minute and maintained at the same temperature for 2 h. After cooling by natural convection of the vessel to room temperature, the obtained pyrolyzed material was ground using an agate mortar to obtain a fine powder. It was then dispersed in 0.5 M HClO<sub>4</sub> and subsequently stirred at 80 °C for 4 h. The acid-treated sample was filtered and washed with water. The procedure was repeated twice and then the obtained black powder was dried under vacuum and recovered.

## **B6. Synthesis of GO-COOH**

A suspension of cyanographene (G-CN) prepared as reported here<sup>7</sup> in water was put in a round bottom glass flask and HNO<sub>3</sub> was slowly added at room temperature until the final concentration of acid in the mixture reached a certain value, of 20%, 40% and 65%, respectively for the samples GA-20, GA-40 and GA-65. It was then heated under reflux at 100 °C while stirring for 24 h. The suspension was then left to cool to room temperature and then washed through centrifugation. After the solid stopped precipitating, acidic water (pH 4) was added to the mixture in order to induce precipitation by protonating the material and reducing its dispersibility. Stable aqueous

suspensions of the obtained samples were prepared by adjusting the pH of the purified suspension to ~8.

## **Appendix C: Apparatus and experimental procedures**

### **C.1 Electrochemical apparatus**

All electrochemical experiments were performed at room temperature using an Autolab 302 N electrochemical workstation (Metrohm). Electrochemical impedance spectroscopy (EIS) measurements were performed using a frequency response analyzer (FRA, AutoLab 302 N, Metrohm) at room temperature. For the rotating disk electrode (RDE) tests a glassy-carbon rotating disk electrode (Autolab RDE, Metrohm) was employed.

### **C.2 Full Cell testing**

#### **C.2.1 Direct Alcohol Fuel Cells testing apparatus**

The active fuel cell system, was purchased from Scribner-Associates (USA) and has a 25 cm<sup>2</sup> fuel cell fixture and an effective electrode area of 5 cm<sup>2</sup>. The MEAs were put together by mechanically pressing the anode, the cathode and a commercial Tokuyama A-201 anion exchange membrane obtained from Tokuyama Corporation. The anode was realized with a 2.25 cm<sup>2</sup> nickel foam (Heze Tianyu Technology Development Co, China), onto which was spread the appropriate amount of dense catalytic ink. The ink was prepared by introducing the catalyst (45 mg) into a 5 mL polyethylene container together with 26 mg of an aqueous 10 wt% dispersion of polytetrafluoroethylene (PTFE) to produce a binder loading of 5 wt% and 50 mg of water. The cathode used consisted in a carbon cloth 2.5x2.5 cm square containing a Fe-Co/C cathode electrocatalyst prepared by a method reported in a previous work.<sup>8,9</sup> The temperature of the cell under working conditions was kept at 60 °C by a thermocouple positioned inside the end plate at the cathode side. The fuel (water solution containing ethylene glycol or 1,2-propanediol 2 M in 2 M KOH) was delivered to the anode at 1 mL min<sup>-1</sup> with a peristaltic pump. The oxygen flow to the cathode was set at 0.05 mL min<sup>-1</sup> and the humidification temperature regulated at 40 °C. The fuel cell performance was monitored with an ARBIN BT-2000 5A 4 channels instrument. Fuel cell polarization curves were collected with 10 mV s<sup>-1</sup> scan rate from OCP to 0.1 V. Galvanostatic experiments were undertaken at a constant current density of 50 mA cm<sup>-2</sup>. The cell potential was

monitored, and the tests were stopped when the potential reached 0 V. Fuel exhausts were quantitatively and qualitatively analysed by  $^{13}\text{C}\{^1\text{H}\}$  NMR spectroscopy and HPLC.

### C.2.2 Anion Exchange Membrane Fuel Cells

Membrane-electrode assembly (MEA) preparation: the catalyst was deposited on gas diffusion electrode (GDE) for fabricating AEM-FC electrodes as described in previous publications.<sup>10–12</sup> Before preparing the electrocatalyst ink, a previously synthesized ETFE-based RG anion-exchange ionomer (AEI) powder, containing benzyltrimethylammonium functional groups was ground in a mortar for 10 min. The AEI powder was synthesized via the radiation-grafting of vinylbenzyl chloride onto an ETFE powder (Fluon Z8820X, supplied by AGC Europe) with subsequent amination using trimethylamine. For each cathode GDE, an ink was prepared by mixing Pt/C (Alfa Aesar, Johnson Matthey HiSpec 4000, 40% wt Pt) and AEI powder (20% wt of the total solid mass) together with 1 mL water and 9 mL 2-propanol. After being sonicated for 30 min the cathode catalyst ink was sprayed onto a Toray TGP-H-60 carbon paper gas diffusion substrate (Alfa Aesar, non-teflonated). It was then dried in air. For the anode GDEs, Pd-CeO<sub>2</sub>/C was used as electrocatalyst (with 20% wt AEI). The 5 cm<sup>2</sup> GDEs were loaded with  $0.30 \pm 0.02 \text{ mg}_{\text{Pd}} \text{ cm}^{-2}$  and  $0.40 \pm 0.02 \text{ mg}_{\text{Pt}} \text{ cm}^{-2}$  for anode and cathode electrodes, respectively. All electrodes and AEMs (made from radiation-grafting 15  $\mu\text{M}$  LDPE with VBC followed by amination with TMA, ion-exchange capacity (IEC) = 2.54 mmol/g) were immersed in aqueous KOH solution (1 mol L<sup>-1</sup>) for 1 h and then washed thoroughly in water (to remove excess KOH) before being assembled into a 5 cm<sup>2</sup> fuel cell fixture (Scribner Associates, USA) using 5 N m torque. An 850e fuel cell test station (Scribner Associates, USA) was used for testing the cell performances. The fuel cell temperature was kept at 80 °C and H<sub>2</sub> and O<sub>2</sub> fed with flow rates of 1 and 2 L min<sup>-1</sup>. The gases were supplied to the anode and cathode, respectively, with no back-pressurization. The MEAs were activated by discharging the cell at a constant voltage of 0.5 V during cell heating, until a steady current density was observed. Beginning-of-life AEM-FC performance data were collected under controlled galvanostatic discharge steps where data (at each current density) were recorded after potentials had stabilized. The internal ohmic resistances were estimated using the 850e instrument's internal current interrupt method.

### **C.3 H<sub>2</sub> temperature programmed desorption (H<sub>2</sub>-TPD) apparatus**

The spectra of Pd-CeO<sub>2</sub>/C and Pd/C were collected using an AutoChem 2920 (Micromeritics) operated in the flowing mode. A thermal conductivity detector (TCD) was employed to determine the H<sub>2</sub> concentration. The samples (0.1-0.2 g) were placed in the quartz reactor, and, after removing adsorbed water by heat treating the samples at 200 °C for 30 min, H<sub>2</sub> adsorption was carried out at 60 °C with a mixture of 10 vol.% H<sub>2</sub>/Ar at a flow rate of 50 mL min<sup>-1</sup>. Afterwards, the gas mixture was switched to Ar with a flow rate of 50 ml min<sup>-1</sup> until obtaining the baseline of TCD signal. Thermal desorption spectra were recorded with a temperature ramp of 10, 20 and 30 °C min<sup>-1</sup> up to 500 °C. The spectra were deconvoluted using skewed lognormal distribution.

### **C.4 Thermogravimetric apparatus**

For the thermogravimetric analysis (TGA), a TGA Q500 (TA Instruments) under air was used to analyze approximately 1 mg of each sample, equilibrating at 100 °C, and following a ramp of 10 °C min<sup>-1</sup> up to 800 °C.

### **C.5 Raman spectroscopy apparatus**

Raman spectra were recorded on a inVia Renishaw microspectrometer equipped with a Nd:YAG laser using an excitation wavelength of 532 nm. Preparation of the samples was carried out via deposition of the powder onto silicon wafers. For each sample, 5 points were recorded and averaged.

### **C.6 Transmission Electron Microscopy apparatus**

TEM micrographs were collected with a TEM Philips EM208, using an acceleration voltage of 100 kV. Samples were dispersed in ethanol and drop cast onto a TEM grid (200 mesh, copper, carbon only). High resolution TEM (HRTEM) were performed on a JEOL 2200FS microscope operating at 200 kV, equipped with an Energy Dispersive Spectrometer (EDS), in-column energy (Omega) filter, and high-angle annular dark-field (HAADF) detector.

### **C.7 X-ray powder diffraction spectroscopy apparatus**

X-ray powder diffraction (XRD) analysis were performed on a PANalytical X'PERT PRO diffractometer at room temperature, employing CuK $\alpha$  radiation ( $\lambda = 1.54187 \text{ \AA}$ ) and a PW3088/60-graded multilayer parabolic X-ray mirror for Cu radiation. The spectra were collected in the  $2\theta$  range from 5.0 to 120.08, with a continuous scan mode using an acquisition step size of  $2\theta = 0.02638$  and a counting time of 49.5 s.

### **C.8 N<sub>2</sub> Physisorption apparatus**

N<sub>2</sub> physisorption experiments were carried out on a Micrometrics ASAP 2020 automatic analyzer. The samples were first degassed in vacuum at 120 °C for 12 h prior to N<sub>2</sub> adsorption at liquid nitrogen temperature.

### **C.9 X-Ray Photoelectron Spectroscopy apparatus**

For XPS experiments, a SPECS Sage HR 100 spectrometer equipped with a non-monochromatic X ray source of Magnesium with a K $\alpha$  line of 1253.6 eV energy and 250 W was employed. The samples, placed perpendicular to the analyzer axis were calibrated using the 3d<sub>5/2</sub> line of Ag with a full width at half maximum (FWHM) of 1.1 eV. An electron flood gun was used to compensate for charging during XPS data acquisition. Measurements were made in an ultra-high vacuum (UHV) chamber with a selected resolution of 30 and 15 eV of Pass Energy and 0.5 and 0.15 eV/step for the survey and high-resolution spectra, respectively. CasaXPS 2.3.16 PR 1.6 software was used to fit the XPS data. In the case reported, the Shirley-type background subtraction was employed, and all curves were defined as 40% Lorentzian, 60% Gaussian. Atomic ratios were computed from experimental intensity ratios and normalized by atomic sensitivity factors.

### **C.10 X-ray absorption spectroscopy (XAS) apparatus**

Measurements were carried out at the Pd L<sub>3</sub>-edge in the transmission mode at the beamline 8-ID at the NSLS-II, Brookhaven National Laboratory. The data were processed and fitted using the IFEFFIT-based Athena<sup>13</sup> and Artemis<sup>13</sup> programs. Scans were calibrated, aligned and normalized with background removed using the IFEFFIT suite<sup>14</sup> (version 1.2.9, IFEFFIT Copyright 2005,

Matthew Newville, University of Chicago, <http://cars9.uchicago.edu/ifeffit/>). The  $\chi(R)$  were modeled using single scattering paths calculated by FEFF6.<sup>15</sup>

### **C.11 Nuclear Magnetic Resonance spectroscopy apparatus**

NMR spectra were acquired with a with a Bruker Avance DRX 400 spectrometer. Deuterated solvents (Sigma-Aldrich) used for NMR measurements were dried with activated molecular sieves; 1,4-dioxane was used as internal standard for product quantification.

### **C.12 High Performance Liquid Chromatography**

A UFLC Shimadzu Chromatograph equipped with refraction index detector (RID) was used; the column is a GRACE-Alltech OA-1000 Organic Acids (300mm x 6.5mm), thermostated at 35 °C. The eluent was 0.01 N H<sub>2</sub>SO<sub>4</sub> and the eluent flow was 0.8 mL min<sup>-1</sup>.

### C.13 References

- (1) Bard, A. J.; Faulkner, L. R. *Electrochemical Methods Fundamentals and Applications*; John Wiley & Sons, I., Ed.; 2001.
- (2) Blum, V.; Gehrke, R.; Hanke, F.; Havu, P.; Havu, V.; Ren, X.; Reuter, K.; Scheffler, M. Ab Initio Molecular Simulations with Numeric Atom-Centered Orbitals. *Comput. Phys. Commun.* **2009**, *180* (11), 2175–2196.
- (3) Van Lenthe, E.; Baerends, E. J.; Snijders, J. G. Relativistic Total Energy Using Regular Approximations. *J. Chem. Phys.* **1994**, *101* (11), 9783–9792.
- (4) Perdew, J. P.; Burke, K.; Ernzerhof, M. Generalized Gradient Approximation Made Simple. *Phys. Rev. Lett.* **1996**, *77* (18), 3865–3868.
- (5) Skulason, E.; Tripkovic, V.; Bjorketun, M. E.; Gudmundsdottir, S.; Karlberg, G.; Rossmeisl, J.; Bligaard, T.; Jonsson, H.; Nørskov, J. K. Modeling the Electrochemical Hydrogen Oxidation and Evolution Reactions on the Basis of Density Functional Theory Calculations. *J. Phys. Chem. C* **2010**, *114* (12), 110913.
- (6) Cargnello, M.; Wieder, N. L.; Montini, T.; Gorte, R. J.; Fornasiero, P. Synthesis of Dispersible Pd@CeO<sub>2</sub> Core-Shell Nanostructures by Self-Assembly. *J. Am. Chem. Soc.* **2010**, *132* (4), 1402–1409.
- (7) Bakandritsos, A.; Pykal, M.; Boński, P.; Jakubec, P.; Chronopoulos, D. D.; Poláková, K.; Georgakilas, V.; Čépe, K.; Tomanec, O.; Ranc, V.; et al. Cyanographene and Graphene Acid: Emerging Derivatives Enabling High-Yield and Selective Functionalization of Graphene. *ACS Nano* **2017**, *11* (3), 2982–2991.
- (8) Bambagioni, V.; Bianchini, C.; Filippi, J.; Lavacchi, A.; Oberhauser, W.; Marchionni, A.; Moneti, S.; Vizza, F.; Psaro, R.; Dal Santo, V.; et al. Single-Site and Nanosized Fe-Co Electrocatalysts for Oxygen Reduction: Synthesis, Characterization and Catalytic Performance. *J. Power Sources* **2011**, *196* (5), 2519–2529.
- (9) Chen, Y.; Bellini, M.; Bevilacqua, M.; Fornasiero, P.; Lavacchi, A.; Miller, H. A.; Wang, L.; Vizza, F. Direct Alcohol Fuel Cells: Toward the Power Densities of Hydrogen-Fed Proton Exchange Membrane Fuel Cells. *ChemSusChem* **2015**, *8* (3), 524–533.
- (10) Wang, L.; Magliocca, E.; Cunningham, E. L.; Mustain, W. E.; Poynton, S. D.; Escudero-Cid, R.; Nasef, M. M.; Ponce-Gonzalez, J.; Bance-Souahli, R.; Slade, R. C. T.; et al. An Optimised Synthesis of High Performance Radiation-Grafted Anion-Exchange Membranes. *Green*

*Chem.* **2017**, *19* (3), 831–843.

- (11) Wang, L.; Brink, J. J.; Liu, Y.; Herring, A. M.; Ponce-González, J.; Whelligan, D. K.; Varcoe, J. R. Non-Fluorinated Pre-Irradiation-Grafted (Peroxidated) LDPE-Based Anion-Exchange Membranes with High Performance and Stability. *Energy Environ. Sci.* **2017**, *10* (10), 2154–2167.
- (12) Lu, Y.; Wang, L.; Preuß, K.; Qiao, M.; Titirici, M. M.; Varcoe, J.; Cai, Q. Halloysite-Derived Nitrogen Doped Carbon Electrocatalysts for Anion Exchange Membrane Fuel Cells. *J. Power Sources* **2017**, *372* (November), 82–90.
- (13) Newville, M. IFEFFIT: Interactive XAFS Analysis and FEFF Fitting. *J. Synchrotron Radiat.* **2001**, *8*, 322–324.
- (14) Newville, M.; Livin, P.; Yacoby, Y.; Rehr, J. J.; Stern, E. A. Near-Edge x-Ray-Absorption Fine Structure of Pb: A Comparison of Theory and Experiment. *Phys. Rev. B* **1993**, *47* (21), 14126–14131.
- (15) Ankudinov, A.; Ravel, B.; Rehr, J. J.; Conradson, S. D. Real-Space Multiple-Scattering Calculation and Interpretation of X-Ray-Absorption near-Edge Structure. *Phys. Rev. B - Condens. Matter Mater. Phys.* **1998**, *58* (12), 7565–7576.